Università degli Studi di Napoli Federico II

Doctoral Thesis

Cosmological probes from weak lensing analysis on galaxy clusters

Author:
Lorenzo Ingoglia

Supervisors:
Pr. Giovanni Covone
Dr. Mauro Sereno

A thesis submitted in fulfillment of the requirements for the degree of Doctor of Physics

in the

34^{th} Cycle
Department of Physics

March 10, 2022

Declaration of Authorship

I, Lorenzo INGOGLIA, declare that this thesis titled, "Cosmological probes from weak lensing analysis on galaxy clusters" and the work presented in it are my own. I confirm that:

- This work was done wholly or mainly while in candidature for a research degree at this University.
- Where any part of this thesis has previously been submitted for a degree or any other qualification at this University or any other institution, this has been clearly stated.
- Where I have consulted the published work of others, this is always clearly attributed.
- Where I have quoted from the work of others, the source is always given. With the exception of such quotations, this thesis is entirely my own work.
- I have acknowledged all main sources of help.
- Where the thesis is based on work done by myself jointly with others, I have made clear exactly what was done by others and what I have contributed myself.

Signed: Lorenzo Ingoglia

Date: March 10, 2022

"*Looking at the universe as a whole; cosmology, the birth, life and death of the whole universe, we used to have a nice simple model. Then we had to add things like dark energy, and our nice simple picture is getting messier and messier and messier.*"

Jocelyn Bell Burnell - Beautiful Minds

"*Astronomy is useful because it raises us above ourselves; it is useful because it is grand... It shows us how small is man's body, how great his mind, since his intelligence can embrace the whole of this dazzling immensity, where his body is only an obscure point, and enjoy its silent harmony.*"

Henri Poincaré - La Valeur de la Science

"*Something deeply hidden had to be behind things.*"

Albert Einstein - Autobiographical Notes

"*The history of astronomy is a history of receding horizons.*"

Edwin P. Hubble - Realm of the Nebulae

"*We've always defined ourselves by the ability to overcome the impossible. And we count these moments. These moments when we dare to aim higher, to break barriers, to reach for the stars, to make the unknown known. We count these moments as our proudest achievements... And that our greatest accomplishments cannot be behind us, because our destiny lies above us.*"

Cooper - Interstellar

"*Do or do not, there is no try.*"

Yoda - Star Wars

UNIVERSITÀ DEGLI STUDI DI NAPOLI FEDERICO II

Abstract

Monte Sant'Angelo Campus
Department of Physics

Doctor of Physics

Cosmological probes from weak lensing analysis on galaxy clusters

by Lorenzo INGOGLIA

The Universe is composed of matter distributed on the large scale as a web-like structure. Galaxy clusters are located at the densest regions of the cosmic structure, the dark matter halos. Therefore, studying this class of objects gives crucial insights into the evolution of the matter distribution in the Universe and precious clues on the nature of the enigmatic dark matter. The dark matter, largely dominant in the halos, is invisible with direct observations. However, we can determine the dark matter distribution around galaxy clusters by means of weak gravitational lensing. This method takes advantage of the deflection of light induced by massive objects, namely clusters of galaxies, to derive their mass density profiles on scales reaching the halo boundaries and beyond, extending into the regime of the large-scale structure.

Galaxy clusters and their hosts, the halos, are biased tracers of the underlying matter density field. This effect is characterized by the so-called halo bias, a parameter scaling the density profiles driven by the correlated matter distribution around galaxy clusters. During my thesis, I investigated the relation between the halo mass and the halo bias derived from stacked weak lensing profiles of about 7000 AMICO galaxy clusters. This catalog is assessed from the third data release of KiDS, the ESO public survey. Stacking the profiles is a process that reduces the statistical noise of the lensing signal and increases the quality of the measured parameters. We thus split the cluster sample into 14 redshift-richness bins and derived the halo bias and the virial mass in each bin by means of a standard Bayesian inference. It is carried out by a fiducial density model broken in a one-halo term, identified with the galaxy cluster halo and its physical characteristics (mass, concentration, etc), and a two-halo term, associated with matter distributed in distinct pairs of halos and directly proportional to the halo bias. The two terms of the halo profile correlate in such a way that the halo bias follows an increasing function of mass. This relation has been shown and modeled in several theoretical studies based on N-body numerical simulations, in the framework of the ΛCDM standard cosmological model. The results of our study show an agreement within 2σ between our estimation of the halo bias and theoretical predictions. The measurements of the average mass and bias over the stacked density profile of the full cluster catalog give $\mathrm{M}_{200c} = (4.9 \pm 0.3) \times 10^{13} \mathrm{M}_{\odot}/h$ and $\mathrm{b_h}\sigma_8^2 = 1.2 \pm 0.1$. Considering the degenerated form of the halo bias and the additional prior of a bias-mass relation from numerical simulations, we constrained the normalization of the matter power spectrum. We found $\sigma_8 = 0.63 \pm 0.10$ with the matter density of the Universe set at $\Omega_\mathrm{m} = 0.3$. Even if a fixed cosmology does not allow to complete a fully independent cosmological inference, this result agrees with

other studies based on CMB data, cluster clustering, cluster counts, and cosmic shear analyses within 2σ.

In the upcoming years, the next generation of sky surveys will provide deeper and wider catalogs of data for cosmologists to answer modern inquiries. As part of my thesis, I have been involved in the development of a numerical tool in the context of the Science Ground Segment data processing pipeline of the Euclid consortium. COMB-CL is a python module (at the moment, in a state of prototype) that aims to measure the weak lensing mass of galaxy clusters. The code is built in such a way that catalogs of cluster and galaxy properties (position, redshift, shear, color, etc) are input and, given a fiducial cosmology and a model for the halo density profile, catalogs of weak lensing profiles and related masses are output. This toolkit has been accepted and will be reviewed in a paper of the key project LE3-CL-2 regarding the characterization of the properties of detected galaxy clusters.

Acknowledgements

While reminding these past three years, my thoughts go to every single person who accompanied me during my Ph.D., in both good and hard times. It is difficult for me to resume all these moments spent in a few words, as they are numerous. Instead, I will try to acknowledge everyone I met, supported me, or shared these memories with me.

Before going through more personal details, I would like to address my warm thanks to the reviewers for their deep interest to my work, their careful reading of my manuscript and their relevant questions and remarks throughout my defense.

Giovanni, I would like to especially thank you for your fantastic leadership. Working under your guidance deeply helped me to better organize my tasks and strengthened my efficiency. You always challenged me to go above and beyond what I could do and, thanks to your instructions, I learned the real job of an astrophysicist. My special thank also goes to you, Mauro. You taught me to work with a cautiously and rigorous approach, and your pertinent remarks were extremely precious to progress as a scientist. More generally, I thank both of you for your kind advice and your strong support during all this period.

Thank you as well to the AMICO collaboration: Giovanni, Mauro, Carlo, Mario, Federico, Giorgio, Lauro, Matteo, Gianluca, Valerio, Feliciana, Denis, Emanuella, Gabriele and Sandro. Our meetings were extremely valuable for my work as your various feedback and your significant contribution has been fundamental for the publication of the study on AMICO clusters.

Many thanks to the COMB-CL team, and in particular to Samuel. Your scientific and technical knowledge has been considerable support for improving my skills. Collaborating with you on this promising project is a really pleasant experience as you have always been nice and concise in your communication.

My thesis has been achieved thanks to the University of Napoli Federico II. I would like to express my deepest gratitude to the administrative and maintenance members of which, specifically Guido for his kind involvement in the Ph.D. student life.

I would like to acknowledge a thousand times the students of the Ph.D. office. Alex, Pegah, Pratibha, and Zahra, your friendship has been real support during this pandemic period. I will always remember the funny moments we spend at the university or in the city center. I would also like to thank Mattia, Andrea, Luca, Raphaele, and the other students for the sweet time spent together, in particular, these delicious pizze shared at lunch and dinner.

A part of my thoughts go to my master thesis advisors at LAM, Eric and Carlo, who rightly recommended me this Ph.D. and continuously gave me their support all along with my thesis.

To conclude, I will switch to my native tongue to thank my friends and family members. Comme vous le savez, cette thèse fut une rude épreuve pour moi, c'est pourquoi je tenais à tou·te·s vous remercier pour votre soutien. Merci aux potes avec qui j'ai partagé le début de cette expérience au LAM, et même si nous étions distancés par nos travaux respectifs j'ai apprécié prendre de nos nouvelles à chaque instant. Je remercie également mes ami·e·s de longue date qui ont toujours été là pour moi. Franchement c'était super de vous avoir tout au long de cette thèse. Bien entendu un énorme merci à mes parents, mon frère, ma soeur, mes cousin·e·s et tou·te·s celles et ceux qui s'incluent comme membres de cette famille pour votre soutien psychologique, vos conseils et votre aide dans ce parcours. Chacun·e de vous m'a apporté la ressource nécessaire pour réaliser le chemin parcouru. Et enfin je tenais à te remercier, toi qui m'a accompagné de la meilleure des façons dès le début de cette aventure, car sans toi rien de cela n'aurait été possible. Ton soutien en particulier dans les moments les plus difficiles a été pour moi indispensable à l'aboutissement de ce projet. Merci infiniement à vous tou·te·s.

Contents

Declaration of Authorship iii

Abstract vii

Acknowledgements ix

1 Introduction 1
- 1.1 Overview of the Universe . . . 1
  - 1.1.1 History of cosmology . . . 1
  - 1.1.2 Timeline of the Universe . . . 3
  - 1.1.3 Expansion of the Universe . . . 3
- 1.2 Standard model of cosmology . . . 4
  - 1.2.1 Cosmological principle . . . 5
  - 1.2.2 Cosmological probes . . . 5
  - 1.2.3 General relativity . . . 5
  - 1.2.4 FLRW metric . . . 6
  - 1.2.5 Cosmological parameters . . . 8
  - 1.2.6 Cosmological distances . . . 10
- 1.3 Growth of structures . . . 12
  - 1.3.1 Density perturbations . . . 12
  - 1.3.2 Matter distribution . . . 14
  - 1.3.3 Non-linear evolution . . . 18
  - 1.3.4 Bias of halos . . . 21
- 1.4 Clusters of galaxies . . . 22
  - 1.4.1 Cluster formation . . . 22
  - 1.4.2 Cluster properties . . . 22
  - 1.4.3 Cluster observations . . . 24
- 1.5 Purposes of the thesis . . . 25

2 Theoretical framework 27
- 2.1 Formalism of weak gravitational lensing . . . 27
  - 2.1.1 Lens equations . . . 27
  - 2.1.2 Convergence and shear . . . 29
  - 2.1.3 Convergence power spectrum . . . 32
- 2.2 Models of the halo density . . . 34
  - 2.2.1 One-halo term . . . 35
  - 2.2.2 Miscentering correction . . . 37
  - 2.2.3 Two-halo term . . . 38
- 2.3 Predictions of the halo mass . . . 39
  - 2.3.1 Halo concentration . . . 39
  - 2.3.2 Halo bias . . . 41

3 Data analysis **45**
3.1 Description of the KiDS data 45
3.1.1 Third data release 45
3.1.2 Sources catalog 47
3.1.3 AMICO clusters 48
3.2 Lensing processing of catalogs 51
3.2.1 Lensing computation 51
3.2.2 Stacked signal 54
3.2.3 Selection method 54
3.3 Sources of error and fitting process 59
3.3.1 Statistical uncertainty 60
3.3.2 Systematic effect 60
3.3.3 MCMC method 65
3.4 Results of the study 67
3.4.1 Primary outcomes 67
3.4.2 Mass-richness relation 69
3.4.3 Cluster sparsity 69
3.4.4 Mass-concentration relation 72
3.4.5 Mass-bias relation 74
3.4.6 Cosmological inference 76

4 Euclid project **81**
4.1 Mission of the Euclid consortium 81
4.1.1 Scientific objectives 81
4.1.2 Ground segment 83
4.2 COMB-CL numerical toolkit 85
4.2.1 Global description 85
4.2.2 Data products 86
4.2.3 Prototype structure 87
4.2.4 LSS covariance 89
4.2.5 Development forecasts 89

5 Conclusion **93**
5.1 Summary 93
5.2 Discussion 95
5.3 Perspectives 96

Bibliography **99**

A Related publications **113**

List of Figures

1.1 Universe history . . . 4
1.2 CMB anisotropies . . . 6
1.3 Curvature of space . . . 7
1.4 Universe scale evolution . . . 9
1.5 Universe energy evolution . . . 10
1.6 Cosmological distances . . . 12
1.7 Window functions . . . 14
1.8 Correlation functions . . . 15
1.9 Power spectra . . . 17
1.10 Variance functions . . . 17
1.11 Millennium simulation . . . 19
1.12 Halo mass functions . . . 20
1.13 Overdensity for collapse . . . 21
1.14 Distribution of galaxies . . . 23
1.15 Abell 1689 matter content . . . 24

2.1 Diagram of light deflection . . . 28
2.2 Diagram of a lens system . . . 30
2.3 Convergence power spectra . . . 33
2.4 Halo model . . . 35
2.5 Theoretical mass-concentration relations . . . 40
2.6 Theoretical mass-bias relations . . . 42

3.1 KiDS-DR3 tiles distribution . . . 46
3.2 KiDS-DR3 redshift distribution . . . 48
3.3 AMICO cluster redshift-richness distribution . . . 50
3.4 Shear profile of J225151.12-332409 cluster . . . 53
3.5 AMICO KiDS-DR3 stacked shear profile . . . 55
3.6 *gri* color-color diagram . . . 57
3.7 Redshift distribution of color-color selected sources . . . 58
3.8 Bootstrap correlation matrices . . . 61
3.9 Randoms redshift distribution . . . 63
3.10 Randoms stacked shear profiles . . . 64
3.11 Halo parameters posteriors . . . 66
3.12 Constraints on AMICO stacked shears . . . 68
3.13 AMICO mass-richness relation . . . 71
3.14 Halo sparsity of AMICO clusters . . . 73
3.15 AMICO mass-concentration relation . . . 75
3.16 AMICO mass-concentration relation . . . 76
3.17 Posterior distributions for σ_8 . . . 78
3.18 Results on σ_8 . . . 79

4.1 Footprint of Euclid . . . 82

4.2 EC SGS architecture 84
4.3 COMB-CL data products 86
4.4 COMB-CL prototype structure 88
4.5 LSS covariance matrix 90

List of Tables

3.1 Pattern of the redshift-richness bins . . . 54
3.2 Contamination of *gri*-CC selections in COSMOS . . . 59
3.3 Halo parameters results . . . 70
3.4 Results on σ_8 . . . 77

List of Abbreviations

AMICO	**A**daptive **M**atched **I**dentifier (of) **C**lustered **O**bjects
BAOs	**B**aryon **A**coustic **O**scillations
BCG	**B**rightest **C**luster **G**alaxy
BMO	**B**altz-**M**arshall-**O**guri
BPZ	**B**ayesian **P**hotometric-**z**
CC	**C**olor-**C**olor
CDF	**C**umulative **D**istribution **F**unction
CFHTLenS	**C**anada **F**rance **H**awaii **T**elescope **Len**sing **S**urvey
CMB	**C**osmic **M**icrowave **B**ackground
COSMOS	**Cosm**ic Ev**o**lution **S**urvey
Dec	**Dec**lination
DM	**D**ark **M**atter
EC	**E**uclid **C**onsortium
ESA	**E**uropean **S**pace **A**gency
ESO	**E**uropean **S**pace **O**rganization
FLRW	**F**riedmann-**L**emaître-**R**obertson-**W**alker
FoV	**F**ield **o**f **V**iew
GALEV	**Gal**laxy **Ev**olution
GAMA	**G**alaxy **A**nd **M**ass **A**ssembly
GR	**G**eneral **R**elativity
HMF	**H**alo **M**ass **F**unction
HSC	**H**yper **S**uprime-**C**am
HST	**H**ubble **S**pace **T**elescope
HZ	**H**arrison-**Z**eldovich
ICM	**I**ntraCluster **M**edium
KiDS	**Ki**lo-**D**egree **S**urvey
LSS	**L**arge-**S**cale **S**tructures
LSST	**L**arge **S**ynoptic **S**urvey **T**elescope
MCMC	**M**arkov **C**hain **M**onte **C**arlo
MOC	**M**ission **O**perations **C**entre
NFW	**N**avarro-**F**renck-**W**hite
ODR	**O**rthogonal **D**istance **R**egression
OGS	**O**peration **G**round **S**egment
OU	**O**rganization **U**nit
PDF	**P**robability **D**ensity **F**unction
PSF	**P**oint **S**pread **F**unction
RA	**R**ight **A**ascension
RMS	**R**oot **M**ean **S**quare
SDSS	**S**loan **D**igital **S**ky **S**urvey
SED	**S**pectral **E**nergy **D**istribution
SGS	**S**cience **G**round **S**egment
SNR	**S**ignal (to) **N**oise **R**atio
SOC	**S**cience **O**perations **C**entre

SPT	**S**outh **P**ole **T**elescope
SWG	**S**cience **W**orking **G**roup
SZ	**S**unyaev-**Z**eldovich
VLT	**V**ery **L**arge **T**elescope
VST	**V**LT **S**urvey **T**elescope
WL	**W**eak **L**ensing
WMAP	**W**ilkinson **M**icrowave **A**nisotropy **P**robe

Physical Constants

Speed of Light	$c = 2.997\,924\,58 \times 10^{8}\,\mathrm{m\,s^{-1}}$
Gravitational Constant	$G = 6.674\,30 \times 10^{-11}\,\mathrm{m^{3}\,kg^{-1}\,s^{-2}}$
Solar mass	$M_{\odot} = 1.988\,47 \times 10^{30}\,\mathrm{kg}$
Parsec	$\mathrm{pc} = 3.085\,677\,581 \times 10^{16}\,\mathrm{m}$
Hubble Constant	$H_0 = 100\,h\,\mathrm{km\,s^{-1}\,Mpc^{-1}}$

List of Symbols

a	scale factor	
b_h	halo bias	
c	concentration	
D/d	distance	m
h	Hubble parameter	
k	wavenumber	m^{-1}
M/m	mass	kg
P	matter power spectrum	m^{-3}
R/r	radial distance	m
t	time	s
T	temperature	K
W/w	weight	
z	redshift	
δ	overdensity	
Δ	dimensionless matter power spectrum	
ξ	matter correlation function	
ε	ellipticity	
γ	shear	
κ	convergence	
Ω	dimensionless density	
$\hat{\alpha}$	deflection angle	rad
β	angular position	rad
θ	apparent angle	rad
ρ	matter density	$kg\,m^{-3}$
Σ	surface matter density	$kg\,m^{-2}$

À ma famille, mes amis, et celle qui se reconnaîtra.

Chapter 1

Introduction

The Universe has always been a source of curiosity to mankind by how vast and unknown it is. A large number of riddles remain unsolved despite the fast and efficient progress of science in the last decades, as each discovery gives way to new questions. Amongst the breakthroughs is the uncovering of dark matter and dark energy as the principal ingredients of the standard cosmological model. Our knowledge of the origin and the evolution of the cosmic flows has strongly increased with this model but still needs to be completed by the study of the matter distribution within the largest and the most massive cosmological objects in the Universe: clusters of galaxies. Weak gravitational lensing is a relatively recent method permitting to measure the mass component of such gravitationally bound systems, whether it is visible or dark, and without requiring any assumption about their composition or dynamical state. This technique is a powerful tool to probe cosmology.

This Thesis contributes to developing our understanding of the essence of matter by studying its distribution in galaxy clusters. This introduction will review the history of cosmology and the evolution of an expanding Universe, the model that today best describes such Universe, the global physical processes leading to the growth of structures, and the cosmological framework of galaxy clusters as baselines to complete a thorough analysis on large optical surveys.

1.1 Overview of the Universe

Regarding the well-known "Big Bang" Theory, the Universe arises from a 13.8 years ago primordial singularity, giving birth to hundreds of billion galaxies, each of them containing the same amount of stars among which the Sun allowed to create life on earth.

1.1.1 History of cosmology

Cosmology is the study of the formation, evolution, and interaction of the various components of the Universe, from galaxies and clusters to the large-scale structure, from the early moments to nowadays. Since the beginning of human being, astrophysical observations has always been a source of motivation to better understand our Universe. This curiosity gave rise to various beliefs and modelings across civilizations, becoming preciser as soon as advanced technology allowed new observations and brought to discoveries.

In the beginning, anthropologists think our ancestors, animated by faith in a magic Universe, incarnated heavenly bodies with spirits, in particular the Sun and the Moon considered as two distinct bodies, one belonging to the day and the other to the night. As time goes by, civilizations gave more importance and power to these spirits and disconnected them from nature. They transformed spirits into gods and their vision of the Universe turned mythical. The first Mesopotamian civilizations (3000-2000 B.C.) believed in the Babylonian mythology in which the world arises from a conflict between the cosmic primordial chaos and the gods. Almost at the same period, the Egyptians gave to the god of Sun, Râ, a central role in their mythology related to the existence of life. In the Indian mythical Universe, Brahma, the god creator, conceived the world during his dream. In this mythology, the cycles of the cosmos are associated with Brahma's breath: the Universe is contracting when Brahma expires and is expanding when Brahma inspires. This recall the discovery of the expansion of the Universe by Hubble. Each cycle lasts about 8.6 billion years, which is surprisingly consistent with modern cosmology, as the age of the Universe is about 14 billion years. Over time, humans remarked how the cosmos is regular: the periodic appearance of the Moon, the Sun, and the positions of the stars in the sky relative to the seasons or the fixed patterns designed by the stars. Humans used all these comforting phenomena to enhance their life being, as with the navigation or the prediction of seasons, essential for agriculture. A perfect example of the historical astronomical instrument is the Stonehenge monument in the south of England, a huge cosmic calendar built by a 4000 years old civilization marking the passage of seasons.

With the emergence of mathematics in ancient Greece (500-300 B.C.), the concept of a geocentric Universe composed of spheres on which lie cosmic objects (the Moon, the planets, the Sun and the stars, the Earth being at the center of the spheres) arrived with Pythagoras and Plato. Aristotle resumed the idea by increasing the number of spheres to 55 due to the irregular movements of the planets compared to the stars ("planet" means "vagabond" in ancient Greek), and improved the model by adding a metaphysical dimension: the straight separation between an "imperfect" earth, on which all the natural movements of elements are vertical (dirt and water fall while air and fire rise), and a "perfect" sky, where the object follow a circular uniform movement. Later on, due to the erratic trajectories of the planets, Ptolemy (100-200 A.D.) moved their position on smaller spheres called "epicycle", centered on the celestial sphere.

This model is accepted during the 15 next century until the Copernican revolution. With novel and preciser observations on the dynamics of planets, the limited Ptolemaic system couldn't explain their trajectories and Nicolas Copernicus solved this problem by redefining the spheres of the planets, including the Earth, centered on the Sun. Around the years 1600, Johannes Kepler deduced from the observations of Tycho Brahe that the planets follow an elliptical trajectory and derived the famous Kepler's laws governing the movements of the planets. The Copernican revolution has been supported with the first observations of telescopes built by the Italian Galileo. However, the heliocentric system caused many conflicts with the Church since it denied the central position of humans in the Universe. For instance, Galileo has been forced to renounce the Copernican system, while Giordano Bruno, a Dominican monk supporting the idea of infinite worlds, has been sentenced to be burned alive. The Church's hostility against the novel theories of the Universe disrupted advances and progress in sciences.

It's only at the end of the 17th century that Isaac Newton (1687) published the laws of universal gravitation. By connecting the dynamics of objects on Earth (and the famous apple falling from the tree) to the dynamics of a celestial object, Newton removed the limits between the Earth and the sky set one thousand years ago by Aristotle. The movement of a body becomes predictable with mathematical equations, and our vision of the Universe turned deterministic.

The latest century has been primordial in the progress of astrophysics and cosmology, in particular thanks to the publication of the General Relativity by Albert

Einstein in 1915 (Einstein, 1915) and the first models of the Universe (de Sitter, 1917; Friedmann, 1924; Lemaitre, 1926). The standard cosmological model, detailed in Section 1.2, is considered the model that currently best describes all astrophysical observations. This model is based on the solutions to Einstein's field equations in the framework of General Relativity and general assumptions of isotropy and homogeneity of the Universe on large scales.

1.1.2 Timeline of the Universe

Due to the lack of observations it is still unclear what happened right after the Big Bang, but according to the standard model of cosmology (see Section 1.2), the Universe cools down through a phase of exponential expansion, the "inflation", in which small inhomogeneities appears in the matter density field. The first nuclei of hydrogen and helium are created about one second right after the Big Bang during a phase called "primordial nucleosynthesis", which ends about three minutes later. During the next 380000 years, the Universe is formed of an extremely hot and dense plasma of particles (protons and electrons). At this stage, the Universe is too dense and hot to diffuse its light, since all the emitted photons are immediately absorbed by the plasma. Once the Universe becomes sufficiently cold, the first atoms are assembled from the free electrons and nuclei during the "recombination" phase, and let the first light of the Universe, the cosmic microwave background (CMB), to be diffused with the "matter-radiation decoupling" phase. As the Universe is expanding, it becomes neutral as a diffuse gas of hydrogen and helium emitting no light. This period is called the "dark ages". This gas then condensates into the first stars during the "reionization epoch", which follows the hierarchical formation of galaxies, clusters, and the large-scale structure. The second phase of accelerated expansion starts at the age of about 7 billion years. The source of this acceleration is supposedly assumed to be a cosmological fluid with negative pressure, the Dark Energy, which today dominates the energy budget of the Universe. Figure 1.1 resumes the evolution of the Universe, from its birth to the present time.

1.1.3 Expansion of the Universe

The expansion of the Universe is an observable phenomenon first predicted by Lemaître (1927) and first measured by Hubble (1929). In particular, the distances of galaxies D and their recessional velocity V are linearly related as:

$$\mathrm{V} = \mathrm{H}_0 \mathrm{D}. \tag{1.1}$$

This equation is known as the Hubble law, where H_0 is the Hubble's constant at the current epoch and has a dimension of the inverse of the time. H_0 is roughly estimated with cosmological surveys and, since its value might vary with novel measurements, is often written as:

$$\mathrm{H}_0 = 100h \text{ km s}^{-1} \text{ Mpc}^{-1} , \tag{1.2}$$

where h is the dimensionless Hubble parameter. During the past years, we have had difficulties accurately determining h. For example the Planck Collaboration et al. (2020) found $h \simeq 0.67$ with CMB data, while we measured with Hubble Space Telescope observations of variable stars in the nearby Universe $h \simeq 0.72$ (Soltis, Casertano, and Riess, 2021). The value of H_0 varies with the cosmological epoch because the Universe is not expanding at the same speed during its evolution. From the Friedmann-Lemaître-Robertson-Walker (FLRW) metric introduced in Section 1.2.4,

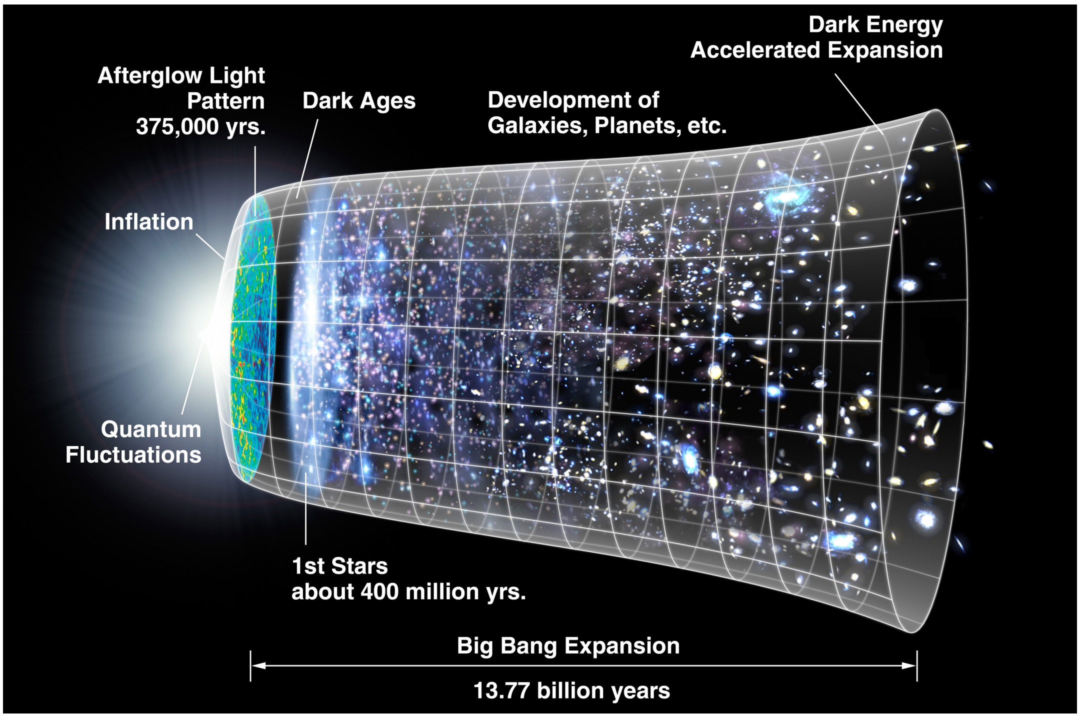

FIGURE 1.1: Timeline of the Universe: a schematic view of the history of the Universe. The different epochs are represented chronologically in slices from the left to the right. (Credits: NASA/WMAP)

we can estimate the Hubble's constant at a given epoch with:

$$H(t) = \frac{\dot{a}(t)}{a(t)}\,, \tag{1.3}$$

where a(t) is called the scale factor of the Universe at time t. It is described by the "redshift" effect, analogous to the Doppler effect: consider a photon emitted by a source in the Universe, its wavelength λ_e is shifted toward lower frequencies during its travel time t due to the expansion of the environmental spacetime structure, and its light will be seen redder than expected by the eye. Consider that the photon has a wavelength λ_a at its arrival, the scale factor is given by:

$$a(t) = \frac{\lambda_e}{\lambda_a} = \frac{1}{1+z}\,, \tag{1.4}$$

where z is the redshift parameter used to characterize the distance and the epoch of a given source. In the present time, $z = 0$ and $a = 1$.

1.2 Standard model of cosmology

The standard model of Cosmology, also known as the ΛCDM model, is the latest incarnation of our understanding of the origin and the evolution of the Universe. The Λ in the theory's name accounts for the presence of dark energy, and CDM stands for "cold dark matter" as dark matter is supposedly comprised of cold slow-moving particles that do not emit electromagnetic radiation, thus they also appear dark. However, the gravitational effect of dark matter can be observed on visible material, such as galaxy clusters (see Section 1.4)).

1.2.1 Cosmological principle

The standard model relies on a fundamental assumption that is the cosmological principle. To derive its cosmological model, Einstein made the following hypothesis: the Universe is isotropic and homogeneous. In other words, from any point in the Universe, it is uniformly distributed in any direction of the sky as far as we observe. The isotropy does not imply homogeneity and vice versa. For instance, if the matter distribution is given as a function of the distance from us, the Universe is isotropic but not homogeneous, while if the Universe is composed of a uniform magnetic field, it can be homogeneous but not isotropic.

The cosmological principle is validated by observations of the CMB and the distribution of galaxies at large scales. However, it can only be valid on scales sufficiently large, and as soon as we consider smaller scales, e.g. within the solar system or up to the nearby galaxies, its condition is no more true.

1.2.2 Cosmological probes

The standard model is today the most accurate model to describe our Universe, approved by cosmological probes handled in the latest century. In particular, it arises from three major observational pieces of evidence:

1. The discovery of the recession of galaxies by Edwin Hubble using Henrietta Leavitt's period-luminosity relation on Cepheid variables, which derives the empirical law that is today referred to as the Hubble law. It describes the fact that galaxies move away from us at a velocity proportional to their distance and is considered as the first observational evidence that the Universe is expanding (Hubble, 1929).

2. The chemical abundance of primordial elements, predicted by the standard model with abundances of hydrogen and helium in the local Universe of about 75% and 25% respectively. With measurements of light elements in stars, quasars, and the interstellar medium (Burbidge et al., 1957; Steigman, 2006), these fractions have been verified.

3. The fortuitous discovery of the cosmic microwave background by Penzias and Wilson (1965), an isotropic black body radiation at 2.725K. These primordial photons have been released at the epoch of matter-radiation decoupling more than 13 billion years ago. Due to the expansion of the Universe and the cooling phase of the photons, this temperature indicates the primordial Universe was extremely hot ($\sim$ 3000K). Today's observations (Planck Collaboration et al., 2020) show small anisotropies in the temperature at the scale of 1 degree, of the order of $\Delta T/T = 10^{-5}$, as shown in Figure 1.2.

1.2.3 General relativity

A second fundamental principle of the standard model is that the dynamics of the Universe are governed by General Relativity (GR), derived by Einstein in 1915 from Special Relativity. In contrast with Newtonian physics, GR is a theory of gravitation that does not consider gravity as a force but as a manifestation of the curvature of spacetime. This theory changes the form of the mass definition in classical mechanics to a more general form, described by the famous Einstein's field equation, a relation

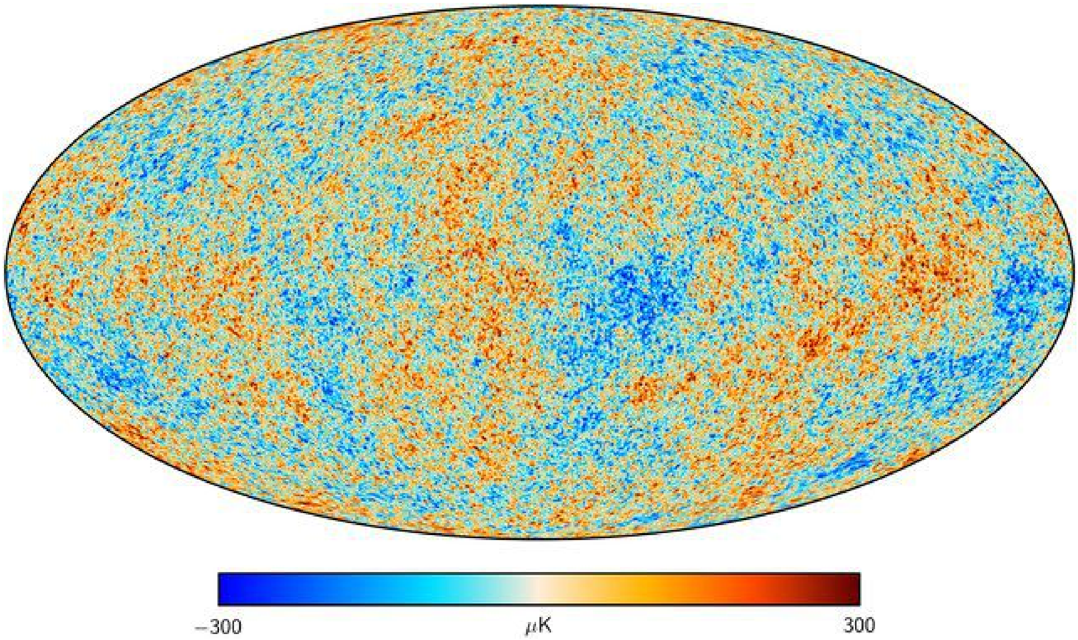

FIGURE 1.2: The 2018 *Planck* map of the cosmic microwave background. The fluctuation in temperature shows that the early Universe was slightly anisotropic. (Credits: ESA/Planck Collaboration et al., 2020)

between the energy in the Universe and its geometry:

$$R_{\mu\nu} - \frac{1}{2}Rg_{\mu\nu} + \Lambda g_{\mu\nu} = \frac{8\pi G}{c^4}T_{\mu\nu} \ . \tag{1.5}$$

In this equation, $g_{\mu\nu}$ is the metric tensor, $R_{\mu\nu}$ is the Ricci tensor derived from the derivatives of $g_{\mu\nu}$, R is the scalar curvature given by the trace of $R_{\mu\nu}$, G is the gravitational constant, c is the speed of light and $T_{\mu\nu}$ is the stress-energy tensor that describes the density of energy and momentum in spacetime. The cosmological constant Λ is introduced two years after the publication of GR by Einstein to counterbalance the effect of gravity and be conform with a Universe in static equilibrium. When Hubble showed the expansion of the Universe, later on, the mathematician Alexander Friedmann found that the "original" GR equations were in agreement with these observations, and suggested removing the constant from Equation (1.5), which Einstein qualified as his "biggest blunder". The cosmological constant is not in contradiction with a dynamic Universe. At the end of the latest century, observations on distant supernovae (Riess et al., 1998; Perlmutter et al., 1999) showed that the Universe was in accelerated expansion. This discovery assumes that the Universe is today composed of dominant energy, the so-called dark energy, which requires a strictly positive Λ.

1.2.4 FLRW metric

A metric is a mathematical tool that determines how to calculate distances in space. In the case of our four-dimensional space, a distance s is described with a three-dimensional element of space l and a one-dimensional element of time t on infinitesimal scales as:

$$ds^2 = c^2dt^2 - dl^2 \ . \tag{1.6}$$

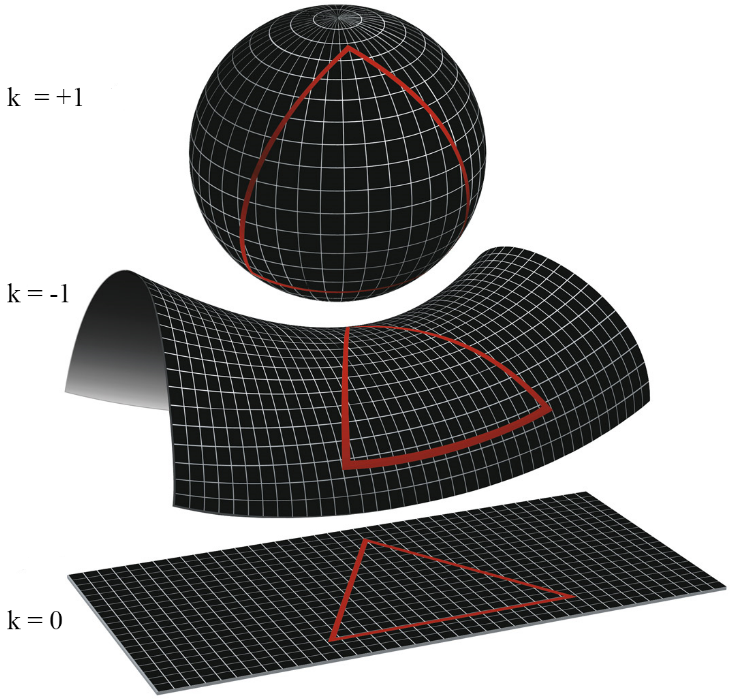

FIGURE 1.3: Possible curvatures of the Universe, represented as a plane. From top to bottom, the cases of a closed Universe, an open Universe, and a flat Universe. (Credits: NASA/WMAP)

The minus sign between the element of time and the elements of space indicates that ds^2 can be negative, for instance, if two distant events are reported at the same time. Note that the factors in front of the coordinates compose the $g_{\mu\nu}$ tensor. In the specific case of light travels, $ds^2 = 0$ is the shortest path between two points. These lines are also called geodesics.

In the context of a flat static Universe, the spatial distance between two events can be described with spherical coordinates where $dl^2 = dr^2 + r^2 d\Omega^2$, r being the radial component and Ω the angular one such that $d\Omega^2 \equiv d\theta^2 + \sin^2\theta d\phi^2$. During the next years after the publication of GR, four scientists - Friedmann, Lemaître, Robertson, Walker - derived an exact solution of Equation (1.5) in the framework of a homogeneous, isotropic, and expanding Universe:

$$ds^2 = c^2 dt^2 - a^2(t) d\chi^2 \, , \tag{1.7}$$

where $d\chi$ is an element of comoving distance on a hypersurface. The "comoving" term refers to a coordinate system decoupling from the impact of the expansion, further discussed in Section 1.2.6. The geometry of the Universe is defined by its curvature as:

$$d\chi^2 = \frac{dr^2}{1 - kr^2} + r^2 d\Omega^2 \, . \tag{1.8}$$

The topology of the Universe is characterized by a connected path. A schematic analogy of this mathematical concept is presented in Figure 1.3 with a 2D space. Suppose a connected path is designed as a triangle onto this surface, the values of its angles vary according to the geometry of the surface.

Back to the Universe space, its morphology is related to the curvature parameter k as:

- $k = 1$ defines a spherical space, then the sum of the triangle's angles is larger than π and the Universe is closed.
- $k = 0$ defines a Euclidean space, then the sum of the triangle's angles is equal to π and the Universe is flat.
- $k = -1$ defines a hyperbolic space, then the sum of the triangle's angles is lower than π and the Universe is open.

We notice that in the latter case, the Universe volume could be infinite.

1.2.5 Cosmological parameters

From the assumption of the cosmological principle, the Universe can be described with a perfect fluid in thermodynamic equilibrium, and its pressure p and density ρ injected in the stress-energy tensor. We can thus decompose the total energy of the Universe as a sum of several components: matter, radiation, dark energy, and curvature of space. Their density are respectively noted ρ_m, ρ_r, $\rho_\Lambda = \Lambda/(8\pi G)$ and $\rho_k = -3kc^2/(8\pi G a^2)$. Their pressure is written as a function of their density given by the equation of state $p \equiv \omega\rho$, where $\omega = 0$ for matter, $\omega = 1/3$ for radiation, $\omega = -1$ for dark energy, and $\omega = -1/3$ for curvature (the dark energy component has a strong negative pressure, causing the counterintuitive notion of a gravitational repulsive effect).

If we inject the FLRW metric in the Einstein's field equation we now obtain the Friedmann equations, which govern the expansion of space and the dynamic of the Universe:

$$\left(\frac{\dot{a}}{a}\right)^2 = \frac{8\pi G\rho}{3} - \frac{kc^2}{a^2} + \frac{\Lambda c^2}{3} , \tag{1.9}$$

$$\frac{\ddot{a}}{a} = \frac{4\pi G\rho}{3} - \left(1 + \frac{3\omega}{c^2}\right) + \frac{\Lambda c^2}{3} . \tag{1.10}$$

In the literature, we commonly express the density of the various components of the Universe relative to this critical density: $\Omega = \rho/\rho_c$. The critical density is, by definition, the total density for a flat Universe ($k = 0$) without dark energy ($\Lambda = 0$). If we substitute these values in Equation (1.9) and combine with Equation (1.3), we find:

$$\rho_c = \frac{3H^2}{8\pi G} . \tag{1.11}$$

Today, its value is approximately $\rho_{c,0} \simeq 2.775\ 10^{11}\ h^2\ M_\odot\ \mathrm{Mpc}^{-3}$. Hence, the dimensionless density parameters are:

$$\Omega_m = \frac{\rho_m}{\rho_c},\ \Omega_r = \frac{\rho_r}{\rho_c},\ \Omega_\Lambda = \frac{\Lambda}{3H^2},\ \Omega_k = -\frac{k}{a^2H^2} . \tag{1.12}$$

We can finally rewrite Equation (1.9) as the total energy budget of the Universe:

$$\Omega_{tot} \equiv \Omega_m + \Omega_r + \Omega_\Lambda + \Omega_k = 1 , \tag{1.13}$$

and express the Hubble's constant as a function of redshift:

$$H(z) = H_0 E(z) . \tag{1.14}$$

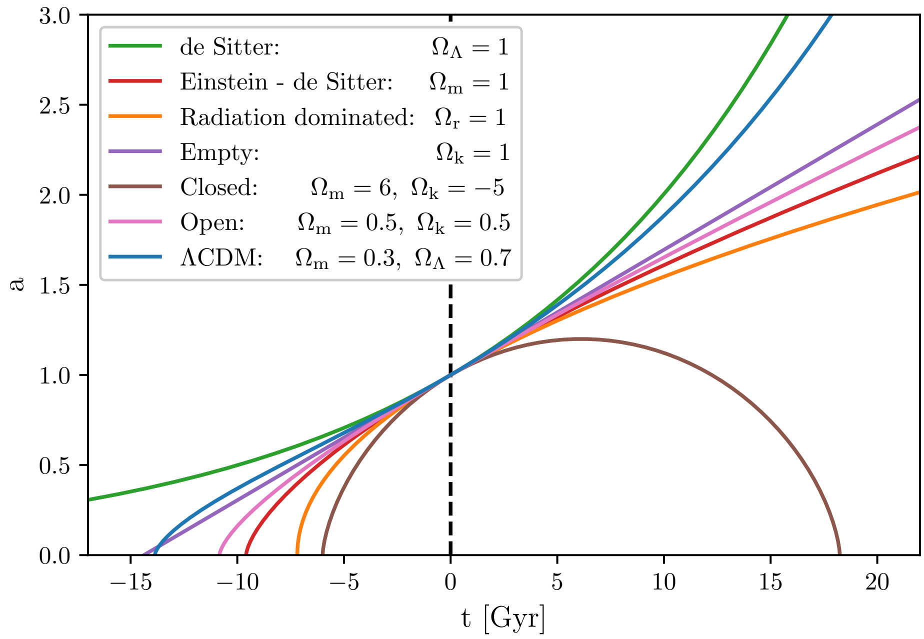

FIGURE 1.4: Hypothetical scenarios for the evolution of the Universe. We compare the scale factor and its evolution over time with different predictions given in a - de Sitter, Einstein - de Sitter, radiation dominated, empty, closed, open, and ΛCDM - Universe. The dashed vertical line indicates the present epoch.

Here E is the dimensionless Hubble parameter, defined as:

$$\mathrm{E(z)} \equiv \sqrt{\Omega_\Lambda + \Omega_k(1+z)^2 + \Omega_m(1+z)^3 + \Omega_r(1+z)^4}\ , \tag{1.15}$$

where the density parameters Ω are taken at their present-day value.

The dimensionless cosmological parameters (H_0, Ω_m, Ω_r, Ω_Λ, Ω_k) at the present epoch constitute the essential materials to describe the Universe properties (its geometry, size, components, etc) and to predict their evolution (as they are a function of time). One of these scenarios would lead to an unrealistic Universe in which there is no matter or radiation at the present time, only driven by its expansion. Such Universe, that its total density is dominated by the dark energy density, is called de Sitter (1917). Alternatively, we can easily imagine a Universe dominated by its radiation, or completely empty if its today's energy budget is given by the space curvature density. A more realistic perspective is the idea of a flat static Universe, without cosmological constant Λ and where the matter density equals the critical density at the latest times. This model, originally proposed by Einstein and de Sitter (1932), has been privileged until the early 1990s. However, following the first observations of the CMB, the measurements of the Hubble's constant, and the discovery of the accelerating Universe in 1998, this model has been progressively replaced over year by the modern ΛCDM model, where dark energy makes up 70% of the present energy density while matter contributes around 30%. Figure 1.4 shows the different scenarios for the evolution of the relative size of the Universe.

The luminous matter of the Universe does not compose the total budget for the matter density. Indeed, the matter content also includes the matter that we do not

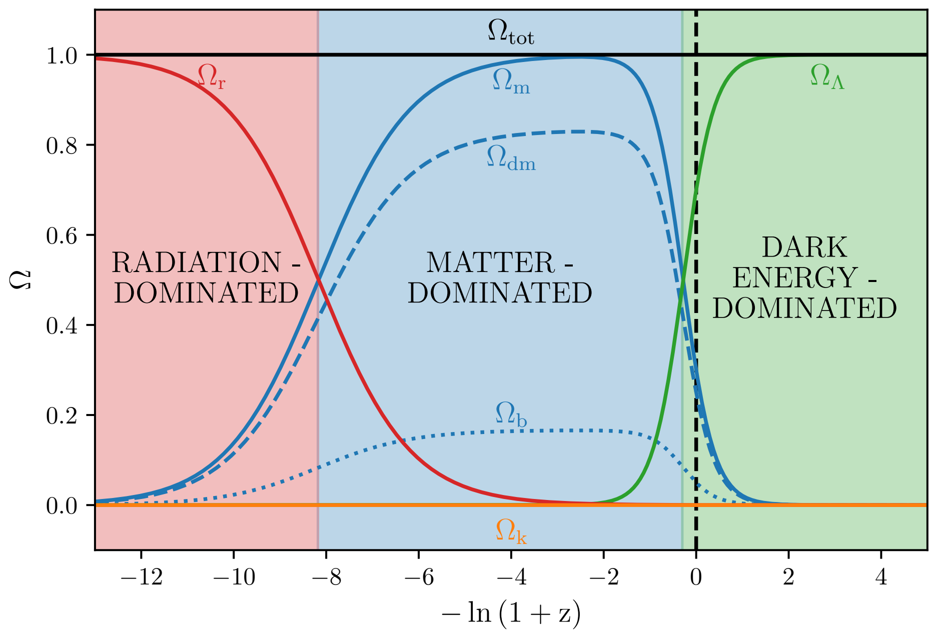

FIGURE 1.5: Evolution of the density parameters in the framework of the ΛCDM model. The history of the Universe can be decomposed into three phases of radiation, matter, and dark energy domination. The dashed vertical line indicates the present epoch.

see directly. Among the big riddles of modern Cosmology is the "missing matter" of the Universe. The first evidence of this problem has been raised with observations led on Coma, a cluster of galaxies: Zwicky (1933) found that its dynamical mass was about 400 times bigger than that associated with luminous matter. Later on, measurements of the dynamics of galaxies or gravitational lensing in clusters of galaxies forced astrophysicists to introduce the contribution from an invisible matter to explain observations, the so-called Dark Matter. The nature of dark matter remains today a mystery, but there are essentially three hypotheses to explain it: baryonic (objects too faint to be observed), non-baryonic (WIMPS, supersymmetric particles), modified gravity. What we know is that the fraction of dark matter contribution is today 25% of the Universe, while the baryonic matter is about 5% such that $\Omega_m = \Omega_{dm} + \Omega_b$.

Throughout this thesis we assume a spatially flat ΛCDM model for the Universe, with the following matter, dark energy and baryonic density parameters at the present time $\Omega_m = \Omega_{tot} - \Omega_\Lambda = 0.3$, $\Omega_{dm} = \Omega_m - \Omega_b = 0.25$, and Hubble parameter $H_0 = 70$ km s^{-1} Mpc^{-1}. In Figure 1.5 we illustrate the evolution of the density parameters across time. With this model, we can dissociate three distinct periods of domination in the history of the Universe: at the early time the Universe is dominated by radiation, then matter decoupled from light and formed structures (atoms, stars, galaxies, clusters, and the large-scale structure) and finally Universe expansion started to accelerate under dark energy effects.

1.2.6 Cosmological distances

Because the Universe is expanding, distances are computed differently than in a static Universe. In cosmology, with dissociate *proper* and *comoving* distances. The proper distance is the physical distance of an object that lies at a given epoch of the Universe.

Due to the expansion, this distance varies with cosmic time. In contrast, the comoving distance is a distance that factors out the expansion of the Universe and does not depend on time. At the present time, the two distances are equals. Otherwise, the proper distance D_P of an object at a given cosmic time t and a given comoving radial distance r from us, is connected to the comoving distance D_C as:

$$D_P(r,t) = a(t)D_C = a(t)\int_0^r \frac{dr'}{\sqrt{1-kr'^2}} \ , \tag{1.16}$$

where $D_C = \int d\chi$ is derived from Equation (1.8). The comoving distance is given by a geodesic, and thus satisfies $ds^2 = 0$. From Equation (1.7), we can clearly see that $d\chi = cdt/a$. We thus derive the comoving distance of two distinct objects lying along the line of sight at redhifts z_1 and z_2, with $z_1 < z_2$, as:

$$D_C(z_1,z_2) = \int_{z_1}^{z_2} d\chi = D_H\int_{z_1}^{z_2} \frac{dz'}{E(z')} \ , \tag{1.17}$$

where $D_H = c/H_0$ is the today's Hubble horizon. If the two objects are separated on the sky plane by an angle $\delta\theta$, they are distant of $\delta\theta D_M$, where D_M is the transverse comoving distance and depends on the space curvature:

$$D_M = \begin{cases} \frac{D_H}{\sqrt{\Omega_k}}\sinh\left(\frac{\sqrt{\Omega_k}D_C}{D_H}\right) & (\Omega_k > 0), \\ D_C & (\Omega_k = 0), \\ \frac{D_H}{\sqrt{\Omega_k}}\sin\left(\frac{\sqrt{\Omega_k}D_C}{D_H}\right) & (\Omega_k < 0). \end{cases} \tag{1.18}$$

Alternatively, we can characterize the distance to an object of angular extent θ and proper size l with the angular diameter distance $D_A \equiv l/\theta$, if θ is sufficiently small. By definition, if you increase D_A by a factor of two, then the angular extent of the object diminishes by half. At a given cosmic time, the angular extent object is $\theta = l/D_P$, and therefore the angular diameter distance between two distant objects is:

$$D_A(z_1,z_2) = D_P(z_1,z_2) = \frac{D_M(z_1,z_2)}{1+z_2} \ . \tag{1.19}$$

This distance is often used in gravitational lensing formalism since lense objects are deflecting source light among a transverse plane permitting to derive mass density profiles.

Another way to compute distances in cosmology is to measure the observed flux F of a source, i.e. the amount of photons receipt per unit surface per unit time, from an object with known intrinsic luminosity L. The luminosity distance, D_L , is defined such that if you increase D_L by a factor, the observed flux will diminish as the square of the factor such that $D_L \equiv \sqrt{L/(4\pi F)}$. The energy of each photon is decreased because of the redshifting of the photons. Etherington (1933) derived the relation between angular diameter distance and the luminosity distance:

$$D_L(z_1,z_2) = D_A(z_1,z_2)(1+z_2)^2 \ . \tag{1.20}$$

All these distances in a flat ΛCDM Universe are shown in Figure 1.6, from us and as functions of redshift.

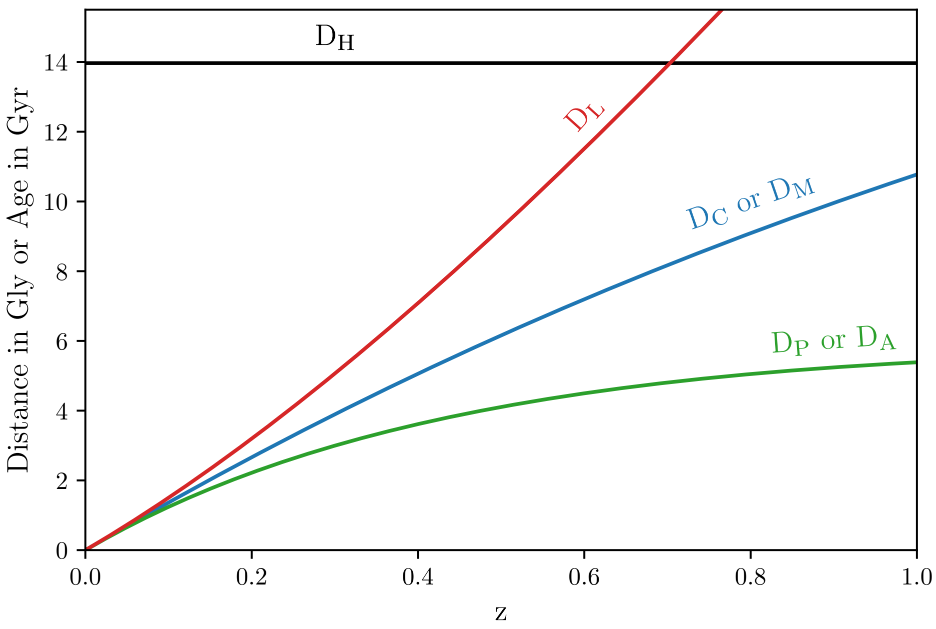

FIGURE 1.6: Distances in cosmology, as a function of redshift. We present here the Hubble (black), proper (green), comoving (blue), angular diameter distances (green), and luminosity (red) distances.

1.3 Growth of structures

The Universe on large scales is well described by the Friedmann equations (1.9) & (1.10) when the conditions of the cosmological principle are satisfied. However, we saw on smaller scales that the density field of the CMB presents small anisotropies (see Section 1.2.1), and observations of the local Universe show an inhomogeneous distribution of the galaxies (e.g. de Lapparent, Geller, and Huchra, 1986). In this section, we will review how these structures grow and evolve from the small initial perturbations recovered in the CMB up to today's large-scale structure.

1.3.1 Density perturbations

The perturbation theory describes the evolution of inhomogeneities in the cosmic fluid. The density field ρ of this fluid shows fluctuations around the mean density $\bar{\rho}$ as:

$$\rho = \bar{\rho}(1+\delta) \ , \tag{1.21}$$

where δ is called the overdensity parameter.

Assuming an adiabatic fluid in the linear regime and its dynamics ruled by the Newtonian dynamics, valid as long as we consider marginal density fluctuations (i.e. $\delta << 1$) without heat exchanged between particle elements and scales much smaller than the Hubble horizon, the Friedmann equations simplify and we derive the proper Jeans length:

$$\lambda_J = c_s \sqrt{\frac{\pi}{G\bar{\rho}}} \ . \tag{1.22}$$

Here c_s is the sound speed defined as $c_s \equiv \sqrt{\partial p / \partial \rho}$. The Jeans length defines the scale above which gravity takes overpressure forces and collapses the density perturbation.

For smaller scales, the pressure forces are strong enough to effectively resist gravity and perturbations oscillate. During the radiation domination epoch, the radiative pressure of photons prevents the collapse of perturbations at small scales. This phenomenon is responsible for oscillations in the density distribution of visible matter, the Baryonic Acoustic Oscillations (BAOs), analogous to sound waves created in the air by pressure differences. The BAOs are dominant in the density distribution of the CMB and propagate in today's distribution of galaxies, long after the matter-radiation decoupling (Eisenstein et al., 2005). Perturbations that we recover in the plasma of the early Universe are thus not singular in cosmic history but evolve linearly from an initial state δ_{init} with the so-called growth factor D. This time evolution can be decomposed into the sum of a growing and a decaying mode as:

$$\delta(z) = D^{+}(z)\delta^{+}_{\mathrm{init}} + D^{-}(z)\delta^{-}_{\mathrm{init}} \ . \tag{1.23}$$

Hence, the density contrast δ is a quantity fully described by its comoving coordinate $\mathbf{x}$. Another simple way to describe the perturbations is to decompose the overdensity field into the Fourier space. We introduce the Fourier transform $\tilde{\delta}$ of the density contrast δ, defined in the comoving plane waves $\mathbf{k}$ as:

$$\delta(\mathbf{x}) = \int \frac{d^3k}{(2\pi)^3}\tilde{\delta}(\mathbf{k})e^{-i\mathbf{k}\cdot\mathbf{x}} \ , \quad \tilde{\delta}(\mathbf{k}) = \int d^3x\,\delta(\mathbf{x})e^{i\mathbf{k}\cdot\mathbf{x}} \ . \tag{1.24}$$

In practice, it is impossible to measure the density perturbation at a particular comoving coordinate, because it requires a fixed volume. What we instead want to do is to apply some sort of filter to the density field and measure the density within this filter. We thus replace the density field $\delta(\mathbf{x})$ by a density field smoothed over some volume of radial coordinate $\mathbf{r}$:

$$\delta_{\mathrm{R}}(\mathbf{x}) = \int d^3r\,W(\mathbf{r})\delta(\mathbf{x}+\mathbf{r}) \ , \quad \tilde{\delta}_{\mathrm{R}}(\mathbf{k}) = \tilde{\delta}(\mathbf{k})\tilde{W}(\mathbf{r}) \ . \tag{1.25}$$

Since this is a convolution, it is convenient in practice to switch in Fourier space, as we know from the convolution theorem in Fourier analysis that this is a simple multiplication of Fourier transforms. The function W_{R} is called the window function, and $\tilde{W}_{\mathrm{R}}$ is its Fourier transform. This filter defines the density field over a volume of radial aperture R. In cosmology three main window functions are mostly used:

- **The spherical top-hat filter** is the most common window function, defined through:

$$W_{\mathrm{TH}}(\mathbf{r}) = \frac{1}{V_{\mathrm{TH}}}\Theta(R-r) \ , \quad \tilde{W}_{\mathrm{TH}}(\mathbf{k}) = \frac{\sin(kR) - kR\cos(kR)}{(kR)^3} \ . \tag{1.26}$$

  Θ is the Heaviside step function and in this case, $V_{\mathrm{TH}} = 4\pi R^3/3$.

- **The Gaussian window function** is defined through:

$$W_{\mathrm{G}}(\mathbf{r}) = \frac{1}{V_{\mathrm{G}}}e^{-r^2/(2R^2)} \ , \quad \tilde{W}_{\mathrm{G}}(\mathbf{k}) = e^{-(kR)^2/2} \ . \tag{1.27}$$

  Here, $V_{\mathrm{G}} = (2\pi)^{3/2}R^3$.

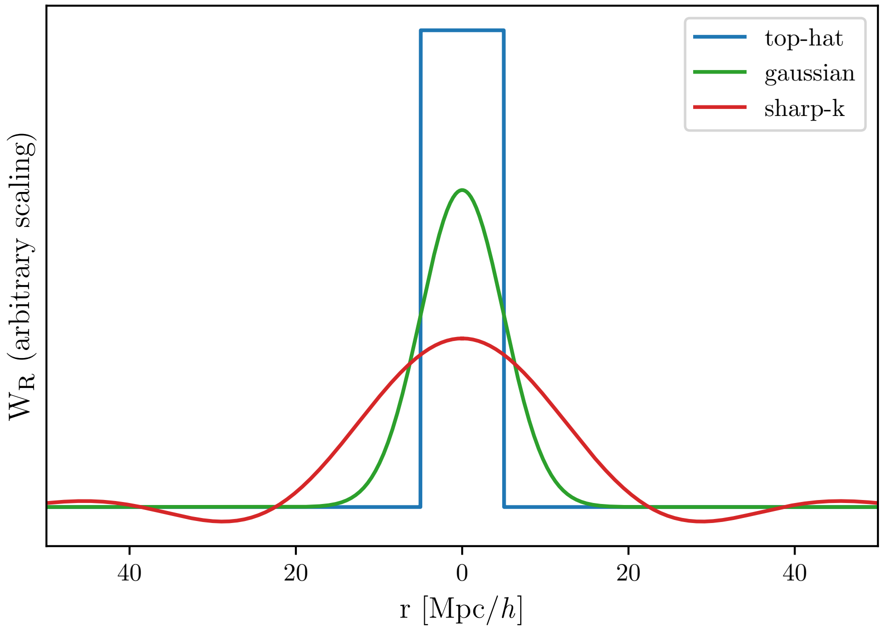

FIGURE 1.7: A comparison of the three window functions discussed in the text. The blue shows the top-hat, the green the Gaussian, and the red the sharp k-space window function. For this particular plot we set $R = 5$ Mpc/h.

- **The sharp k-space filter** is equivalent to the top-hat filter in Fourier space:

$$W_{kTH}(\mathbf{r}) = \frac{3}{V_{kTH}}\left(\frac{R}{r}\right)^3\left(\sin\frac{r}{R} - \frac{r}{R}\cos\frac{r}{R}\right) \ , \quad \tilde{W}_{kTH}(\mathbf{k}) = \Theta(1-kR) \ . \tag{1.28}$$

  The volume $V_{kTH} = 6\pi^2R^3$ satisfies $W_{kTH}(0)V_{kTH} = 1$, which is convenient for theoretical arguments.

An example of the window functions is given in Figure 1.7 in real space assuming the specific case $R = 5$ Mpc/h.

Therefore, we see that the perturbations and their growth can be described independently. Decoupling the spatial-time evolution of perturbations is an effective way to measure the growth of structures in the Universe, as long as we are in the linear regime with scales below the horizon size.

1.3.2 Matter distribution

Now that we have seen that overdensities characterize the density field in the Universe, we are interested in a formal way to represent its distribution on all scales at any cosmic time. The two-point correlation function is a powerful statistical tool to describe this field, assumed to be Gaussian and isotropic in the linear regime. It computes the covariance of δ between two positions in the Universe having a comoving separation $\mathbf{r}$:

$$\xi(r) = \langle \delta(\mathbf{x})\delta(\mathbf{x}+\mathbf{r})\rangle \ , \tag{1.29}$$

where we assume that $\delta(\mathbf{r})$ is statistically homogeneous and isotropic, so $\xi(r)$ depends only on the modulus of the separation $\mathbf{r}$. Similarly, the covariance of the Fourier

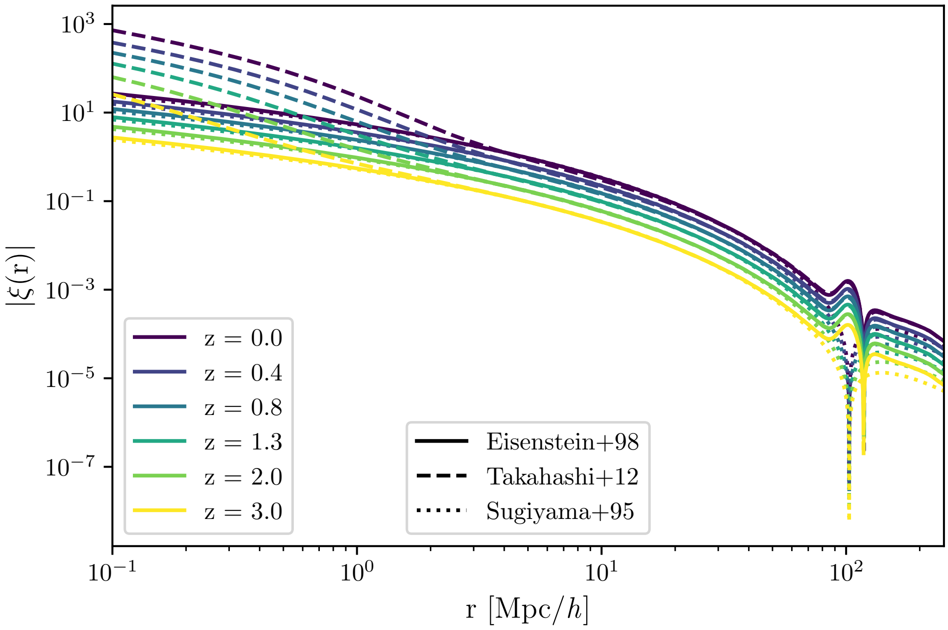

FIGURE 1.8: The absolute value of the matter correlation function as computed in Equation (1.31) at various redshifts. We show the functional form of Sugiyama (1995) and Eisenstein and Hu (1998) in the linear regime and Takahashi et al. (2012) in the non-linear regime.

transform of δ is called the power spectrum, defined as:

$$\langle\tilde{\delta}(\mathbf{k})\tilde{\delta}(\mathbf{k'})\rangle = (2\pi)^3 P(k)\delta_D(\mathbf{k}-\mathbf{k'}) \ , \tag{1.30}$$

where δ_D is the Dirac delta function which ensures that modes of the different wave vector $\mathbf{k}$ are uncorrelated in Fourier space to preserve homogeneity.

Again, the power spectrum $P(k)$ only depends on the modulus of $\mathbf{k}$ because of isotropy. By definition, the power spectrum is the Fourier transform of the two-point correlation function and, under the conditions of homogeneity and isotropy, these two quantities are related as:

$$\begin{aligned} P(k) &= \int d^3r\xi(r)e^{i\mathbf{k}\cdot\mathbf{r}} & \xi(r) &= \int \frac{d^3k}{(2\pi)^3}P(k)e^{-i\mathbf{k}\cdot\mathbf{r}} \\ &= 4\pi\int r^2 dr\xi(r)j_0(kr) \ , & &= \frac{1}{2\pi^2}\int k^2 dk P(k) j_0(kr) \ . \end{aligned} \tag{1.31}$$

The function $j_0(x) \equiv \sin(x)/x$ is the spherical Bessel function of order zero. The correlation function is displayed in Figure 1.8 evolving in redshifts. The function is computed in a linear regime and a non-linear regime as discussed in Section 1.3.3.

Because each Fourier mode of the density field evolves independently, the linear power spectrum can be derived at any cosmic time from a linear growth of the power spectrum at the recombination epoch. Inflationary theories typically predict that the primordial power spectrum is given in the following form, known as the Harrison-Zeldovich spectrum (HZ, Harrison, 1970; Zeldovich, 1972):

$$P_{HZ}(k) = A_s k^{n_s} \ , \tag{1.32}$$

where A_s is the amplitude of scalar fluctuations and $n_s \simeq 1$ is the scalar spectral index.

During inflation, primordial perturbations are nearly scale-invariant. Some of the fluctuations have Fourier modes with wavelength larger than the horizon. These modes enter the horizon at a later time, during the matter domination epoch. During the radiation domination epoch, Fourier modes are frozen since the Universe is expanding too fast for the density perturbations to collapse under gravity. At the matter-radiation equality epoch, the dark matter fluctuations start to grow and the baryonic matter perturbations fluctuate into the BAOs under the effect of gravity and radiative pressure. At the recombination epoch, the pressure becomes weaker than gravity and all modes start to grow. Because the HZ power spectrum does not account for the growth of density perturbations once they enter the horizon, the primordial power spectrum after recombination, at the beginning of the matter domination era, is given by:

$$P_{\mathrm{init}}(k) = P_{\mathrm{HZ}}(k) T^2(k) \ , \tag{1.33}$$

where $T(k)$ is a "transfer function" that takes into account the effects of gravitational amplification of a density perturbation mode of wavelength k.

After recombination and in the linear regime, each Fourier mode evolves independently following Equation (1.23) and the linear power spectrum therefore just scales as:

$$P_L(k, z) = P_{\mathrm{init}}(k) D_+^2(z) \ . \tag{1.34}$$

The precise estimation of $T(k)$ demands sophisticated numerical calculations of the time evolution of the density perturbation amplitudes in each Fourier mode. Bardeen et al. (1986) and later Sugiyama (1995) give a complete description of the transfer function, including BAO wiggles, but this description is not as accurate as the model described in Eisenstein and Hu (1998) and Eisenstein and Hu (1999). These two functional forms are shown in Figure 1.9 as functions of redshift. We also display the spectrum in the non-linear regime (see Section 1.3.3).

In the linear regime we know that δ is distributed as a Gaussian, and by linear combination δ_R as well. The overdensity field delta is thus characterized by a mean and variance. The mean is equal to zero because the density field ρ in Equation (1.21) should return the mean density of the Universe on average. The variance of the field can be easily computed as:

$$\sigma^2(R) \equiv \langle \delta_R^2(\mathbf{r}) \rangle = \frac{1}{2\pi^2} \int k^2 dk P_L(k) \tilde{W}_R^2(k) \tag{1.35}$$

Figure 1.10 shows the root mean square (RMS) variance given at various redshifts for the three cosmological filters presented in Section 1.3.1.

A major aspect of the variance is the normalization of the matter power spectrum σ_8. This parameter defines the RMS fluctuations $\sigma(R)$ on scales of 8 Mpc/h in a spherical top-hat filter at the present epoch. More importantly, the square of σ_8 is a direct normalization factor of the linear matter power spectrum. In cosmological analyses, the power spectrum normalization is a crucial parameter for models to describe the growth of structures. It is generally combined with the matter-energy density because of a tension when measuring the two cosmological parameters with WL methods, which is quantified using the $S_8 \equiv \sigma_8 \sqrt{\Omega_m/0.3}$ parameter.

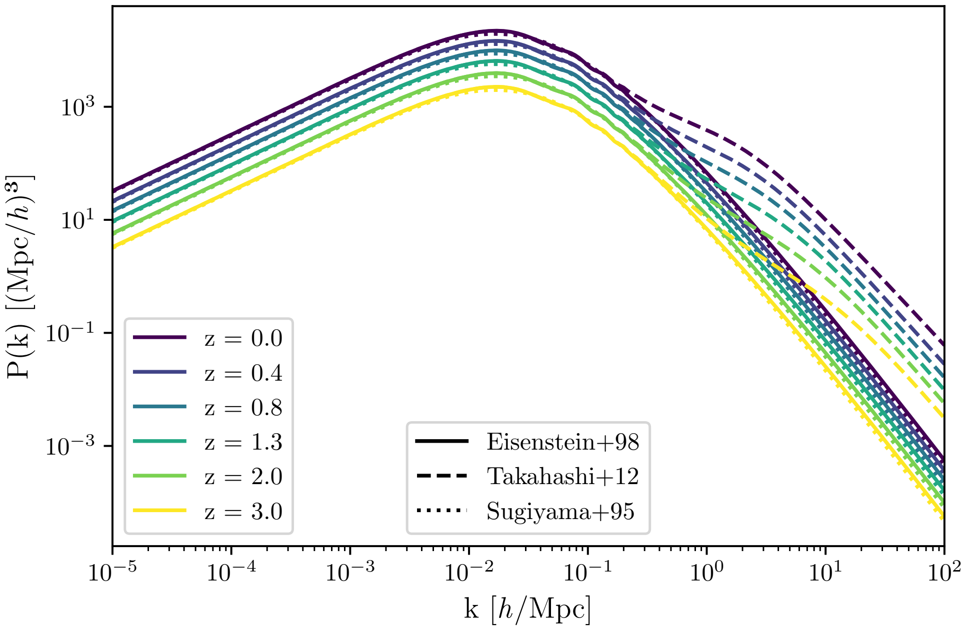

FIGURE 1.9: The matter power spectrum as computed in Equations (1.34) & (1.36) at various redshifts. We show the functional form of Sugiyama (1995) and Eisenstein and Hu (1998) in the linear regime and Takahashi et al. (2012) in the non-linear regime.

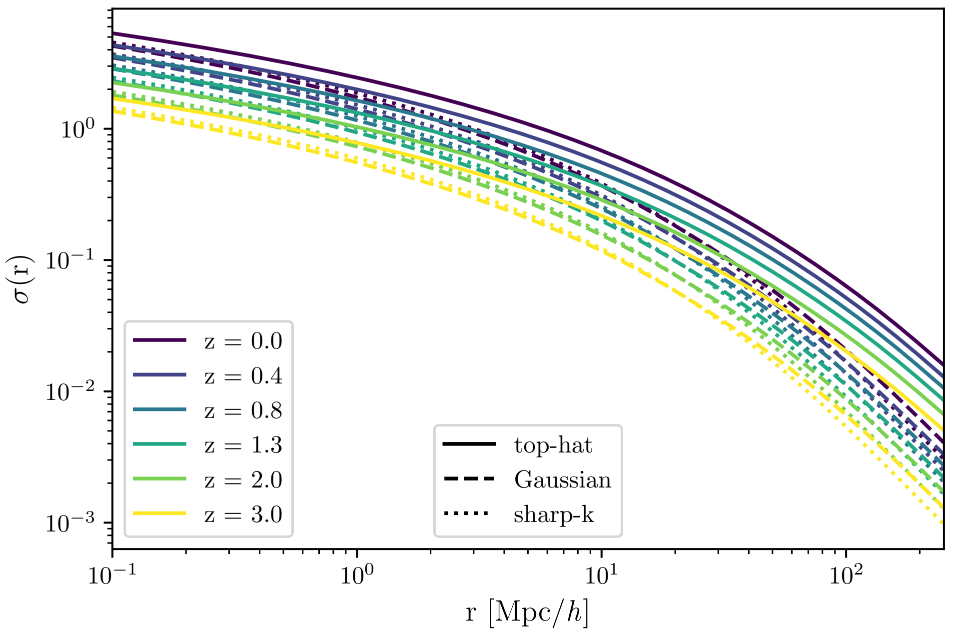

FIGURE 1.10: The RMS overdensity variance functions as computed in Equation (1.35) at various redshifts. We show the functional form of Eisenstein and Hu (1998) in top-hat (1.26), Gaussian (1.27) and sharp-k (1.28) filters.

1.3.3 Non-linear evolution

The linear equations of field provide an excellent description of gravitational instability for small density fluctuations ($\delta \ll 1$) but break down when the perturbations are comparable to the mean density of the Universe. The analytical development of the cosmological perturbation theory to higher orders is increasingly complex. In practice, the two-point statistic equations are hardly raised to order beyond three (Bernardeau et al., 2002). Typically, the second-order equations of perturbation theory allow reaching maximum scales $k \simeq 0.2\ h/\mathrm{Mpc}$ with sufficient precision (Taruya et al., 2012). These developments only describe the analytical evolution of the density field in the weakly non-linear regime ($\delta \sim 1$), which marks the limit between the two regimes. For a correct treatment of the non-linear development, one has to rely on numerical simulations or analytical models.

Amongst the most successful numerical methods, we recover the N-body simulations. They decompose the matter distribution into a dynamical system of N dark matter particles, whose velocities at some initial time are typically slightly perturbed according to some assumed power spectrum. The initial state is chosen such that the linear regime holds on all scales considered. Particles evolve under the influence of gravity of all other particles, which shows the formation of voids and dense regions called halos, all connected with filaments. This structure forms and amplifies with time (see Figure 1.11). The equations of motion are then solved at any step of the evolution of the simulation. This track requires powerful machines and cosmologists often deal with a trade-off between the size of the simulation box and the resolution of the particle system. For instance one of the most famous simulations is the Millennium simulation (Springel et al., 2005) which covers the evolution of $N = 2160^3$ particles in a box of size $V = 500\ (\mathrm{Mpc}/h)^3$. Figure 1.11 highlights four slices of this simulation from $z = 18.3$ to nowadays. Results of N-body simulations are then used to develop phenomenological models or fitting formulae of density field statistics in the non-linear regime. For example, Peacock and Dodds (1996) provided a fitting formula of the non-linear matter power spectrum based on a scaling ansatz presented in Hamilton et al. (1991). With the results of a large library of cosmological N-body simulations using power-law initial spectra, Smith et al. (2003) proposed a new model of $P(k)$, the so-called halofit model. This model is revised by Takahashi et al. (2012) with higher resolution N-body simulations. It is broken down in the following sum:

$$\Delta^2_{\mathrm{NL}}(k) = \Delta^2_{\mathrm{Q}}(k) + \Delta^2_{\mathrm{H}}(k)\ , \tag{1.36}$$

where $\Delta^2(k) \equiv k^3 P(k)/(2\pi^2)$. The term Δ_{Q} describes the distribution of the density field on the large scales, typically $k \leq 0.1\ h/\mathrm{Mpc}$, while Δ_{H} dominates on smaller scales where the non-linear regime mostly impacts the density field. The non-linear spectrum is given in terms of the linear matter power spectrum, and growths according the evolution of $P_{\mathrm{L}}(k, z)$. The correlation function and the matter power spectrum in non-linear regime are shown for a set of different redshifts in Figures 1.8 & 1.9.

An alternative approach is to rely on the model of the spherical collapse of dark matter halos. The idea is that the distribution of dark matter in the Universe can be considered as composed of virialized overdense clouds of dark matter called halos. These structures would form from the collapse of a spherically symmetric overdensity. While realistic density perturbations are not spherical, the analytical solution of such configuration provides useful insights into the non-linear collapse of more realistic situations. Assuming an Einstein - de Sitter Universe ($\Omega_{\mathrm{m}} = 1$), the equations of dynamics can be solved (Gunn and Gott, 1972) and the overdensity extrapolated

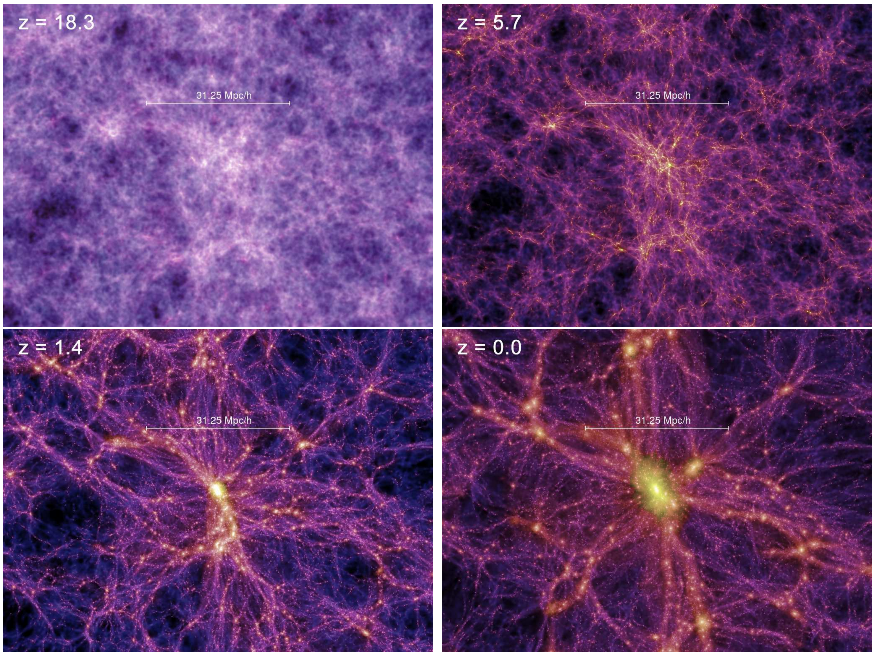

FIGURE 1.11: Slices of the Millennium simulation with evolving redshift. The four pannels show the state of the N-body system at redshift z = 18.3 (upper left), z = 5.7 (upper right), z = 1.4 (lower left) and z = 0 (lower right). (Credits: Springel et al., 2005)

according to linear perturbation theory. By tracking the evolution of the density inside a sphere of constant mass, the structure collapse when the linear overdensity reaches the critical value:

$$\delta_c = \frac{3}{20}(12\pi)^{2/3} \simeq 1.686 \ . \tag{1.37}$$

We call this parameter the linear density contrast. We commonly use δ_c to derive the peak height parameter of a halo, which quantifies how big a fluctuation in the linear density field this halo corresponds to. This quantity is computed as the ratio of the critical overdensity of collapse to the variance of the linear density field on the scale of the halo:

$$\nu \equiv \frac{\delta_c}{\sigma} \ . \tag{1.38}$$

For example, halos with peak height one correspond to peaks that have just reached a variance equal to the collapse overdensity at a given redshift, and should thus be collapsing. Halos of smaller peak height have, on average, already collapsed in the past, and halos of higher peak height will, on average, collapse in the future.

In a realistic situation, a sphere with overdensity δ_c does not collapse into a point of infinite density but reaches the virialized equilibrium when the total energy equals half of the potential energy. In this configuration, the ratio between the density inside the virialized sphere and the mean density of the Universe is (White, 2001):

$$\Delta_v \equiv \frac{\rho(r < r_{vir})}{\bar{\rho}} = 18\pi^2 \simeq 178 \ . \tag{1.39}$$

The parameter Δ_v is widely used in cosmology because it characterizes the halo with a fiducial density. In Equation (1.39), the halo density is compared with the mean

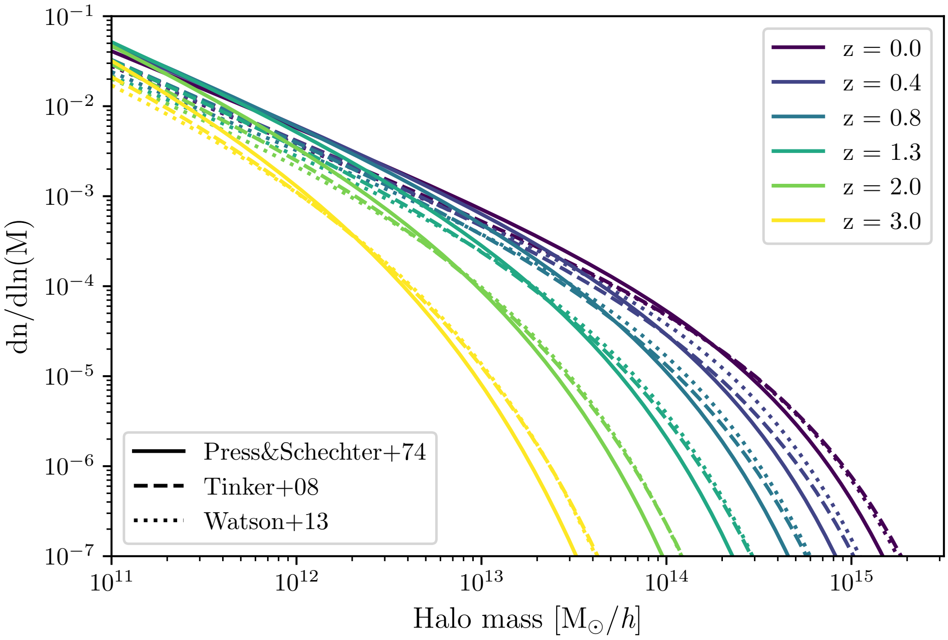

FIGURE 1.12: The halo mass functions as computed in Equation (1.40) at various redshifts. We show the functional form of Press and Schechter (1974), Tinker et al. (2008) and Watson et al. (2013).

density in an Einstein - de Sitter Universe ($\bar{\rho} = \rho_m$), but it can also be defined compared with the mean matter density $\Delta_m \equiv \rho/\rho_m$ or the critical density $\Delta_c \equiv \rho/\rho_c$ in a ΛCDM cosmology. This development of the non-linear evolution describes the dark matter halos as virialized objects characterized only by their mass enclosed in spheres of overdensity $\Delta_{m/c}$. The most popular choices are $\Delta_{m/c} = 200, 500$. An important property of halos is their distribution over mass, the so-called halo mass function (HMF). The Press & Schechter formalism (Press and Schechter, 1974) predicts the probability of finding an overdensity in a Gaussian random field at or above the linear density contrast for spherical collapse. The number of halos is distributed over mass as:

$$\frac{dn}{d\ln(M)} = f(\sigma)\frac{\rho_m}{M}\frac{d\ln(\sigma^{-1})}{d\ln(M)} , \tag{1.40}$$

where σ is the RMS variance as computed in Equation (1.35) of a spherical top hat containing the Lagrangian mass $M = 4\pi R^3/(3\rho_m)$. The function $f(\sigma)$ is known as the halo multiplicity function and varies according to the model we rely on. For example, Tinker et al. (2008) improved the HMF using 22 independent N-body simulations with about 10^9 particles to obtain a fit of the multiplicity function. More recently Watson et al. (2013) used a suite of very large ($3072^3 - 6000^3$ particles) cosmological N-body simulations to derive multiple redshift-independent models of the mass function.

In Figure 1.12 we show the HMF given by these three models plotted over a set of redshifts. We see that halos with smaller masses form more frequently than higher mass, and their number decreases as M^{-2} until a cutoff which for larger mass shows an exponential drop. This cutoff is basically set for masses reaching the non-linear mass M_*, given by $\sigma(M_*) = \delta_c$. This behavior is related to the hierarchical scenario for the formation of cosmic structures(Lacey and Cole, 1993; Lacey and Cole, 1994): the low mass halos first form and then assemble in more massive halos, which makes

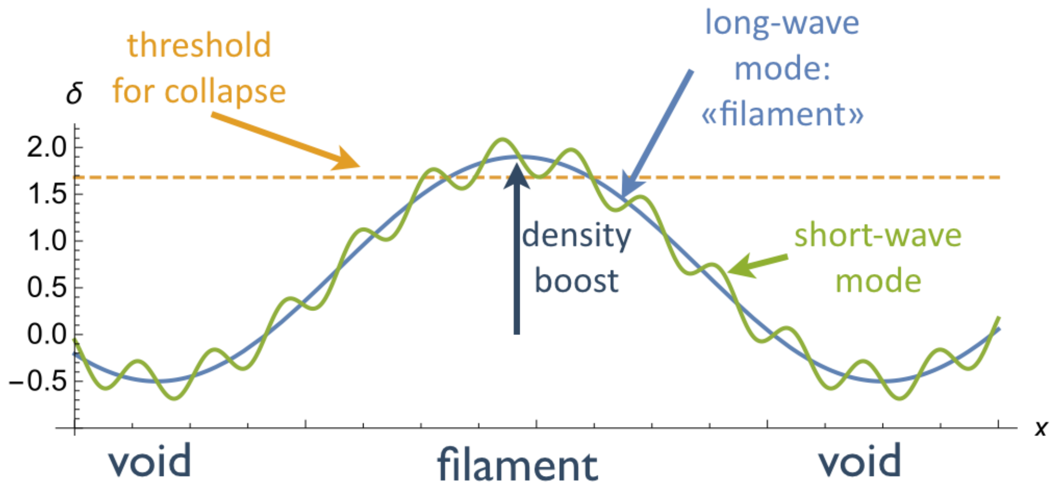

FIGURE 1.13: Illustration of the combination of short and long wave modes in the overdensity field compared with the linear density contrast δ_c as the threshold for collapsing structures. The densest regions account for ideal conditions to form halos, while less dense regions are underpopulated areas. The distribution of halos is thus biased compared with the distribution of the matter density field. (Credits: Codis, 2016)

their number lower and lower.

1.3.4 Bias of halos

Because dark matter halos are distinct objects in the Universe, they could be used to probe the total distribution of matter. Practically speaking, halos are not sampling the matter density field uniformly since they mostly form in the high-density regions. As a consequence, we say that dark matter halos are biased tracers of the background matter density field. This idea was first described by Kaiser (1984) and refined in Bardeen et al. (1986) with the enhanced clustering of Abell galaxy clusters.

In Figure 1.13, we illustrate this fact. An overdensity is collapsing as soon as it reaches the linear density contrast δ_c. As the overdensity field is composed of short and long wave modes, it reaches this threshold only in specific regions of the Universe. Thus, the probability to form halos is higher in regions sufficiently dense, letting the rest of the Universe underpopulated. Several groups have further developed this idea within the framework of the Press & Schechter formalism (e.g., Mo and White, 1996; Sheth and Tormen, 1999; Sheth, Mo, and Tormen, 2001; Giocoli et al., 2010a), deriving quantitative predictions for the correlation between the halo density field and the underlying matter distribution within the hierarchical scenario for the formation of cosmic structures. The relation between the dark matter halo density contrast, δ_h, and the total dark matter density contrast in the linear regime, δ_m, is described by the so-called halo bias parameter, b_h, defined as:

$$b_h \equiv \frac{\delta_h}{\delta_m} \,. \tag{1.41}$$

The halo bias constitutes a crucial parameter in cosmological studies as it directly relates the overdensity field from the linear perturbation theory to non-Gaussian peaks. First observations have been led very recently. For instance, during the past decade, Johnston et al. (2007b) measured the halo bias in the framework of a weak lensing analysis. It is also predicted by numerical simulations (e.g. Tinker et al., 2010), which makes ideal conditions to test such models on measurements derived from recent observational data. Driving novel cosmological analyses on this parameter is a promising breakthrough in our understanding of the formation and evolution of structures in the Universe.

1.4 Clusters of galaxies

Galaxy clusters are the most massive virialized structures in the Universe. This makes them crucial laboratories as they occupy a special place in the hierarchy of cosmic structures, at the crossroads of galaxy evolution and cosmological studies. According to the hierarchical scenario of the evolution of cosmic structures (Peebles, 1980; Voit, 2005), they arise from the collapse of initial density perturbations having a typical comoving scale of about 10 Mpc$/h$ (Peebles, 1993; Borgani, 2008). Above these scales, gravitational clustering is essentially in a linear regime and the dynamics are mostly driven by the Hubble flow, while the non-linear regime is prominent on smaller scales. Moreover, in the inner cluster regions, astrophysical processes such as gas cooling, star formation, feedback from supernovae, and active galactic nuclei modify the evolution of the halo properties like the density profile, the subhalo mass function, etc (Rasia, Tormen, and Moscardini, 2004; Rasia et al., 2006; Giocoli et al., 2010b; Despali, Giocoli, and Tormen, 2014; Despali et al., 2016; Angelinelli et al., 2020). Galaxy clusters thus provide an ideal tool to study the physical mechanisms driving the formation and evolution of cosmic structures in the mildly non-linear regime (Tormen, 1998; Springel et al., 2001).

1.4.1 Cluster formation

Galaxies are not distributed randomly, but they gather forming groups and clusters of galaxies. Galaxy clusters are hosted in the densest regions of the matter density field: the halos. While a cluster is characterized thanks to its baryonic materials, the galaxies, its formation is dominated by its main component, the dark matter. The hierarchical scenario seen in Section 1.3.3 tends to indicate that clusters form from smaller galaxy groups that merge at a later time in the history of Universe (for example, see Adami et al., 2013). As shown in Figure 1.11, the early density fluctuations at $\mathrm{z} = 18.3$ amplified in this web structure at $\mathrm{z} = 1.4$, and the materials spread through filaments into the node, the halo where the cluster lies. This filamentary structure is well observed in Figure 1.14, in particular through spectroscopic surveys (e.g. SDSS or 2dFGRS, York et al., 2000; Colless et al., 2001) and mock catalogues derived from numerical simulations (e.g. Millennium, Springel et al., 2005). Galaxies having different speeds along the filaments start forming small galaxy groups before they finally reach the galaxy clusters (Bond, Kofman, and Pogosyan, 1996). The redshift at which galaxies gather in clusters is still in debate, but most of them seem to form around $\mathrm{z} = 1.4$, while the farthest ones are detected at $\mathrm{z} \sim 1.5-2$ (Santos et al., 2011; Gobat et al., 2011).

1.4.2 Cluster properties

In the current paradigm, galaxy clusters are thought to be made of three main components: galaxies, dark matter, and gas in the IntraCluster Medium (ICM) (White

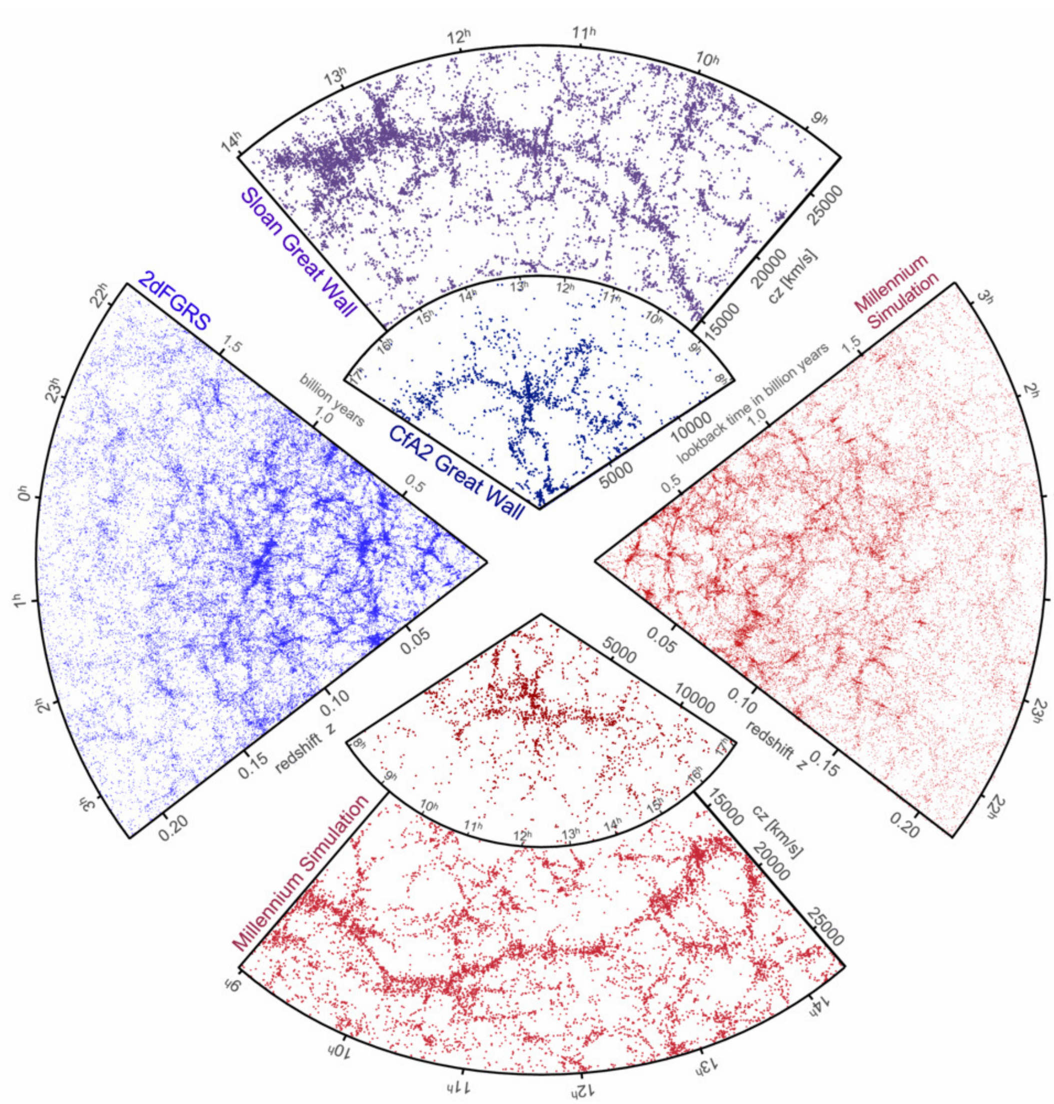

FIGURE 1.14: The galaxy distribution from spectroscopic redshift surveys (blue, Geller and Huchra, 1989; York et al., 2000; Colless et al., 2001) and mock catalogues constructed from the Millennium cosmological simulation (red, Springel et al., 2005). (Credits: Springel, Frenk, and White (2006))

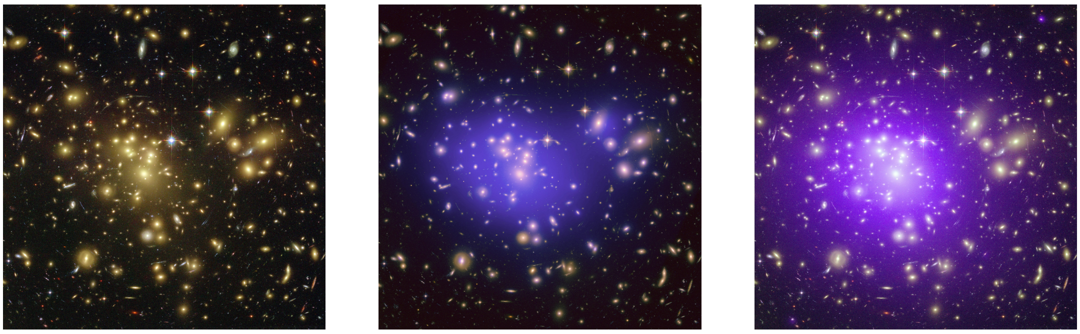

(A) Optical (HST)   (B) Optical (HST) + DM (HST)   (C) Optical (HST) + X-rays (Chandra)

FIGURE 1.15: The spatial distribution of the different matter components in the Abell 1689 galaxy cluster. (A) Distribution of galaxies in the optical as observed with HST. (B) Distribution of dark matter (blue) reconstructed with strong gravitational lensing in HST. (C) Distribution of the ICM (purple) in X-rays with Chandra. (Credits: Optical: NASA/STScI; X-ray: NASA/CXC/MIT/E.-H Peng et al; Dark matter: NASA, ESA, E. Jullo (JPL/LAM), P. Natarajan (Yale) and J-P. Kneib (LAM)

and Rees, 1978). Typically, their diameters are about $1 - 5$ Mpc$/h$ and total masses $10^{13} - 10^{15}$ $\mathrm{M}_{\odot}/h$, rarely exceeding $10^{16}\mathrm{M}_{\odot}/h$.

Galaxies in clusters are usually counted from ten to hundreds but represent only a small fraction of the cluster total mass, less than 5-10%. Generally, the brightest cluster galaxy (BCG) is used to define the center of the clusters of galaxies. However, this position is often shifted with the "real" center position of the total mass distribution in galaxy clusters due to environmental effects, for example in the case of a cluster merger.

Dark matter is the main component of galaxy clusters in terms of mass content, about 85% of the total mass. It can be probed with the lensing effect of a massive cluster onto a background source, bending the path of its light ray toward the observer. In practice, we measured lensing in a strong or weak regime, which relies on the strength of the deflection potential. This effect is insensitive to the nature of matter, which allows estimating the total mass of the cluster.

The ICM is composed of baryonic gas known as ionized hydrogen lying between galaxies, accounting for about 10-15% of the total mass. Early in the cluster formation, it is heated by gravitational field to $10^7 - 10^8$ K. The electrons in this hot plasma thus emit in X-ray through thermal Bremsstrahlung.

Figure 1.15 shows the distribution of the three matter content described above in the Abell 1689 galaxy cluster.

1.4.3 Cluster observations

Galaxy clusters can be observed with different segments composing the light spectrum.

We have seen that the X-ray band allows the detection of the ICM in clusters. This emission was first observed with the Coma cluster (Felten et al., 1966; Gursky et al., 1971). Later, X-ray surveys, such as the ROSAT-All-sky survey (RASS, 1990), the X-ray Multi-Mirror Mission (XMM-Newton, 1999), or the Chandra X-ray Observatory (1999), were driven by space telescope as Earth's atmosphere do not allow observations on its surface. The most recent telescope, eROSITA, was launched in

July 2019 and will allow accurate measurements of the ICM and novel X-ray detection of astronomical sources.

In the radio domain, the ICM can also be probed through the inverse Compton scattering of CMB photons of hot electrons. This effect, known as the Sunyaev-Zel'dovich effect (Sunyaev and Zeldovich, 1980), was measured in hundreds of clusters. It turned out to be an effective way to detect galaxy clusters and study properties of the ICM (e.g. Planck Collaboration et al., 2016, for its application to the Planck survey).

Visible and near-infrared bands are prominent to detect galaxies, and studying their number density, luminosity distribution, or velocity dispersion profile are effective methods to find clusters. For example, the location of galaxies in the color-magnitude panel tells us about their membership to a cluster, and algorithms known as "redmapper" (e.g. the red-sequence Matched-filter Probabilistic Percolation, Rykoff et al., 2014) take advantage of this feature to detect galaxy clusters. An alternative way is to rely on Optimal Filtering algorithms (Maturi et al., 2005; Bellagamba et al., 2011). This method identifies overdensities of galaxies associated with galaxy clusters taking into account their spatial, magnitude, and photometric redshift distributions (Radovich et al., 2017). Finally, optical observations are used to infer the gravitational lensing property of galaxy clusters and measure their mass. We will further discuss this effect in the following chapter.

1.5 Purposes of the thesis

With this section, I would like to remind the major points seen in this chapter and introduce the ensuing inquiries that we investigated during my thesis.

Because we have always observed and tried to understand our surrounding Universe, we are currently providing faithful cosmological models to our observations (Section 1.1). In particular, the standard model of cosmology gives an accurate description of the Universe in the framework of the cosmological principle, where the Universe is seen as a homogeneous and isotropic fluid in accelerated expansion. Its geometry is described with an FLRW metric and the dynamic of its content provided with the Friedmann equations (1.9) & (1.10). With this configuration, the evolution of the Universe is governed by a set of parameters defining the cosmological framework of the study (Section 1.2). More specifically, the matter component evolves as a Gaussian and isotropic field of inhomogeneities fluctuating around the mean density of the Universe. On scales sufficiently small, the perturbations collapse into virialized halos forming the so-called large-scale structure. The overdensity field of the Universe is not probed uniformly by the halos, but we recognize a bias into their distribution: the halo bias (Section 1.3). Galaxy clusters are astronomical objects that lie in specific regions of the sky, the halos. Hence, clusters are mostly formed with dark matter, invisible with direct observations. However, we can locate them through their baryonic components, the galaxies, or the ICM, and indirect observations of their total mass can be led with gravitational lensing (Section 1.4).

Galaxy clusters constitute crucial objects to answer a large number of cosmological questions. Indeed, as we have seen, they are predominantly made of dark matter, one of the principal riddles in today's cosmology. Thus, measuring the total mass of clusters is a prominent scientific breakthrough to better understand the nature of dark matter. As already mentioned, a method that allows such observation is gravitational lensing. Because clusters are combined with massive halos, they are also primordial to study the bias of the halos. The halo bias is consistent with the density profiles of the halos on large scales. To reach these scales and derive general properties of clusters, a statistical analysis is required with gravitational lensing in the weak regime. This tool is an effective way to compute density profiles in clusters from catalogs of data. However, halo mass and halo bias can be extracted in a given aperture only assuming a model of the halo density profile. In Chapter 2, we detail the theoretical framework of the weak gravitational lensing formalism and the predicted density profiles of the halo. The halo bias is also derived with numerical simulations in the framework of the ΛCDM model from the halo mass. This relation and the lack of measurement on this parameter give great opportunities to establish novel cosmological studies. I present the set of data used for our cosmological analysis in Chapter 3 and the results obtained from this study. More importantly, the next generation of telescopes will provide larger and deeper catalogs of data. These surveys are essential to increase our knowledge of the physical mechanism governing the evolution of the large-scale structure. Hence, the development of advanced numerical materials is required for the incoming investigations. I introduce in Chapter 4 the COMB-CL package which aims at measuring weak lensing mass for Euclid detected clusters. Finally, all these topics will be reviewed as a conclusion in Chapter 5 and the forthcoming cosmological perspective will be discussed.

Chapter 2

Theoretical framework

With this chapter, I would like to outline the theoretical framework required for the analysis of the data. As a first step, the lensing formalism will be detailed as it is primordial for the completion of the mass density profiles of galaxy clusters. In this section, I will begin with the basic lens equations, go toward the different physical aspects of gravitational lensing, give a detailed description of convergence and shear parameters and finally extend the overview of the lensing formalism to the convergence power spectrum. Thereafter, to contrast the density profiles of galaxy clusters derived with WL, I will define the density model of the halos. It is decomposed into various components, namely the one-halo term, a correction factor, and the two-halo term. Finally, the last section will be focused on the theoretical relations between the halo mass and other parameters of the halo model: the concentration and the halo bias.

2.1 Formalism of weak gravitational lensing

Gravitational lensing is a physical phenomenon that occurs when light is deflected by massive objects. Such an event has been discovered in the early XIX century (Soldner, 1804) with the deflection of a light ray of a star in the background of the sun. Since, many observations have been realized, specifically with galaxies (Zwicky, 1937) and galaxy clusters (Lynds and Petrosian, 1986; Soucail et al., 1988). Gravitational lensing opened a large field of study in astrophysics, as its intrinsic physical properties allow to derive the mechanisms of the non-visible matter. The standard approach to gravitational lensing has been laid out in several reviews, lecture notes and textbooks (e.g. Schneider, Ehlers, and Falco, 1992; Narayan and Bartelmann, 1996; Seitz and Schneider, 1997; Bartelmann and Schneider, 2001; Bartelmann, 2010; Kilbinger, 2015).

2.1.1 Lens equations

As predicted by general relativity, objects with important mass curve space-time. Because light follows geodesics, light rays are deflected nearby high densities and images in the background are distorted compared with their real shape. Assuming the Newtonian gravitational potential $\Phi \ll c^2$ as a small perturbation, we can rewrite the metric of the Universe seen in Equation (1.6) as:

$$ds^2 = \left(1 + \frac{2\Phi}{c^2}\right) c^2 dt^2 - \left(1 - \frac{2\Phi}{c^2}\right) dl^2 \ . \tag{2.1}$$

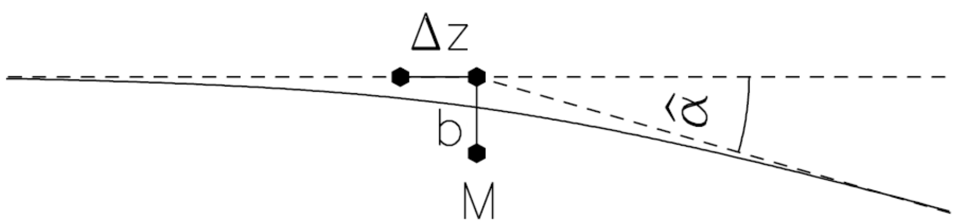

FIGURE 2.1: Diagram of the deflection of a light ray around a point mass. (Credits: Narayan and Bartelmann, 1996)

With the propagation condition for light $ds^2 = 0$, we can rearrange this equation and find the effective light speed in a weak gravitational field:

$$c' = \frac{dl}{dt} \simeq c\left(1 + \frac{2\Phi}{c^2}\right) \ , \tag{2.2}$$

where $\Phi/c^2 \ll 1$ was used in a first order Taylor expansion. We see that a weak gravitational field has the effective index of refraction:

$$n = \frac{c}{c'} \simeq 1 - \frac{2\Phi}{c^2} \ . \tag{2.3}$$

Conventionally normalized such as to vanish at infinity, the gravitational potential is negative and the index of refraction larger than unity. Assuming a point mass M at the origin of a coordinate system and a light ray propagating parallel to the z axis and passing the point mass at an impact parameter b as in Figure 2.1, the gravitational potential is given by:

$$\Phi = -\frac{GM}{\sqrt{b^2 + z^2}} \ . \tag{2.4}$$

We can now apply the Fermat's principle, which states that a light ray travels along an optical path τ between two fixed point A and B along which the travel time is extremal, giving at the first-order:

$$\delta\tau = \delta \int_A^B \frac{c}{n} dt = 0 \ . \tag{2.5}$$

The deflection angle $\hat{\alpha}$ of a lens of mass M is directly derived from the variation of τ with respect to the variation of the light path:

$$\vec{\hat{\alpha}} = \frac{2}{c^2} \int \vec{\nabla}_\perp \Phi d\lambda \ , \tag{2.6}$$

where $\vec{\nabla}_\perp$ is the gradient with respect to the normal direction and λ is an arbitrary parameter related to the light path. The integral over a light path is complicated to carry out, but it can be approximated by integration over a straight line, and injecting Equation (2.4) in Equation (2.6) gives:

$$\vec{\hat{\alpha}}(b) = \frac{2R_S}{b} , \tag{2.7}$$

where $R_S \equiv 2GM/c^2$ is known as the Schwarzschild radius of the lensing point mass.

Consider now the typical lens system displayed in Figure 2.2. We see that a light ray traveling close to the lens is deflected by an angle $\hat{\alpha}$, as identically shown in Figure 2.1. In this schema, D_s, D_l, and D_{ls} are the angular diameter distances from the observer to the source, from the observer to the lens, and from the lens to the source, respectively. The lens is assumed to be thin compared to the overall extent of the lens system, which holds for isolated objects such as galaxy clusters but not for extended lenses such as the large-scale structure. With this approximation, the light path is considered straight toward the observer, and the angles $\hat{\alpha}$, β, and θ are small compared with unity. We can then derive the following relation:

$$\vec{\beta} = \vec{\theta} - \vec{\alpha} , \tag{2.8}$$

where $\vec{\alpha}$ is the reduced deflection angle introduced with:

$$\vec{\alpha} = \frac{D_{ls}}{D_s}\vec{\hat{\alpha}} . \tag{2.9}$$

As processed in Equation (2.6), the reduced deflection angle can be written as a gradient:

$$\vec{\alpha}(\vec{\theta}) = \frac{2}{c^2}\frac{D_{ls}}{D_l D_s}\int \vec{\nabla}_\perp \Phi(D_l\vec{\theta}, z)dz . \tag{2.10}$$

It is convenient to describe gravitational lensing equations as a function of the angular position $\vec{\theta}$ in the sky pane. With this formalism, gradients need to be taken with respect to angles rather than perpendicular distances:

$$\vec{\nabla}_\theta = D_l^{-1}\vec{\nabla}_\perp . \tag{2.11}$$

Thus, Equation (2.10) turns into:

$$\vec{\alpha} = \vec{\nabla}_\theta \psi \;\text{ with }\; \psi \equiv \frac{2}{c^2}\frac{D_{ls}}{D_l D_s}\int \Phi dz . \tag{2.12}$$

The quantity ψ is called the deflection potential or the lensing potential.

2.1.2 Convergence and shear

Taking gradient of the reduced deflection angle leads to the Laplacian of the lensing potential:

$$\vec{\nabla}_\theta \vec{\alpha} = \vec{\nabla}_\theta^2 \psi = \frac{2}{c^2}\frac{D_l D_{ls}}{D_s}\int \vec{\nabla}_\perp^2 \Phi dz . \tag{2.13}$$

In the above equation, we have replaced the Laplacian with respect to the angle coordinate with the Laplacian with respect to perpendicular physical coordinates. We can extend the definition of the Laplacian with respect to the complete physical coordinate:

$$\vec{\nabla}^2 = \vec{\nabla}_\perp^2 + \frac{\partial^2}{\partial z^2} , \tag{2.14}$$

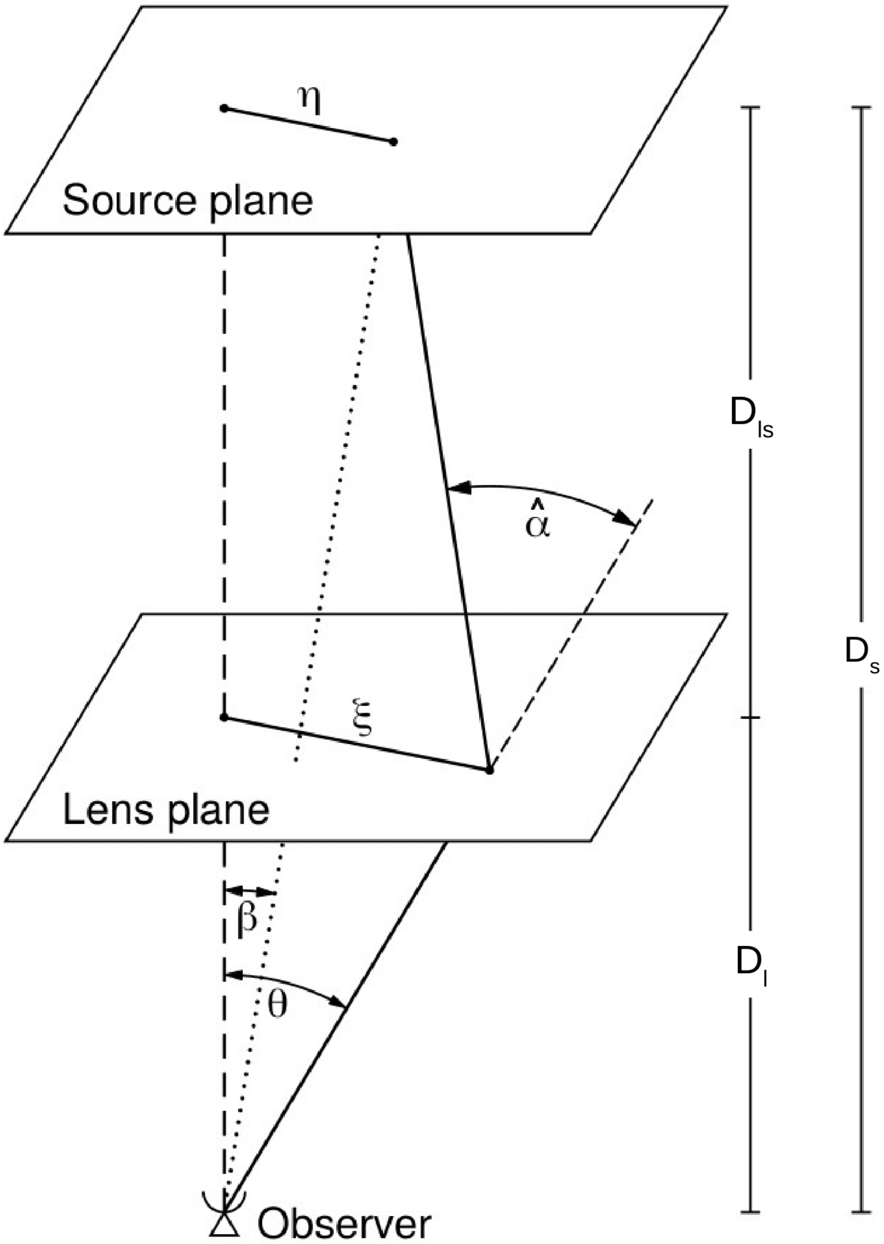

FIGURE 2.2: Diagram of a typical lens system. (Credits: Bartelmann and Schneider, 2001)

and derive with the Poisson's equation:

$$\vec{\nabla}^2\Phi = 4\pi G\rho \ . \tag{2.15}$$

Here ρ is the matter density of the field. The Poisson's equation can be inserted into Equation (2.13) considering $\partial\Phi/\partial z \simeq 0$, as the extent of the lens is small compared to the cosmological distances involved, giving:

$$\vec{\nabla}_\theta^2\psi = 2\frac{\Sigma}{\Sigma_{cr}} \equiv 2\kappa \ , \tag{2.16}$$

where the surface mass density and the critical surface mass density are respectively defined as $\Sigma \equiv \int \rho$ and:

$$\Sigma_{cr} \equiv \frac{c^2}{4\pi G}\frac{D_s}{D_l D_{ls}} \ . \tag{2.17}$$

The parameter κ is the dimensionless surface mass density also called convergence. Practically speaking, its variation corresponds to an isotropic deformation of the image of the source by the lens. If its value is negative, then the source shape will appear smaller, and if positive bigger. The efficiency of the lens depends on the combination between its density and its position along the line of sight. Indeed, Equation (2.16) is maximized when Σ is high and Σ_{cr} is low. Thus in Euclidean space, lensing is more efficient when the lens is located at a half distance of the source.

So far we have reviewed the formalism of gravitational lensing in the most general case. Let us now switch to the specific case that is weak lensing. In this regime, we consider angular size much smaller than any typical scale of variation in the deflection angle. The intrinsic angular size of the source and its corresponding image is connected with the Jacobian matrix $\mathcal{A}$:

$$\mathcal{A}_{ij} \equiv \frac{\partial\vec{\beta}_i}{\vec{\theta}_j} = \delta_{ij} - \psi_{ij} \ , \tag{2.18}$$

with $\psi_{ij} \equiv \partial^2\psi/\theta_i\theta_j$ are the second partial derivative of the lensing potential. We can relate the Jacobian matrix with Equation (2.16) by taking its trace:

$$\mathrm{tr}\mathcal{A} = 2 - \vec{\nabla}_\theta^2\psi = 2(1-\kappa) \ . \tag{2.19}$$

When subtracting it from $\mathcal{A}$ by means of the unit matrix $\mathcal{I}$, we obtain the shear matrix:

$$\Gamma \equiv -\left(\mathcal{A} - \frac{1}{2}(\mathrm{tr}\mathcal{A})\mathcal{I}\right) \ , \tag{2.20}$$

which components are:

$$\begin{aligned} \gamma_1 &\equiv \Gamma_{11} = -\Gamma_{22} = \frac{1}{2}(\psi_{11} - \psi_{22}) \ , \\ \gamma_2 &\equiv \Gamma_{12} = \Gamma_{21} = \psi_{12} \ . \end{aligned} \tag{2.21}$$

If Equations (2.19) & (2.21) are taken together with Equation (2.20), we arrive at the final form of the Jacobian matrix:

$$\mathcal{A} = (1-\kappa)\mathcal{I} - \Gamma = \begin{pmatrix} 1-\kappa-\gamma_1 & -\gamma_2 \\ -\gamma_2 & 1-\kappa+\gamma_1 \end{pmatrix} \ . \tag{2.22}$$

Because lensing does change the apparent solid angle of a source, we determine how the angular size of a source is magnified compared with its image by the magnification factor μ. It is expressed as the inverse determinant of $\mathcal{A}$ following:

$$\mu \equiv \frac{1}{\det\mathcal{A}} = \frac{1}{(1-\kappa)^2 - |\gamma|^2} \ , \tag{2.23}$$

where the quantity $\gamma \equiv \gamma_1 + i\gamma_2$ is the complex form of the shear which translates into anisotropic deformations of the image of the source by the lens. More specifically, sources initially have an intrinsic unlensed ellipticity ε_s, which is converted by cosmic shear into the observed ellipticity ε. One describes this deformed ellipse by its minor and major axes (a, b), and from the position angle ϕ of the source relative to the lens, as:

$$\varepsilon = |\varepsilon| e^{2i\phi} \ , \ \text{with } |\varepsilon| = \frac{a-b}{a+b} \ . \tag{2.24}$$

It is convenient to factor out the multiplicative term $(1-\kappa)$ from Equation (2.22) and thereby introduce the reduced shear observable:

$$g \equiv \gamma/(1-\kappa) \ , \tag{2.25}$$

and its conjugate version g^*. Considering $|g| \leq 1$, we can relate shear and ellipticity with:

$$\varepsilon = \frac{\varepsilon_s + g}{1 + g^*\varepsilon_s} \ . \tag{2.26}$$

In the WL limit $\gamma \ll 1$ and $\kappa \ll 1$, yielding $\varepsilon \approx \varepsilon_s + g$. Assuming that sources are randomly oriented, their complex intrinsic ellipticities average to zero, so $\langle\varepsilon\rangle = \langle\gamma\rangle$. Therefore, the average ellipticity of background galaxies is a direct observable of the shear induced by foreground matter.

The two components of the complex shear are defined relative to a local Cartesian space and are conveniently decomposed into a tangential and a cross component:

$$\begin{aligned} \gamma_+ &\equiv -\Re\left(\gamma e^{-2i\phi}\right) = -\left(\gamma_1 \cos 2\phi + \gamma_2 \sin 2\phi\right) \ , \\ \gamma_\times &\equiv -\Im\left(\gamma e^{-2i\phi}\right) = -\left(\gamma_2 \cos 2\phi - \gamma_1 \sin 2\phi\right) \ , \end{aligned} \tag{2.27}$$

respectively. Noticing the minus sign in the exponential, it is agreed that for an axially symmetric mass distribution the tangential component returns a positive value around an overdensity, while a negative value characterizes underdensities. On the other hand, the cross component of the shear does not hold any mass information, and thus averages to zero, in the absence of systematic uncertainties.

2.1.3 Convergence power spectrum

So far, we have assumed gravitational lensing in the thin lens approximation, that is the size of the lens is negligible compared with the overall extent of the lens system. This configuration is clearly not appropriate for more extended lenses along the line of sight, for instance, the large-scale structure of the Universe. To correct this problem, distances involved for the lensing potential definition in Equation (2.12) should be integrated with Φ along the line-of-sight. However, because our Universe is expanding, it is more convenient now to describe the spacing between objects in terms of comoving distance. In Section 1.2.6 we have seen that comoving and angular diameter distances remain the same in a spatially flat Universe. Let consider χ the comoving angular diameter distance in spatially flat space-time and χ_s the source distance, we now can

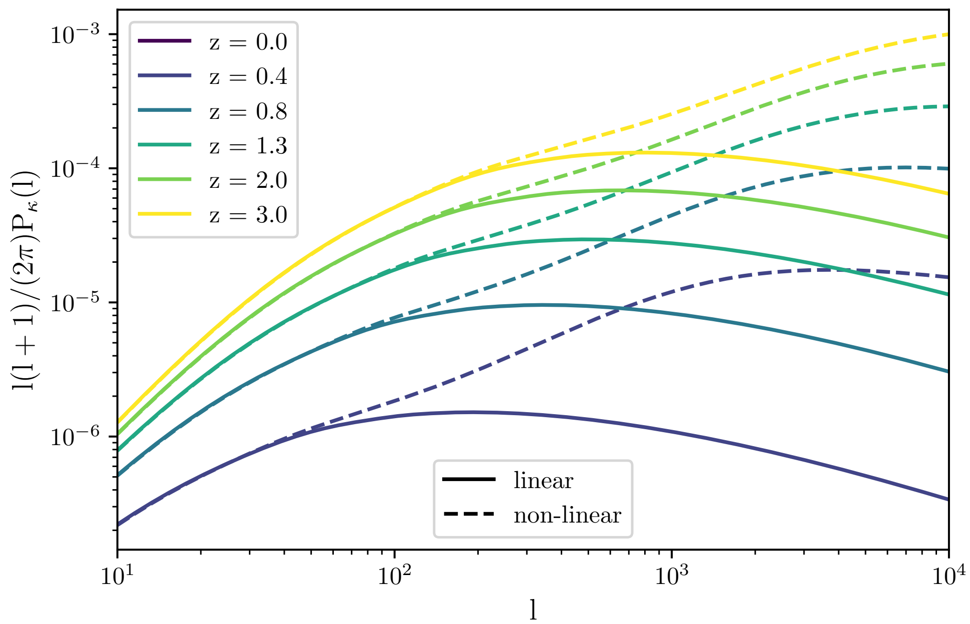

FIGURE 2.3: The convergence power spectrum as computed in Equation (2.32) at various redshifts. We show the functional form with linear and non-linear matter power spectra computed in Equations (1.34) & (1.36).

proceed with the following conversion:

$$\frac{D_{ls}}{D_l D_s} \longrightarrow \frac{\chi_s - \chi}{\chi_s \chi} \ , \tag{2.28}$$

and the deflection potential becomes:

$$\psi = \frac{2}{c^2} \int_0^{\chi_s} d\chi \frac{\chi_s - \chi}{\chi_s \chi} \Phi(\chi \vec{\theta}, \chi) \ . \tag{2.29}$$

The lensing quantities $\vec{\alpha}$, κ and γ are now defined in terms of ψ of Equation (2.29). In particular, the convergence is converted from Equation (2.16) using the Poisson's equation into the effective convergence:

$$\kappa = \frac{3}{2} \frac{H_0^2}{c^2} \Omega_m \int_0^{\chi_s} d\chi \frac{\chi(\chi_s - \chi)}{a(\chi)\chi_s} \delta(\chi) \ , \tag{2.30}$$

where the overdensity δ is taken from Equation (1.21) and a is the scale factor as defined in Equation (1.4). This expression is a projection of the density contrast along with comoving coordinates, weighted by a geometrical factor involving distances between the observer and the source. Similarly, the matter power spectrum is expressed in terms of the density contrast in Equation (1.30), we can derive the convergence power spectrum in terms of the effective convergence:

$$\langle \tilde{\kappa}(\mathbf{l}) \tilde{\kappa}(\mathbf{l}') \rangle = (2\pi)^3 P_\kappa(l) \delta_D(\mathbf{l} - \mathbf{l}') \ , \tag{2.31}$$

where the complex Fourier transform $\tilde{\kappa}$ of the convergence is a function of the 2D wave vector $\mathbf{l} \equiv \chi\mathbf{k}$. Again due to statistical homogeneity and isotropy, the convergence power spectrum only depends on the modulus l. Taking the square of Equation (2.30) in Fourier space, we get an analytical form of the convergence power spectrum:

$$P_\kappa(l) = \frac{9}{4}\frac{H_0^4}{c^4}\Omega_m^2 \int_0^{\chi_s} d\chi \left[\frac{\chi(\chi_s - \chi)}{a(\chi)\chi_s}\right]^2 P\left(\frac{l}{\chi}, \chi\right) , \tag{2.32}$$

where P is the matter power spectrum. This result can be derived using the Limber's approximation, which only collects modes that lie in the plane of the sky, thereby neglecting correlations along the line of sight. We see that P_κ is an integral over the comoving distance from the observer to the source, but given this functional form it can be computed in terms of redshift corresponding to the source redshift of the lens system. For example, in Figure 2.3 we show the convergence power spectrum computed at different source redshifts. We also display the two forms provided with the linear and non-linear regimes driving the matter power spectrum shape.

2.2 Models of the halo density

In this section we explore the theoretical mass density distribution of the halo, also called the halo model. All the terms in this relation depend on the surface density Σ. It is computed by the projection over the line of sight of the excess matter density $\Delta\rho$ in a sphere centered on the halo as:

$$\Sigma(R) = \int_{-\infty}^{\infty} \Delta\rho\left(\sqrt{R^2 + \chi^2}\right) d\chi . \tag{2.33}$$

$\Delta\rho$ includes the two terms of the halo model from the halo-matter correlation function ξ_{hm}:

$$\Delta\rho = \rho_m \xi_{hm} , \tag{2.34}$$

and the mean matter density $\rho_m \equiv \Omega_m \rho_c$ must be computed in physical units at the redshift of the sample. The critical density ρ_c is related to the first of the Friedmann equations and is defined as in Equation (1.11).

In WL, we average this quantity over the disk to derive the mean surface density enclosed within the radius R:

$$\overline{\Sigma}(< R) = \frac{2}{R^2}\int_0^R R'\Sigma\left(R'\right) dR' . \tag{2.35}$$

In the following and for the terms contributing to the halo model, we are interested in the main lens structure, which comprises the total mass of the halo and its concentration. The study of the relation of the halo mass and the halo concentration, developed in Section 2.3, is also driven by this main component. In addition, we include the contribution of possibly miscentered density profiles. Finally, we complete the halo model with the correlated matter component that allows the cosmological study from the analysis of the halo bias.

For the cosmological analysis developed in the next chapter, the total surface mass density profile is modeled with the terms, described at the following, and their associated marginalized parameters:

$$\Sigma_{tot} = \Sigma_{\substack{1h \\ \text{BMO} \\ \text{mis}}}(M_{200c}, c_{200c}, \sigma_{off}, f_{off}) + \Sigma_{\substack{2h \\ \text{lin}}}(b_h \sigma_8^2) . \tag{2.36}$$

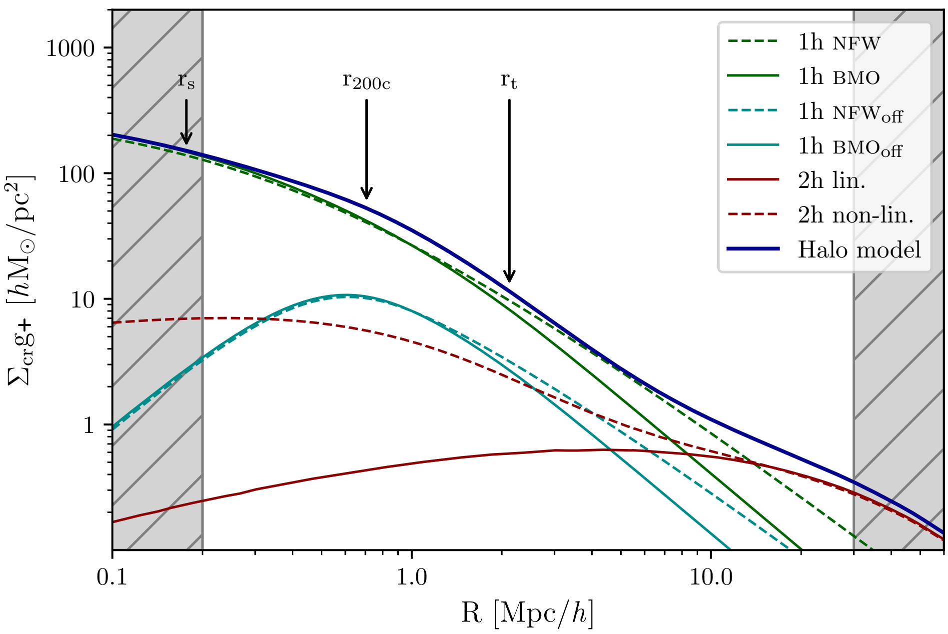

FIGURE 2.4: The halo model (blue) is composed of the BMO halo mass profile (thick green, Baltz, Marshall, and Oguri, 2009), its off-centered contribution (thick cyan, Johnston et al., 2007a) and the second term derived from the linear matter power spectrum (thick red, Eisenstein and Hu, 1999). For comparison, we show the centered / off-centered NFW mass profile (dashed green / cyan, Navarro, Frenk, and White, 1997) and the surrounding matter term with a non-linear power spectrum (dashed red, Takahashi et al., 2012). The density profile is computed in this example for a halo at $z_l = 0.2$ with a total mass $M_{200c} = 10^{14}\ M_\odot/h$, a concentration $c_{200c} = 4$ and a bias set at $b_h = 1$ (with $\sigma_8 = 0.8$. The variance and the fraction of an off-centered population contribute to the profile with $\sigma_{off} = 0.25$ Mpc/h and $f_{off} = 0.25$. Finally, the reduced shear is given for an effective source redshift $z_s = 1$, while the non-shaded area reveals the range allowed by the stacked WL analysis.

Mass and bias are the two most critical variables among the five free parameters since they both act on the amplitudes of the one-halo and two-halo terms, respectively. For example, Figure 2.4 shows Equation (2.36) in blue with $z_l = 0.2$, $z_s = 1$, $M_{200c} = 10^{14}\ M_\odot/h$, $c_{200c} = 4$, $\sigma_{off} = 0.25$ Mpc/h, $f_{off} = 0.25$ and $b_h\sigma_8^2 = 0.8^2$.

In Figure 2.4 we display, as an example, the complete model for a given mass, concentration, bias, and redshift of the halo.

2.2.1 One-halo term

The correlation between the halo and its own matter content is given by the halo matter density profile ρ_h:

$$\xi_{1h} = \frac{\rho_h}{\bar{\rho}_m} - 1 \ . \tag{2.37}$$

Analytic calculations and numerical simulations suggest that dark matter halos have a symmetric density profile in a spherical aperture (Navarro, Frenk, and White, 1996).

More recent studies look at the impact of the triaxiality of the halos as a new source of uncertainty in the WL signal (Oguri et al., 2005; Meneghetti et al., 2010; Sereno and Umetsu, 2011). This systematics involves a larger scatter of the mass and over-estimates the concentration when triaxial clusters are aligned with the line of sight.

Several works, such as Navarro, Frenk, and White (1997) and Bullock et al. (2001) provided a specific analytical form for the halo distribution, also called the Navarro-Frenk-White (NFW) density profile, in which the density varies with the distance from the center r as:

$$\rho_{\rm NFW} = \frac{\rho_s}{(r/r_s)(1+r/r_s)^2} \,, \tag{2.38}$$

where $\rho_s = \rho_c \delta_c$ is the scale density and r_s the scale radius. The overdensity contrast δ_c can be expressed as a function of the concentration c and the overdensity factor Δ as:

$$\delta_c = \frac{\Delta c^3}{3m\,(c)} \,. \tag{2.39}$$

The function m(c) depends on the choice of density profile and on the concentration parameter as in Equation(2.43). Thereafter, we adopt the common virial value $\Delta = 200c$, relating to a spherical volume with a density 200 times higher than the critical density of the Universe. Hence, we parametrize the scale radius as:

$$r_s = r_{200c}/c_{200c} \,. \tag{2.40}$$

We leave the concentration within that sphere free in order to study the relation between the mass and the concentration in Section 3.4.4. A second approach would be to consider an existing mass-concentration scaling relation, e.g. from Merten et al. (2015a) based on X-ray selected galaxy clusters of the Cluster Lensing And Supernova Survey with Hubble (CLASH, Postman et al., 2012), or from simulations (e.g. Child et al., 2018, see Section 2.3.1). The 3D NFW profile can be analytically converted into a 2D version and thereby extended to an excess surface mass density version following Golse and Kneib (2002).

A specific and additional feature for the halo model is to include stripping effects by tidal forces. These phenomena represent an important challenge for modeling DM substructures of halos (Taylor and Babul, 2004; Oguri and Lee, 2004) and their measurements provide significant tests for CDM simulations (Hayashi et al., 2003; Taylor and Babul, 2005). In particular, tides strip external regions of subhalos resulting in the disruption of their hosted halo and modify its outer density profile in a steeper way (Okamoto and Habe, 1999). The NFW profile has a non-physical divergence of its total mass (Takada and Jain, 2003). The Baltz-Marshall-Oguri (BMO, Baltz, Marshall, and Oguri, 2009) profile is a smoothly truncated version of the NFW profile which allows circumventing this problem with infinite mass. This profile presents the following shape:

$$\rho_{\rm BMO} = \frac{\rho_s}{(r/r_s)(1+r/r_s)^2}\left(\frac{r_t^2}{r^2+r_t^2}\right)^2 \,. \tag{2.41}$$

Stripping expects the cold dark matter halos to be smoothly-truncated and their density to collapse beyond the tidal radius, set at (Covone et al., 2014; Sereno et al., 2017; Bellagamba et al., 2019):

$$r_t = 3r_{200c} \,. \tag{2.42}$$

This configuration of the truncation radius derives from a fitting method involving a convergence model on ray-tracing simulations (Oguri and Hamana, 2011). The BMO profile also provides less biased estimates of mass and concentration with respect to the NFW profile, and better describes the density profile at the transition scales between the one-halo and two-halo terms. Baltz, Marshall, and Oguri (2009) provide an analytical expression for the surface mass density. The function m in Equation (2.39) differs according to the profile as (Oguri and Hamana, 2011):

$$\begin{aligned} m_{\rm NFW} &= \ln(1+c) - \frac{c}{1+c} \\ m_{\rm BMO} &= \frac{\tau^2}{2(\tau^2+1)^3(1+c)(\tau^2+c^2)} \\ &\times \Big[c(\tau^2+1)\{c(c+1) - \tau^2(c-1)(2+3x) - 2\tau^4\} \\ &+ \tau(c+1)(\tau^2+c^2)\{2(3\tau^2-1)\arctan(c/\tau) \\ &+ \tau(\tau^2-3)\ln(\tau^2(1+c)^2/(\tau^2+c^2))\}\Big] \ , \end{aligned} \tag{2.43}$$

where:

$$\tau \equiv r_t/r_s \ . \tag{2.44}$$

We display the NFW and BMO surface mass density profiles in Figure 2.4. We indicate r_s, r_{200c} and r_t locations with vertical arrows.

2.2.2 Miscentering correction

Since galaxy clusters are detected with cluster finder algorithms as discussed in Section 1.4.3, the location of their center is attributed to the detector. For example, redmapper often use the location of the BCG as the barycenter of the total mass distribution of the cluster, but it is biased as this position is in fact shifted with the dark matter halo center.

The Optimal Filtering algorithm later discussed in Section 3.1.3, detects clusters from overdensities of the spatial distribution of galaxies. The location of their center is assumed to be known. Because the algorithm detects overdensities from the galaxies distribution, we do not rely on the peaks related to the fluctuations in the total matter distribution. Instead, as the detection of clusters is based on the identification of galaxy overdensities, the adopted cluster center corresponds to the peak in the projected space of the galaxy distribution. This peak may not coincide with the barycenter of the DM distribution.

In reality, we expect the detected pixel position of the cluster center to possibly be shifted with respect to the center of the halo. Skibba and Macciò (2011) and George et al. (2012) discussed the importance of locating the centers of dark matter halos in order to properly estimate their mass profiles. Miscentering is expected to be a small fraction with respect to the cluster radius, under the assumption that light traces dark matter (Zitrin et al., 2011b; Zitrin et al., 2011a; Coe et al., 2012; Merten et al., 2015b; Donahue et al., 2016). However, radial miscentering is larger for optical clusters selected in a survey with a complex mask footprint.

Hence, we introduce the radial displacement of the cluster center $R_{\rm off}$, while the off-centered density profile is the average of the centered profile over a circle drawn around the incorrect center (Yang et al., 2006; Johnston et al., 2007a):

$$\Sigma_{\rm off}(R|R_{\rm off}) = \frac{1}{2\pi}\int_0^{2\pi} \Sigma_{\rm cen}\left(\sqrt{R^2 + R_{\rm off}^2 + 2RR_{\rm off}\cos\theta}\right) d\theta \ . \tag{2.45}$$

This term holds for an isolated galaxy cluster. We extend the profile to a global population of galaxy clusters so that the off-centered contribution is given by:

$$\overline{\Sigma}_{\rm off}(R|\sigma_{\rm off}) = \int_0^\infty P(R_{\rm off}, \sigma_{\rm off}) \Sigma_{\rm off}(R|R_{\rm off}) dR_{\rm off} \ , \tag{2.46}$$

where the displaced distances $R_{\rm off}$ follows a Rayleigh distribution with parameter $\sigma^2_{\rm off}$ (Simet et al., 2017; Melchior et al., 2017):

$$P(R_{\rm off}, \sigma_{\rm off}) = \frac{R_{\rm off}}{\sigma^2_{\rm off}} \exp\left[-\frac{1}{2}\left(\frac{R_{\rm off}}{\sigma_{\rm off}}\right)^2 \right] . \tag{2.47}$$

Considering $f_{\rm off}$ as the fraction of the off-centered population, the total miscentered density profile can be modeled as:

$$\Sigma_{\rm mis}(R|\sigma_{\rm off}, f_{\rm off}) = (1 - f_{\rm off})\Sigma_{\rm cen}(R) + f_{\rm off}\overline{\Sigma}_{\rm off}(R|\sigma_{\rm off}) \ . \tag{2.48}$$

Since this mainly impacts the central region of the halo profile, we reduce the correction to the one-halo component of the model. The miscentering effect is illustrated in Figure 2.4 with the two elements of the above sum. From the figure, we can also see that the miscentering parameters are degenerate with the halo concentration.

2.2.3 Two-halo term

On large scales, the lensing signal of the halo is dominated by correlated matter, e.g. neighboring halos or filaments, rather than its own matter content. The two-halo term usually contributes to the whole profile at $R \gtrsim 10$ Mpc$/h$. Following the standard approach, this signal is proportional to the matter-matter correlation function ξ_m through the halo bias b_h:

$$\xi_{2h} = b_h \xi_m \ . \tag{2.49}$$

We derive the matter correlation function at radius r from the Fourier transform of the dimensionless matter power spectrum $\Delta^2(k) \equiv P(k)k^3/\left(2\pi^2\right)$, and the first-order spherical Bessel function $j_0(x) = \sin x / x$:

$$\xi_m = \int_0^\infty \frac{\Delta^2(k)}{k} j_0(kr) dk \ . \tag{2.50}$$

We illustrate the second term of the surface mass density profile in Figure 2.4 assuming bias $b_h = 1$. We also display results given by the linear matter power spectrum (Eisenstein and Hu, 1998; Eisenstein and Hu, 1999) and by the non-linear matter power spectrum computed assuming the so-called halofit model (Takahashi et al., 2012). A halo mass of $M_{200c} = 10^{14}$ $M_\odot/h$ and concentration of $c_{200c} = 4$ contribute 15% and 25%, respectively, to the whole profile at the intermediate scale $R = 3.16$ Mpc$/h$, considering the BMO miscentered profile as the one-halo term. We focus on the linear version since we provide a comparative analysis with theoretical mass-bias relations (e.g. Tinker et al., 2010, see Section 2.3.2) derived from simulations, where results are given in terms of "peak height" in the linear density field. However, it is important to keep in mind that the non-linear version of the power spectrum shows a non-negligible contribution of mass fluctuations at small and intermediate scales. The second term of the halo model is parameterized in terms of a degenerate value of the halo bias with σ_8^2. This parameter defines the RMS fluctuations $\sigma(M)$ for a mass enclosed in a comoving sphere of radius 8 Mpc$/h$. This actually corresponds to the typical scale for the formation of galaxy clusters. The parameter σ_8^2 also derives from the matter power spectrum as a normalization factor and permits the cosmological inference of the product $b_h\sigma_8^2$ (see Section 3.4.6).

2.3 Predictions of the halo mass

The model of density profile shown in the previous section accounts for three major halo parameters: mass, concentration, and bias. While the mass of the halo is prominent for the analytical description of the model, the two other variables can be expressed in terms of the first one. Indeed, numerous numerical simulations show that the halo concentration and the halo bias are related to the halo mass. At the following, we detail the theoretical relations of the halo mass with respect to the halo concentration and the halo bias.

2.3.1 Halo concentration

Halo concentration is determined by the mean density of the Universe at the epoch of halo formation (Neto et al., 2007; Giocoli, Tormen, and Sheth, 2012). Thus, clusters that assemble later are expected to have a lower concentration than older clusters, formed when the mean density was higher. This determines a clear correlation with the halo mass in such a way that the halo concentration is expected to be a decreasing function of the halo mass. Results from simulated data show this relation, but this behavior between the concentration and the total mass has also been tested observationally (e.g. Okabe et al., 2010). Many of these studies measure the density profile of simulated halos and constrain a mass-concentration relation according to models, mostly NFW. A large number of them do not directly fit functions of mass, but instead operate the the peak height parameter of the halos as defined in Equation (1.38). In this case, the RMS variance of the field is described with the halo mass, computed from the Lagrangian radius of the halos as:

$$M = \frac{4\pi R^3}{3}\rho_m \ . \tag{2.51}$$

Different fitting methods can produce inconsistent results, thus we shall account for numerous theoretical predictions to better enlarge the field of study of the concentration. All these functions presented in this thesis are displayed in Figure 2.5.

Duffy et al. (2008) measure the mass-concentration relation with a NFW profile using N-body simulations with a fiducial Wilkinson Microwave Anisotropy Probe year 5 (WMAP5) cosmology. They find an additional dependency between the halo mass and redshift, best modeled as a power law.

Bhattacharya et al. (2013) predict the concentration with the halo mass from dark matter simulations run in the framework of a WMAP7 cosmology in the redshift range $0 < z < 2$. The best-fitted relation gives the concentration as a power-law function of the peak height parameter.

Dutton and Macciò (2014) use a set of simulations to detect halos with spherical overdensity algorithm and fit NFW profiles in a Planck Collaboration et al. (2014) cosmology. They derive a power-law relation between mass and concentration.

Meneghetti et al. (2014) present an analysis of the N-body/hydrodynamical simulations that aimed at estimating the expected concentration-mass relation for the Cluster Lensing and Supernova Survey with Hubble (CLASH) cluster sample. With NFW

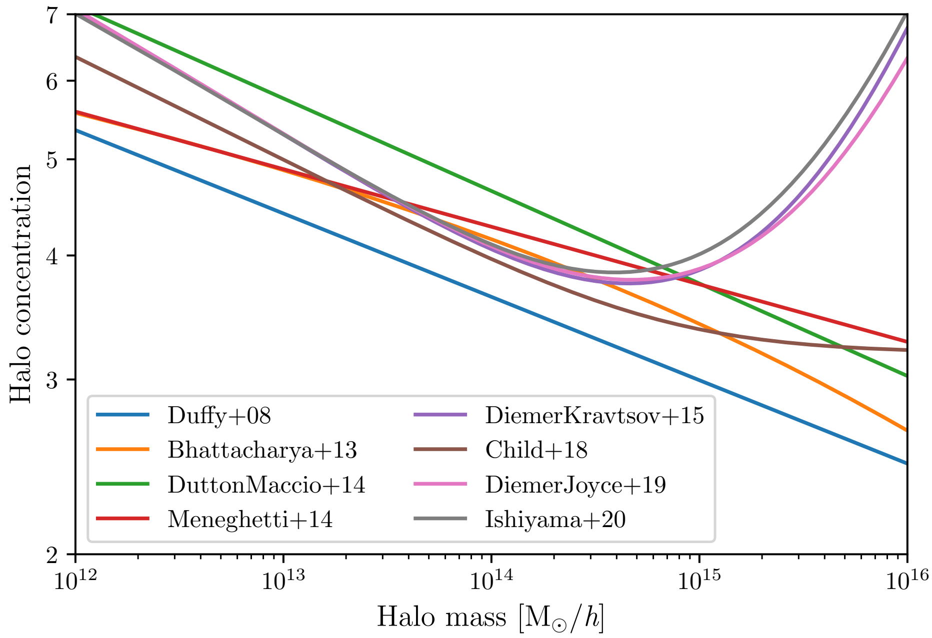

FIGURE 2.5: Relations between the mass and the halo concentration at lens redshift $z_l = 0.3$. The relations derive from results given by different theoretical analyses, respectively Duffy et al. (2008), Bhattacharya et al. (2013), Dutton and Macciò (2014), Meneghetti et al. (2014), Diemer and Kravtsov (2015), Child et al. (2018), Diemer and Joyce (2019), and Ishiyama et al. (2020).

and alternative versions of density models, they provide a mass-redshift-concentration relation.

Diemer and Kravtsov (2015) give a universal model in $c_{200c} - \nu$ space without applying for specific cosmology. This complex model makes use of the matter power spectrum slope to correct from residual deviations in the relation. This parameter is defined as:

$$n = \frac{\mathrm{dln}P(k)}{\mathrm{dln}k} . \tag{2.52}$$

This feature makes the relation highly sensitive to the cosmological framework, as n is directly involved in the amplitude of the power law.

Child et al. (2018) combine two very large cosmological N-body simulations to measure mass and concentration of the halos with a NFW profile. They fit is a power-law function, dependent on the non-linear mass instead of the peak height. This relation covers a redshift range of $0 < z < 4$.

Diemer and Joyce (2019) model is an improved version of Diemer and Kravtsov (2015). It is based on a mathematical derivation of the evolution of concentration at the low-mass end of the relation. This functional form is more physically motivated, and allows fewer free parameters (six instead of seven). In addition to the logarithmic slope of the matter power spectrum seen in Equation (2.52), it involves the effective exponent of linear growth defined as:

$$\alpha_{\mathrm{eff}} = -\frac{\mathrm{dln}D_+}{\mathrm{dln}(1+z)} . \tag{2.53}$$

Because of the improved functional form, the model improves the fit, particularly in the case of scale-free cosmologies.

Ishiyama et al. (2020) recalibrate Diemer and Joyce (2019) model with a new set of large high resolution simulations. The model provides median concentrations only but was calibrated for a larger number of overdensity definitions Δ.

2.3.2 Halo bias

The halo bias, introduced in Section 1.3.3, is essential to model the two-halo terms. It quantifies the excess clustering of halos over the clustering of dark matter. As with concentration, bias is predicted as a function of either mass or peak height with numerical simulations. Such theoretical relation represents crucial probes for cosmological analyses. Practically speaking, halos are detected in simulated data and their bias is assessed by measuring the halo power spectrum and computing its ratio with the linear matter power spectrum:

$$b_h^2 = \frac{P_h}{P_L} . \tag{2.54}$$

The square of the halo bias is taken because we consider the ratio of power spectra, while in Equation (1.41) the bias is derived from the ratio of overdensity parameters. In contrast with concentration-mass relations, studies that constrain mass-bias relations are fewer but do not present strong inconsistency. All of them show that bias is predicted as an increasing function of the mass, and at fixed mass that the halo bias varies with redshift. We account here for three different predictions of the halo bias. We select these models because all provide models with a redshift dependency, which is more consistent with observed galaxy clusters. We show such models in Figure 2.6 for a set of lens redshifts.

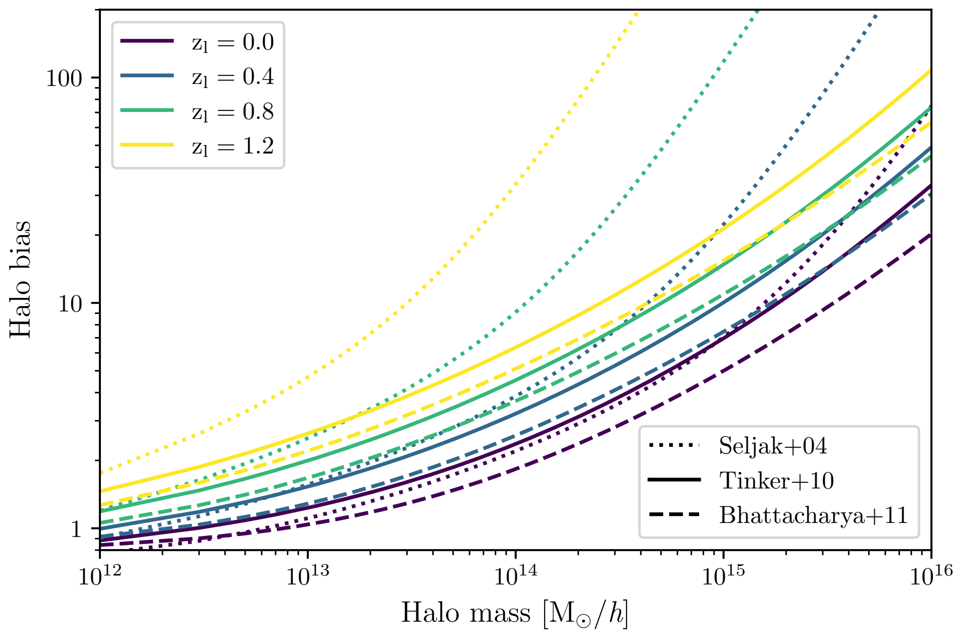

FIGURE 2.6: Relations between the mass and the halo bias at different lens redshift. The relations derive from results given by different theoretical analyses, respectively Seljak and Warren (2004), Tinker et al. (2010), and Bhattacharya et al. (2011).

The first relation is derived in Seljak and Warren (2004). The authors use a set of N-body simulations to explore the average halo bias relation as a function of halo mass. The relation is given under the form of a power law of the mass ratio $\mathrm{x} = \mathrm{M}/\mathrm{M}_*$, which best fit gives:

$$\begin{aligned} \mathrm{b_h} &= 0.53 + 0.39\mathrm{x}^{0.45} + \frac{0.13}{40\mathrm{x}+1} + 5\times 10^{-4}\mathrm{x}^{1.5} \\ &+ \log_{10}(\mathrm{x})\left[0.4(\Omega_\mathrm{m} - 0.3 + \mathrm{n_s} - 1) + 0.3(\sigma_8 - 0.9 + h - 0.7)\right] \ . \end{aligned} \tag{2.55}$$

This relation is drastically different compared with the two others because it directly involves cosmological parameters, and the local variable is considered as the mass. This parametric model is limited since it has been constrained with galaxy halos, which represent a much smaller size and mass than clusters. Moreover, the results of this study showed that predictions of the halo bias are relatively different from 10% to 50% with the simulated data.

A prominent study of theoretical prediction of the halo bias is processed in Tinker et al. (2010). They calibrate the dependence of the large-scale bias on the mass by analysing the clustering of dark matter halos based on dark-matter only cosmological simulations. It is presented with the following form:

$$\begin{aligned} \mathrm{b_h} &= 1 - \left[1 + 0.24\mathrm{y}e^{-(4/\mathrm{y})^4}\right]\frac{\nu^{0.44\mathrm{y}-0.88}}{\nu^{0.44\mathrm{y}-0.88} + \delta_\mathrm{c}^{0.44\mathrm{y}-0.88}} \\ &+ 0.183\nu^{1.5} + \left[0.019 + 0.107\mathrm{y} + 0.19e^{-(4/\mathrm{y})^4}\right]\nu^{2.4} \ , \end{aligned} \tag{2.56}$$

where $\mathrm{y} \equiv \log_{10}\Delta$. The function is very convenient for analyses as it is adaptable to any value of the overdensity contrast. This study find a 6% scatter about the best-fit bias relation with simulations.

An alternative model is provided by Bhattacharya et al. (2011). A bias model is derived using the peak-background split function of Sheth and Tormen (1999). This function is used to predict the halo bias in Lagrangian space. Then bias is computed with the following:

$$b_h = 1 + \frac{0.788\nu^2/(1+z)^{0.01} - 1.795}{\delta_c} + \frac{2 \times 0.807}{\delta_c \left[1 + 0.788\nu^2 0.807/(1+z)^{0.01}\right]} \ . \tag{2.57}$$

They find a corresponding change with simulations of 10% to 15%.

Chapter 3

Data analysis

This chapter is focused on the cosmological study presented in Ingoglia et al. (2022). In the previous chapter, we have seen the theoretical tools to understand the physical mechanisms behind weak gravitational lensing. The terms and the parameters composing the model of the halo density profile can be articulated in order to contrast with the lensing signal around galaxy clusters. The halo parameters such as concentration and bias correlate with the halo mass which allows driving a cosmological analysis accounting for extensive surveys.

In the following, we describe the catalogs of data used for the analysis. From such materials, we derive the density profiles of galaxy clusters and explain the process that maximizes the statistical efficiency of the lensing signal. Then, we detail the sources of uncertainty that stem from the WL measurements and how to correct them. At this stage, the full signal is processed and ready for cosmological constraints. We thus describe the Bayesian statistics that allows extracting the cosmological parameters of the halo model. Finally, we expose the results of this study and additional products which should be extended in another publication.

3.1 Description of the KiDS data

Data are prominent to rule cosmological studies, as they allow to generate sufficient materials for analyses. For an accurate lensing signal, we have to look for deep and dense source samples in such a way that the statistical number of background sources increases while the contamination of foreground and cluster member galaxies is small. In the following, we provide a global overview of the survey. Then, we give a complete description of the sources and lenses catalogs used for the data analysis.

3.1.1 Third data release

For European astronomy, the reference ground telescope is the ESO's Very Large Telescope (VLT) on Cerro Paranal in the Atacama Desert of northern Chile. The study is based on the optical wide-field imaging Kilo-Degree Survey (KiDS, de Jong et al., 2013). The survey is managed by the 268 Megapixel OmegaCAM imager (Kuijken, 2011), presently located on the VLT Survey Telescope (VST, Capaccioli and Schipani, 2011). This camera is ideal for such a survey, as it was specifically designed to provide superb and uniform image quality over a large, $1^\circ \times 1^\circ$, field of view (FoV). KiDS encompasses two areas of the extragalactic sky in four broad-band filters (*ugri*), split into an equatorial stripe (KiDS-N), and a second one centered around the South Galactic Pole (KiDS-S). KiDS was designed primarily to map the matter distribution in the Universe through weak gravitational lensing and photometric redshift measurements

The data set that we use for this work is the Data Release 3[1] (DR3, de Jong et al.,

[1] http://kids.strw.leidenuniv.nl/DR3

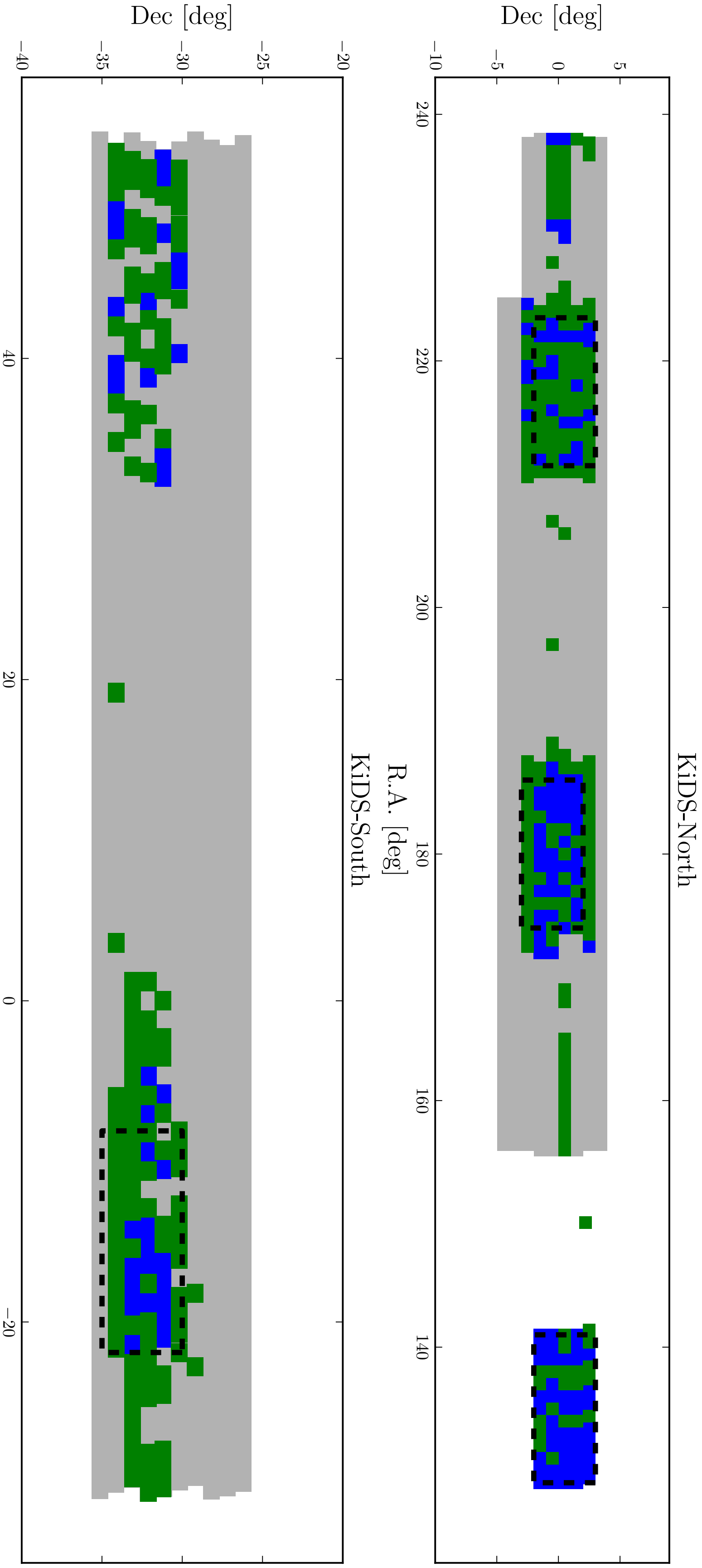

FIGURE 3.1: Sky distribution of KiDS-N (top) and KiDS-S (bottom) tiles. In green the tiles released in the current DR3, and in blue in the previous releases DR1 and DR2. The multi-band source catalog covers the combined area (blue + green) and the target KiDS area is shown in grey. Black dashed lines delineate the locations of the GAMA fields. (Credits: de Jong et al., 2017)

2017). It covers a total area of approximately 450 $\deg^2$ for 440 survey tiles distributed in five patches following the Galaxy And Mass Assembly survey convention (GAMA, Driver et al., 2011, G9/G12/G15 within KiDS-N and G23/GS within KiDS-S). In contrast, the first two data releases of KiDS (DR1 & DR2, de Jong et al., 2015; Kuijken et al., 2015) contain a total of 148 survey tiles covering an area of about ~ 450 $\deg^2$, which makes DR3 almost three times larger. This intermediate release includes one-third of the final KiDS area, which will ultimately reach 1350 $\deg^2$. Figure 3.1 shows the distribution of KiDS tiles in the sky plane for both DR3 and DR1+DR2 releases, in comparison with the full target area. Released data products include calibrated, stacked images and their weights, as well as masks and single-band source lists for 292 survey tiles not previously released, and a multi-band, aperture-matched source catalog encompassing all survey tiles released in DR3. The multi-color KiDS data are reduced and calibrated with the ASTRO-WISE system (Valentijn et al., 2007; Begeman et al., 2013). The data release is complemented by several additional data products, mainly photometric redshift, and WL shear catalogs.

3.1.2 Sources catalog

Numerous sources, deep photometric data, accurate redshifts, and qualitative shears are primary criteria to handle a relevant WL study. We use the weak lensing data set based on KiDS-DR3, also called the "KiDS-450" (K450 in the figures) data set. It is initially covered by 454 tiles, which after masking overlapping tiles, provides an effective area of 360.3 $\deg^2$. Hildebrandt et al. (2017) present a complete tomographic cosmic shear analysis of KiDS-450. Only galaxies with reliable shape measurements are included in this catalog.

Image data reduction for weak lensing is performed with the THELI pipeline (Erben et al., 2005; Schirmer, 2013) on KiDS-450 r-band images for which the best-seeing dark time is reserved. Then the shear is estimated from the shape of a galaxy using the *lens*fit likelihood based model-fitting method (Miller et al., 2007; Miller et al., 2013; Kitching et al., 2008; Fenech Conti et al., 2017). It is a Bayesian method that measures the components $(\varepsilon_1, \varepsilon_2)$ of the complex ellipticity given in Equation (2.24) for each individual galaxy whose surface is assumed to fit with a likelihood. These quantities are still affected by a small multiplicative and additive bias. To correct for these biases, the measured ellipticity component is calibrated with two empirical parameters, namely m and c, as (Fenech Conti et al., 2017):

$$\varepsilon_{\mathrm{i}}^{\mathrm{true}} = \frac{\varepsilon_{\mathrm{i}}^{\mathrm{meas}} - \mathrm{c_i}}{1 + \bar{\mathrm{m}}} \ . \tag{3.1}$$

In KiDS-450, the additive shear calibration parameter is directly applied to the galaxy's ellipticities, while the multiplicative shear bias parameter is computed individually in each galaxy by *lens*fit and must be corrected retrospectively as an average weighted quantity. Indeed, because faint galaxies have more noisy ellipticity measures than bright galaxies, the *lens*fit method makes use of a weighting system based on the inverse-variance of the likelihood surface.

Photometric redshifts are derived from KiDS-450 galaxy photometry in the *ugri*-bands. They are estimated with the Bayesian code BPZ (Benítez, 2000). BPZ is widely used in astronomy and is amongst the most accurate code when combined with the best available spectral energy distribution (SED) templates (Hildebrandt et al., 2010). This code fits a redshift likelihood model and derives the posterior probability distribution which peaks at the supposed redshift position of the source. The method is also effectively used for CFHTLenS data in Hildebrandt et al. (2012). The redshift

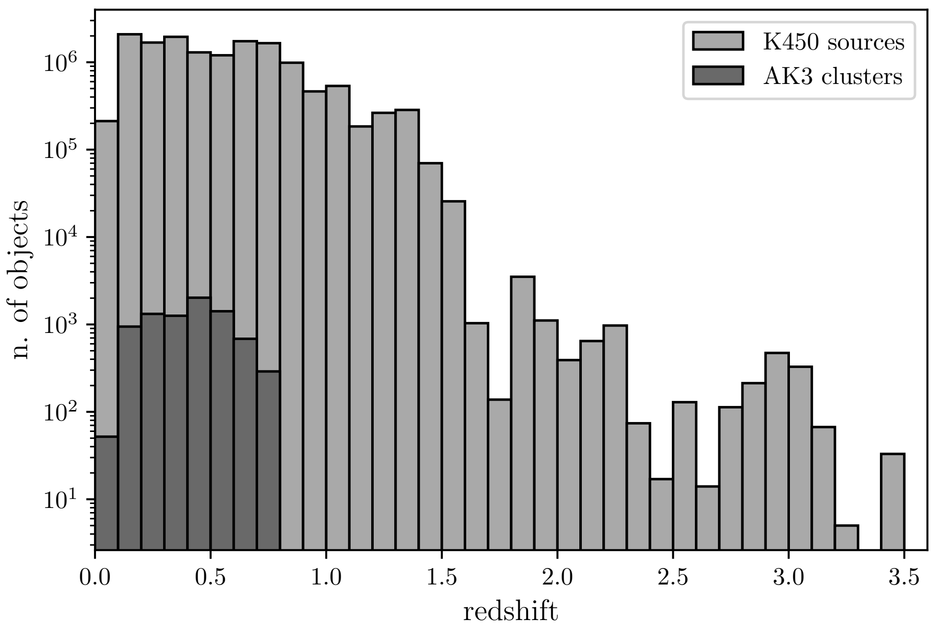

FIGURE 3.2: Redshift distributions of AMICO KiDS-DR3 clusters (dark gray) and KiDS-450 galaxies (light gray).

distribution of the galaxies is shown in Figure 3.2 in light-gray in comparison with the clusters. Sources accounted for the WL signal aim at exceeding the redshift range of the lenses in order to limit the number of foreground galaxies.

The final catalog comprises 14,650,348 sources identified as galaxies and has an effective number density of $\mathrm{n_{eff}} = 8.53\ \mathrm{arcmin}^{-2}$, defined as (Heymans et al., 2012):

$$\mathrm{n_{eff}} = \frac{1}{\Omega}\frac{(\sum \mathrm{w_s})^2}{\sum \mathrm{w_s^2}} \ , \tag{3.2}$$

where Ω is the total area of the survey excluding masked regions and $\mathrm{w_s}$ is the *lens*fit weight of each galaxy of the survey.

3.1.3 AMICO clusters

We use the galaxy cluster catalog obtained from the application of the Adaptive Matched Identifier of Clustered Objects algorithm (AMICO, Bellagamba et al., 2018) on KiDS-DR3 data (AK3 in the figures). AMICO is a robust cluster finder algorithm that is also selected to form part of the Euclid analysis pipeline (Euclid Collaboration et al., 2019). The algorithm exploits the Optimal Filtering technique (Maturi et al., 2005; Bellagamba et al., 2011) and aims at maximizing the signal-to-noise ratio (SNR) for the detection of objects following a physical model for clusters. In a nutshell, it identifies overdensities of galaxies associated with galaxy clusters taking into account their spatial, magnitude, and photometric redshift distributions (Radovich et al., 2017).

Specifically, AMICO convolves the 3D galaxy distribution with a redshift-dependent filter, defined as the ratio between M, a model of the density of galaxies per unit magnitude and solid angle, and N, the field galaxy distribution. It results in a 3D amplitude map, where every peak constitutes a possible detection of clusters:

$$A(\theta_c, z_c) \propto \sum_{i=1}^{N_{gal}} \frac{M(\theta_i - \theta_c, m_i)p_i(z_c)}{N(m_i, z_c)} , \quad (3.3)$$

where θ_i and θ_c are the positions on the sky of the galaxy and the cluster center, respectively, m_i and p_i are the magnitudes and the photometric redshift distribution of the galaxy and z_c is the redshift of the cluster. The above sum runs over all the N_{gal} galaxies of the catalog. The cluster model M is constructed by a luminosity function and a radial profile which parameters have been extracted from the observed galaxy population of SZ-detected clusters (Hennig et al., 2017), as detailed in Maturi et al. (2019). In addition, AMICO assigns to each galaxy i a probability to be a member of a detected cluster j according to:

$$P(i \in j) \equiv P_{f,i} \frac{A(\theta_j, z_j)M_j(\theta_i - \theta_j, m_i)p_i(z_j)}{A(\theta_j, z_j)M_j(\theta_i - \theta_j, m_i)p_i(z_j) + N(m_i, z_j)} , \quad (3.4)$$

where $P_{f,i}$ is the field probability of the i-*th* galaxy before the j-*th* detection is defined (for more details, see Bellagamba et al., 2018). By definition, the sum of membership probabilities for each detected structure will roughly correspond to the number of visible members. This quantity can be use as richness proxy of the cosmic structure j:

$$\lambda_j^* \equiv \sum_{i=1}^{N_{gal}} P(i \in j)F_{ij} , \quad (3.5)$$

where F_{if} is a selection function that filters the galaxies as:

$$F_{ij} = \begin{cases} 1 & \text{if } m_i < m_*(z_j) + 1.5 \text{ and } R_i < R_{200c}(z_j) , \\ 0 & \text{otherwise} . \end{cases} \quad (3.6)$$

The magnitude and radial cuts m_* and R_{200c} are parameters used for the cluster model constructed in Maturi et al. (2019). The typical magnitude m_* as a function of redshift is derived from a stellar population evolutionary model with a decaying starburst at redshift $z = 3$ and a Chabrier initial mass function (IMF, Bruzual and Charlot, 2003). The parameter R_{200c} derives from a typical NFW profile, where the mean concentration is taken at $c_{200c} = 3.59$ for a corresponding mass of $M_{200c} = 10^{14}\ M_\odot/h$ (Hennig et al., 2017).

Finally, for each cluster, AMICO returns central angular positions, redshift, SNR of the detection, amplitude A, and effective richness λ_*.

AMICO KiDS-DR3 catalog is fully described in Maturi et al. (2019). It contains 7988 candidate galaxy clusters covering an effective area of 377 $\deg^2$. Clusters are detected above a fixed threshold of SNR $= 3.5$. The catalog encompasses an intrinsic richness range of $2 < \lambda_* < 140$ and a redshift range $0.1 \leq z < 0.8$. The richness and redshift distributions are presented in Figure 3.3. From the figure, we can see that the richness slightly increases with redshift, which indicates that rich galaxy clusters are found at high redshift in agreement with the hierarchical scenario of the cosmic structures. Conversely, poor and distant clusters are not detected due to their low SNR. These blank regions are usually associated with low levels of completeness (i.e. the fraction between detected and mock galaxy clusters), as shown in Figure 13 of Maturi et al. (2019).

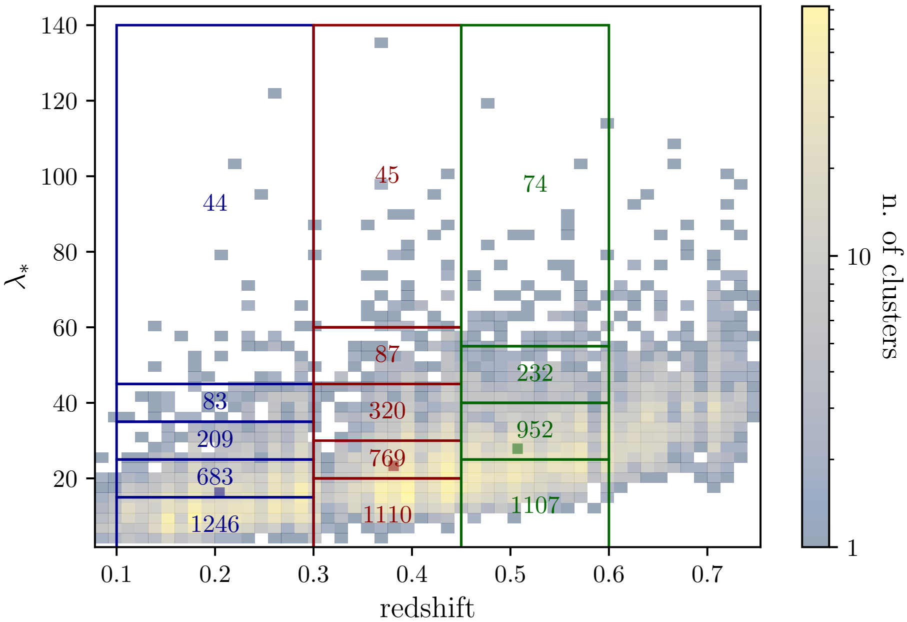

FIGURE 3.3: AMICO KiDS-DR3 clusters in the redshift-richness plane with SNR $\geq$ 3.5. Colored rectangles correspond to the redshift-richness bins used in the following analysis (see Section 3.2.2); the number of clusters enclosed in each bin is displayed. Single colored squares show the mean values in each redshift bin computed as in Equation (3.18).

3.2 Lensing processing of catalogs

In the previous section, we have introduced the set of data used for the analysis. Now we present the technical and computational details to extract a high-resolution WL signal from such catalogs of data. In particular, we first describe the global lensing measurements. Then, we focus on an effective way to select background sources and reduce the contamination on the lensing signal. Lastly, we explain how to increase the quality of the lensing signal with a stacking method.

3.2.1 Lensing computation

In Section 2.1.2, we have seen that the tangential component of the complex shear, γ_+, is an observable of the surface density distribution around a massive object. On the other hand, Section 2.2 provides the model that best describes the surface density profile of halos. It is possible to relate the shear to this physical quantity through the excess surface mass density $\Delta\Sigma$, defined as (Sheldon et al., 2004):

$$\Delta\Sigma \equiv \overline{\Sigma} - \Sigma = \Sigma_{\rm cr}\gamma_+ \ , \tag{3.7}$$

where $\overline{\Sigma}$, Σ and $\Sigma_{\rm cr}$ are given in Equations (2.33) & (2.35) & (2.17). However, in WL what is observed from sources like galaxies is not the shear, but their ellipticity defined in Equation (2.24). Equation (2.26) shows that ϵ is not determined in terms of γ, but in terms of the reduced shear g. Then the reduced shear is a more direct observable than the shear, which remains an approximation of the source ellipticities. However, the reduced shear is not directly included in the definition of the differential excess surface density. So we link these two quantities using the convergence $\kappa \equiv \Sigma/\Sigma_{\rm cr}$ in Equation (3.7) and derive:

$$g_+ = \frac{\Delta\Sigma}{\Sigma_{\rm cr} - \Sigma} \ . \tag{3.8}$$

The ellipticity still remains an indirect observable of the shear and the reduced shear. So we denote the corresponding excess surface mass density for tangential and cross components as:

$$\widetilde{\Delta\Sigma}_{+/\times} \equiv \Sigma_{\rm cr}\epsilon_{+/\times} \ . \tag{3.9}$$

When measuring the ellipticity as a function of radial distance, the signal is very noisy and becomes noisier with the distance. To correct for this spurious signal, we compute lensing at a given distance from the cluster center by stacking the radial position and the ellipticity of the i-*th* galaxy source over the j-*th* radial annulus. Thereby, we assess the two observables using their weighted mean as:

$$R_j = \left(\frac{\sum_{i\in j} w_{{\rm ls},i} R_i^{-\alpha}}{\sum_{i\in j} w_{{\rm ls},i}} \right)^{-1/\alpha} \ , \tag{3.10}$$

and:

$$\widetilde{\Delta\Sigma}_j = \left(\frac{\sum_{i\in j} w_{{\rm ls},i} \Sigma_{{\rm cr},i} \epsilon_i}{\sum_{i\in j} w_{{\rm ls},i}} \right) \frac{1}{1+K_j} \ . \tag{3.11}$$

The lens-source weight of the i-*th* source is:

$$w_{{\rm ls},i} = w_{s,i} \Sigma_{{\rm cr},i}^{-2} \ , \tag{3.12}$$

and $w_{s,i}$ is the *lens*fit inverse-variance source weight as defined in Miller et al. (2013). Here, K_j is the weighted mean of the *lens*fit multiplicative bias m_i introduced to calibrate the shear on average (see previous section):

$$K_j = \frac{\sum_{i\in j} w_{ls,i} m_i}{\sum_{i\in j} w_{ls,i}} \ . \tag{3.13}$$

The effective radius in Equation (3.10) is estimated with a shear-weighted mean and computed by approximating the shear profile as a power-law, with $\alpha = 1$. Sereno et al. (2017), which explored different methods to assess the mean radius, found that this configuration makes the fitting procedure to shear profiles less dependent on the binning scheme. We compute the average inverse surface critical density of a cluster to derive the effective redshift of its background sources z_{back} in each radial bin also following Sereno et al. (2017):

$$\Sigma_{cr}^{-1}(z_{back}) = \frac{\sum_{i\in j} w_{s,i} \Sigma_{cr,i}^{-1}}{\sum_{i\in j} w_{s,i}} \ . \tag{3.14}$$

This estimate permits us to compute the modeled reduced shear in Equation (3.8) as an average quantity, and not consider each individual source redshift for the computation of the critical surface density.

A preliminary measurement of the statistical errors of the two observables in Equations (3.10) & (3.11) is given by the weighted standard deviation of the radial distances:

$$\sigma_{R,j}^2 = \frac{\sum_{i\in j} w_{ls,i} \left(R_i - R_j\right)^2}{\sum_{i\in j} w_{ls,i}} \ , \tag{3.15}$$

and by the standard error of the weighted mean:

$$\sigma_{\widetilde{\Delta\Sigma},j}^2 = \frac{1}{\sum_{i\in j} w_{ls,i}} \ , \tag{3.16}$$

respectively. Notice that taking Equation (3.12) into account, dimension on the error of $\widetilde{\Delta\Sigma}$ turns to a surface mass density dimension.

A more complete way to assess the uncertainty given by the averaged signal is to compute the covariance matrix as in Section 3.3.1. This statistical measurement of the noise includes the errors which propagate among the radial bins.

In the following, we provide lensing profiles sampled in 30 annuli corresponding to 31 logarithmically equispaced radii in the range $[0.1, 30]$ Mpc$/h$. This choice is justified since our analysis both require small and large scales to identify the two terms of the halo model. We discard the four inner annuli of the measured shear profile to avoid contamination from cluster member galaxies and the contribution of the BCG in the resulting density profiles (Bellagamba et al., 2019). In that order, effects of miscentering are minimized as the lensing signal is considered only for $R \gtrsim 0.2$ Mpc$/h$. This measurement is also repeated around random lens points to compensate for the systematic signal, as discussed later in Section 3.3.2.

We illustrate the process of stacking the shear signal in Figure 3.4, where a 2D distribution of selected sources around the AMICO cluster J225151.12-332409 is shown (more details in the following section). For visual convenience in the illustration, we highlighted only 12 of the 31 radii in the radial range $[0.35, 3]$ Mpc$/h$. The tangential and the cross components of $\widetilde{\Delta\Sigma}$ associated with the 10 annuli are additionally displayed in the bottom panel. Remark that larger bins account for more numerous sources, but this statistics is compensated with a noisier signal, while vice versa, the closer cluster center bins have fewer sources which lensing highly affect.

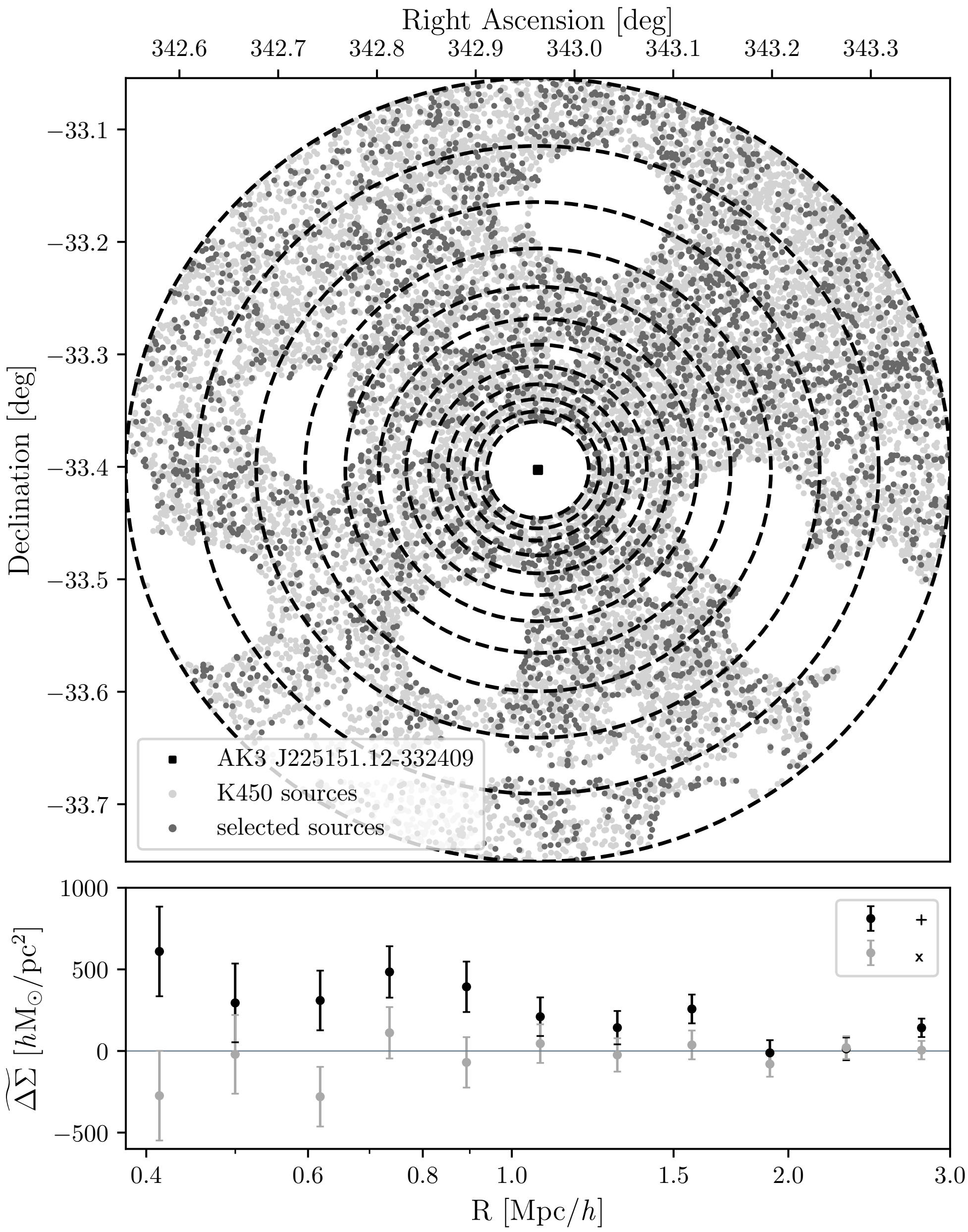

FIGURE 3.4: *Top panel*: Illustration of eleven of the thirty annuli in the radial range $[0.35, 3]$ Mpc/h, for the AMICO cluster J225151.12-332409. The sources shown are selected following the cut discussed in Section 3.2.3. Blank regions indicate masks (Hildebrandt et al., 2017). *Bottom panel*: Tangential and cross components of the excess surface mass density (Equation 3.11) of J225151.12-332409. Vertical error bars are derived from Equation (3.16).

TABLE 3.1: Pattern of the redshift-richness bins designed for the WL analysis.

z_l	λ_*				
$[0.1, 0.3[$	$[0, 15[$	$[15, 25[$	$[25, 35[$	$[35, 45[$	$[45, 140[$
$[0.3, 0.45[$	$[0, 20[$	$[20, 30[$	$[30, 45[$	$[45, 60[$	$[60, 140[$
$[0.45, 0.6[$	$[0, 25[$	$[25, 40[$	$[40, 55[$	$[55, 140[$	

3.2.2 Stacked signal

In WL, stacking across radial bins does not provide sufficient accurate signal to constrain precisely the two parameters of the halo model (see Section 2.2) and derive generic mass relations (see Sections 2.3.1 & 2.3.2). Instead, we can stack the shear profiles of individual halos across properties of galaxy clusters. Therefore, we consider 14 cluster bins combined in redshift and richness. Table 3.1 shows the binning pattern, also displayed in cells in the z_l vs λ_* diagram in Figure 3.3. The binning scheme mostly follows Bellagamba et al. (2019) to provide nearly uniform WL SNR per bin. The only difference is for the last redshift bin, in which a larger number of clusters are considered for intermediate richness ranges. In this way, we compensate for the numerous galaxy clusters in the higher richness bin and homogenize the distribution of clusters in this redshift bin with the two other redshift bins.

Considering the j-*th* radial bin of the k-*th* galaxy cluster, the corresponding stacked observable in the K-*th* cluster bin is:

$$O_{j,K} = \frac{\sum_{k\in K} W_{j,k} O_{j,k}}{\sum_{k\in K} W_{j,k}} \,, \tag{3.17}$$

with $W_{j,k} = \sum_{i\in j} w_{ls,i}$. The shear estimate is not accurate since the correction of the multiplicative bias has already been applied via Equation (3.11) to the signal of each individual galaxy cluster, while it should be corrected over the averaged measure of the bin. We compute the effective value of the cluster observable O_k, e.g. richness or redshift of cluster k, among the cluster bins K through a lensing-weighted mean (e.g. Umetsu et al., 2014):

$$O_K = \frac{\sum_{k\in K} W_k O_k}{\sum_{k\in K} W_k} \,, \tag{3.18}$$

where $W_k = \sum_j W_{j,k}$ is the total weight of the cluster k for the whole area of the cluster profile.

Figure 3.5 shows the stacked profile of AMICO clusters considering the full richness range and the redshift $0.1 \leq z_l < 0.6$ as the selection proposed in the next section.

3.2.3 Selection method

Gravitational lensing is an accurate method to measure cluster density profiles only when effective discriminations between background sources, and foreground and cluster member galaxies are considered. Indeed, the relative position of a source tells us if the galaxy is lensed, in the case where the source lies in the background of the cluster, or contaminated, in the case where the source lies in the foreground of the cluster or belongs to the cluster. It is known that contaminated galaxies usually dilute the resulting lensing signal (Broadhurst et al., 2005; Medezinski et al., 2007). Therefore, the more contaminated sources impact the lensing computations, the more spurious becomes the signal. Conversely, the less lensed sources contribute to the stacked shear

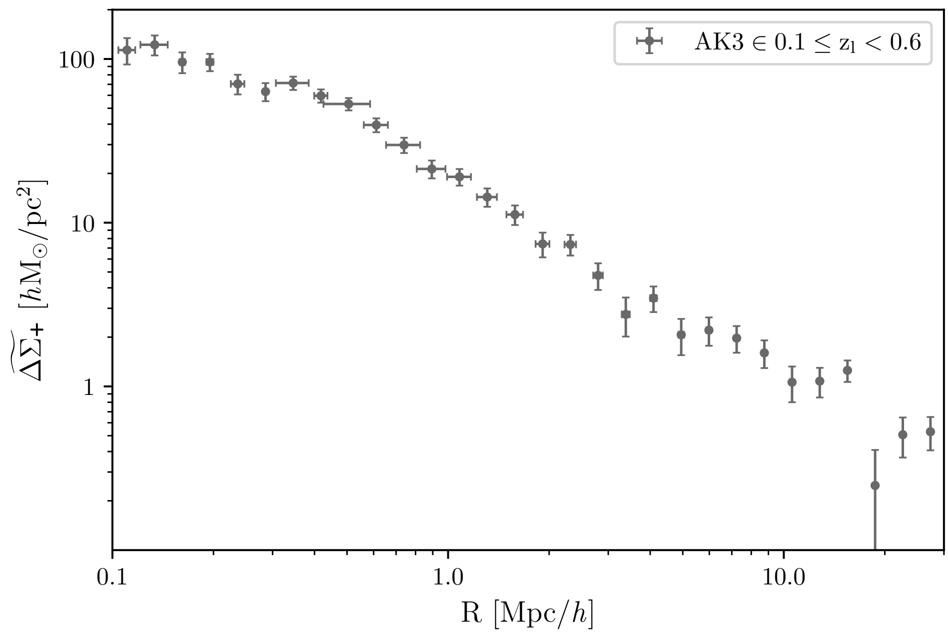

FIGURE 3.5: The stacked matter density profile of AMICO KiDS-DR3 clusters with $0.1 \leq z_l < 0.6$. The signal is computed assuming the combined selections given in Equation (3.23). Horizontal and vertical bars are derived from Equations (3.15) and (3.16).

profile, the less is the statistical power of the signal. It becomes clear that the efficiency of weak lensing relies on the statistical equilibrium of a thorough selection of clusters and sources.

First of all, we consider galaxy clusters selected in the redshift range $z_l \in [0.1, 0.6[$, as done in Bellagamba et al. (2019). We select clusters at $z_l < 0.6$ because the color-color cut in Equation (3.22) is very effective for sources at $z_s > 0.6$. Furthermore, remote clusters convey a lower density of background sources. Objects at $z_l < 0.1$ are discarded because of the reduced lensing power of low mass clusters and the inferior photometric redshift accuracy of the sources. The final sample consists of 6961 clusters (87.1% of the whole catalog). In Figure 3.5 we plot the mass density profile obtained for the complete cluster sample assuming the combined selection of sources given in Equation (3.23).

A preliminary approach to select sources would rely only on the redshift position of sources and lenses. From this assumption, we can consider a broad selection as:

$$z_s > z_l + \Delta z \ , \tag{3.19}$$

where z_s is the best-fitting BPZ photometric redshift of the source, z_l is the lens redshift, and $\Delta z = 0.05$ is a secure interval to balance uncertainties coming from photometric redshifts. However, this criterion is not sufficient to remove misplaced galaxies, as SED photometry usually provides inaccurate redshift positions. In order to significantly reduce the probability of a galaxy being at redshift equal to or lower than the cluster, we could select galaxies according to their redshift posterior probability distribution. We additionally apply a more accurate redshift filter following the work of Bellagamba et al. (2019) and Sereno et al. (2017):

$$(0.2 \le \mathrm{z_s} \le 1) \wedge (\texttt{ODDS} \ge 0.8) \wedge \left(\mathrm{z_{s,min}} > \mathrm{z_l} + \Delta \mathrm{z}\right) \ . \tag{3.20}$$

The first selection encloses the range for which we expect the most reliable photometric redshifts given the available bands (*ugri*) and thus excludes galaxies whose redshift is less robust. The ODDS parameter from the KiDS shear catalog accounts for the probability density function (PDF) of the redshift: a high value indicates a high reliability of the best photo-z estimate. The parameter $\mathrm{z_{s,min}}$ measures the lower bound of the 2σ confidence interval of the PDF.

A complementary approach is based on the source distribution in the color-color (CC) panel. This method uses the properties of the CC diagram to separate or classify galaxies. A color is, by definition, the difference between two magnitudes. In KiDS-DR3, the most reliable colors are given by the *gri*-bands, therefore we take a look at the KiDS-450 sources in the (r-i) vs (g-r)-color-color (hereafter dubbed *gri*-CC) plane. Preliminary works are provided in Medezinski et al. (2010), which highlight a strong correlation between the location in the (r-i) vs (g-r) diagram and the galaxy redshift. More specifically, Figure 3 in Medezinski et al. (2010) lays out in colored areas various populations of sources for three different Subaru clusters (e.g. cluster members in green). The paper shows *gri*-CC selected sources in the galaxy cluster A1703, for which Broadhurst et al. (2008) and Oguri et al. (2009) initially performed a WL analysis. Two singular areas in the color-color plane are clearly identified as background sources of A1703, efficiently selected at $\mathrm{z_s} \gtrsim 0.6$ and displayed in blue/red in the figure of the study. They present the following segmentation:

$$\begin{aligned} &[(\mathrm{g-r} < 2.17(\mathrm{r-i}) - 0.37) \wedge (\mathrm{g-r} < 1.85 - 0.6(\mathrm{r-i}))] \\ &\quad \vee (\mathrm{g-r} < 0.47 - 0.4(\mathrm{r-i})) \vee (\mathrm{r-i} < -0.06) \ . \end{aligned} \tag{3.21}$$

Following an original proposal by Oguri et al. (2012), Bellagamba et al. (2019) exploit another relevant selection specific to KiDS-DR3, which effectively filters galaxies beyond $\mathrm{z_s} \simeq 0.7$, obtaining:

$$(\mathrm{g-r} < 0.3) \vee (\mathrm{r-i} > 1.3) \vee (\mathrm{g-r} < \mathrm{r-i}) \ . \tag{3.22}$$

This last selection was tested in Covone et al. (2014), Sereno et al. (2017) and Sereno et al. (2018) and Bellagamba et al. (2019), and conserves 97% of galaxies with CFHTLenS spectroscopic redshifts above $\mathrm{z_s} \gtrsim 0.63$ (Sereno et al., 2017).

In order to evaluate the efficiency of the *gri*-CC cuts explored in Equations (3.22) and (3.21), we are interested in testing them over the Cosmic Evolution Survey 30-Bands photometric catalog[2] (COSMOS, Ilbert et al., 2009). The full sample consists of 385,065 galaxies with very accurate photometric redshifts reliable up to magnitude $i < 25$. In Figure 3.6, we present the COSMOS sources selected with the two *gri*-CC criteria. As a comparison, we generate evolving tracks using the GALEV[3] code (Kotulla et al., 2009). This tool simulates the evolution of galaxies in terms of color over cosmological timescales. We run the code with different Hubble - de Vaucouleurs galaxy morphological types: Non-barred spiral Sa-type, Barred-spiral Sb-type, Lenticular S0-type, and Elliptical E-type.

With this plot, we are interested in the contamination of objects belonging to the redshift range of $0.2 < \mathrm{z_s} < 0.6$, in agreement with the selection of clusters. We

[2] https://irsa.ipac.caltech.edu/data/COSMOS/
[3] http://www.galev.org/

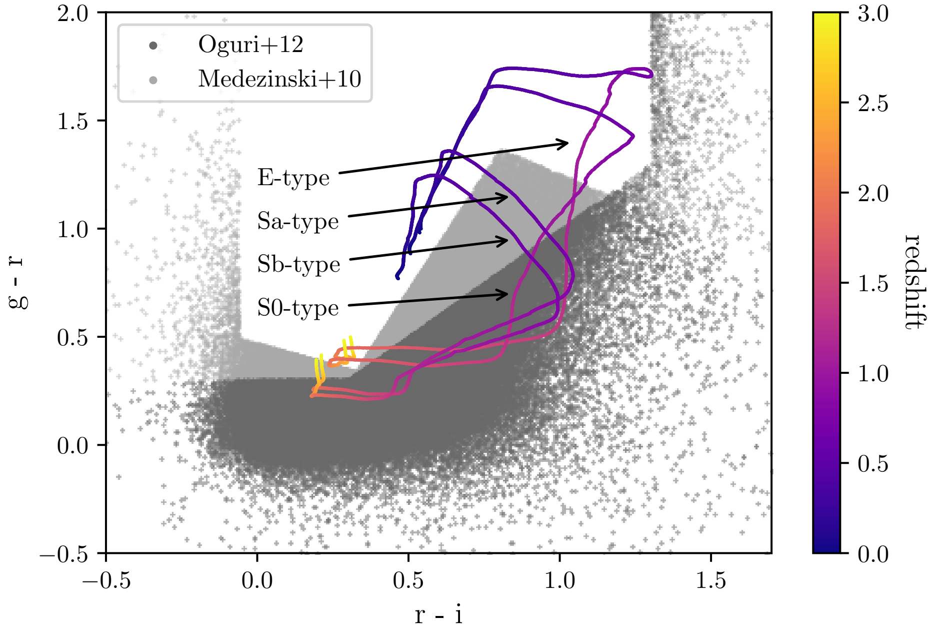

FIGURE 3.6: (r-i) vs (g-r) diagram. We show the selections discussed in this article, following previous complementary works (Equations 3.22 and 3.21, Oguri et al., 2012; Medezinski et al., 2010, respectively). We additionally show the evolving tracks of spiral, lenticular and elliptical galaxies in the *gri*-CC plane obtained using the GALEV code (Kotulla et al., 2009).

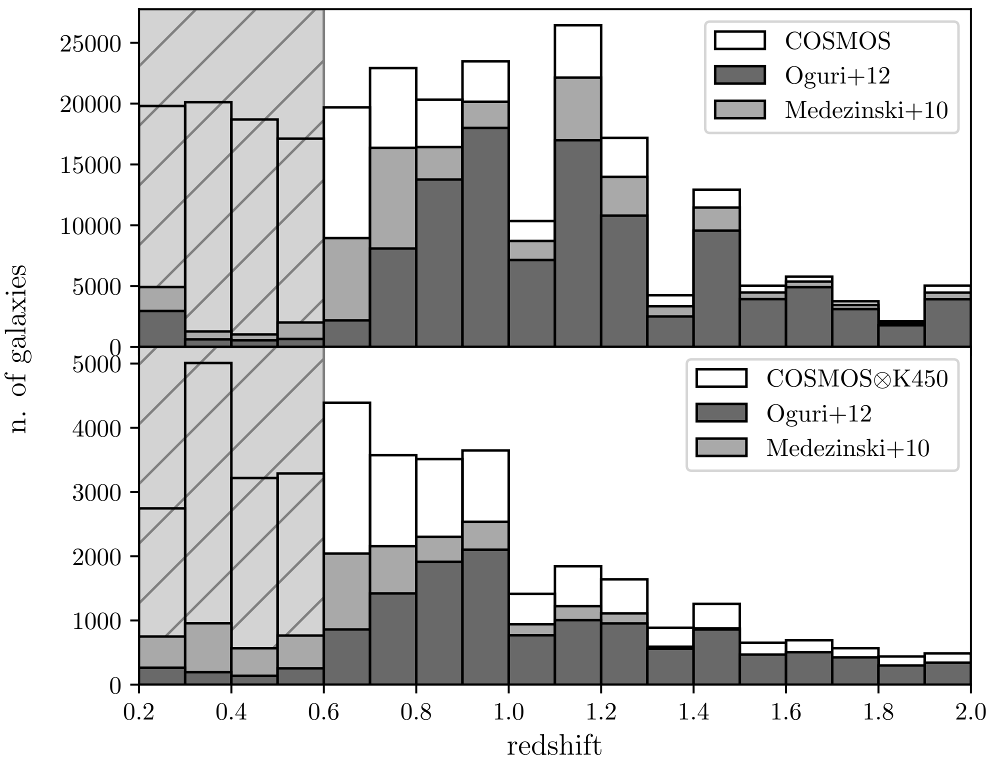

FIGURE 3.7: COSMOS (Ilbert et al., 2009) and COSMOS⊗KiDS-450 photometric redshift distributions for the full samples and their dedicated *gri*-CC selections. The shaded region highlights the contamination area, which corresponds to the cluster redshift range $[0.1, 0.6[$.

TABLE 3.2: Contamination of *gri*-CC selections in COSMOS (up) and COSMOS⊗KiDS-450 (down). We compare the fraction of selected sources with the total number of sources and of contaminated sources above $z_s > 0.6$ with selected sources.

CC-cut	N. of sources	Total fraction (%)	Contamination fraction (%)
None	385065	100	44.2
Medezinski et al. (2010)	17049	44.3	5.4
Oguri et al. (2012)	125754	32.6	3.8
None	47619	100	40.2
Medezinski et al. (2010)	20540	43.1	14.8
Oguri et al. (2012)	14857	31.2	5.7

report these numbers in Table (3.2). The cut shown in Oguri et al. (2012) encompasses 125,754 galaxies with 96.2% background sources for the corresponding redshift threshold $z_s \geq 0.6$. On the other hand, the selection done by Medezinski et al. (2010) counts 170,429 (35.5% more), and 94.6% of them lie over $z_s \geq 0.6$. In the top panel of Figure 3.7, we see that both cuts efficiently remove contaminating members in COSMOS, with a higher number of background galaxies for Equation (3.21). The contamination fraction given by Equation (3.22) is fully consistent with Sereno et al. (2017).

Besides this observation, a more reliable analysis would be to consider the cross-matched catalog COSMOS⊗KiDS-450 as the 47,619 COSMOS sources within KiDS-450. The lower panel of Figure 3.7 provides this distribution and Table 3.2 shows that 14,857 of them are filtered by Oguri et al. (2012) and 20,540 by Medezinski et al. (2010). Respectively, 94.3% and 85.2% of selected sources appear to be uncontaminated. These statistics highlight higher contamination from Equation (3.21) and more efficient removal of contaminated KiDS-450 sources for Equation (3.22) but still has some drawbacks due to the limited number of objects. Another explanation for the main difference between the two cuts is the unequal reduction of galaxies from COSMOS to the cross-match data set. KiDS-450 sources in COSMOS are few at $z_s > 1$, where Medezinski et al. (2010) is consequently selecting more sources than Oguri et al. (2012) in COSMOS only, while the proportion of galaxies at $z_s < 1$ remains high in both catalogs. In that sense, we prefer to retain Equation (3.22) as the principal *gri*-CC selection for this work.

Finally, we formulate the selection of the background sources by combining the following Equations as follows:

$$(3.19) \wedge [(3.20) \vee (3.22)] \ . \tag{3.23}$$

As a further restriction for the selection presented in this study, we restricted the source redshifts to the range $z_s > 0.2$. This complementary selection is assumed since a large fraction of sources are below this limit, which might increase the contamination of nearby clusters (Sereno et al., 2017).

3.3 Sources of error and fitting process

This section discusses the sources of error that arise when computing a stacked lensing profile. Because WL is processed with statistical calculations, fluctuations in the resulting signal occur. This effect propagates across the bins and can be translated with covariance matrices. Moreover, the lensing computations are affected by a signal that systematically shifts the profile. This can be balanced by removing the signal given by random lenses. Finally, once the systematic signal is removed, we constrain the final WL profiles with a Bayesian analysis taking into account the statistical covariance matrices.

3.3.1 Statistical uncertainty

Stacked WL signals are a comprehensive assessment of the profile given by a galaxy cluster population, but possible deviations arise due to statistical uncertainties and systematic biases. While the systematic noise can be efficiently corrected for using the random fields, the statistical uncertainty of the stacked shear is essentially described by its covariance matrix. It can be decomposed into the contributions of large intrinsic variations of the shapes of galaxies (shape noise, e.g. Mandelbaum et al., 2013; Sereno and Ettori, 2015; Viola et al., 2015), correlated and uncorrelated structures (e.g. Hoekstra, 2001; Hoekstra, 2003; Hoekstra et al., 2011; Umetsu et al., 2011; Gruen et al., 2015), and intrinsic scatter of the mass measurement (e.g. Metzler, White, and Loken, 2001; Gruen et al., 2011; Becker and Kravtsov, 2011; Gruen et al., 2015). The statistical uncertainty is dominated by the shape noise of the sources (McClintock et al., 2019), which has already been accounted for in Equation (3.16). However, since galaxies contribute to the signal in different radial and redshift-richness bins, we may expect covariance terms to be significant between radii in identical and distinct pairs of stacked profiles. In order to estimate the statistical error of the stacked WL measurements, we use a bootstrap method with replacement. This technique makes use of random sampling data and repeats the process a given number of times to better estimate statistical measurements (mean, variance, confidence intervals, etc). We, therefore, construct the covariance matrix from each pair of radial bins ij over $\mathrm{N} = 1000$ bootstrap realizations of the source catalog:

$$\mathrm{C_{ij}} = \frac{\sum_{\mathrm{n}\in\mathrm{N}} \left(\widetilde{\Delta\Sigma}_{\mathrm{i,n}} - \overline{\widetilde{\Delta\Sigma}}_{\mathrm{i}}\right)\left(\widetilde{\Delta\Sigma}_{\mathrm{j,n}} - \overline{\widetilde{\Delta\Sigma}}_{\mathrm{j}}\right)}{\mathrm{N}-1} \text{ , with } \overline{\widetilde{\Delta\Sigma}} = \frac{\sum_{\mathrm{n}\in\mathrm{N}} \widetilde{\Delta\Sigma}_{\mathrm{n}}}{\mathrm{N}} \,. \tag{3.24}$$

The correlation matrix quantifies the dependency between the bins, and can be derived from the covariance profile:

$$\mathrm{R_{ij}} = \frac{\mathrm{C_{ij}}}{\sqrt{\mathrm{C_{ii}C_{jj}}}} \,. \tag{3.25}$$

Figure 3.8 displays the correlation matrices for the cluster bin $\mathrm{z_l}\otimes\lambda_* = [0.3, 0.45[\otimes[30, 45[$ and the cross-covariances with the low and high redshift-richness bins $[0.1, 0.3[\otimes[0, 15[$ and $[0.45, 0.6[\otimes[55, 140[$. The correlation matrices do not show any strong contribution from off-diagonal terms, while the diagonal components encompass the majority of the statistical noise. We still consider the full covariance of each individual cluster bin to quantify the statistical uncertainty of the stacked WL signal, in order to account for the dependency between the radii of the bin when fitting the data. Furthermore, we combine uncertainties of the galaxy cluster signal and the random signal detailed in the next section by summing their covariances. These matrices are used when measuring the halo parameters in Section 3.3.3.

3.3.2 Systematic effect

We performed stacked shear analysis around random lens points following the same process used in Section 3.2. This spurious signal characterizes the residual systematic

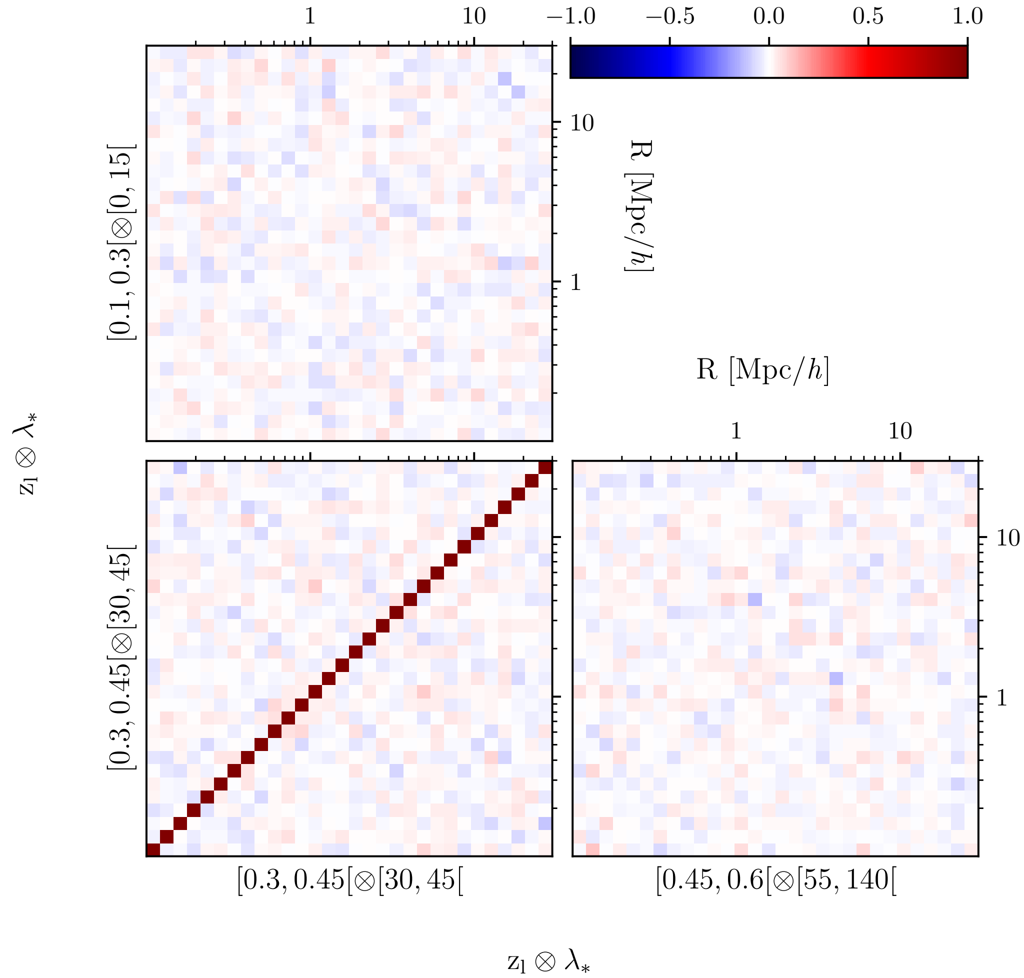

FIGURE 3.8: Bootstrap correlation matrix of $\widetilde{\Delta\Sigma}$, computed as in Equation (3.25) from $z_l \otimes \lambda_*$ selected bins. Here, we investigate the bin $[0.3, 0.45[\otimes[30, 45[$ correlated with itself (bottom left panel), with the bin $[0.1, 0.3[\otimes[0, 15[$ (top panel) and with the bin $[0.45, 0.6[\otimes[55, 140[$ (bottom right panel). The statistical uncertainty is mainly provided by the diagonal terms, while the off-diagonal terms are nearly consistent with zero, suggesting that radial and redshift-richness bins do not correlate.

effects, usually coming either from the edges of the detector (Miyatake et al., 2015), the imperfect correction of optical distortion (Mandelbaum et al., 2005) or the incorrect estimation of the redshift (McClintock et al., 2019). If none of these effects impact the profile, the random stacked shear should vanish, while it deviates from zero as soon as the systematic bias is apparent (Miyatake et al., 2015). The random signal is finally subtracted from the shear profiles of the stacked bins to correct these uncertainties.

We built a random catalog over the full (RA,Dec) sources range considering the KiDS-450 footprint of masked areas. Each equatorial random position is uniformly sampled over a `Nside=2048` pixel HEALPIX map and associated to a redshift random position. We sample random redshift from an inverse transform method, assuming AMICO redshifts to follow a Weibull distribution (e.g. Pen et al., 2003):

$$n \equiv \frac{\beta}{\Gamma\left(\frac{1+\alpha}{\beta}\right)} \frac{1}{z_0} \left(\frac{z_l}{z_0}\right)^{\alpha} \exp\left[-\left(\frac{z_l}{z_0}\right)^{\beta}\right] . \tag{3.26}$$

The parameters α, β and z_0 are marginalized and constrained to track the real distribution of AMIC KiDS-DR3 redshifts. We find:

- $\alpha = 1.06$
- $\beta = 4.81$
- $z_0 = 0.59$

Figure 3.9 shows the distribution of random and AMICO lenses. Random redshifts follow the Weibull distribution and tend to recover the same distribution as clusters of galaxies for a more realistic representation of the random signal.

Rykoff et al. (2016) suggest an efficient way to generate a random richness component from a depth map of the source catalog. However, their study is based on the redmapper algorithm for cluster detection which considerably differs from AMICO. Moreover, due to the absence of a depth map in KiDS-450, we cannot assign richness parameters to our random catalog. Still, the presence of random redshifts is a robust feature for the random catalog as we can associate the stacked random signal to each redshift bin. Finally, the number of random points exceeds the number of real galaxy clusters by 15976 lenses in order to fully cover the 3D field of AMICO KiDS-DR3 lenses.

A simple test to check the correct processing of the subtraction of the systematics is to look at the tangential and cross stacked shear profile of the random lenses. The top panels of Figure 3.10 present three different profiles derived from AMICO cross, random cross, and random tangential signals. While the tangential component of random points remains consistent with zero, the cross signal of the lower redshift bin reveals that systematics largely impact the shear in the last radial bins, and consequently might distort the estimation of the halo bias if no correction is applied. Looking deeply at the cross signal of the five KiDS-DR3 patches, we observe that only three of them are significantly affected. We relate these systematics to the geometry of the field, which at some point is irregular in those specific patches. Indeed, since the lower redshift bin needs a larger field of view to compute stacked shear over a fixed large radial profile, the resulting signal is much more sensitive to the discontinuities of the field (e.g. isolated tiles). Hamana et al. (2013) suggest that the point spread function (PSF) in the shape measurement of galaxies located at the edge of the FoV is imperfectly corrected. This biased PSF anisotropy sensitively impacts the shear of galaxies, which consequently breaks the symmetry of the intrinsic ellipticity and leads

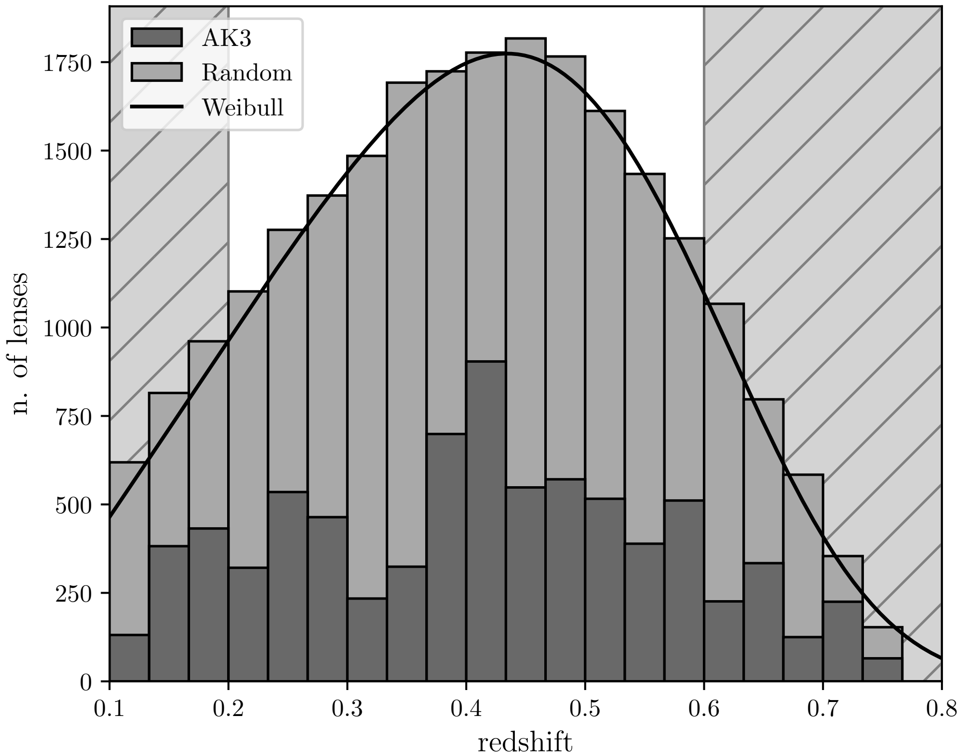

Figure 3.9: The redshift distribution of AMICO and random lenses. The random redshifts are sampled with an inverse transform method from the PDF described in Equation (3.26). The black curve describes this function and aims at simulating the distribution of the AMICO redshifts. The shaded regions delineate the redshift range of selected clusters discussed in Section 3.2.3.

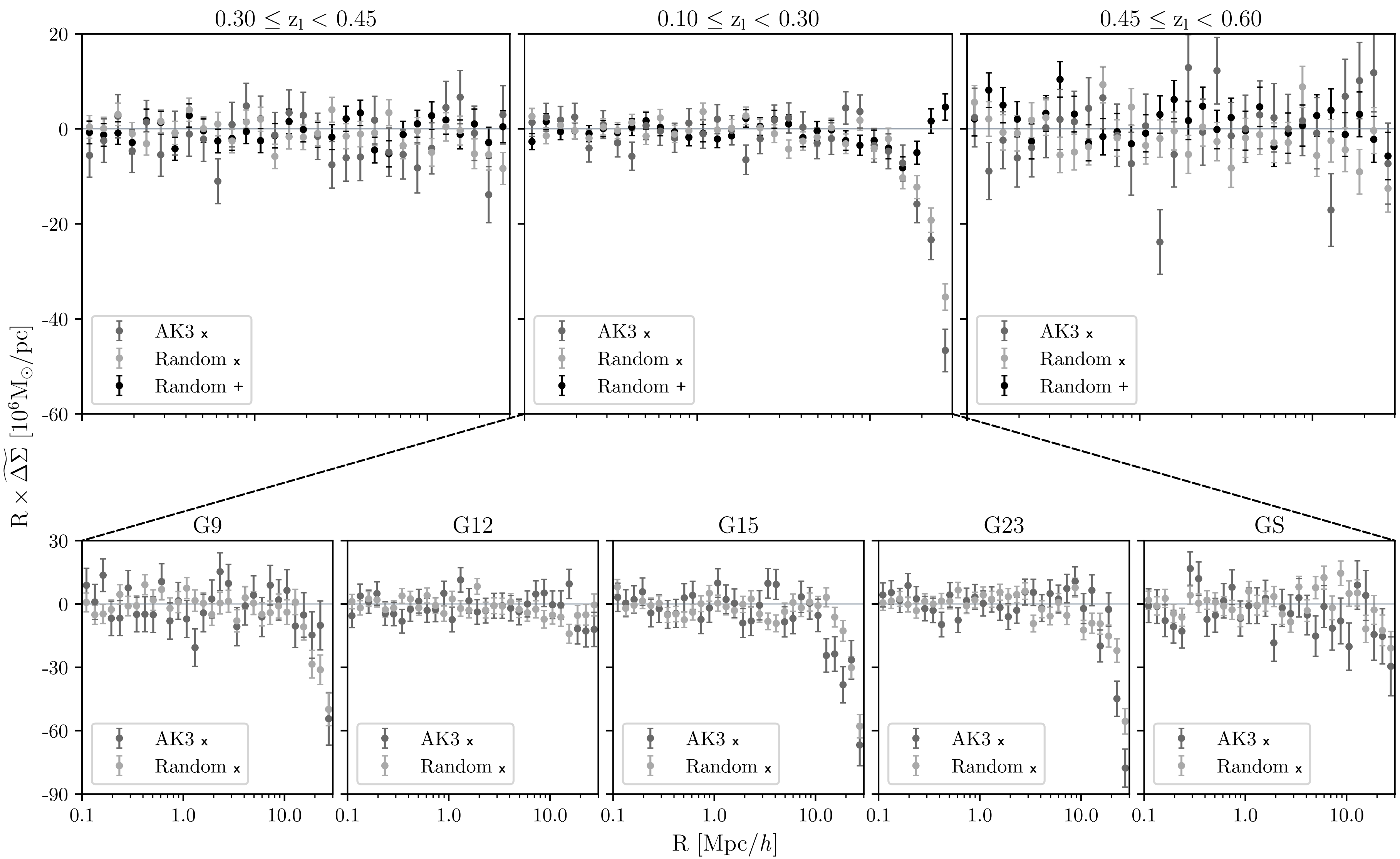

FIGURE 3.10: Differential density profiles of the cross component of AMICO lenses and the cross and tangential components of random lenses in the three redshift bins. The cross signals in the five KiDS DR3 patches of the lower redshift bin are also displayed. A significant deviation from the zero horizontal line indicates the presence of a systematic effect. It reveals an incomplete correction of the PSF of galaxies located close to the FoV edge.

to a non-zero cross component. However, since the subtraction of the two signals gives a signal consistent with zero, the correction suppresses this systematic effect and the final version of the data is ready for the analysis (see Section 3.3.3).

3.3.3 MCMC method

In Bayesian statistics, the Monte Carlo Markov Chain (MCMC) method is commonly used to sample posterior distributions. The best parameters are found with the maximum likelihood distribution, giving the highest probability of the sample (also given by minimizing the χ^2-distribution). In this specific study, the likelihood function is the joint probability of getting the measurement $\widetilde{\Delta\Sigma}$ with the parameters $\theta = [\log_{10} \mathrm{M}_{200c}, c_{200c}, \sigma_{\mathrm{off}}, f_{\mathrm{off}}, b_h\sigma_8^2]$ given the model $\Delta\Sigma$. This probability distribution is assumed to be normal and multiplied over the radial bins (i, j) of the profile to provide a global approximation of the variable:

$$\mathcal{L}(\theta) \equiv p\left(\widetilde{\Delta\Sigma}|\theta\right) \propto \exp\left(-\frac{\chi^2}{2}\right) , \tag{3.27}$$

where:

$$\chi^2 = \sum_{i,j} \left(\widetilde{\Delta\Sigma}_i - \Delta\Sigma_i\right) C_{ij}^{-1} \left(\widetilde{\Delta\Sigma}_j - \Delta\Sigma_j\right) , \tag{3.28}$$

and C_{ij} is the covariance matrix described in Section 3.3.1.

The χ^2 parameter is a good indicator of the goodness of fit of a statistical model. Its probability distribution depends on the degree of freedom which is the difference between the number of observations considered in the analysis and the number of variables in the halo model, here $df = 26 - 5 = 21$. In a goodness-of-fit test, the null hypothesis assumes that there is no significant difference between the observed and the expected values. Considering a significance level of $\alpha = 0.01$ defining the critical χ^2 values on the left and right tails of the distribution, the null hypothesis is verified if $8.9 < \chi^2 < 38.9$.

The likelihood is defined in the prior uniform distribution of the halo parameters having the following conservative bounds (Bellagamba et al., 2019):

- $\log_{10}\left(\mathrm{M}_{200c}/\left(\mathrm{M}_\odot/h\right)\right) \in [12.5, 15.5]$
- $c_{200c} \in [1, 20]$
- $\sigma_{\mathrm{off}} \in [0, 0.5]$ Mpc$/h$
- $f_{\mathrm{off}} \in [0, 0.5]$
- $b_h\sigma_8^2 \in [0, 20]$

We based the Bayesian inference on the `emcee`[4] algorithm (Foreman-Mackey et al., 2013), which uses an affine-invariant sampling method initially introduced in Goodman and Weare (2010). The cosmological parameters are defined for the fit as in Section 1.2.5.

We adopted an ensemble sampler with 32 walkers over a chain of 10,000 steps, giving a total size of 320,000 walkers to sample the posterior distribution. This scheme was already adopted in McClintock et al. (2019). We define the burn-in phase as being twice the integrated autocorrelation time τ_f of our chain f. This parameter is used to define the number of samples needed to reduce the relative error on the estimate. In

[4] https://emcee.readthedocs.io/

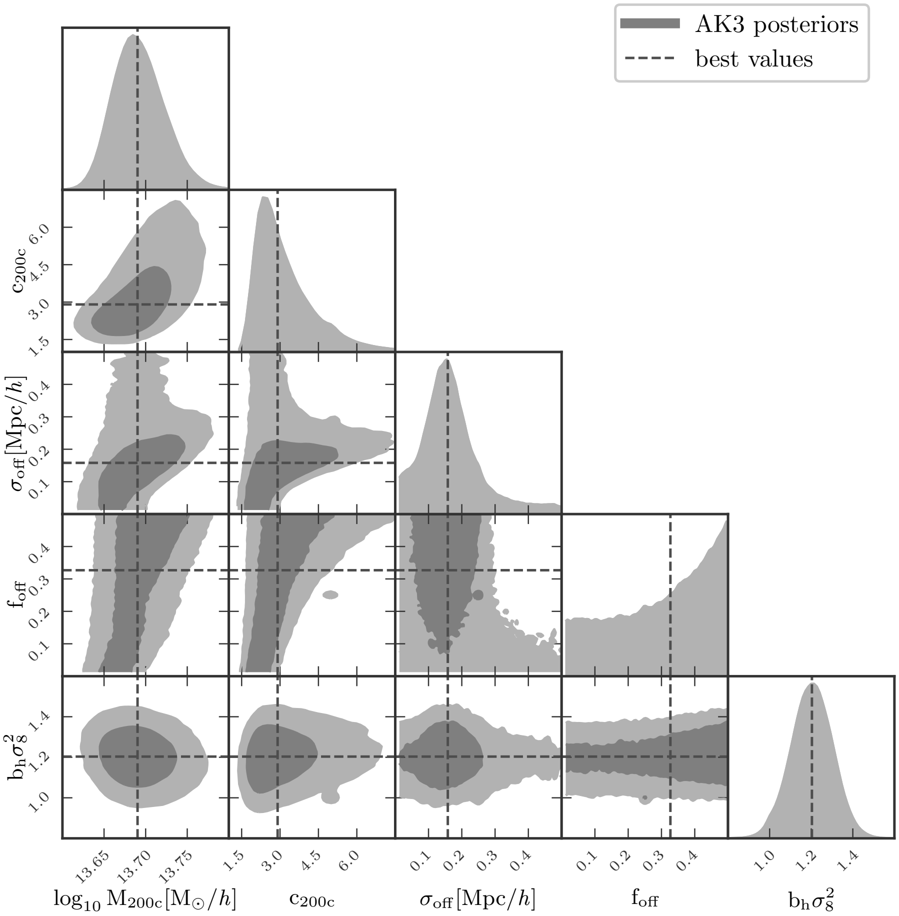

FIGURE 3.11: Posterior distributions arising from the halo model and the density profile derived in this study. The median of the marginalized distribution of the mass, concentration, off-centering parameters, and bias are displayed as dashed lines. The 2D posterior distributions also show the 68% and 95% confidence regions in shaded grey regions.

addition, we tested if the MCMC converge to a single value by running the potential scale reduction factor $\hat{R}$ (see Gelman and Rubin, 1992). Convergence is reached if the criterion $\hat{R} < 1.1$ is satisfied.

In Figure 3.11, we show the joint posterior distributions given by the sampler for the total profile shown in Figure 3.5. In the case of a normal PDF (as for the halo mass and bias), the 16*th*-84*th* and 2*th*-98*th* percentiles highlight 1σ and 2σ confidence regions forming ellipsoids in the 2D parameter space. In the opposite case, the percentiles show distorted ellipsoidal regions which define the errors on the parameter. For example the f_{off} posterior distribution gives errors larger than the prior boundaries, while we expect the posterior of the parameter to follow a Gaussian-like distribution within the limits defined by the prior function. This effect suggests that the parameter is imprecisely constrained. Nevertheless, the sampler distributions of the parameters of interest (i.e. mass, concentration, and bias) converge significantly, which makes it possible to consistently exploit their relation. For the following, we define the error on the parameters as the 1σ confidence interval, specifically approximated here with the region where 68% of walkers lie around the mean.

3.4 Results of the study

The WL analysis gives results when constraining the halo model discussed in Section 2.2 on the stacked shear density profiles derived in Section 3.2.2. Specifically, we extract the halo parameters into 14 redshift-richness bins using the MCMC method presented in the previous section. Then we derive scaling relations with mass and richness and compare them with alternative studies in KiDS-DR3. We discuss the sparsity of AMICO galaxy clusters as additional material for further studies. Results on the halo concentration the power-law relation with mass results are also analyzed. We subsequently show the main results on the halo bias, and its relation with the halo mass. This relation is finally used to test the matter power spectrum normalization.

3.4.1 Primary outcomes

In Figure 3.12, we obtain the shear profiles for the AMICO KiDS-DR3 galaxy clusters split into 14 redshift-richness bins, from 0.2 to 30 Mpc/h. We also show the fitted model and its components within its 1σ confidence region. We also compute the SNR over the full lensing profile as:

$$\frac{\mathrm{S}}{\mathrm{N}} = \sum_{\mathrm{j}} \frac{\widetilde{\Delta\Sigma}_{\mathrm{j}}}{\sigma_{\widetilde{\Delta\Sigma}_{\mathrm{j}}}} \,, \tag{3.29}$$

where the error on $\widetilde{\Delta\Sigma}$ derives from Equation (3.16) and the sum runs over the radial bins j. We associate to each bin the χ^2 computed as in Equation (3.28), which indicates that all pass the goodness-of-fit test presented in Section 3.3.3.

Table 3.3 shows the best fit values for the halo mass, the sparsity, the concentration, and the halo bias in each cluster bin with the 68% confidence bounds. The parameters computed over the stacked profile of the full catalog are also displayed in the first row and correspond to the dashed values shown in Figure 3.11 with $\chi^2 = 29.8$, which suggests that the goodness-of-fit test has been passed, as for the other bins. The mean redshift and the mean richness of the lenses are computed as in Equation (3.18), while the mean redshift of the sources is the effective redshift z_{back} in Equation (3.14). We additionally measure the mass from a fitting in the radial range [0.2, 3.16] Mpc/h assuming the same priors for the full profile, unlike the bias derived from Tinker et al. (2010). These measurements are in good agreement with Bellagamba et al. (2019)

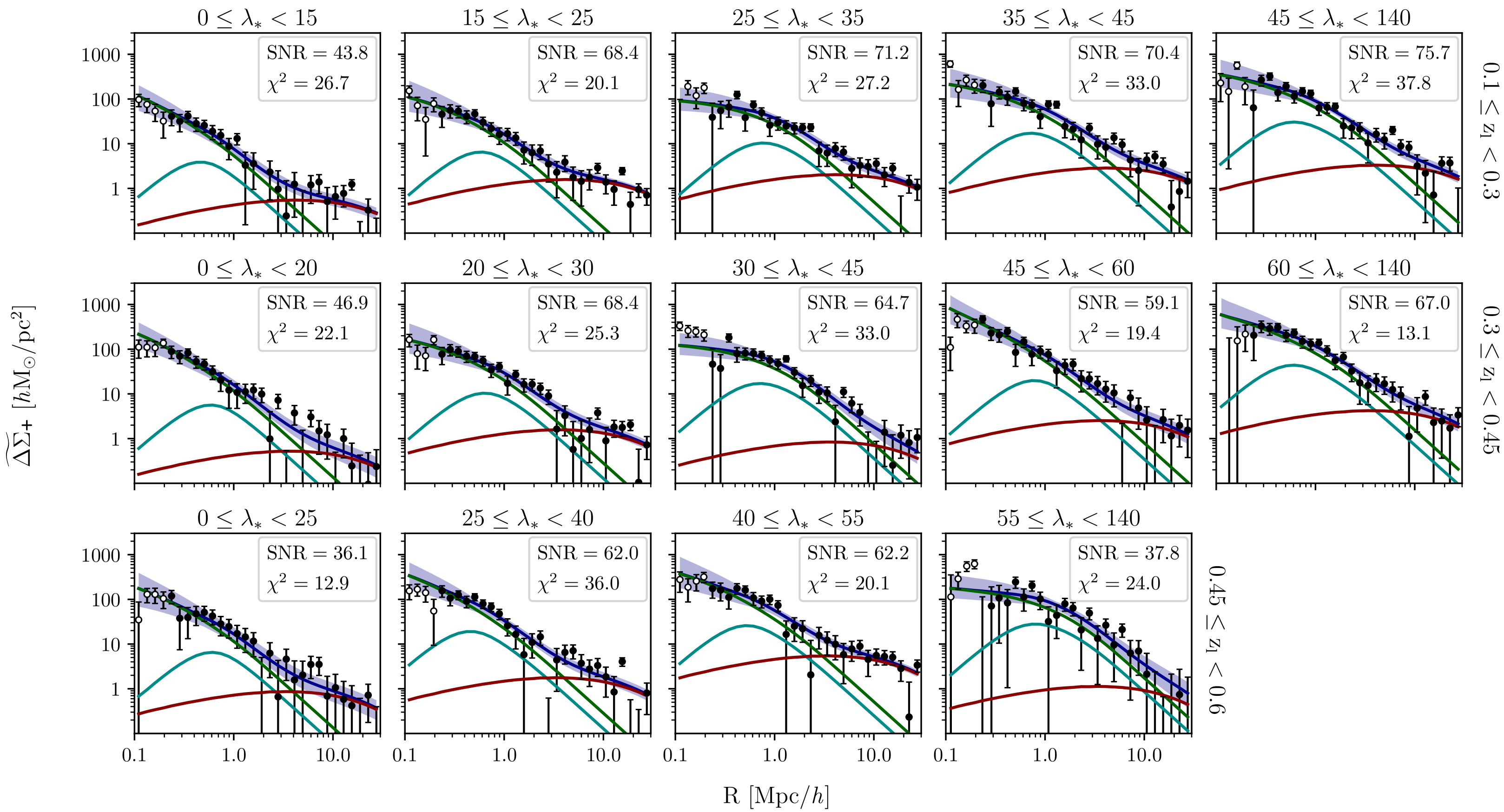

FIGURE 3.12: The stacked shear profiles and the halo model (blue) corresponding to the fitted parameters, with the 1σ confidence interval (blue region). Each row corresponds to a redshift bin, while each panel corresponds to an associated richness bin. The top right legends show the SNR, computed from each radial bin and summed over the $[0.2, 30]$ Mpc/h radial range, and the χ^2 computed as in Equation (3.28) given by the $50th$ percentile parameters. The model components: the main halo term (green), the off-centered contribution (cyan), and the correlated matter term (red). Empty points show the first four radial bins not considered in the fit.

and show for the two lower redshift bins a relative percentage difference within $\sim 5\%$ (see Figure 3.13). This variation could be explained by the different choice for the radial bins within 3.16 Mpc/h: 14 logarithmically equispaced annuli were used in the previous study, while in this work we selected the radial bins within 3.16 Mpc/h over the full radial range of the shear profile. These two definitions make the profiles and the derived measurements of the mass slightly different.

3.4.2 Mass-richness relation

The average redshift and richness of the lenses in each redshift bin are shown in Figure 3.3, and follow the global trend given by the removal of low mass clusters at high redshift for AMICO clusters with SNR < 3.5. Figure 3.12 shows that the differential density at a given radius increases with richness, suggesting a clear correlation between cluster mass and richness. Figure 3.13 shows the relation between the mass and the effective richness of the cluster bins. We fit this relation assuming the following power law in logarithmic scale:

$$\log_{10} \frac{\mathrm{M_{200c}}}{\mathrm{M_{piv}}} = \alpha + \beta \log_{10} \frac{\lambda_*}{\lambda_{\mathrm{piv}}} + \gamma \log_{10} \frac{\mathrm{E(z)}}{\mathrm{E(z_{piv})}} , \tag{3.30}$$

where E(z) derives from Equation (1.15) and $\mathrm{M_{piv}} = 10^{14}\mathrm{M_\odot}/h$, $\lambda_{\mathrm{piv}} = 30$, and $\mathrm{z_{piv}} = 0.35$ corresponding to the median values for AMICO KiDS-DR3 in Bellagamba et al. (2019). We estimate the parameters of this multi-linear function applying an orthogonal distance regression method (`ODR`[5]), involving mass, richness and redshift uncertainties. The fit gives:

- $\alpha = 0.007 \pm 0.019$
- $\beta = 1.72 \pm 0.09$
- $\gamma = -1.35 \pm 0.70$.

As Figure 3.13 shows, these results are in remarkable agreement with Bellagamba et al. (2019) despite the different definition of richness bins at high redshifts and the different fitting method. In addition, they are also perfectly consistent with Lesci et al. (2020) and Sereno et al. (2020), regardless of the different approaches employed to fit the scaling relation.

The positive correlation between shear signal and richness is shown in Figure 3.12 at large radii and implies a strong correlation between the bias and the mass. The SNR of individual radial bins at large scales is relatively low due to the poor quality of the shear produced by low mass clusters and increases with the richness. The highest redshift-richness bin shows a particularly low SNR with a low amplitude for the shear profile, where usually we expect the signal amplitudes at small and large scales to be high in large richness bins. The poor quality of the lensing signal in this specific bin also impacts the halo mass and bias with a downward trend.

3.4.3 Cluster sparsity

As parallel analysis of Ingoglia et al. (2022), we study the halo sparsity of AMICO KiDS-DR3 clusters. Originally introduced by Balmès et al. (2014), the sparsity is

[5] https://docs.scipy.org/doc/scipy/reference/odr.html

TABLE 3.3: Mass, sparsity, concentration, and bias resulting from the fit with their errors given in separate rows as different redshift and richness bins. These values correspond to the 16*th*, 50*th*, and 84*th* percentiles of the posterior distributions. We also show the mass measurement in the radial range [0.2, 3.16] Mpc/h in brackets. Mean richness ($\bar{\lambda}_*$), lens redshift ($\bar{z}_l$) and source redshift ($\bar{z}_s$) are computed from Equations (3.18) and (3.14) and their errors are assumed to be the RMS weighted sample deviation. We report both the number of clusters N_l and the fraction of clusters relative to the full selected cluster sample in each redshift-richness bin.

z_l	λ_*	$\bar{z}_l$	$\bar{\lambda}_*$	$\bar{z}_s$	N_l	$\log_{10}(M_{200c}/(M_\odot/h))$	$s_{200c,500c}$	c_{200c}	$b_h\sigma_8^2$
[0.1, 0.6[	[0, 140[	0.372 ± 0.005	19.92 ± 0.50	0.763 ± 0.004	6961 (100.0%)	$13.69^{+0.03}_{-0.03}$ $(13.68^{+0.03}_{-0.03})$	$1.47^{+0.39}_{-0.20}$	$2.90^{+1.43}_{-0.70}$	$1.20^{+0.10}_{-0.10}$
[0.1, 0.3[	[0, 15[	0.192 ± 0.004	10.25 ± 0.21	0.700 ± 0.004	1246 (17.9%)	$13.24^{+0.08}_{-0.08}$ $(13.23^{+0.08}_{-0.08})$	$1.29^{+0.20}_{-0.08}$	$9.27^{+6.85}_{-5.05}$	$0.60^{+0.18}_{-0.18}$
[0.1, 0.3[	[15, 25[	0.216 ± 0.005	18.94 ± 0.28	0.726 ± 0.006	683 (9.8%)	$13.56^{+0.08}_{-0.08}$ $(13.58^{+0.08}_{-0.07})$	$1.56^{+0.29}_{-0.22}$	$4.25^{+5.18}_{-2.05}$	$1.71^{+0.24}_{-0.25}$
[0.1, 0.3[	[25, 35[	0.226 ± 0.009	29.09 ± 0.51	0.742 ± 0.011	209 (3.0%)	$14.01^{+0.07}_{-0.07}$ $(14.04^{+0.07}_{-0.07})$	$1.91^{+0.23}_{-0.25}$	$1.64^{+1.00}_{-0.46}$	$2.19^{+0.46}_{-0.46}$
[0.1, 0.3[	[35, 45[	0.232 ± 0.017	39.61 ± 0.83	0.740 ± 0.020	83 (1.2%)	$14.29^{+0.06}_{-0.07}$ $(14.30^{+0.06}_{-0.07})$	$1.54^{+0.20}_{-0.16}$	$3.17^{+2.23}_{-1.10}$	$3.07^{+0.76}_{-0.77}$
[0.1, 0.3[	[45, 140[	0.228 ± 0.019	56.05 ± 5.86	0.747 ± 0.022	44 (0.6%)	$14.53^{+0.05}_{-0.06}$ $(14.52^{+0.06}_{-0.06})$	$1.44^{+0.12}_{-0.10}$	$3.95^{+2.25}_{-1.21}$	$3.56^{+1.01}_{-1.04}$
[0.3, 0.45[	[0, 20[	0.374 ± 0.005	15.13 ± 0.38	0.860 ± 0.002	1110 (15.9%)	$13.60^{+0.08}_{-0.08}$ $(13.60^{+0.08}_{-0.08})$	$1.28^{+0.15}_{-0.07}$	$9.31^{+6.57}_{-4.58}$	$0.52^{+0.28}_{-0.26}$
[0.3, 0.45[	[20, 30[	0.388 ± 0.005	24.16 ± 0.39	0.863 ± 0.003	769 (11.0%)	$13.87^{+0.07}_{-0.07}$ $(13.93^{+0.07}_{-0.07})$	$1.64^{+0.28}_{-0.22}$	$3.65^{+3.71}_{-1.54}$	$1.57^{+0.36}_{-0.35}$
[0.3, 0.45[	[30, 45[	0.390 ± 0.008	35.94 ± 0.94	0.863 ± 0.004	320 (4.6%)	$14.20^{+0.06}_{-0.06}$ $(14.19^{+0.06}_{-0.06})$	$1.85^{+0.23}_{-0.22}$	$1.63^{+0.82}_{-0.43}$	$0.83^{+0.52}_{-0.47}$
[0.3, 0.45[	[45, 60[	0.393 ± 0.015	50.94 ± 1.86	0.866 ± 0.008	87 (1.2%)	$14.40^{+0.08}_{-0.08}$ $(14.39^{+0.07}_{-0.08})$	$1.27^{+0.10}_{-0.06}$	$10.65^{+5.73}_{-4.52}$	$2.51^{+1.02}_{-1.02}$
[0.3, 0.45[	[60, 140[	0.381 ± 0.022	75.81 ± 9.29	0.860 ± 0.012	45 (0.6%)	$14.64^{+0.06}_{-0.06}$ $(14.66^{+0.06}_{-0.06})$	$1.42^{+0.12}_{-0.11}$	$5.11^{+3.15}_{-1.62}$	$4.20^{+1.42}_{-1.43}$
[0.45, 0.6[	[0, 25[	0.498 ± 0.006	19.76 ± 0.53	0.887 ± 0.003	1107 (15.9%)	$13.60^{+0.10}_{-0.11}$ $(13.58^{+0.10}_{-0.11})$	$1.32^{+0.26}_{-0.10}$	$6.53^{+7.74}_{-3.97}$	$0.82^{+0.40}_{-0.39}$
[0.45, 0.6[	[25, 40[	0.518 ± 0.008	30.75 ± 0.74	0.888 ± 0.003	952 (13.7%)	$13.94^{+0.06}_{-0.06}$ $(13.93^{+0.06}_{-0.06})$	$1.29^{+0.12}_{-0.07}$	$8.43^{+6.54}_{-3.76}$	$1.68^{+0.47}_{-0.46}$
[0.45, 0.6[	[40, 55[	0.513 ± 0.018	46.14 ± 1.54	0.888 ± 0.006	232 (3.3%)	$14.19^{+0.07}_{-0.08}$ $(14.23^{+0.07}_{-0.08})$	$1.41^{+0.17}_{-0.13}$	$6.18^{+5.77}_{-2.65}$	$5.16^{+0.89}_{-0.91}$
[0.45, 0.6[	[55, 140[	0.516 ± 0.028	66.69 ± 8.22	0.888 ± 0.012	74 (1.1%)	$14.56^{+0.08}_{-0.10}$ $(14.54^{+0.10}_{-0.11})$	$1.94^{+0.21}_{-0.25}$	$1.50^{+0.77}_{-0.36}$	$1.07^{+1.21}_{-0.75}$

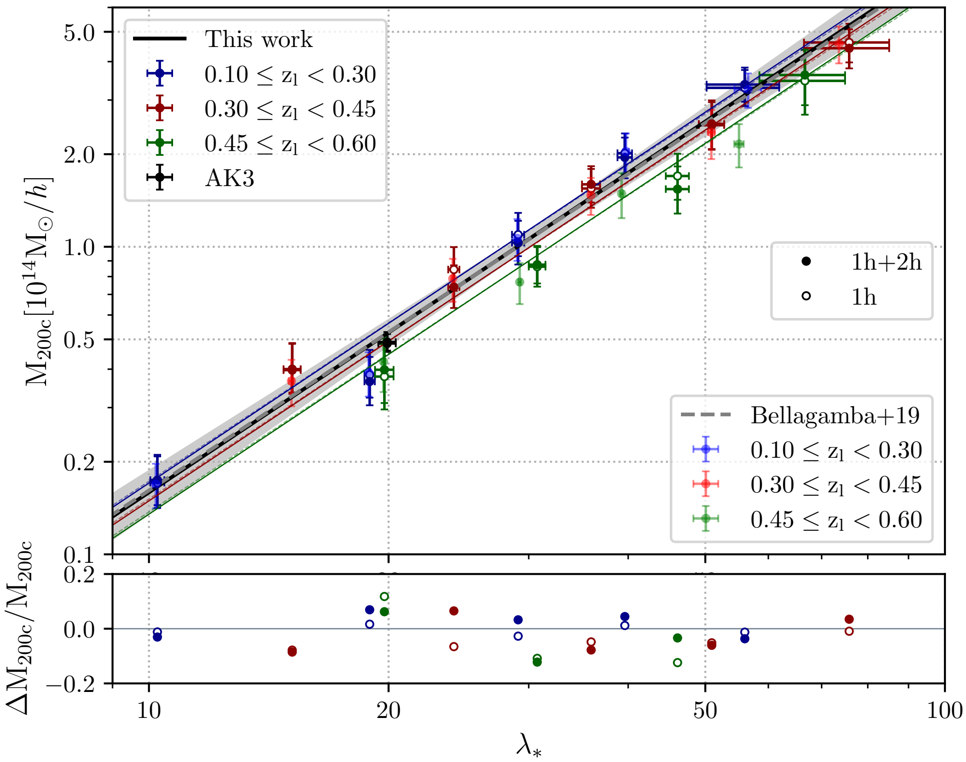

FIGURE 3.13: Mass-richness scaling relation for the full catalog (black) and the low (blue), intermediate (red), and high (green) redshift bins. The thick line corresponds to the model formulated in Equation (3.30). Full and empty data points represent the measurements over the whole radial profile and the central region of the halo, respectively. We compared our results with those presented in Bellagamba et al. (2019). The fainter colored points represent the data and the dashed lines represent the model. The relative change with respect to the results of this work is displayed in the bottom panel.

defined as the ratio of halo masses enclosed in apertures of different overdensities:

$$s_{\Delta_1,\Delta_2} \equiv \frac{M_{\Delta_1}}{M_{\Delta_2}} \,, \tag{3.31}$$

with $\Delta_1 < \Delta_2$. The physical meaning of the halo sparsity is simply the excess of mass contained in the annulus large of $\Delta r = r_{\Delta_2} - r_{\Delta_1}$. This parameter is particularly interesting because it does not depend on the specific choice of Δ_1, as soon as its value is not taken too small. Sparsity thus provides crucial insights on the halo mass profile without requiring information on its mass. This characteristic implies that the average value of the sparsity can be derived from the halo mass function, as defined in Equation (1.40) (see Balmès et al., 2014):

$$\int_{M_{\Delta_2}^{\min}}^{M_{\Delta_2}^{\max}} \frac{dn}{d\ln(M_{\Delta_2})} \frac{d\ln(M_{\Delta_2})}{M_{\Delta_2}} = \langle s_{\Delta_1,\Delta_2} \rangle \int_{\langle s_{\Delta_1,\Delta_2}\rangle M_{\Delta_2}^{\min}}^{\langle s_{\Delta_1,\Delta_2}\rangle M_{\Delta_2}^{\max}} \frac{dn}{d\ln(M_{\Delta_1})} \frac{d\ln(M_{\Delta_1})}{M_{\Delta_1}} \,. \tag{3.32}$$

This equation can be solved numerically to compute the ensemble average sparsity $\langle s_{\Delta_1,\Delta_2} \rangle$. Alternatively, we can derive the sparsity analytically considering a given density profile of the halo, using the definition of the overdensity contrast in Equation (2.39) as:

$$\delta_c = \frac{\Delta_1 c_{\Delta_1}^3}{3m\left(c_{\Delta_1}\right)} = \frac{\Delta_2 c_{\Delta_2}^3}{3m\left(c_{\Delta_2}\right)} \,. \tag{3.33}$$

Assuming the definition of the concentration in Equation (2.40) and the Lagrangian transformation in Equation (2.51), we can express the mass M_{Δ_2} in terms of the concentration c_{Δ_1}. In the stacked WL analysis, we constrained the mass $M_{\Delta_1} = M_{200c}$, and in that respect we derive here the sparsity with respect to the mass aperture $M_{\Delta_2} = M_{500c}(c_{200c})$. We justify this choice since analyses on N-body simulation data show that Equation (3.32) stays valid by a few percent (e.g. Corasaniti and Rasera, 2019).

We show these results in Figure 3.14, also given in Table 3.3, where the mass M_{200c} is taken only in the inner region of the clusters (in parenthesis in Table 3.3). It is compared with the expected sparsity from the halo density models Navarro, Frenk, and White (1997) and Baltz, Marshall, and Oguri (2009), where the concentration is computed as in Diemer and Joyce (2019). The gap between the two models is relatively small compared with the wide range of the measurements confidence segments. The results do not show a strong deviation from these lines, remaining within a 2σ range.

The relation in Equation (3.32) gives sufficient materials to constrain our results as a redshift-dependent equation. It allows to deeply analyze cosmologies, particularly the shared area that the combined Ω_m and σ_8 parameters yield (see e.g. Corasaniti, Sereno, and Ettori, 2021).

3.4.4 Mass-concentration relation

In Section 2.3.1 we introduced the theoretical framework of the relation between the halo mass and the halo concentration. We have seen that many simulations predict the concentration to decrease with the mass. This behavior is supported by our results shown in Figure 3.15. In this figure, our results are compared with the concentration and mass measured with stacked WL data from 130,000 SDSS galaxy groups and clusters (Johnston et al., 2007b) and 1176 CFHTLenS galaxy clusters (Covone et al., 2014). These analyses are consistent within 1σ. The large and asymmetric error bars for the concentration reflect the high sensitivity of this parameter to the inner region

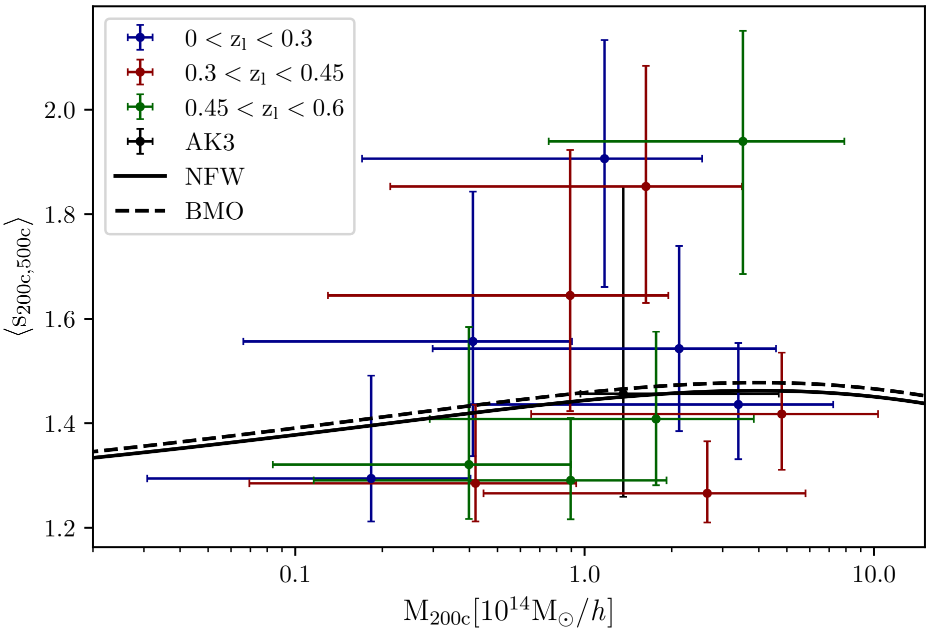

FIGURE 3.14: Sparsity of AMICO KiDS-DR3 clusters for the full catalog (black) and the low (blue), intermediate (red), and high (green) redshift bins. The two lines show the expected values of the sparsity, assuming the NFW and BMO parametric functions in Equation (2.43). In this specific case, the concentration is derived with the Diemer and Joyce (2019) theoretical mass relation.

of the halo density profile, which is poorly covered by our WL analysis. Sereno and Covone (2013), Umetsu et al. (2014) and Sereno et al. (2015b) discussed the effects stemming from the different choices and forms of the priors, and found a log-uniform prior might underestimate the concentration. As done for the redshift-mass-richness relation, we fitted the redshift-concentration-mass relation with a power-law function (Duffy et al., 2008), given as:

$$\log_{10} c_{200c} = \alpha + \beta \log_{10} \frac{M_{200c}}{M_{piv}} + \gamma \log_{10} \frac{1+z}{1+z_{piv}} \,. \tag{3.34}$$

We assume the pivot mass and redshift have the same values as in Equation (3.30), while the multi-linear regression is processed with the `ODR` routine over the full sample. We find:

- $\alpha = 0.62 \pm 0.10$
- $\beta = -0.32 \pm 0.24$
- $\gamma = 0.71 \pm 2.51$.

The large error on γ suggests a weak constraint of the redshift evolution due to the sparse number of data points (Sereno et al., 2017). The black line in Figure 3.15 shows the fitted power-law with the 1σ uncertainty interval, assumed as the range defined by the standard deviations of the estimated parameters and derived from the diagonal terms of the asymptotic form of the covariance matrix (see Fuller, 1987). Because of the small set of data points, the fit in each redshift bin does not provide consistent results for the coefficients. In the plot, we also show the theoretical relations between mass and concentration given by six different analyses of numerical simulations presented in Section 2.3.1 (Duffy et al., 2008; Dutton and Macciò, 2014; Meneghetti et al., 2014; Diemer and Kravtsov, 2015; Child et al., 2018; Diemer and Joyce, 2019; Ishiyama et al., 2020). In the corresponding mass range, our results are in good agreement with the theoretical predictions but have a steeper and lower relation with respect to the results obtained by Sereno et al. (2017) on the PSZ2LenS sample. The average concentration for the full AMICO KiDS-DR3 catalog seems to show a lower value than Equation (3.34) and the theoretical expectations but remains in the 1σ confidence interval.

3.4.5 Mass-bias relation

In Figure 3.16 we show the correlation between the cluster mass and the halo bias for the different redshift bins. The corresponding values are also reported in Table 3.3. These results are also in good agreement with previous results based on stacked WL studies on SDSS (Johnston et al., 2007b) and CFHTLens (Covone et al., 2014; Sereno et al., 2015a) galaxy clusters. As expected with the fourth richness bin at the highest redshift, the Bayesian inference of the halo bias shows a low SNR consistent with the poor quality of the lensing signal at large scales.

As introduced in Section 2.3.2, we can predict the halo bias with the halo mass using dark-matter only cosmological simulations. We mainly refer to Seljak and Warren (2004), Tinker et al. (2010) and Bhattacharya et al. (2011) as theoretical relations, also reported in Figure 3.16 using the corresponding values of σ_8 in Table 3.4. Due to the limited number of points, the data in each redshift bin do not exhibit a strong correlation with the theoretical bias given at the effective redshift of the bin. The black lines present an agreement within 2σ with all our measurements except the

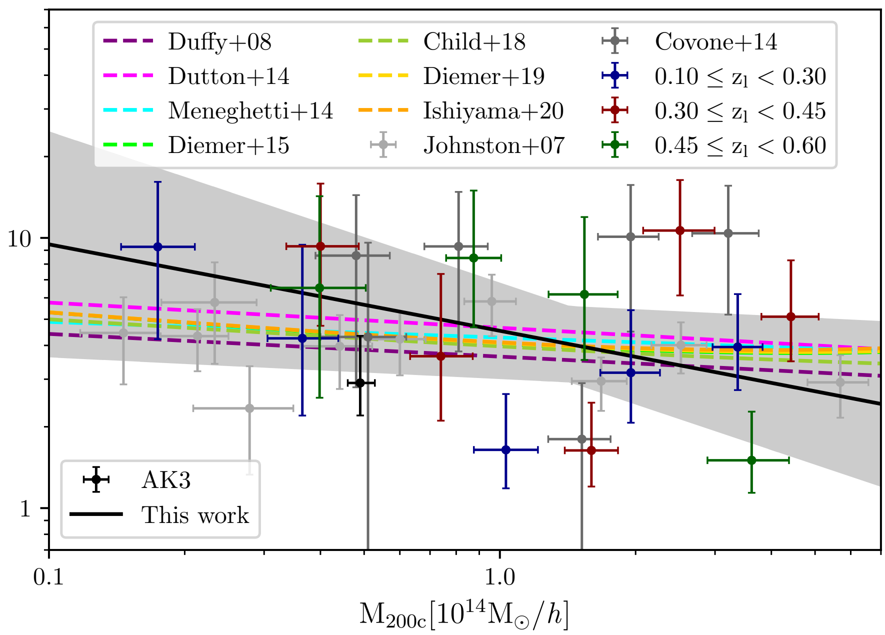

FIGURE 3.15: The relation between the mass and the halo concentration for the full catalog (black) and the low (blue), intermediate (red), and high (green) redshift bins. The results on the concentration are compared with calibrated data from a stacked WL analysis on SDSS and CFHTLenS galaxy clusters (Johnston et al., 2007b; Covone et al., 2014). The thick black line reports the best estimate of the linear regression for Equation (3.34) with its 1σ confidence region. The relation is contrasted with results given by different theoretical analyses (Duffy et al., 2008; Dutton and Macciò, 2014; Meneghetti et al., 2014; Diemer and Kravtsov, 2015; Child et al., 2018; Diemer and Joyce, 2019; Ishiyama et al., 2020).

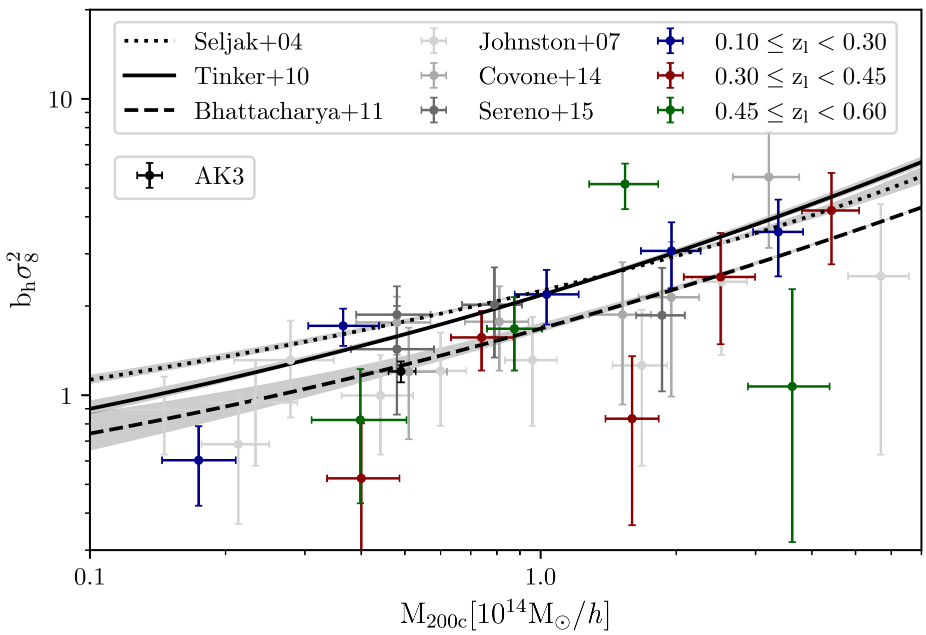

FIGURE 3.16: Halo bias-mass relation for the full catalog (black) and for the low (blue), intermediate (red) and high (green) redshift bins. The results on the halo bias are compared with calibrated data from a stacked WL analysis on SDSS and CFHTLenS galaxy clusters (Johnston et al., 2007b; Covone et al., 2014; Sereno et al., 2015a). Theoretical relations are derived from Seljak and Warren (2004), Tinker et al. (2010), and Bhattacharya et al. (2011) and respectively displayed as dotted, thick, and dashed lines. These functions are computed within their confidence interval using the values of σ_8 reported in Table 3.4.

third richness point for the high redshift bin, which agrees within 3σ due to its high amplitude. We attribute this statistical fluctuation to the low number of clusters in this region of richness-redshift space since the few and the uneven number of objects results in a poorer statistical measurement of the stacked lensing signal.

Measuring the bias-mass relation with AMICO KiDS-DR3 clusters WL signals stands for major improvements in such analysis, as this data set provides sufficient quality shear density profiles to reach the scales where the halo bias dominates. Therefore, mass and bias are assessed with relatively high precision to constrain their relation.

3.4.6 Cosmological inference

Since the halo bias degenerates with σ_8^2, it is important to obtain independent constraints on this cosmological parameter within a ΛCDM framework. Here we let σ_8 be a free parameter in the theoretical mass-bias relation and fit the $b_h\sigma_8^2$ results with the method described in Section 3.3.3, assuming a uniform prior $\sigma_8 \in [0.2, 2.0]$. We use a diagonal covariance matrix, where the variance terms are the square of the errors on the bias defined by the 68% confidence regions. We do not account for the errors on the mass, hence accurate mass measurements are essential to constrain σ_8.

The resulting best fit values of the posteriors given among the combined redshift bins are shown in Table 3.4. Bhattacharya et al. (2011) used the "peak-background

TABLE 3.4: Median, 16*th* and 84*th* percentiles of the posterior distribution for σ_8. We also show the difference, $\Delta\sigma_8$, between σ_8 measured on the median mass values, and σ_8 measured on the mass 16*th* and 84*th* percentile values. The cosmological parameter is given for three relations derived from numerical simulations.

simulation	σ_8	$\Delta\sigma_8$
Seljak and Warren (2004)	$1.01^{+0.05}_{-0.05}$	0.02
Tinker et al. (2010)	$0.63^{+0.11}_{-0.10}$	0.01
Bhattacharya et al. (2011)	$0.66^{+0.19}_{-0.27}$	0.12

split" approach of Sheth and Tormen (1999) to fit the parameters of the mass function. We note that the bias function does not match the numerical results as well as direct calibrations, which could explain the discrepancy with respect to the results obtained with the two other relations. In order to estimate the effect of the mass uncertainty on cosmological inference, we measured σ_8 at masses corresponding to the 16*th* and 84*th* percentiles and noticed a difference with the median masses smaller than the statistical uncertainty of the parameter (see Table 3.4).

Figure 3.17 shows the three posterior distributions for σ_8 obtained in this work compared with the results from the cosmic microwave backround measurements by Planck (Planck Collaboration et al., 2020, Table 2, TT, TE, EE+lowE+lensing) and WMAP (Hinshaw et al., 2013, Table 3, WMAP-only Nine-year). Our constraint on σ_8 with the Seljak and Warren (2004) model, which has a sharp posterior that peaks around $\sigma_8 \sim 1$, highlights a discrepancy larger than 3σ with CMB values. The posteriors given by the Tinker et al. (2010) and Bhattacharya et al. (2011) models overlap within 2σ and 1σ with the CMB data, respectively, but the Bhattacharya et al. (2011) posterior is clearly different from a normal distribution. Because of the small size of the sample and the poor quality of the bias-mass measurements in some bins, our results yield quite broad posteriors that are necessarily in agreement with WMAP and Planck median values.

Finally, in Figure 3.18 we present our reference result from Tinker et al. (2010) in the broader context of recent measurements of σ_8. This model was calibrated for a range of overdensities with respect to the mean density of the universe and can easily be converted to overdensities with respect to the critical density, which makes the bias more reliable for the mass definition M_{200c}. In addition, our $b_h\sigma_8^2$ results given by the Tinker et al. (2010) relation are more reliable in comparative terms, since studies referenced in this paper base their analyses on this relation. In particular, we display the results from clustering and cluster counts studies based on the AMICO galaxy clusters sample (Nanni, Marulli, and Veropalumbo, in prep. Lesci et al., 2020), from cluster counts analyses done on SDSS-DR8 and 2500 deg^2 SPT-SZ Survey data (Costanzi et al., 2019; Bocquet et al., 2019), from galaxy clustering and weak lensing in DES-Y3 (DES Collaboration et al., 2021), and from cosmic shear analysis based on the HSC-Y1 and KiDS-DR4 catalogs (Hikage et al., 2019; Asgari et al., 2021, respectively). We also show the results from Planck (Planck Collaboration et al., 2020, Table 2) and WMAP (Hinshaw et al., 2013, Table 3) measurements.

Since the amplitude of the matter power spectrum correlates with the mean matter density, all these studies derived the combined parameter $S_8 \equiv \sigma_8\sqrt{\Omega_m/0.3}$. In this work, we computed a direct measurement of σ_8, dependent on the specific cosmological model assumed in our analysis. In the figure, we indicate with different symbols the measurements of σ_8 obtained without assuming specific values of the cosmological parameters (empty dots) and those assuming $\Omega_m = 0.3$ (filled dots).

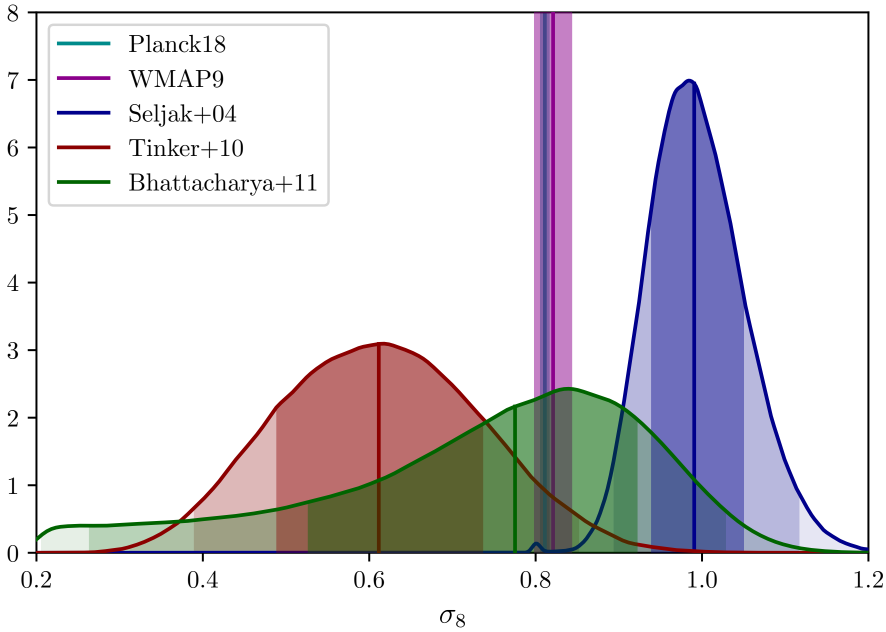

FIGURE 3.17: Posterior distributions for σ_8. The probability function is shown for three halo bias-mass relations, i.e. Seljak and Warren (2004), Tinker et al. (2010) and Bhattacharya et al. (2011), shown in blue, red and green, respectively. The dark to light shaded regions correspond to the $1-2-3\sigma$ intervals. We compare these distributions with the median values of Planck (cyan, Planck Collaboration et al., 2020, Table 2, TT, TE, EE+lowE+lensing) and WMAP (magenta, Hinshaw et al., 2013, Table 3, WMAP-only Nine-year).

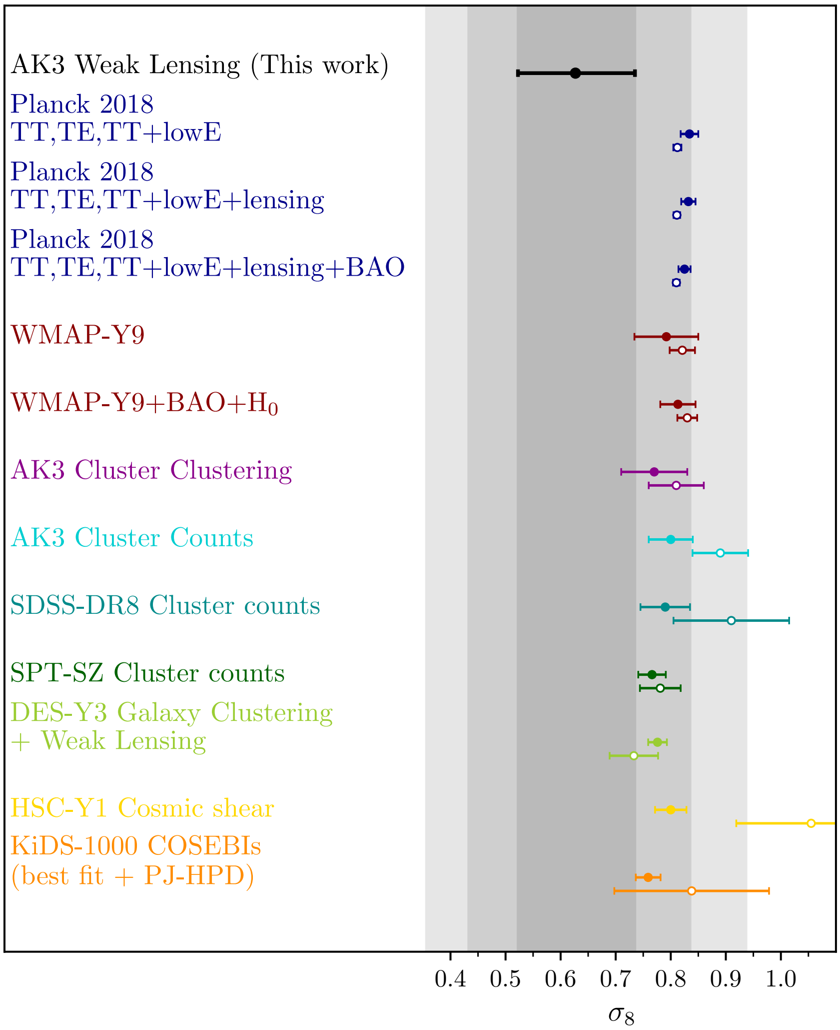

FIGURE 3.18: Comparison with literature results. Our reference σ_8 value is obtained assuming the Tinker et al. (2010) model. We show the median, 16*th* and 84*th* percentiles. We present from top to bottom results obtained in this work (black), Planck Collaboration et al. (2020) (blue), Hinshaw et al. (2013) (red), Nanni, Marulli, and Veropalumbo (in prep.) (magenta), Lesci et al. (2020) (cyan), Costanzi et al. (2019) (turquoise), Bocquet et al. (2019) (green), DES Collaboration et al. (2021) (light green), Hikage et al. (2019) (yellow) and Asgari et al. (2021) (orange). We show the relative constraints on σ_8 in a free cosmology (empty dots) and assuming $\Omega_m = 0.3$ (filled dots). The shaded regions correspond to the 99.7%, 95% and 68% confidence intervals.

Our results are closer to those obtained fixing $\Omega_{\mathrm{m}} = 0.3$, as a low inference of Ω_{m} induces a higher estimate of σ_8, and vice versa. For example, Planck Collaboration et al. (2020) results show a posterior mean slightly higher than with $\Omega_{\mathrm{m}} = 0.3$, while for cosmic shear studies it is slightly lower, hence when fixing Ω_{m} to 0.3 there is a shift in σ_8 to larger values for Planck Collaboration et al. (2020) and lower values for cosmic shear surveys. However, the $2-3\sigma$ regions for the posteriors of the three theoretical relations agree with the results of these external references, regardless of the cosmological dependencies considered, but still have to be taken carefully into consideration because of the poor constraint. The gap of σ_8 results from Seljak and Warren (2004) to Tinker et al. (2010) or Bhattacharya et al. (2011) also stresses the importance of the theoretical model when constraining cosmological parameters in a stacked WL analysis.

Chapter 4

Euclid project

Modern surveys give interesting materials to probe the shaded areas of cosmology. However, they remain quite limited compared with the next generations of surveys, as new telescopes become more technologically advanced with time. Typically, they should map the distribution of matter with unprecedented precision, offering an ideal framework to understand the mechanisms ruling the formation and evolution of the Universe. Thus, analyses of older data are not meaningless since they could be repeated and enhanced on wider and deeper sets of data that provide such surveys. WL is a particularly promising field for the upcoming years, mostly due to its statistical properties when dealing with large catalogs of data. In that respect, developing WL numerical tool to treat novel measurements is primordial to anticipate incoming releases and provide sufficient upstream work for fast and robust scientific results.

In this chapter, we present the numerical development of COMB-CL, a python[1] package that aims to measure the WL mass of galaxy clusters detected in the wide and deep field covered by Euclid. Euclid is one of the most relevant future surveys whose space mission is to map the dark Universe. This mission is organized in a consortium. COMB-CL project consists of a teamwork system, based on the numerical structure developed for the stacked WL analysis of KiDS-DR3 clusters of galaxies. We detail the contents of the tool in order to complete the thesis.

4.1 Mission of the Euclid consortium

The Euclid Consortium[2] (EC) is an astronomical and astrophysical organization selected by the European Space Agency (ESA) that gathers teams of researchers to contribute to the Euclid mission. It is responsible for the technical development of scientific instruments, the production of the data, and for leading the scientific exploitation of the mission until completion. This section focuses on the scientific goals and characteristics of the EC mission, and the Science Ground Segment (SGS) activities to better determine the structural environment of COMB-CL.

4.1.1 Scientific objectives

EC mission, first presented in Laureijs et al. (2011), will investigate the expansion history of the Universe and the evolution of the cosmic structures. The two primary fields of research that Euclid will explore are WL studies and measurements of the BAOs imprinted in the clustering of galaxies. While BAOs provide a direct distance-redshift probe to study the expansion rate of the Universe, WL provides an indirect dark matter probe by combining angular distances, which probes the expansion rate,

[1] https://www.python.org/

[2] https://www.euclid-ec.org/

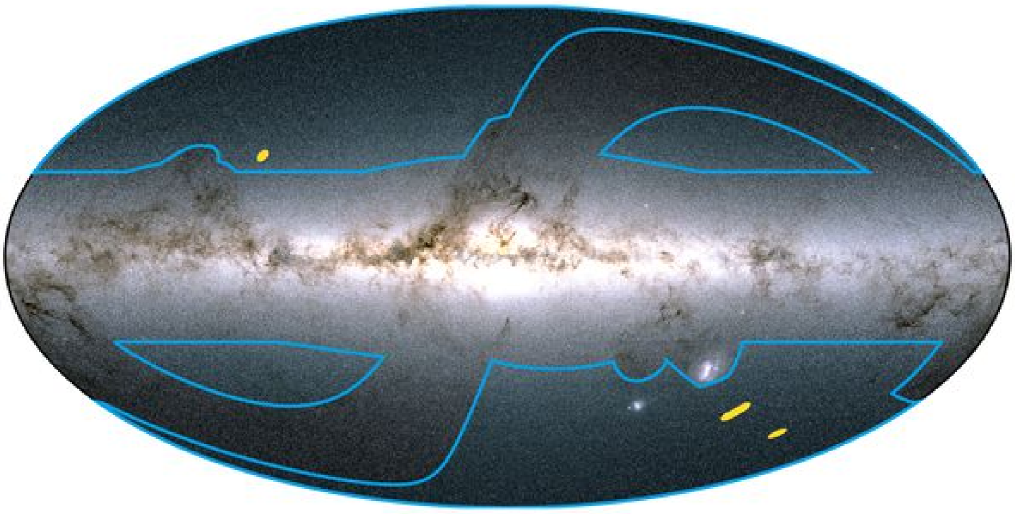

FIGURE 4.1: Footprint of the Euclid survey. In blue the observation area of the principal Euclid Wide Survey mission and in yellow of the Euclid Deep Fields. (Credits: ESA/Euclid Consortium)

and mass density contrasts, which probes the growth rate of structure. These investigations will be complemented by independent analyses on clusters of galaxies derived from Euclid data.

In order to complete these scientific goals, the survey will map the large-scale structure over the entire extragalactic sky by measuring shapes and redshifts of galaxies. It will probe a large fraction of the sky, about 70%, and of the Universe's history, the last 10 billion years, covering 15,000 deg^2 free of contamination by light from the Milky Way and the Solar System up to redshifts $z \sim 2$. Euclid will provide about 2 billion photometric galaxy images used for WL observations (Amendola et al., 2018) and about 30 million of them with accurate spectroscopic redshifts (Pozzetti et al., 2016). The survey will also complete deep field observations distributed over three patches in the sky, for a total surface around 40 deg^2. This auxiliary survey is about 2 magnitudes deeper than the wide survey. It is primarily used for calibrations of the wide survey data but also aims at exploring faint objects in the early Universe, as well as assessing the purity of the spectroscopic observations. The footprint of Euclid is presented in Figure 4.1 with both wide and deep surveys.

Such observations will be possible with the Euclid space telescope, which launch date is scheduled for this year and will complete a 6-year observing mission from the L2 Earth-Sun Lagrangian point. It is composed of mirrors large of 1.2 meters (for the largest one), deflecting observation light towards two instruments: VIS, returning high-resolution images in the 500-800 nm optical band, and NISP, comprising Y, J, and H broad-band filters in the 900-2000 nm near-infrared range. VIS and NISP will reach pixel resolutions of 0.1 arcsec and 0.3 arcsec down to magnitudes 24.5 and 24, respectively, and both will share a common FoV of 0.53 deg^2. In addition, NISP will provide near-infrared spectra with slitless grism spectrographs, one "blue" (920-1250 nm) in the Euclid Deep Fields and three "reds" (1250-1850 nm) with the Euclid Wide Survey.

In terms of comparison with KiDS, Euclid will provide space survey data quality on deep fields, covering an area more than 10 times wider. The data product is also 20 times larger, as KiDS will identify about 100 million galaxies at its completion, versus 2 billion for Euclid. The large fraction spectroscopic data in Euclid will also provide accurate redshift positions. All these characteristics make the Euclid survey a prominent mission to yield promising WL probes in the future years.

4.1.2 Ground segment

During its 6-year space mission, Euclid will deliver a large amount of data, about 2,000 Gbit per day. This flow will be managed and treated by the ground segment of the Euclid mission, composed of two independent sections: the ESA Operations Ground Segment (OGS) and the EC Science Ground Segment (SGS).

The OGS will be in charge of the communication sector with Euclid from the ground station under the responsibility of the Mission Operations Centre (MOC) in Darmstadt, Germany. The MOC will operate the spacecraft and deliver the raw scientific data to the SGS.

The SGS is amongst the most challenging part of this mission. This segment represents the major fraction of the resources provided by the EC. It is responsible for data processing and the production of scientific results. This crucial operation is basically processed in three main levels, interconnected with several Organization Units (OUs) (Pasian et al., 2012):

- Level 1 starts the monitoring process when receiving the raw VIS and NISP images. Then follows the housekeeping telemetry and the production of daily reports. This software level processing is developed by SGS but operates at the Science Operations Centre (SOC) under ESA management. Data edited from telemetry are then transmitted to calibration modules and provide co-added images and spectra to level 2.

- Level 2 is basically merging all the upstream flow of data in stacked images and returns source catalogs where all the multi-wavelength data (photometric and spectroscopic) are aggregated. This flow is conveyed to different OUs, that compute spectroscopic redshifts from the spectra, photometric redshifts from the multi-wavelength images, and shape measurements from the visible images. Such data are stored in catalogs and treated in level 3.

- Level 3 is in charge, with the EC Science Working Groups (SWG), of computing all the high-level science data products. It is organized in work packages covering different scientific areas, namely Galaxy Clustering (GC), Weak Lensing (WL), Clusters of galaxies (CL), Internal Data (ID), and External Data (ED).

The processing structure of SGS routines is regularly alimented with simulated and external data from SWG and ground-based observatories, respectively, to cross-check key points of the pipeline and validate data for the processing of the next OU.

The skeleton is shown in Figure 4.2 with the flow of data going through the pattern of the pipeline. All the processing functions are thus connected to each other with the responsibility to provide robust measurements for scientific results. These materials are specific to the Euclid mission, as they have been developed under the policy of the EC. However, most of these processing functions derive from external studies, which ensure the possibility to analyze alternative data set considering the copyright legacy. The opportunity to adapt these packages on external surveys let the possibility for SGS to pursue activities long after the mission completion.

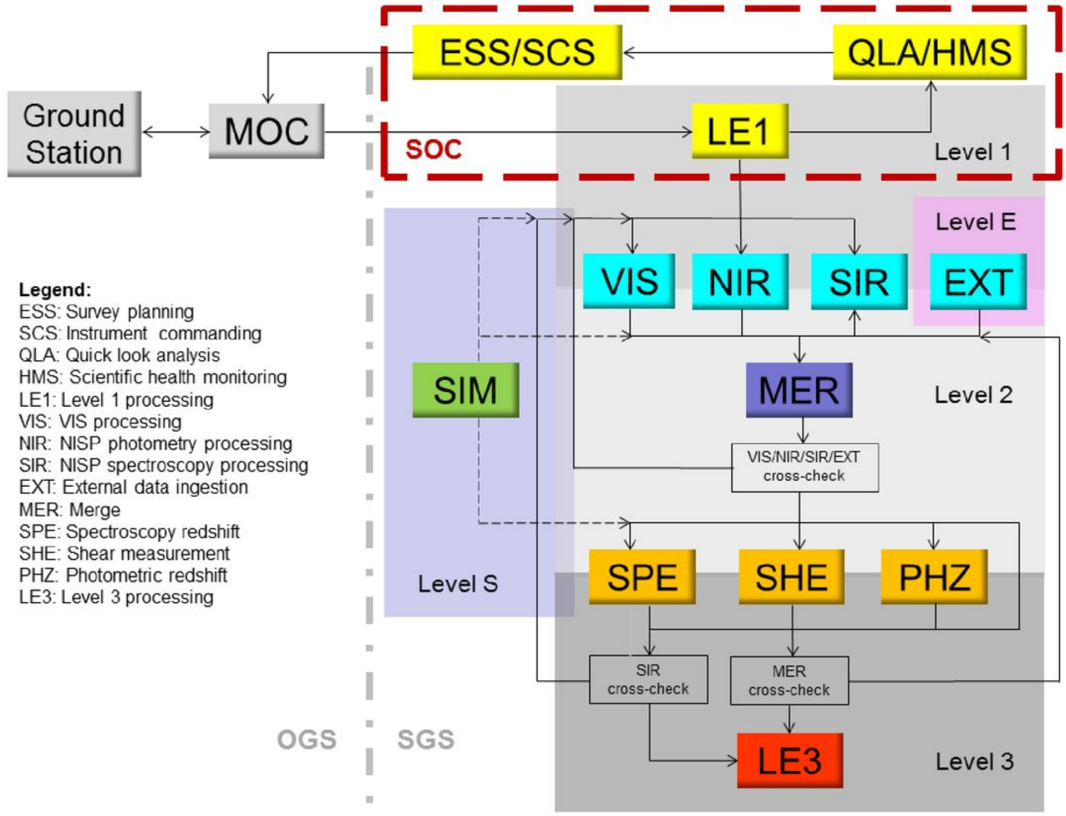

FIGURE 4.2: EC SGS pipeline for Euclid data treatment. This diagram shows the composition of the complete SGS environment down to the level 3 acting for science catalogs. (Credits: Zacchei et al., 2016)

4.2 COMB-CL numerical toolkit

In order to produce data for the EC mission, we have seen that processing functions are necessary. We introduce here the COMB-CL[3] python toolkit in a prototype stage, that will measure WL mass for individual Euclid detected clusters. In the following, we give a global description of the module, we detail the input and output data, then we describe how it is structured, and finally, we predict the additional features that could be implemented in COMB-CL.

4.2.1 Global description

As part of the OU-LE3-CL, we have been involved to develop a python module that measures the mass of Euclid galaxy clusters using their shear density profiles. COMB-CL package is derived from the numerical codes used in the WL stacked analysis on KiDS galaxy clusters (Ingoglia et al., 2022). It basically relies on the materials that produced the results shown in the three previous chapters. The objective of COMB-CL is to provide a code that calculates shear profiles and mass estimates for galaxy clusters.

The module essentially inputs catalogs of sources and lenses, stacks shears over a given radial profile, computes statistical and systematic covariance matrices, defines a flexible halo density model with dependent or independent parameters, fits a lensing signal given a model and covariances, and finally returns halo parameters, including mass, and corresponding shear profiles for each individual galaxy cluster. These steps are more extensively described in the following sections. The module has been developed in such a way that it can be used from any data model, as soon as input catalogs have the correct Euclid-like shape recognizable with the python script.

The project consists of a developer team, that gather weekly for a year to build COMB-CL in a proper format for Euclid. It is settled in regular and technical teleconferences every Monday, freely accessible to everyone concerned with the project. The purposes of these meetings are centered on fixing development and management issues, continuously resumed with minute notes to keep track of the evolution of COMB-CL. The main leaders of COMB-CL are Samuel Farrens[4], Mauro Sereno[5], Martin Vannier[6] and myself[7].

The current status of COMB-CL is a prototype version that is tested for validation using observational and simulated data and external codes. For instance, we use X-ray detected clusters in the Hyper Suprime-Cam (HSC, Umetsu et al., 2020) survey to compare their shear profiles and extract WL masses with COMB-CL. Alternatively, galaxy clusters modeled with hydrodynamical simulations are useful to test their masses, as for THE THREE HUNDRED project (Cui et al., 2018). Finally, CosmoBolognaLib (CBL, Marulli, Veropalumbo, and Moresco, 2016) is a C++ library that collects numerous WL calculations helpful for testing the theoretical side of COMB-CL.

Finally, COMB-CL has been selected as one of the Pre-Launch science Key Project (KP) papers. It occupies the KP-LE3-CL-2 study regarding the "Characterization of the properties of detected galaxy clusters". These KPs coordinate the materials provided by the EC publication group science and SWG units for Euclid data analysis

[3] `https://gitlab.euclid-sgs.uk/PF-LE3-CL/COMB-CL`

[4] samuel.farrens@cea.fr

[5] mauro.sereno@inaf.it

[6] martin.vannier@oca.eu

[7] lorenzo.ingoglia@unina.it

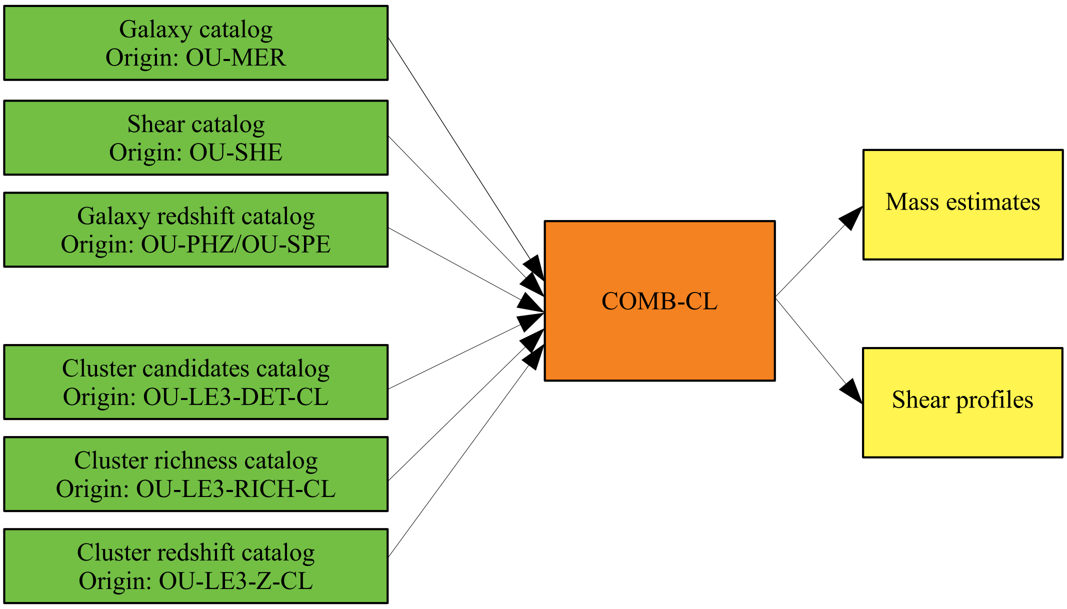

FIGURE 4.3: The COMB-CL inputs and outputs data in the framework of the EC SGS.

in a list of publications distributed over EC members. This coordination aims to avoid overlapping issues and values the cross-exchanges between the sciences processing units.

4.2.2 Data products

The data products are the data that are generated and used by the SGS pipeline. It is described in a public detailed document[8] to better organize the interactions between the numerous OUs. In particular, it details the inputs and outputs required for the different processing functions. Figure 4.3 displays the schematic input-output organization of COMB-CL in Euclid.

The processing functions called by COMB-CL come from level 2 and level 3 OUs of the EC SGS. More specifically, we find:

- The galaxy catalog produced by the OU-MER. It contains most of the data from the list of galaxies and their characteristics. We are particularly interested in the identification number of the sources, their (RA,Dec) positions, and their magnitudes to better select them as background objects.
- The shear catalog given by the OU-SHE. This catalog of data provides the crucial WL information as the ellipticity components of the galaxies, the correction factors (multiplicative and additive), the SNR of the detection to attribute the statistical weight to the source.
- The galaxy redshift catalog, as computed in the OU-PHZ for photometric redshifts or the OU-SPE for spectroscopic redshifts. This is mainly used to select the sources relative to each individual lens, and test the efficiency of these selections with high-resolution spectroscopic redshifts produced within the same data set.
- The galaxy cluster catalog processed by the OU-LE3-DET-CL. This processing function detects clusters of galaxies with two independent algorithms: AMICO

[8] https://euclid.esac.esa.int/dm/dpdd/latest/index.html

and PZWav (Gonzalez, 2014), a code that searches for overdensities on fixed physical scales. The catalog account for the cluster identification, the (RA,Dec) position, and the SNR of the detection. It also stores the cluster redshift and richness, as computed by the OU-LE3-Z-CL and OU-LE3-RICH-CL processing functions for the characterization of the clusters (e.g. binning the profiles in cluster property criteria).

COMB-CL ingests this information and first returns shear profiles and covariance matrices tables, corresponding to each galaxy cluster. With KiDS-DR3 data, the computational time for this process is relatively short (~ 7 s per cluster). Then WL masses are returned for these shear profiles, which requires defining a halo density model previously. It is realized with the `emcee` (Foreman-Mackey et al., 2013) ensemble sampler. This step lasts also a few seconds (~ 30 s per cluster), which allows fast computations for WL masses.

4.2.3 Prototype structure

COMB-CL prototype is an assembly of interconnected classes. These processing functions are called in different submodules of the python package, which can be run independently or in a whole script configured for a complete WL mass measurement. Figure 4.4 highlights the configuration of COMB-CL described in this section. In addition, the package possesses several python notebook tutorials to introduce COMB-CL formally.

First of all, the `Cosmology()` class defines the cosmological framework of the run. It inputs cosmological parameters preset in a YAML file. The user can select the cosmology of interest, or either create a new one from an internal method of the class. The module encapsulates most of the functions seen in Chapter 1. Basically, we find the cosmological parameters and distances, as evolving with redshift, the matter power spectrum, the variance of the overdensity field, or the correlation function. This class is central in the COMB-CL structure, as all the other modules depend on this one.

The children classes `HaloConcentration()` and `HaloBias()` provide the theoretical routines as defined in Sections 2.3.1 and 2.3.2, respectively. This gives the full dependency of COMB-CL to mass measurements, as these functions calculate the halo parameters in terms of the halo mass.

`HaloModel()` is the children class of the two previous methods, and thus the grandchildren of `Cosmology()`. It defines the terms of the model of the halo density profile, particularly the one- and two-halo terms (see Section 2.2). The parameters of the model are identified in this class, namely the halo concentration, bias, or mass given in a region with overdensity Δ.

A central class in COMB-CL is the `ShearProcess()`, as it provides the observational materials to the mass estimates. It inputs the catalogs of sources and lenses, discriminates the background sources according to a selection model, computes the lensing signal by stacking the shears and radii of the sources over a given radial range, bootstraps the stacking process, and calculates the uncorrelated large-scale structure (LSS) covariances. We discuss this last specificity in the next section. The returned outputs are then the shear density profiles and the LSS covariances of the lens catalog.

Finally, the `MCMCFit()` class inputs the density model and measurements described by the `HaloModel()` and `ShearProcess()` classes, to constrain the parameters of interest, which for Euclid clusters is the mass. The user can play with the size of the Markov chains to better fit the data on a suitable computational time and power. This closes the articulation of the module by returning the catalog of measured parameters for the lenses.

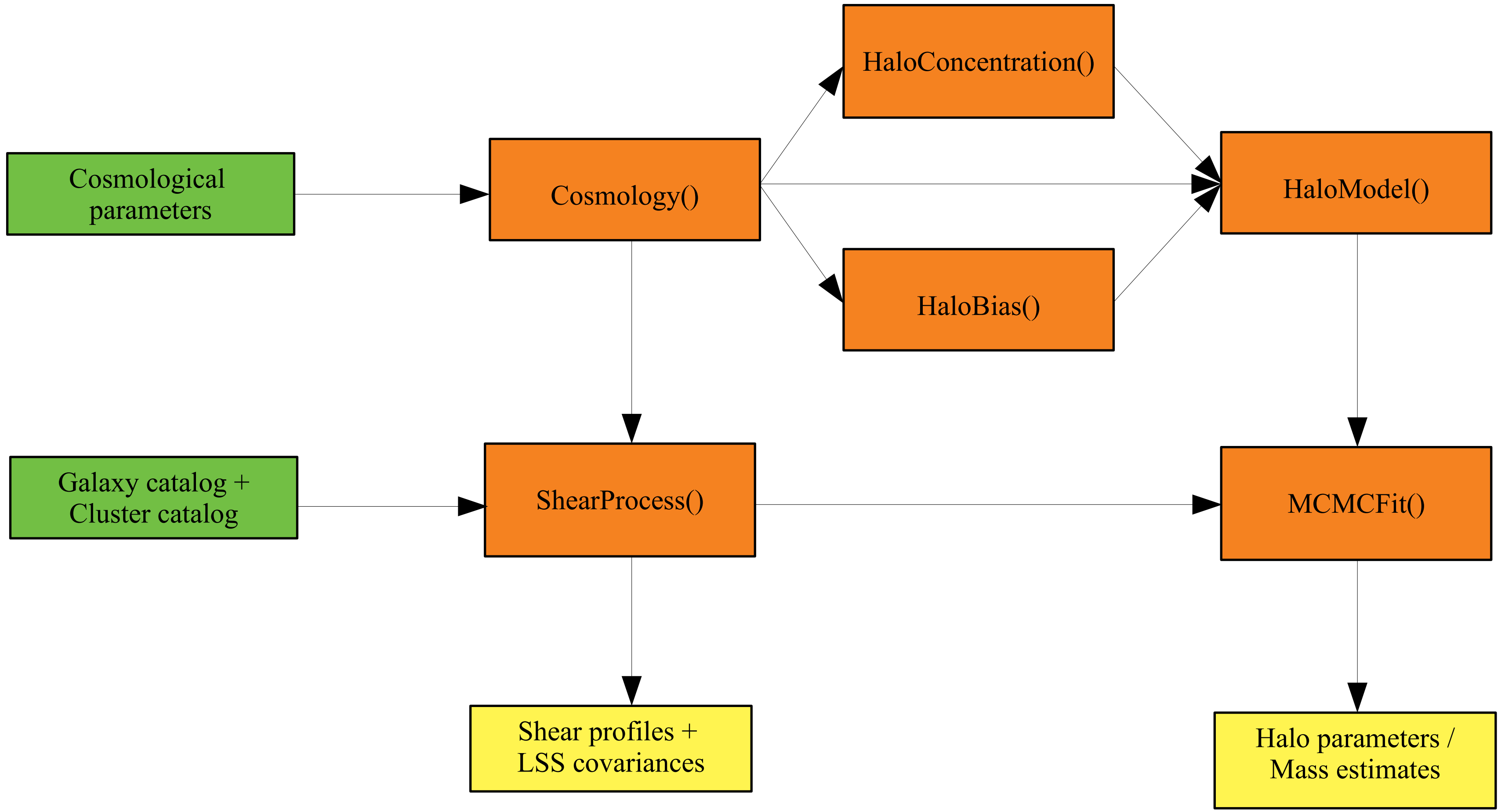

FIGURE 4.4: The skeleton of COMB-CL prototype. The diagram shows the different classes interfering in COMB-CL and the dependencies that connect them.

4.2.4 LSS covariance

As discussed in the previous sections, COMB-CL returns shear profiles of individual lenses. Therefore, it is crucial to estimate properly the statistical and systematic fluctuations recovered in the shear measurements. While the covariance terms were computed by bootstrapping the sources over a population of KiDS clusters in the stacked WL analysis, this method to estimate the statistical noise is less significant over a single galaxy cluster. Indeed, line of sight structures that are not physically linked to the cluster affect its lensing signal. As no random signal can be measured when considering an isolated lens, it is difficult to assess the uncorrelated large-scale structure impacts in the shears with simple bootstraps. Instead we prefer to model this effect using the convergence matter power spectrum as defined in Equation (2.32) as (see Schneider et al., 1998; Hoekstra, 2003):

$$C_{ij} = 2\pi\Sigma_{cr}^2 \int P_\kappa(l) g_i(l) g_j(l) dl \ . \tag{4.1}$$

The function g_i filters the signal between the angular boundaries θ_1, θ_2 of the i-*th* radial bin (Sereno et al., 2018):

$$g(l) = \frac{1}{\pi(\theta_1^2 - \theta_2^2) l} \left[\frac{2}{l} (J_0(l\theta_2) - J_0(l\theta_1)) + \theta_2 J_1(l\theta_2) - \theta_1 J_1(l\theta_1) \right] \ , \tag{4.2}$$

where J_0 and J_1 are the spherical Bessel functions of the first kind of order 0 and 1, respectively.

In addition to this estimate, we consider the variance terms defined as in Equation (3.16) to contribute to the statistical noise of the profiles of single galaxy clusters. For example, we show in Figure 4.5 the correlation matrices as computed in Equation (3.25). We see that the uncorrelated LSS terms contribute at large scales to the signal, while on the full profile the diagonal terms arising from the statistical variance dominate. With this method, we account both for the intrinsic scattering of the shear signal and the effects of the uncorrelated materials over the line of sight.

4.2.5 Development forecasts

COMB-CL is still a prototype and requires to be improved and tested again. Until now, COMB-CL is built to run on KiDS-DR3 data. In that respect, many development works remain to be done. For example, the source selection is suitable for KiDS-450, but novel selections should be implemented with future redshift and color measurements that Euclid will bring. In KiDS-DR3, the shear is only corrected with the multiplicative calibration factor, while Euclid shear correction will account for the additive calibration parameter as shown in Equation (3.1). Some of the dependencies should be removed, as they could not be validated by the EC maturity assessment process. Until now the module runs calling individually the python classes, while the EC community requires a command-line script to be run as part of the COMB-CL pipeline.

In the upcoming year, we are also interested to bring new implementations to the cosmological toolkit. Measurements of WL masses for individual galaxy clusters remain a priority, but stacking the shear density profiles over galaxy clusters could be a prominent additional feature for users that are interested in such stacked WL profiles. Therefore we will also develop the miscentering effect in the halo model routines and bootstrap covariance / cross-covariances in the shear process. Novel halo bias and halo concentration theoretical relations may be implemented in the

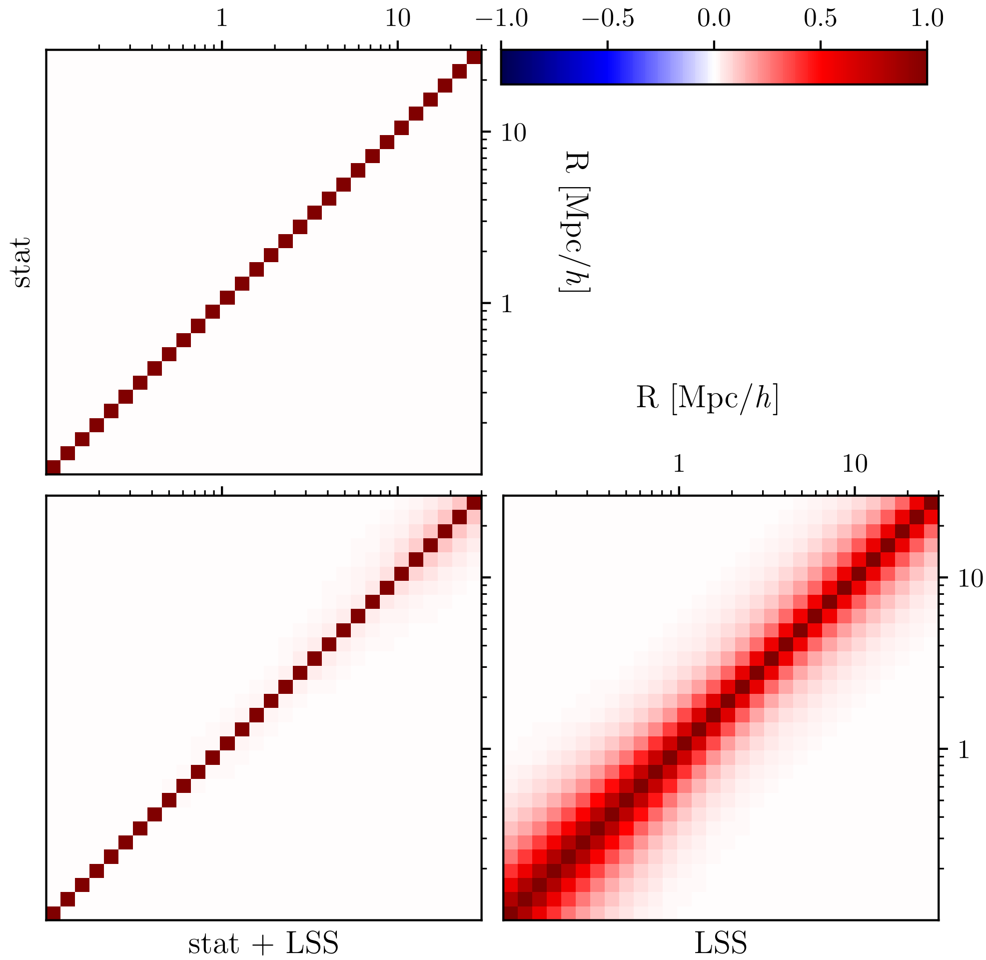

FIGURE 4.5: The statistical and uncorrelated LSS correlation matrix in COMB-CL on AMICO J000151.67-310934 cluster. The plot shows independently the two contributions (up and right) and the combined terms (left).

module following the last outcomes of the scientific community. The fitting process of the shear may be improved by replacing `emcee` with the `dynesty` python package to estimate Bayesian posteriors, which shows a higher efficiency by about 25% over a fixed sample size (Speagle, 2020). In addition, parallelizing the chains would improve the computational time of the MCMC run.

COMB-CL will be complete during the year 2022, with the validation of the KP-LE3-CL-2 paper. The idea of such a toolkit is that it is predominantly used for Euclid people, but also anyone interested in WL processing functions. Full accessibility of the package and clear documentation are keys for reaching as large as possible the scientific community. Some remaining works have to be completed on this domain since not all the processing functions are clearly detailed. Feedbacks of users are therefore relevant since they report many computational mistakes, unclear descriptions, or difficulties using COMB-CL.

Chapter 5

Conclusion

Observational cosmology is a wide field of research, that requires various methodological approaches. Weak gravitational lensing is a prominent and effective method to address challenging problems about the nature of dark matter and dark energy. It is particularly apt to study clusters of galaxies, considered crucial tracers of the matter distribution in the Universe. The work presented here is the result of a 3-years thesis work focused on the analysis of shear measurements in galaxy clusters from the KiDS data. In this final chapter, we summarize the problems addressed in the thesis and review the major results of our study. Finally, we will conclude with a personal discussion on the WL work presented here and with the broad perspectives on the next short and long terms goals in this research domain.

5.1 Summary

In Chapter 1, we introduced the cosmological framework of our analysis. The Universe has always been a source of curiosity, and inquiring minds have produced many models across history to better understand its origin and its evolution. The present-day standard cosmological model remarkably matches recent observations. It assumes a homogeneous and isotropic fluid in expansion but requires two enigmatic components, dark matter and dark energy. Knowledge of the cosmological parameters is crucial since they characterize the dark components of the model. These parameters of the standard model allow us to describe the geometry and the contents of the Universe and thus better grasp the cosmological distances. With this description, we should recover a very smoothed Universe. However, we observe today matter organized in a large cosmic web in the large-scale structure. The main hypothesis to explain this observation is the idea that small inhomogeneities recovered in the early stages of the Universe evolved and amplified by many orders of magnitude, from the quantum scales to the present-day large scales. As provided by many cosmological simulations with the non-linear scenario, matter assembles in overdense regions called halos. Massive halos are coupled with clusters of galaxies, objects mostly composed of dark matter. Therefore, observing galaxy clusters gives significant clues on the distribution of matter in the Universe, although they trace it in a biased way. The connection between clusters and matter distribution is well described by the so-called halo bias parameter.

In Chapter 2, we discussed the theoretical foundations of weak gravitational lensing. Since galaxy clusters are composed mostly of a dark component, gravitational lensing is an adequate method to derive the distribution of invisible matter. It takes advantage of the deflection of a background object's light, the source, by a massive foreground object, the lens. This effect arises from general relativity and is described with the deflection potential of the lens. It induces a deformation of the apparent source shape characterized by shear and convergence parameters. In the weak gravitational field regime, the shear is statistically equivalent to the source ellipticity, which is a powerful method to measure the density profile of the lens. For more extended lenses, such as the whole large-scale structure, the distribution of matter toward the line of sight is well described by the convergence matter power spectrum. Around the halos, we can model the density distribution accounting for a combination of matter terms acting at different scales. The one-halo term describes the density of the main component, the halo. An accurate description is provided by a NFW profile and by its truncated version, the BMO profile. The miscentering effect contributes to the displacement of the center of the halo. The two-halo term originates from the contribution of correlated matter, mainly distributed in distinct pairs of halos. The main parameters of this model are the halo mass, halo concentration, and halo bias. The last two parameters are directly related to the halo mass, as shown by numerous dark matter simulations on cosmological scales.

In Chapter 3, we analyzed the KiDS-DR3 data as presented in Ingoglia et al. (2022). The ESO public survey provides a large sources catalog, the KiDS-450 galaxies, combined with a lens catalog, the AMICO clusters. We processed the lensing signal first by selecting the sources related to each gravitational lens. We relied on a combination of photometric redshifts and color-color selections to discriminate the foreground and background objects. This selection has been tested with external data set to quantify its efficiency. We then stacked the ellipticity of the sources over radial bins on scales sufficiently large to be sensitive to the halo bias. This signal is also stacked over clusters redshift and richness bins to improve the statistical efficiency of the lensing measurements. We estimated the statistical error of the shear using a bootstrap covariance matrix across the radial profile, which showed significant diagonal terms and negligible off-diagonal terms. The systematic effects are accounted for by measuring the signal around random lenses, and removed from the final stacked profiles. Using a common Bayesian MCMC method with linear priors, we constrained the halo parameters with a BMO miscentered profile and a linear two-halo term. Results are shown in Table 3.3. The mass measurements and their relation with the richness of AMICO clusters are in remarkable agreement with previous stacked WL analyses completed on the same data set. In addition to the analysis detailed in the published paper, we also presented the novel outcomes on the cluster sparsity. We assessed the scaling relation between the mass and the concentration and found consistent results with the theoretical predictions. The mass-bias relation is the central purpose of the study, as it allows cosmological inference using theoretical relations. At this aim, we measured the normalization parameter of the matter power spectrum, σ_8, assuming a constant matter density parameter, $\Omega_{\rm m} = 0.3$. The fitted relations are in agreement with the bias data, and the constraints on σ_8 present a consistency we alternative studies that measured this cosmological parameter with a fixed matter density.

In Chapter 4, we described the COMB-CL python toolkit we have built within the Euclid collaboration. Euclid is an ESA space telescope aiming to be launched in 2023. The collaboration is organized in a large consortium of international institutes whose main goal at the moment is to prepare the tools for the scientific exploitation of the large data set. Euclid observations will allow building large catalogs of photometric and spectroscopic data in the optical and near-infrared bands over a large fraction of the sky. The scientific treatment of the data is a major section of the mission and is organized in different levels of processing functions, from the reduction and calibration of the raw data to the production of scientific results. COMB-CL has an important role in the latest stage of this process. The purpose of the package is to measure WL masses of Euclid-detected clusters. To do so, COMB-CL inputs different sets of data derived from various processing units of Euclid. Mainly, it takes catalogs of sources and lenses and derives shear density profiles and mass estimates for each individual lens given a fiducial cosmological model. The python module is divided into several classes, from the basic cosmological routines to the MCMC fitting process. The code also provides covariance measurements to assess the systematic effect of the large-scale structure in the lensing signal. Currently, COMB-CL is a prototype, but it should be operational in the incoming year since it has been selected as one of the pre-launched KP-LE3-CL papers in Euclid.

5.2 Discussion

During the thesis, we addressed many issues related to the stacked WL analysis.

The choice of the appropriate color-color selection among the two selections presented in the paper has been the result of a long discussion because the contamination fraction on COSMOS sources is sensitively the same for the two selective criteria. It is only when COSMOS data are cross-matched with KiDS that we recover a non-negligible difference of contamination.

Another critical point was the choice of the multiplicative calibration parameter to correct the shear measurements. This has been performed for individual galaxy clusters, rather than for the population of clusters enclosed in the bin. Since this correction must be applied as an average quantity and the inner radial bins account for a small number of sources, this choice was well justified. On the other hand, averaging the multiplicative shear bias per galaxy cluster is a process already used in Bellagamba et al. (2019), while we removed the four inner radial bins where the error budget is dominated by statistical uncertainty.

We also discussed the bootstrap method to estimate the covariance components, as the matrix does not show any evidence of off-diagonal terms, as observed in Giocoli et al. (2021a), or with a jackknife process as in Melchior et al. (2017). Nevertheless, the results showed that this method is solid and sufficient for the statistical accuracy reached in our analysis.

As we combined the covariance matrices of AMICO lenses and random lenses, we were also addressed the possible overestimate of the statistical noise of the lensing, as suggested in Singh et al. (2017). As we propagate the statistical uncertainty resulting from a subtraction, we verified the contribution of the covariance of the random signal is smaller than that contributed by the clusters.

In Giocoli et al. (2021b), they provided a similar stacked WL analysis on AMICO clusters. They measured the shear profiles up to 35 Mpc/h and recovered consistent mass measurements with respect to Bellagamba et al. (2019) and our analysis. They defined a different binning scheme since the clusters amplitude as a binning property was favored, while we opted for richness. As a consequence, the scaling relation between the mass and the cluster richness differs from the relation with cluster amplitude. They also deeply investigated the impact of the truncation radius, while we performed a robust analysis of the covariances and cross-covariances and studied the effects of the lensing signal systematics in each patch of the field through the random signal. Both studies were carried out with independent numerical pipelines and followed a process of cross-validation among the KiDS collaboration.

Data analysis has been carried out with Fornax, the computing cluster at the Physics Department of the University Federico II of Naples. Since the numerical tools have been produced from scratch, the codes have been subject to tests and validations. For instance, we compared the lensing signal on PSZ2LenS galaxy clusters (Sereno et al., 2017) for single and stacked data, in order to make sure the selection methods and the stacking were processed correctly. On the other hand, we have tested the different terms of the halo density model with CBL (Marulli, Veropalumbo, and Moresco, 2016) and found consistent results.

In order to build COMB-CL, we rely the structure to `colossus` (Diemer, 2018). This module implements many cosmological routines used by COMB-CL and has been extensively used for checking procedures during the development of COMB-CL. The package also largely makes use of `astropy` (Astropy Collaboration et al., 2018), a python library that contains key functionality and common tools needed in astronomy and astrophysics.

5.3 Perspectives

The topics addressed in this thesis are centered on galaxy clusters WL measurements, but this observational method allows many applications for several cosmological studies. For example, we can play with the different terms and parameters composing the halo density model to investigate a specific feature of the halo. Alternatively, the process of stacking shear data allows many possibilities of study, whether the lensing signal is computed on single lenses or a population of lenses.

The method can be improved, for example with the estimation of surface critical density, by relying on the PDF of the source redshift detection to calculate the average of the inverse parameter for each individual lens:

$$\langle \Sigma_{\rm cr}^{-1} \rangle = \int {\rm d}z_{\rm s} {\rm p}(z_{\rm s}) \Sigma_{\rm cr}^{-1}(z_{\rm s}) \ . \tag{5.1}$$

However, this process requires high-probability tails of the source redshift PDFs, which is not generally the case for large surveys.

Contaminated sources are known to dilute the lensing signal. This dilution can be corrected from the stacked density profile around random positions, but it is also well corrected with the boost factor. Boost factor can be used to compensate the halo density model (e.g. McClintock et al., 2019), or to boost the stacked shear profile (e.g. Medezinski et al., 2018).

Another analysis to explore is the combined inference on σ_8 with $\Omega_{\rm m}$ to constrain the parameter $S_8 \equiv \sigma_8 \sqrt{\Omega_{\rm m}/0.3}$, which would complement the study on σ_8 in Ingoglia et al. (2022) and $\Omega_{\rm m}$ in Giocoli et al. (2021b).

The methodology used in this work will constitute a baseline for future KiDS Data Releases (Kuijken et al., 2019). The fourth release for galaxy shear measurements is already available, and AMICO clusters on this data release are being selected. This will allow an important step forward, as the DR4 includes a 9-band *ugriZYJHK* source catalog from a sky region of about 1000 deg^2, more than the double of DR3.

The HSC survey is now providing its third data release (Aihara et al., 2021), including 600 square degrees of deep multi-color data. This large catalog of data provides the opportunity to run the Euclid cluster cosmology pipeline and operates COMB-CL to measure WL masses. We will also extend the method on similar but larger data sets that combine cluster and shear catalogs.

We have seen that the Euclid survey will manage quantitative and qualitative observations, but we can also rely on Large Synoptic Survey Telescope (LSST, LSST Dark Energy Science Collaboration, 2012) data. LSST will provide high statistics catalogs over a wide and deep field (FoV $\sim 20,000$ deg^2 and $r \sim 27.5$) in 6 photometric bands accounting for about 4 billion sources. These data sets will be fundamental for the study of the halo properties such as mass and bias with stacked WL analyses and will allow robust estimates of the main cosmological parameters.

Finally, the COMB-CL team is continuing its activity and within the next months, results will be present in the publication of the KP-LE3-CL-2 paper on the characterization of the properties of detected galaxy clusters. Large and intensive usage of the SGS pipeline will be performed on Euclid data releases and will permit the spreading of the application of WL lensing tools such as COMB-CL. When the package will be publicly available to the scientific community, it will require maintenance works and novel implementations with the numerical progress of the breakthroughs on observational cosmology.

Bibliography

Adami, C. et al. (Mar. 2013). "Diffuse light in the young cluster of galaxies CL J1449+0856 at z = 2.07". In: *A&A* 551, A20, A20. DOI: 10.1051/0004-6361/201220282. arXiv: 1212.6158 [astro-ph.CO].

Aihara, Hiroaki et al. (Aug. 2021). "Third Data Release of the Hyper Suprime-Cam Subaru Strategic Program". In: *arXiv e-prints*, arXiv:2108.13045, arXiv:2108.13045. arXiv: 2108.13045 [astro-ph.IM].

Amendola, Luca et al. (Apr. 2018). "Cosmology and fundamental physics with the Euclid satellite". In: *Living Reviews in Relativity* 21.1, 2, p. 2. DOI: 10.1007/s41114-017-0010-3. arXiv: 1606.00180 [astro-ph.CO].

Angelinelli, M. et al. (Apr. 2020). "Turbulent pressure support and hydrostatic mass bias in the intracluster medium". In: *MNRAS* 495.1, pp. 864–885. DOI: 10.1093/mnras/staa975. arXiv: 1905.04896 [astro-ph.CO].

Asgari, Marika et al. (Jan. 2021). "KiDS-1000 cosmology: Cosmic shear constraints and comparison between two point statistics". In: *A&A* 645, A104, A104. DOI: 10.1051/0004-6361/202039070. arXiv: 2007.15633 [astro-ph.CO].

Astropy Collaboration et al. (Sept. 2018). "The Astropy Project: Building an Open-science Project and Status of the v2.0 Core Package". In: *AJ* 156.3, 123, p. 123. DOI: 10.3847/1538-3881/aabc4f. arXiv: 1801.02634 [astro-ph.IM].

Balmès, I. et al. (Jan. 2014). "Imprints of dark energy on cosmic structure formation - III. Sparsity of dark matter halo profiles". In: *MNRAS* 437.3, pp. 2328–2339. DOI: 10.1093/mnras/stt2050. arXiv: 1307.2922 [astro-ph.CO].

Baltz, Edward A., Phil Marshall, and Masamune Oguri (Jan. 2009). "Analytic models of plausible gravitational lens potentials". In: *J. Cosmology Astropart. Phys.* 2009.1, 015, p. 015. DOI: 10.1088/1475-7516/2009/01/015. arXiv: 0705.0682 [astro-ph].

Bardeen, J. M. et al. (May 1986). "The Statistics of Peaks of Gaussian Random Fields". In: *ApJ* 304, p. 15. DOI: 10.1086/164143.

Bartelmann, M. and P. Schneider (Jan. 2001). "Weak gravitational lensing". In: *Phys. Rep.* 340.4-5, pp. 291–472. DOI: 10.1016/S0370-1573(00)00082-X. arXiv: astro-ph/9912508 [astro-ph].

Bartelmann, Matthias (Dec. 2010). "TOPICAL REVIEW Gravitational lensing". In: *Classical and Quantum Gravity* 27.23, 233001, p. 233001. DOI: 10.1088/0264-9381/27/23/233001. arXiv: 1010.3829 [astro-ph.CO].

Becker, Matthew R. and Andrey V. Kravtsov (Oct. 2011). "On the Accuracy of Weak-lensing Cluster Mass Reconstructions". In: *ApJ* 740.1, 25, p. 25. DOI: 10.1088/0004-637X/740/1/25. arXiv: 1011.1681 [astro-ph.CO].

Begeman, K. et al. (Jan. 2013). "The Astro-WISE datacentric information system". In: *Experimental Astronomy* 35.1-2, pp. 1–23. DOI: 10.1007/s10686-012-9311-4. arXiv: 1208.0447 [astro-ph.IM].

Bellagamba, F. et al. (May 2011). "Optimal filtering of optical and weak lensing data to search for galaxy clusters: application to the COSMOS field". In: *mnras* 413, pp. 1145–1157. DOI: 10.1111/j.1365-2966.2011.18202.x. arXiv: 1006.0610.

Bellagamba, Fabio et al. (Feb. 2018). “AMICO: optimized detection of galaxy clusters in photometric surveys”. In: *MNRAS* 473.4, pp. 5221–5236. DOI: 10.1093/mnras/stx2701. arXiv: 1705.03029 [astro-ph.CO].

Bellagamba, Fabio et al. (Apr. 2019). “AMICO galaxy clusters in KiDS-DR3: weak lensing mass calibration”. In: *MNRAS* 484.2, pp. 1598–1615. DOI: 10.1093/mnras/stz090. arXiv: 1810.02827 [astro-ph.CO].

Benítez, Narciso (June 2000). “Bayesian Photometric Redshift Estimation”. In: *ApJ* 536.2, pp. 571–583. DOI: 10.1086/308947. arXiv: astro-ph/9811189 [astro-ph].

Bernardeau, F. et al. (Sept. 2002). “Large-scale structure of the Universe and cosmological perturbation theory”. In: *Phys. Rep.* 367.1-3, pp. 1–248. DOI: 10.1016/S0370-1573(02)00135-7. arXiv: astro-ph/0112551 [astro-ph].

Bhattacharya, Suman et al. (May 2011). “Mass Function Predictions Beyond ΛCDM”. In: *ApJ* 732.2, 122, p. 122. DOI: 10.1088/0004-637X/732/2/122. arXiv: 1005.2239 [astro-ph.CO].

Bhattacharya, Suman et al. (Mar. 2013). “Dark Matter Halo Profiles of Massive Clusters: Theory versus Observations”. In: *ApJ* 766.1, 32, p. 32. DOI: 10.1088/0004-637X/766/1/32. arXiv: 1112.5479 [astro-ph.CO].

Bocquet, S. et al. (June 2019). “Cluster Cosmology Constraints from the 2500 deg^2 SPT-SZ Survey: Inclusion of Weak Gravitational Lensing Data from Magellan and the Hubble Space Telescope”. In: *ApJ* 878.1, 55, p. 55. DOI: 10.3847/1538-4357/ab1f10. arXiv: 1812.01679 [astro-ph.CO].

Bond, J. Richard, Lev Kofman, and Dmitry Pogosyan (Apr. 1996). “How filaments of galaxies are woven into the cosmic web”. In: *Nature* 380.6575, pp. 603–606. DOI: 10.1038/380603a0. arXiv: astro-ph/9512141 [astro-ph].

Borgani, S. (2008). “Cosmology with Clusters of Galaxies”. In: *A Pan-Chromatic View of Clusters of Galaxies and the Large-Scale Structure*. Vol. 740. Springer Netherlands, p. 24. DOI: 10.1007/978-1-4020-6941-3_9.

Broadhurst, T. et al. (2005). “The Surprisingly Steep Mass Profile of A1689, from a Lensing Analysis of Subaru Images”. In: *The Astrophysical Journal Letters* 619.2, p. L143. URL: http://stacks.iop.org/1538-4357/619/i=2/a=L143.

Broadhurst, Tom et al. (Sept. 2008). “Comparison of Cluster Lensing Profiles with ΛCDM Predictions”. In: *ApJ* 685.1, p. L9. DOI: 10.1086/592400. arXiv: 0805.2617 [astro-ph].

Bruzual, G. and S. Charlot (Oct. 2003). “Stellar population synthesis at the resolution of 2003”. In: *MNRAS* 344.4, pp. 1000–1028. DOI: 10.1046/j.1365-8711.2003.06897.x. arXiv: astro-ph/0309134 [astro-ph].

Bullock, J. S. et al. (Mar. 2001). “Profiles of dark haloes: evolution, scatter and environment”. In: *MNRAS* 321.3, pp. 559–575. DOI: 10.1046/j.1365-8711.2001.04068.x. arXiv: astro-ph/9908159 [astro-ph].

Burbidge, E. Margaret et al. (Jan. 1957). “Synthesis of the Elements in Stars”. In: *Reviews of Modern Physics* 29.4, pp. 547–650. DOI: 10.1103/RevModPhys.29.547.

Capaccioli, M. and P. Schipani (Dec. 2011). “The VLT Survey Telescope Opens to the Sky: History of a Commissioning”. In: *The Messenger* 146, pp. 2–7.

Child, Hillary L. et al. (May 2018). “Halo Profiles and the Concentration-Mass Relation for a ΛCDM Universe”. In: *ApJ* 859.1, 55, p. 55. DOI: 10.3847/1538-4357/aabf95. arXiv: 1804.10199 [astro-ph.CO].

Codis, Sandrine (Dec. 2016). “Nuisance parameters for large galaxy surveys”. In: *arXiv e-prints*, arXiv:1612.06873, arXiv:1612.06873. arXiv: 1612.06873 [astro-ph.CO].

Coe, Dan et al. (Sept. 2012). “CLASH: Precise New Constraints on the Mass Profile of the Galaxy Cluster A2261”. In: *ApJ* 757.1, 22, p. 22. DOI: 10.1088/0004-637X/757/1/22. arXiv: 1201.1616 [astro-ph.CO].

Colless, Matthew et al. (Dec. 2001). "The 2dF Galaxy Redshift Survey: spectra and redshifts". In: *MNRAS* 328.4, pp. 1039–1063. DOI: 10.1046/j.1365-8711.2001.04902.x. arXiv: astro-ph/0106498 [astro-ph].

Corasaniti, Pier Stefano and Yann Rasera (Aug. 2019). "Average dark matter halo sparsity relations as consistency check of mass estimates in galaxy cluster samples". In: *MNRAS* 487.3, pp. 4382–4392. DOI: 10.1093/mnras/stz1579. arXiv: 1906.02259 [astro-ph.CO].

Corasaniti, Pier-Stefano, Mauro Sereno, and Stefano Ettori (Apr. 2021). "Cosmological Constraints from Galaxy Cluster Sparsity, Cluster Gas Mass Fraction, and Baryon Acoustic Oscillation Data". In: *ApJ* 911.2, 82, p. 82. DOI: 10.3847/1538-4357/abe9a4. arXiv: 2103.03283 [astro-ph.CO].

Costanzi, M. et al. (Oct. 2019). "Methods for cluster cosmology and application to the SDSS in preparation for DES Year 1 release". In: *MNRAS* 488.4, pp. 4779–4800. DOI: 10.1093/mnras/stz1949. arXiv: 1810.09456 [astro-ph.CO].

Covone, G. et al. (Apr. 2014). "Measurement of the Halo Bias from Stacked Shear Profiles of Galaxy Clusters". In: *apjl* 784, L25, p. L25. DOI: 10.1088/2041-8205/784/2/L25. arXiv: 1402.4815.

Cui, Weiguang et al. (Nov. 2018). "The Three Hundred project: a large catalogue of theoretically modelled galaxy clusters for cosmological and astrophysical applications". In: *MNRAS* 480.3, pp. 2898–2915. DOI: 10.1093/mnras/sty2111. arXiv: 1809.04622 [astro-ph.GA].

de Jong, J. T. A. et al. (Jan. 2013). "The Kilo-Degree Survey". In: *Experimental Astronomy* 35, pp. 25–44. DOI: 10.1007/s10686-012-9306-1. arXiv: 1206.1254.

de Jong, Jelte T. A. et al. (Oct. 2015). "The first and second data releases of the Kilo-Degree Survey". In: *A&A* 582, A62, A62. DOI: 10.1051/0004-6361/201526601. arXiv: 1507.00742 [astro-ph.CO].

de Jong, Jelte T. A. et al. (Aug. 2017). "The third data release of the Kilo-Degree Survey and associated data products". In: *aap* 604, A134, A134. DOI: 10.1051/0004-6361/201730747. arXiv: 1703.02991 [astro-ph.GA].

de Lapparent, V., M. J. Geller, and J. P. Huchra (Mar. 1986). "A Slice of the Universe". In: *ApJ* 302, p. L1. DOI: 10.1086/184625.

de Sitter, W. (Nov. 1917). "Einstein's theory of gravitation and its astronomical consequences. Third paper". In: *mnras* 78, pp. 3–28. DOI: 10.1093/mnras/78.1.3.

DES Collaboration et al. (May 2021). "Dark Energy Survey Year 3 Results: Cosmological Constraints from Galaxy Clustering and Weak Lensing". In: *arXiv e-prints*, arXiv:2105.13549, arXiv:2105.13549. arXiv: 2105.13549 [astro-ph.CO].

Despali, G., C. Giocoli, and G. Tormen (Oct. 2014). "Some like it triaxial: the universality of dark matter halo shapes and their evolution along the cosmic time". In: *MNRAS* 443, pp. 3208–3217. DOI: 10.1093/mnras/stu1393. arXiv: 1404.6527.

Despali, G. et al. (Mar. 2016). "The universality of the virial halo mass function and models for non-universality of other halo definitions". In: *MNRAS* 456, pp. 2486–2504. DOI: 10.1093/mnras/stv2842. arXiv: 1507.05627.

Diemer, Benedikt (Dec. 2018). "COLOSSUS: A Python Toolkit for Cosmology, Large-scale Structure, and Dark Matter Halos". In: *ApJS* 239.2, 35, p. 35. DOI: 10.3847/1538-4365/aaee8c. arXiv: 1712.04512 [astro-ph.CO].

Diemer, Benedikt and Michael Joyce (Feb. 2019). "An Accurate Physical Model for Halo Concentrations". In: *ApJ* 871.2, 168, p. 168. DOI: 10.3847/1538-4357/aafad6. arXiv: 1809.07326 [astro-ph.CO].

Diemer, Benedikt and Andrey V. Kravtsov (Jan. 2015). "A Universal Model for Halo Concentrations". In: *ApJ* 799.1, 108, p. 108. DOI: 10.1088/0004-637X/799/1/108. arXiv: 1407.4730 [astro-ph.CO].

Donahue, M. et al. (Mar. 2016). "The Morphologies and Alignments of Gas, Mass, and the Central Galaxies of CLASH Clusters of Galaxies". In: *ApJ* 819, 36, p. 36. DOI: 10.3847/0004-637X/819/1/36. arXiv: 1601.04947.

Driver, S. P. et al. (May 2011). "Galaxy and Mass Assembly (GAMA): survey diagnostics and core data release". In: *MNRAS* 413, pp. 971–995. DOI: 10.1111/j.1365-2966.2010.18188.x. arXiv: 1009.0614.

Duffy, Alan R. et al. (Oct. 2008). "Dark matter halo concentrations in the Wilkinson Microwave Anisotropy Probe year 5 cosmology". In: *MNRAS* 390.1, pp. L64–L68. DOI: 10.1111/j.1745-3933.2008.00537.x. arXiv: 0804.2486 [astro-ph].

Dutton, Aaron A. and Andrea V. Macciò (July 2014). "Cold dark matter haloes in the Planck era: evolution of structural parameters for Einasto and NFW profiles". In: *MNRAS* 441.4, pp. 3359–3374. DOI: 10.1093/mnras/stu742. arXiv: 1402.7073 [astro-ph.CO].

Einstein, A. and W. de Sitter (Mar. 1932). "On the Relation between the Expansion and the Mean Density of the Universe". In: *Proceedings of the National Academy of Science* 18.3, pp. 213–214. DOI: 10.1073/pnas.18.3.213.

Einstein, Albert (Jan. 1915). "Zur allgemeinen Relativitätstheorie". In: *Sitzungsberichte der Königlich Preußischen Akademie der Wissenschaften (Berlin*, pp. 778–786.

Eisenstein, Daniel J. and Wayne Hu (Mar. 1998). "Baryonic Features in the Matter Transfer Function". In: *ApJ* 496.2, pp. 605–614. DOI: 10.1086/305424. arXiv: astro-ph/9709112 [astro-ph].

— (Jan. 1999). "Power Spectra for Cold Dark Matter and Its Variants". In: *ApJ* 511.1, pp. 5–15. DOI: 10.1086/306640. arXiv: astro-ph/9710252 [astro-ph].

Eisenstein, Daniel J. et al. (Nov. 2005). "Detection of the Baryon Acoustic Peak in the Large-Scale Correlation Function of SDSS Luminous Red Galaxies". In: *ApJ* 633.2, pp. 560–574. DOI: 10.1086/466512. arXiv: astro-ph/0501171 [astro-ph].

Erben, T. et al. (July 2005). "GaBoDS: The Garching-Bonn Deep Survey. IV. Methods for the image reduction of multi-chip cameras demonstrated on data from the ESO Wide-Field Imager". In: *Astronomische Nachrichten* 326.6, pp. 432–464. DOI: 10.1002/asna.200510396. arXiv: astro-ph/0501144 [astro-ph].

Etherington, I. M. H. (Jan. 1933). "On the Definition of Distance in General Relativity." In: *Philosophical Magazine* 15.18, p. 761.

Euclid Collaboration et al. (July 2019). "Euclid preparation. III. Galaxy cluster detection in the wide photometric survey, performance and algorithm selection". In: *A&A* 627, A23, A23. DOI: 10.1051/0004-6361/201935088. arXiv: 1906.04707 [astro-ph.CO].

Felten, J. E. et al. (Dec. 1966). "X-Rays from the Coma Cluster of Galaxies". In: *ApJ* 146, pp. 955–958. DOI: 10.1086/148972.

Fenech Conti, I. et al. (May 2017). "Calibration of weak-lensing shear in the Kilo-Degree Survey". In: *mnras* 467, pp. 1627–1651. DOI: 10.1093/mnras/stx200. arXiv: 1606.05337.

Foreman-Mackey, Daniel et al. (Mar. 2013). "emcee: The MCMC Hammer". In: *PASP* 125.925, p. 306. DOI: 10.1086/670067. arXiv: 1202.3665 [astro-ph.IM].

Friedmann, A. (Dec. 1924). "Über die Möglichkeit einer Welt mit konstanter negativer Krümmung des Raumes". In: *Zeitschrift fur Physik* 21.1, pp. 326–332. DOI: 10.1007/BF01328280.

Fuller, Wayne A. (1987). *Measurement error models.* Wiley-Interscience.

Geller, Margaret J. and John P. Huchra (Nov. 1989). "Mapping the Universe". In: *Science* 246.4932, pp. 897–903. DOI: 10.1126/science.246.4932.897.

Gelman, Andrew and Donald B. Rubin (Jan. 1992). “Inference from Iterative Simulation Using Multiple Sequences”. In: *Statistical Science* 7, pp. 457–472. DOI: 10.1214/ss/1177011136.

George, M. R. et al. (Sept. 2012). “Galaxies in X-Ray Groups. II. A Weak Lensing Study of Halo Centering”. In: *apj* 757, 2, p. 2. DOI: 10.1088/0004-637X/757/1/2. arXiv: 1205.4262 [astro-ph.CO].

Giocoli, C., G. Tormen, and R. K. Sheth (May 2012). “Formation times, mass growth histories and concentrations of dark matter haloes”. In: *MNRAS* 422, pp. 185–198. DOI: 10.1111/j.1365-2966.2012.20594.x. arXiv: 1111.6977 [astro-ph.CO].

Giocoli, C. et al. (Oct. 2010a). “Halo model description of the non-linear dark matter power spectrum at k $\gg$ 1Mpc^{-1}”. In: *MNRAS* 408, pp. 300–313. DOI: 10.1111/j.1365-2966.2010.17108.x. arXiv: 1003.4740 [astro-ph.CO].

Giocoli, C. et al. (May 2010b). “The substructure hierarchy in dark matter haloes”. In: *MNRAS* 404, pp. 502–517. DOI: 10.1111/j.1365-2966.2010.16311.x. arXiv: 0911.0436.

Giocoli, Carlo et al. (Mar. 2021b). “AMICO galaxy clusters in KiDS-DR3: cosmological constraints from large-scale stacked weak lensing profiles”. In: *arXiv e-prints*, arXiv:2103.05653, arXiv:2103.05653. arXiv: 2103.05653 [astro-ph.CO].

— (Sept. 2021a). “AMICO galaxy clusters in KiDS-DR3. Cosmological constraints from large-scale stacked weak lensing profiles”. In: *A&A* 653, A19, A19. DOI: 10.1051/0004-6361/202140795. arXiv: 2103.05653 [astro-ph.CO].

Gobat, R. et al. (Feb. 2011). “A mature cluster with X-ray emission at z = 2.07”. In: *A&A* 526, A133, A133. DOI: 10.1051/0004-6361/201016084. arXiv: 1011.1837 [astro-ph.CO].

Golse, G. and J. P. Kneib (Aug. 2002). “Pseudo elliptical lensing mass model: Application to the NFW mass distribution”. In: *A&A* 390, pp. 821–827. DOI: 10.1051/0004-6361:20020639. arXiv: astro-ph/0112138 [astro-ph].

Gonzalez, A. (July 2014). “Cluster detection via wavelets”. In: *Building the Euclid Cluster Survey - Scientific Program*, p. 7.

Goodman, Jonathan and Jonathan Weare (Jan. 2010). “Ensemble samplers with affine invariance”. In: *Communications in Applied Mathematics and Computational Science* 5.1, pp. 65–80. DOI: 10.2140/camcos.2010.5.65.

Gruen, D. et al. (Sept. 2011). “Optimizing weak lensing mass estimates for cluster profile uncertainty”. In: *MNRAS* 416.2, pp. 1392–1400. DOI: 10.1111/j.1365-2966.2011.19135.x. arXiv: 1104.2596 [astro-ph.CO].

Gruen, D. et al. (June 2015). “Cosmic variance of the galaxy cluster weak lensing signal”. In: *MNRAS* 449.4, pp. 4264–4276. DOI: 10.1093/mnras/stv532. arXiv: 1501.01632 [astro-ph.CO].

Gunn, James E. and III Gott J. Richard (Aug. 1972). “On the Infall of Matter Into Clusters of Galaxies and Some Effects on Their Evolution”. In: *ApJ* 176, p. 1. DOI: 10.1086/151605.

Gursky, H. et al. (Aug. 1971). “A Strong X-Ray Source in the Coma Cluster Observed by UHURU”. In: *ApJ* 167, p. L81. DOI: 10.1086/180765.

Hamana, Takashi et al. (Oct. 2013). “Toward Understanding the Anisotropic Point Spread Function of Suprime-Cam and Its Impact on Cosmic Shear Measurement”. In: *PASJ* 65, 104, p. 104. DOI: 10.1093/pasj/65.5.104. arXiv: 1304.4992 [astro-ph.IM].

Hamilton, A. J. S. et al. (June 1991). “Reconstructing the Primordial Spectrum of Fluctuations of the Universe from the Observed Nonlinear Clustering of Galaxies”. In: *ApJ* 374, p. L1. DOI: 10.1086/186057.

Harrison, E. R. (May 1970). "Fluctuations at the Threshold of Classical Cosmology". In: *Phys. Rev. D* 1.10, pp. 2726–2730. DOI: 10.1103/PhysRevD.1.2726.
Hayashi, Eric et al. (Feb. 2003). "The Structural Evolution of Substructure". In: *ApJ* 584.2, pp. 541–558. DOI: 10.1086/345788. arXiv: astro-ph/0203004 [astro-ph].
Hennig, C. et al. (June 2017). "Galaxy populations in massive galaxy clusters to z = 1.1: colour distribution, concentration, halo occupation number and red sequence fraction". In: *MNRAS* 467.4, pp. 4015–4035. DOI: 10.1093/mnras/stx175. arXiv: 1604.00988 [astro-ph.GA].
Heymans, C. et al. (Nov. 2012). "CFHTLenS: the Canada-France-Hawaii Telescope Lensing Survey". In: *mnras* 427, pp. 146–166. DOI: 10.1111/j.1365-2966.2012.21952.x. arXiv: 1210.0032.
Hikage, Chiaki et al. (Apr. 2019). "Cosmology from cosmic shear power spectra with Subaru Hyper Suprime-Cam first-year data". In: *PASJ* 71.2, 43, p. 43. DOI: 10.1093/pasj/psz010. arXiv: 1809.09148 [astro-ph.CO].
Hildebrandt, H. et al. (Nov. 2010). "PHAT: PHoto-z Accuracy Testing". In: *A&A* 523, A31, A31. DOI: 10.1051/0004-6361/201014885. arXiv: 1008.0658 [astro-ph.CO].
Hildebrandt, H. et al. (Apr. 2012). "CFHTLenS: improving the quality of photometric redshifts with precision photometry". In: *mnras* 421, pp. 2355–2367. DOI: 10.1111/j.1365-2966.2012.20468.x. arXiv: 1111.4434.
Hildebrandt, H. et al. (Feb. 2017). "KiDS-450: cosmological parameter constraints from tomographic weak gravitational lensing". In: *mnras* 465, pp. 1454–1498. DOI: 10.1093/mnras/stw2805. arXiv: 1606.05338.
Hinshaw, G. et al. (Oct. 2013). "Nine-year Wilkinson Microwave Anisotropy Probe (WMAP) Observations: Cosmological Parameter Results". In: *ApJS* 208.2, 19, p. 19. DOI: 10.1088/0067-0049/208/2/19. arXiv: 1212.5226 [astro-ph.CO].
Hoekstra, H. (May 2001). "The effect of distant large scale structure on weak lensing mass estimates". In: *A&A* 370, pp. 743–753. DOI: 10.1051/0004-6361:20010293. arXiv: astro-ph/0102368 [astro-ph].
Hoekstra, H. et al. (Jan. 2011). "The Mass-L_X Relation for Moderate Luminosity X-ray Clusters". In: *apj* 726, 48, p. 48. DOI: 10.1088/0004-637X/726/1/48. arXiv: 1011.0549.
Hoekstra, Henk (Mar. 2003). "How well can we determine cluster mass profiles from weak lensing?" In: *MNRAS* 339.4, pp. 1155–1162. DOI: 10.1046/j.1365-8711.2003.06264.x. arXiv: astro-ph/0208351 [astro-ph].
Hubble, Edwin (Mar. 1929). "A Relation between Distance and Radial Velocity among Extra-Galactic Nebulae". In: *Proceedings of the National Academy of Science* 15.3, pp. 168–173. DOI: 10.1073/pnas.15.3.168.
Ilbert, O. et al. (Jan. 2009). "Cosmos Photometric Redshifts with 30-Bands for 2-deg^2". In: *apj* 690, pp. 1236–1249. DOI: 10.1088/0004-637X/690/2/1236. arXiv: 0809.2101.
Ingoglia, Lorenzo et al. (Jan. 2022). "AMICO galaxy clusters in KiDS-DR3: Measurement of the halo bias and power spectrum normalization from a stacked weak lensing analysis". In: *arXiv e-prints*, arXiv:2201.01545, arXiv:2201.01545. arXiv: 2201.01545 [astro-ph.CO].
Ishiyama, Tomoaki et al. (July 2020). "The Uchuu Simulations: Data Release 1 and Dark Matter Halo Concentrations". In: *arXiv e-prints*, arXiv:2007.14720, arXiv:2007.14720. arXiv: 2007.14720 [astro-ph.CO].
Johnston, D. E. et al. (Feb. 2007a). "Cross-Correlation Lensing: Determining Galaxy and Cluster Mass Profiles from Statistical Weak-Lensing Measurements". In: *apj* 656, pp. 27–41. DOI: 10.1086/510060. eprint: astro-ph/0507467.

Johnston, David E. et al. (Sept. 2007b). "Cross-correlation Weak Lensing of SDSS galaxy Clusters II: Cluster Density Profiles and the Mass–Richness Relation". In: *arXiv e-prints*, arXiv:0709.1159, arXiv:0709.1159. arXiv: 0709.1159 [astro-ph].

Kaiser, N. (Sept. 1984). "On the spatial correlations of Abell clusters." In: *ApJ* 284, pp. L9–L12. DOI: 10.1086/184341.

Kilbinger, Martin (July 2015). "Cosmology with cosmic shear observations: a review". In: *Reports on Progress in Physics* 78.8, 086901, p. 086901. DOI: 10.1088/0034-4885/78/8/086901. arXiv: 1411.0115 [astro-ph.CO].

Kitching, T. D. et al. (Oct. 2008). "Bayesian galaxy shape measurement for weak lensing surveys - II. Application to simulations". In: *MNRAS* 390.1, pp. 149–167. DOI: 10.1111/j.1365-2966.2008.13628.x. arXiv: 0802.1528 [astro-ph].

Kotulla, Ralf et al. (June 2009). "GALEV evolutionary synthesis models - I. Code, input physics and web interface". In: *MNRAS* 396.1, pp. 462–484. DOI: 10.1111/j.1365-2966.2009.14717.x. arXiv: 0903.0378 [astro-ph.CO].

Kuijken, K. (Dec. 2011). "OmegaCAM: ESO's Newest Imager". In: *The Messenger* 146, pp. 8–11.

Kuijken, K. et al. (Dec. 2015). "Gravitational lensing analysis of the Kilo-Degree Survey". In: *mnras* 454, pp. 3500–3532. DOI: 10.1093/mnras/stv2140. arXiv: 1507.00738.

Kuijken, K. et al. (May 2019). "The fourth data release of the Kilo-Degree Survey: ugri imaging and nine-band optical-IR photometry over 1000 square degrees". In: *A&A* 625, A2, A2. DOI: 10.1051/0004-6361/201834918. arXiv: 1902.11265 [astro-ph.GA].

Lacey, C. and S. Cole (Dec. 1994). "Merger Rates in Hierarchical Models of Galaxy Formation - Part Two - Comparison with N-Body Simulations". In: *MNRAS* 271, p. 676. DOI: 10.1093/mnras/271.3.676. arXiv: astro-ph/9402069 [astro-ph].

Lacey, Cedric and Shaun Cole (June 1993). "Merger rates in hierarchical models of galaxy formation". In: *MNRAS* 262.3, pp. 627–649. DOI: 10.1093/mnras/262.3.627.

Laureijs, R. et al. (Oct. 2011). "Euclid Definition Study Report". In: *arXiv e-prints*, arXiv:1110.3193, arXiv:1110.3193. arXiv: 1110.3193 [astro-ph.CO].

Lemaitre, G. (Jan. 1926). "Note on de Sitter's Universe". In: *Publications du Laboratoire d'Astronomie et de Geodesie de l'Universite de Louvain* 2, pp. 37–41.

Lemaître, G. (Jan. 1927). "Un Univers homogène de masse constante et de rayon croissant rendant compte de la vitesse radiale des nébuleuses extra-galactiques". In: *Annales de la Société Scientifique de Bruxelles* 47, pp. 49–59.

Lesci, G. F. et al. (Dec. 2020). "AMICO galaxy clusters in KiDS-DR3: cosmological constraints from counts and stacked weak-lensing". In: *arXiv e-prints*, arXiv:2012.12273, arXiv:2012.12273. arXiv: 2012.12273 [astro-ph.CO].

LSST Dark Energy Science Collaboration (Nov. 2012). "Large Synoptic Survey Telescope: Dark Energy Science Collaboration". In: *arXiv e-prints*, arXiv:1211.0310, arXiv:1211.0310. arXiv: 1211.0310 [astro-ph.CO].

Lynds, R. and V. Petrosian (Sept. 1986). "Giant Luminous Arcs in Galaxy Clusters". In: *Bulletin of the American Astronomical Society*. Vol. 18, p. 1014.

Mandelbaum, R. et al. (June 2013). "Cosmological parameter constraints from galaxy-galaxy lensing and galaxy clustering with the SDSS DR7". In: *mnras* 432, pp. 1544–1575. DOI: 10.1093/mnras/stt572. arXiv: 1207.1120.

Mandelbaum, Rachel et al. (Aug. 2005). "Systematic errors in weak lensing: application to SDSS galaxy-galaxy weak lensing". In: *MNRAS* 361.4, pp. 1287–1322. DOI: 10.1111/j.1365-2966.2005.09282.x. arXiv: astro-ph/0501201 [astro-ph].

Marulli, F., A. Veropalumbo, and M. Moresco (Jan. 2016). "CosmoBolognaLib: C++ libraries for cosmological calculations". In: *Astronomy and Computing* 14, pp. 35–42. DOI: 10.1016/j.ascom.2016.01.005. arXiv: 1511.00012 [astro-ph.CO].

Maturi, M. et al. (Nov. 2005). "An optimal filter for the detection of galaxy clusters through weak lensing". In: *aap* 442, pp. 851–860. DOI: 10.1051/0004-6361:20042600. eprint: astro-ph/0412604.

Maturi, Matteo et al. (May 2019). "AMICO galaxy clusters in KiDS-DR3: sample properties and selection function". In: *MNRAS* 485.1, pp. 498–512. DOI: 10.1093/mnras/stz294. arXiv: 1810.02811 [astro-ph.CO].

McClintock, T. et al. (Jan. 2019). "Dark Energy Survey Year 1 results: weak lensing mass calibration of redMaPPer galaxy clusters". In: *MNRAS* 482.1, pp. 1352–1378. DOI: 10.1093/mnras/sty2711. arXiv: 1805.00039 [astro-ph.CO].

Medezinski, E. et al. (July 2007). "Using Weak-Lensing Dilution to Improve Measurements of the Luminous and Dark Matter in A1689". In: *apj* 663, pp. 717–733. DOI: 10.1086/518638. eprint: astro-ph/0608499.

Medezinski, E. et al. (June 2010). "Detailed cluster mass and light profiles of A1703, A370 and RXJ1347-11 from deep Subaru imaging". In: *mnras* 405, pp. 257–273. DOI: 10.1111/j.1365-2966.2010.16491.x. arXiv: 0906.4791.

Medezinski, Elinor et al. (Jan. 2018). "Planck Sunyaev-Zel'dovich cluster mass calibration using Hyper Suprime-Cam weak lensing". In: *Publications of the Astronomical Society of Japan* 70, S28, S28. DOI: 10.1093/pasj/psx128. arXiv: 1706.00434 [astro-ph.CO].

Melchior, P. et al. (Aug. 2017). "Weak-lensing mass calibration of redMaPPer galaxy clusters in Dark Energy Survey Science Verification data". In: *mnras* 469, pp. 4899–4920. DOI: 10.1093/mnras/stx1053. arXiv: 1610.06890 [astro-ph.CO].

Meneghetti, M. et al. (May 2010). "Weighing simulated galaxy clusters using lensing and X-ray". In: *A&A* 514, A93, A93. DOI: 10.1051/0004-6361/200913222. arXiv: 0912.1343 [astro-ph.CO].

Meneghetti, M. et al. (Dec. 2014). "The MUSIC of CLASH: Predictions on the Concentration-Mass Relation". In: *ApJ* 797.1, 34, p. 34. DOI: 10.1088/0004-637X/797/1/34. arXiv: 1404.1384 [astro-ph.CO].

Merten, J. et al. (June 2015a). "CLASH: The Concentration-Mass Relation of Galaxy Clusters". In: *ApJ* 806.1, 4, p. 4. DOI: 10.1088/0004-637X/806/1/4. arXiv: 1404.1376 [astro-ph.CO].

Merten, J. et al. (June 2015b). "CLASH: The Concentration-Mass Relation of Galaxy Clusters". In: *ApJ* 806, 4, p. 4. DOI: 10.1088/0004-637X/806/1/4. arXiv: 1404.1376.

Metzler, Christopher A., Martin White, and Chris Loken (Feb. 2001). "The Effect of the Cosmic Web on Cluster Weak Lensing Mass Estimates". In: *ApJ* 547.2, pp. 560–573. DOI: 10.1086/318406. arXiv: astro-ph/0005442 [astro-ph].

Miller, L. et al. (Nov. 2007). "Bayesian galaxy shape measurement for weak lensing surveys - I. Methodology and a fast-fitting algorithm". In: *MNRAS* 382, pp. 315–324. DOI: 10.1111/j.1365-2966.2007.12363.x. arXiv: 0708.2340 [astro-ph].

Miller, L. et al. (Mar. 2013). "Bayesian galaxy shape measurement for weak lensing surveys - III. Application to the Canada-France-Hawaii Telescope Lensing Survey". In: *MNRAS* 429, pp. 2858–2880. DOI: 10.1093/mnras/sts454. arXiv: 1210.8201 [astro-ph.CO].

Miyatake, Hironao et al. (June 2015). "The Weak Lensing Signal and the Clustering of BOSS Galaxies. I. Measurements". In: *ApJ* 806.1, 1, p. 1. DOI: 10.1088/0004-637X/806/1/1. arXiv: 1311.1480 [astro-ph.CO].

Mo, H. J. and S. D. M. White (Sept. 1996). "An analytic model for the spatial clustering of dark matter haloes". In: *MNRAS* 282.2, pp. 347–361. DOI: 10.1093/mnras/282.2.347. arXiv: astro-ph/9512127 [astro-ph].

Nanni, F., F. Marulli L. Moscardini, and etc. Veropalumbo (in prep.). "AMICO galaxy clusters in KiDS-DR3: constraints on cosmological parameters and on the mass-richness relation from the clustering of galaxy clusters". in preparation.

Narayan, Ramesh and Matthias Bartelmann (June 1996). "Lectures on Gravitational Lensing". In: *arXiv e-prints*, astro-ph/9606001, astro–ph/9606001. arXiv: astro-ph/9606001 [astro-ph].

Navarro, Julio F., Carlos S. Frenk, and Simon D. M. White (May 1996). "The Structure of Cold Dark Matter Halos". In: *ApJ* 462, p. 563. DOI: 10.1086/177173. arXiv: astro-ph/9508025 [astro-ph].

— (Dec. 1997). "A Universal Density Profile from Hierarchical Clustering". In: *ApJ* 490.2, pp. 493–508. DOI: 10.1086/304888. arXiv: astro-ph/9611107 [astro-ph].

Neto, A. F. et al. (Nov. 2007). "The statistics of Λ CDM halo concentrations". In: *MNRAS* 381, pp. 1450–1462. DOI: 10.1111/j.1365-2966.2007.12381.x. eprint: arXiv:0706.2919.

Newton, Isaac (1687). *Philosophiae Naturalis Principia Mathematica. Auctore Js. Newton*. DOI: 10.3931/e-rara-440.

Oguri, Masamune and Takashi Hamana (July 2011). "Detailed cluster lensing profiles at large radii and the impact on cluster weak lensing studies". In: *MNRAS* 414.3, pp. 1851–1861. DOI: 10.1111/j.1365-2966.2011.18481.x. arXiv: 1101.0650 [astro-ph.CO].

Oguri, Masamune and Jounghun Lee (Nov. 2004). "A realistic model for spatial and mass distributions of dark halo substructures: An analytic approach". In: *MNRAS* 355.1, pp. 120–128. DOI: 10.1111/j.1365-2966.2004.08304.x. arXiv: astro-ph/0401628 [astro-ph].

Oguri, Masamune et al. (Oct. 2005). "Can the Steep Mass Profile of A1689 Be Explained by a Triaxial Dark Halo?" In: *The Astrophysical Journal* 632.2, pp. 841–846. DOI: 10.1086/452629. URL: https://doi.org/10.1086/452629.

Oguri, Masamune et al. (July 2009). "Subaru Weak Lensing Measurements of Four Strong Lensing Clusters: Are Lensing Clusters Overconcentrated?" In: *ApJ* 699.2, pp. 1038–1052. DOI: 10.1088/0004-637X/699/2/1038. arXiv: 0901.4372 [astro-ph.CO].

Oguri, Masamune et al. (Mar. 2012). "Combined strong and weak lensing analysis of 28 clusters from the Sloan Giant Arcs Survey". In: *MNRAS* 420.4, pp. 3213–3239. DOI: 10.1111/j.1365-2966.2011.20248.x. arXiv: 1109.2594 [astro-ph.CO].

Okabe, Nobuhiro et al. (June 2010). "LoCuSS: Subaru Weak Lensing Study of 30 Galaxy Clusters". In: *PASJ* 62, p. 811. DOI: 10.1093/pasj/62.3.811. arXiv: 0903.1103 [astro-ph.CO].

Okamoto, Takashi and Asao Habe (May 1999). "Formation and Evolution of Galactic Halos in Clusters of Galaxies". In: *ApJ* 516.2, pp. 591–603. DOI: 10.1086/307126. arXiv: astro-ph/9811362 [astro-ph].

Pasian, Fabio et al. (Sept. 2012). "Science ground segment for the ESA Euclid Mission". In: *Software and Cyberinfrastructure for Astronomy II*. Ed. by Nicole M. Radziwill and Gianluca Chiozzi. Vol. 8451. Society of Photo-Optical Instrumentation Engineers (SPIE) Conference Series, p. 845104. DOI: 10.1117/12.926026.

Peacock, J. A. and S. J. Dodds (June 1996). "Non-linear evolution of cosmological power spectra". In: *MNRAS* 280.3, pp. L19–L26. DOI: 10.1093/mnras/280.3.L19. arXiv: astro-ph/9603031 [astro-ph].

Peebles, P. J. E. (1980). *The large-scale structure of the universe.* Princeton University Press.

— (1993). *Principles of Physical Cosmology.* Princeton University Press.

Pen, Ue-Li et al. (Dec. 2003). "The three-dimensional power spectrum of dark and luminous matter from the VIRMOS-DESCART cosmic shear survey". In: *MNRAS* 346.3, pp. 994–1008. DOI: 10.1111/j.1365-2966.2003.07152.x. arXiv: astro-ph/0304512 [astro-ph].

Penzias, A. A. and R. W. Wilson (July 1965). "A Measurement of Excess Antenna Temperature at 4080 Mc/s." In: *ApJ* 142, pp. 419–421. DOI: 10.1086/148307.

Perlmutter, S. et al. (June 1999). "Measurements of Ω and Λ from 42 High-Redshift Supernovae". In: *ApJ* 517.2, pp. 565–586. DOI: 10.1086/307221. arXiv: astro-ph/9812133 [astro-ph].

Planck Collaboration et al. (Nov. 2014). "Planck 2013 results. XVI. Cosmological parameters". In: *A&A* 571, A16, A16. DOI: 10.1051/0004-6361/201321591. arXiv: 1303.5076 [astro-ph.CO].

Planck Collaboration et al. (Sept. 2016). "Planck 2015 results. XXVII. The second Planck catalogue of Sunyaev-Zeldovich sources". In: *A&A* 594, A27, A27. DOI: 10.1051/0004-6361/201525823. arXiv: 1502.01598 [astro-ph.CO].

Planck Collaboration et al. (Sept. 2020). "Planck 2018 results. VI. Cosmological parameters". In: *A&A* 641, A6, A6. DOI: 10.1051/0004-6361/201833910. arXiv: 1807.06209 [astro-ph.CO].

Postman, Marc et al. (Apr. 2012). "The Cluster Lensing and Supernova Survey with Hubble: An Overview". In: *ApJS* 199.2, 25, p. 25. DOI: 10.1088/0067-0049/199/2/25. arXiv: 1106.3328 [astro-ph.CO].

Pozzetti, L. et al. (May 2016). "Modelling the number density of Hα emitters for future spectroscopic near-IR space missions". In: *A&A* 590, A3, A3. DOI: 10.1051/0004-6361/201527081. arXiv: 1603.01453 [astro-ph.GA].

Press, William H. and Paul Schechter (Feb. 1974). "Formation of Galaxies and Clusters of Galaxies by Self-Similar Gravitational Condensation". In: *ApJ* 187, pp. 425–438. DOI: 10.1086/152650.

Radovich, M. et al. (Feb. 2017). "Searching for galaxy clusters in the Kilo-Degree Survey". In: *aap* 598, A107, A107. DOI: 10.1051/0004-6361/201629353. arXiv: 1701.02954 [astro-ph.CO].

Rasia, E., G. Tormen, and L. Moscardini (June 2004). "A dynamical model for the distribution of dark matter and gas in galaxy clusters". In: *MNRAS* 351, pp. 237–252. DOI: 10.1111/j.1365-2966.2004.07775.x. eprint: arXiv:astro-ph/0309405.

Rasia, E. et al. (July 2006). "Systematics in the X-ray cluster mass estimators". In: *MNRAS* 369, pp. 2013–2024. DOI: 10.1111/j.1365-2966.2006.10466.x. eprint: arXiv:astro-ph/0602434.

Riess, Adam G. et al. (Sept. 1998). "Observational Evidence from Supernovae for an Accelerating Universe and a Cosmological Constant". In: *AJ* 116.3, pp. 1009–1038. DOI: 10.1086/300499. arXiv: astro-ph/9805201 [astro-ph].

Rykoff, E. S. et al. (Apr. 2014). "redMaPPer. I. Algorithm and SDSS DR8 Catalog". In: *ApJ* 785.2, 104, p. 104. DOI: 10.1088/0004-637X/785/2/104. arXiv: 1303.3562 [astro-ph.CO].

Rykoff, E. S. et al. (May 2016). "The RedMaPPer Galaxy Cluster Catalog From DES Science Verification Data". In: *ApJS* 224.1, 1, p. 1. DOI: 10.3847/0067-0049/224/1/1. arXiv: 1601.00621 [astro-ph.CO].

Santos, J. S. et al. (July 2011). "Discovery of a massive X-ray luminous galaxy cluster at z = 1.579". In: *A&A* 531, L15, p. L15. DOI: 10.1051/0004-6361/201117190. arXiv: 1105.5877 [astro-ph.CO].

Schirmer, M. (Dec. 2013). "THELI: Convenient Reduction of Optical, Near-infrared, and Mid-infrared Imaging Data". In: *ApJS* 209.2, 21, p. 21. DOI: 10.1088/0067-0049/209/2/21. arXiv: 1308.4989 [astro-ph.IM].

Schneider, Peter, Jürgen Ehlers, and Emilio E. Falco (1992). *Gravitational Lenses.* DOI: 10.1007/978-3-662-03758-4.

Schneider, Peter et al. (June 1998). "A new measure for cosmic shear". In: *MNRAS* 296.4, pp. 873–892. DOI: 10.1046/j.1365-8711.1998.01422.x. arXiv: astro-ph/9708143 [astro-ph].

Seitz, C. and P. Schneider (Feb. 1997). "Steps towards nonlinear cluster inversion through gravitational distortions. III. Including a redshift distribution of the sources." In: *A&A* 318, pp. 687–699. eprint: astro-ph/9601079.

Seljak, Uroš and Michael S. Warren (Nov. 2004). "Large-scale bias and stochasticity of haloes and dark matter". In: *MNRAS* 355.1, pp. 129–136. DOI: 10.1111/j.1365-2966.2004.08297.x. arXiv: astro-ph/0403698 [astro-ph].

Sereno, M. and S. Ettori (July 2015). "CoMaLit - IV. Evolution and self-similarity of scaling relations with the galaxy cluster mass". In: *mnras* 450, pp. 3675–3695. DOI: 10.1093/mnras/stv814.

Sereno, Mauro and Giovanni Covone (Sept. 2013). "The mass-concentration relation in massive galaxy clusters at redshift ~1". In: *MNRAS* 434.1, pp. 878–887. DOI: 10.1093/mnras/stt1086. arXiv: 1306.6096 [astro-ph.CO].

Sereno, Mauro and Keiichi Umetsu (Oct. 2011). "Weak- and strong-lensing analyses of the triaxial matter distribution of Abell 1689". In: *MNRAS* 416.4, pp. 3187–3200. DOI: 10.1111/j.1365-2966.2011.19274.x. arXiv: 1105.4994 [astro-ph.CO].

Sereno, Mauro et al. (June 2015a). "New constraints on σ_8 from a joint analysis of stacked gravitational lensing and clustering of galaxy clusters". In: *MNRAS* 449.4, pp. 4147–4161. DOI: 10.1093/mnras/stv280. arXiv: 1410.5438 [astro-ph.CO].

Sereno, Mauro et al. (May 2015b). "The mass-concentration relation in lensing clusters: the role of statistical biases and selection effects". In: *MNRAS* 449.2, pp. 2024–2039. DOI: 10.1093/mnras/stv416. arXiv: 1410.4568 [astro-ph.CO].

Sereno, Mauro et al. (Dec. 2017). "PSZ2LenS. Weak lensing analysis of the Planck clusters in the CFHTLenS and in the RCSLenS". In: *MNRAS* 472.2, pp. 1946–1971. DOI: 10.1093/mnras/stx2085. arXiv: 1703.06886 [astro-ph.CO].

Sereno, Mauro et al. (July 2018). "Gravitational lensing detection of an extremely dense environment around a galaxy cluster". In: *Nature Astronomy* 2, pp. 744–750. DOI: 10.1038/s41550-018-0508-y. arXiv: 1807.04277 [astro-ph.CO].

Sereno, Mauro et al. (Sept. 2020). "CoMaLit - VI. Intrinsic scatter in stacked relations. The weak lensing AMICO galaxy clusters in KiDS-DR3". In: *MNRAS* 497.1, pp. 894–905. DOI: 10.1093/mnras/staa1902. arXiv: 2006.16264 [astro-ph.CO].

Sheldon, E. S. et al. (May 2004). "The Galaxy-Mass Correlation Function Measured from Weak Lensing in the Sloan Digital Sky Survey". In: *aj* 127, pp. 2544–2564. DOI: 10.1086/383293. eprint: astro-ph/0312036.

Sheth, Ravi K., H. J. Mo, and Giuseppe Tormen (May 2001). "Ellipsoidal collapse and an improved model for the number and spatial distribution of dark matter haloes". In: *MNRAS* 323.1, pp. 1–12. DOI: 10.1046/j.1365-8711.2001.04006.x. arXiv: astro-ph/9907024 [astro-ph].

Sheth, Ravi K. and Giuseppe Tormen (Sept. 1999). "Large-scale bias and the peak background split". In: *MNRAS* 308.1, pp. 119–126. DOI: 10.1046/j.1365-8711.1999.02692.x. arXiv: astro-ph/9901122 [astro-ph].

Simet, M. et al. (Apr. 2017). “Weak lensing measurement of the mass-richness relation of SDSS redMaPPer clusters”. In: *mnras* 466, pp. 3103–3118. DOI: 10.1093/mnras/stw3250. arXiv: 1603.06953.

Singh, Sukhdeep et al. (Nov. 2017). “Galaxy-galaxy lensing estimators and their covariance properties”. In: *MNRAS* 471.4, pp. 3827–3844. DOI: 10.1093/mnras/stx1828. arXiv: 1611.00752 [astro-ph.CO].

Skibba, Ramin A. and Andrea V. Macciò (Sept. 2011). “Properties of dark matter haloes and their correlations: the lesson from principal component analysis”. In: *MNRAS* 416.3, pp. 2388–2400. DOI: 10.1111/j.1365-2966.2011.19218.x. arXiv: 1103.1641 [astro-ph.CO].

Smith, R. E. et al. (June 2003). “Stable clustering, the halo model and non-linear cosmological power spectra”. In: *MNRAS* 341.4, pp. 1311–1332. DOI: 10.1046/j.1365-8711.2003.06503.x. arXiv: astro-ph/0207664 [astro-ph].

Soldner, J. (Jan. 1804). “Über die Ablenkung eines Lichtstrahls von seiner geradlinigen Bewegung durch die Attraktion eines Weltkörpers, an welchem er nahe vorbeigeht”. In: *Annalen der Physik* 370.15, pp. 593–604. DOI: 10.1002/andp.19213701503.

Soltis, John, Stefano Casertano, and Adam G. Riess (Feb. 2021). “The Parallax of ω Centauri Measured from Gaia EDR3 and a Direct, Geometric Calibration of the Tip of the Red Giant Branch and the Hubble Constant”. In: *ApJ* 908.1, L5, p. L5. DOI: 10.3847/2041-8213/abdbad. arXiv: 2012.09196 [astro-ph.GA].

Soucail, G. et al. (Feb. 1988). “The giant arc in A 370 : spectroscopic evidence for gravitational lensing from a source at Z=0.724.” In: *A&A* 191, pp. L19–L21.

Speagle, Joshua S. (Apr. 2020). “DYNESTY: a dynamic nested sampling package for estimating Bayesian posteriors and evidences”. In: *MNRAS* 493.3, pp. 3132–3158. DOI: 10.1093/mnras/staa278. arXiv: 1904.02180 [astro-ph.IM].

Springel, V. et al. (Dec. 2001). “Populating a cluster of galaxies - I. Results at z=0”. In: *MNRAS* 328, pp. 726–750. DOI: 10.1046/j.1365-8711.2001.04912.x. eprint: arXiv:astro-ph/0012055.

Springel, Volker, Carlos S. Frenk, and Simon D. M. White (Apr. 2006). “The large-scale structure of the Universe”. In: *Nature* 440.7088, pp. 1137–1144. DOI: 10.1038/nature04805. arXiv: astro-ph/0604561 [astro-ph].

Springel, Volker et al. (June 2005). “Simulations of the formation, evolution and clustering of galaxies and quasars”. In: *Nature* 435.7042, pp. 629–636. DOI: 10.1038/nature03597. arXiv: astro-ph/0504097 [astro-ph].

Steigman, Gary (Oct. 2006). “The cosmological evolution of the average mass per baryon”. In: *J. Cosmology Astropart. Phys.* 2006.10, 016, p. 016. DOI: 10.1088/1475-7516/2006/10/016. arXiv: astro-ph/0606206 [astro-ph].

Sugiyama, Naoshi (Oct. 1995). “Cosmic Background Anisotropies in Cold Dark Matter Cosmology”. In: *ApJS* 100, p. 281. DOI: 10.1086/192220. arXiv: astro-ph/9412025 [astro-ph].

Sunyaev, R. A. and Ya. B. Zeldovich (Feb. 1980). “The velocity of clusters of galaxies relative to the microwave background - The possibility of its measurement.” In: *MNRAS* 190, pp. 413–420. DOI: 10.1093/mnras/190.3.413.

Takada, Masahiro and Bhuvnesh Jain (Apr. 2003). “The three-point correlation function in cosmology”. In: *MNRAS* 340.2, pp. 580–608. DOI: 10.1046/j.1365-8711.2003.06321.x. arXiv: astro-ph/0209167 [astro-ph].

Takahashi, Ryuichi et al. (Dec. 2012). “Revising the Halofit Model for the Nonlinear Matter Power Spectrum”. In: *ApJ* 761.2, 152, p. 152. DOI: 10.1088/0004-637X/761/2/152. arXiv: 1208.2701 [astro-ph.CO].

Taruya, Atsushi et al. (Nov. 2012). "Direct and fast calculation of regularized cosmological power spectrum at two-loop order". In: *Phys. Rev. D* 86.10, 103528, p. 103528. DOI: 10.1103/PhysRevD.86.103528. arXiv: 1208.1191 [astro-ph.CO].

Taylor, James E. and Arif Babul (Mar. 2004). "The evolution of substructure in galaxy, group and cluster haloes - I. Basic dynamics". In: *MNRAS* 348.3, pp. 811–830. DOI: 10.1111/j.1365-2966.2004.07395.x. arXiv: astro-ph/0301612 [astro-ph].

— (Dec. 2005). "The evolution of substructure in galaxy, group and cluster haloes - III. Comparison with simulations". In: *MNRAS* 364.2, pp. 535–551. DOI: 10.1111/j.1365-2966.2005.09581.x. arXiv: astro-ph/0410049 [astro-ph].

Tinker, Jeremy et al. (Dec. 2008). "Toward a Halo Mass Function for Precision Cosmology: The Limits of Universality". In: *ApJ* 688.2, pp. 709–728. DOI: 10.1086/591439. arXiv: 0803.2706 [astro-ph].

Tinker, Jeremy L. et al. (Dec. 2010). "The Large-scale Bias of Dark Matter Halos: Numerical Calibration and Model Tests". In: *ApJ* 724.2, pp. 878–886. DOI: 10.1088/0004-637X/724/2/878. arXiv: 1001.3162 [astro-ph.CO].

Tormen, G. (June 1998). "The assembly of matter in galaxy clusters". In: *MNRAS* 297, pp. 648–656. eprint: arXiv:astro-ph/9802290.

Umetsu, Keiichi et al. (Sept. 2011). "A Precise Cluster Mass Profile Averaged from the Highest-quality Lensing Data". In: *ApJ* 738.1, 41, p. 41. DOI: 10.1088/0004-637X/738/1/41. arXiv: 1105.0444 [astro-ph.CO].

Umetsu, Keiichi et al. (Nov. 2014). "CLASH: Weak-lensing Shear-and-magnification Analysis of 20 Galaxy Clusters". In: *ApJ* 795.2, 163, p. 163. DOI: 10.1088/0004-637X/795/2/163. arXiv: 1404.1375 [astro-ph.CO].

Umetsu, Keiichi et al. (Feb. 2020). "Weak-lensing Analysis of X-Ray-selected XXL Galaxy Groups and Clusters with Subaru HSC Data". In: *ApJ* 890.2, 148, p. 148. DOI: 10.3847/1538-4357/ab6bca. arXiv: 1909.10524 [astro-ph.CO].

Valentijn, E. A. et al. (Oct. 2007). "Astro-WISE: Chaining to the Universe". In: *Astronomical Data Analysis Software and Systems XVI*. Ed. by R. A. Shaw, F. Hill, and D. J. Bell. Vol. 376. Astronomical Society of the Pacific Conference Series, p. 491. arXiv: astro-ph/0702189 [astro-ph].

Viola, M. et al. (Oct. 2015). "Dark matter halo properties of GAMA galaxy groups from 100 square degrees of KiDS weak lensing data". In: *MNRAS* 452.4, pp. 3529–3550. DOI: 10.1093/mnras/stv1447. arXiv: 1507.00735 [astro-ph.GA].

Voit, G. Mark (Apr. 2005). "Tracing cosmic evolution with clusters of galaxies". In: *Reviews of Modern Physics* 77.1, pp. 207–258. DOI: 10.1103/RevModPhys.77.207. arXiv: astro-ph/0410173 [astro-ph].

Watson, William A. et al. (Aug. 2013). "The halo mass function through the cosmic ages". In: *MNRAS* 433.2, pp. 1230–1245. DOI: 10.1093/mnras/stt791. arXiv: 1212.0095 [astro-ph.CO].

White, M. (Feb. 2001). "The mass of a halo". In: *A&A* 367, pp. 27–32. DOI: 10.1051/0004-6361:20000357. arXiv: astro-ph/0011495 [astro-ph].

White, S. D. M. and M. J. Rees (May 1978). "Core condensation in heavy halos - A two-stage theory for galaxy formation and clustering". In: *MNRAS* 183, pp. 341–358. DOI: 10.1093/mnras/183.3.341.

Yang, Xiaohu et al. (2006). "Weak lensing by galaxies in groups and clusters – I. Theoretical expectations". In: *Monthly Notices of the Royal Astronomical Society* 373.3, pp. 1159–1172. DOI: 10.1111/j.1365-2966.2006.11091.x. eprint: /oup/backfile/content_public/journal/mnras/373/3/10.1111_j.1365-2966.2006.11091.x/1/mnras0373-1159.pdf. URL: http://dx.doi.org/10.1111/j.1365-2966.2006.11091.x.

York, Donald G. et al. (Sept. 2000). "The Sloan Digital Sky Survey: Technical Summary". In: *AJ* 120.3, pp. 1579–1587. DOI: 10.1086/301513. arXiv: astro-ph/0006396 [astro-ph].

Zacchei, Andrea et al. (July 2016). "Management of the science ground segment for the Euclid mission". In: *Software and Cyberinfrastructure for Astronomy IV*. Ed. by Gianluca Chiozzi and Juan C. Guzman. Vol. 9913. Society of Photo-Optical Instrumentation Engineers (SPIE) Conference Series, 99131B. DOI: 10.1117/12.2232934.

Zeldovich, Yaa B. (Jan. 1972). "A hypothesis, unifying the structure and the entropy of the Universe". In: *MNRAS* 160, 1P. DOI: 10.1093/mnras/160.1.1P.

Zitrin, A. et al. (Dec. 2011a). "The Cluster Lensing and Supernova Survey with Hubble (CLASH): Strong-lensing Analysis of A383 from 16-band HST/WFC3/ACS Imaging". In: *ApJ* 742.2, 117, p. 117. DOI: 10.1088/0004-637X/742/2/117. arXiv: 1103.5618 [astro-ph.CO].

Zitrin, Adi et al. (Jan. 2011b). "Strong-lensing analysis of a complete sample of 12 MACS clusters at z > 0.5: mass models and Einstein radii". In: *MNRAS* 410.3, pp. 1939–1956. DOI: 10.1111/j.1365-2966.2010.17574.x. arXiv: 1002.0521 [astro-ph.CO].

Zwicky, F. (Jan. 1933). "Die Rotverschiebung von extragalaktischen Nebeln". In: *Helvetica Physica Acta* 6, pp. 110–127.

— (Oct. 1937). "On the Masses of Nebulae and of Clusters of Nebulae". In: *apj* 86, p. 217. DOI: 10.1086/143864.

Appendix A

Related publications

As a major part of my thesis, I've been involved in the KiDS team to study the weak lensing signal on AMICO galaxy clusters. To do so I developed numerical tools for the analysis of the data and derived scientific results showed as python plots. These materials have been discussed and approved during numerous and regular meetings of the AMICO working group and internal KiDS discussions. Finally, from this work ensued a publication in the Monthly Notices of the Royal Astronomical Society (MNRAS) scientific journal at the latter stage of my Ph.D: Ingoglia et al. (2022). It consists of a 3-years old collaborative work of 22 authors for this cosmological study.

A parallel study on the halo sparsity, also introduced in Section 3.4.3, has not yet been sent for review to the KiDS collaboration so I do not include it in the appendix.

Finally, the second paper of the pre-launch key project LE3-CL-2 of the Euclid consortium will concern the development analysis of the COMB-CL package described in Section 4.2. This project will result during the year 2022 and the publication nearly follow as a consistent piece of work of our future projects regarding the emphasis on the Euclid collaboration.

MNRAS 000, 1–20 (2021) Preprint 6 January 2022 Compiled using MNRAS LaTeX style file v3.0

AMICO galaxy clusters in KiDS-DR3: Measurement of the halo bias and power spectrum normalization from a stacked weak lensing analysis

Lorenzo Ingoglia[1,2,3,⋆], Giovanni Covone[1,2,3], Mauro Sereno[5,6], Carlo Giocoli[5,4,6], Sandro Bardelli[5], Fabio Bellagamba[4], Gianluca Castignani[4,5], Samuel Farrens[11], Hendrik Hildebrandt[14,15], Shahab Joudaki[16,17], Eric Jullo[10], Denise Lanzieri[11,1], Giorgio F. Lesci[4,5], Federico Marulli[4,5,6], Matteo Maturi[12,13], Lauro Moscardini[4,5,6], Lorenza Nanni[4,18], Emanuela Puddu[2], Mario Radovich[7], Mauro Roncarelli[4], Feliciana Sapio[8,9,1], Carlo Schimd[10]

[1] *Department of Physics - University of Naples "Federico II", Via Cinthia, 80126 Fuorigrotta, Napoli, Italy*
[2] *INAF - Capodimonte Astronomical Observatory, Salita Moiariello 16, 80131 Napoli, Italy*
[3] *INFN - Naples Section, Strada Comunale Cinthia, 80126 Napoli, Italy*
[4] *Department of Physics and Astronomy "A. Righi" - University of Bologna, Via Piero Gobetti 93/2, 40129 Bologna, Italy*
[5] *INAF - Astrophysics and Space Science Observatory of Bologna, Via Piero Gobetti 93/3, 40129 Bologna, Italy*
[6] *INFN - Bologna Section, Viale Berti Pichat 6/2, 40127 Bologna, Italy*
[7] *INAF - Padua Astronomical Observatory, Vicolo dell'Osservatorio, 5, 35122 Padova, Italy*
[8] *Department of Physics - University of Roma "La Sapienza", Piazzale Aldo Moro, 2, 00185 Roma, Italy*
[9] *INAF - Istituto di Astrofisica e Planetologia Spaziali (IAPS), Via del Fosso del Cavaliere, 100, 00133 Roma, Italy*
[10] *Aix-Marseille University, CNRS, CNES, LAM, Marseille, France*
[11] *AIM, CEA, CNRS, Université Paris-Saclay, Université de Paris, Sorbonne Paris Cité, F-91191 Gif-sur-Yvette, France*
[12] *Center for Astronomy - University of Heidelberg, Albert-Ueberle-Straße 2, 69120 Heidelberg, Germany*
[13] *Institute of Theoretical Physics - University of Heidelberg, Albert-Ueberle-Straße 2, 69120 Heidelberg, Germany*
[14] *Institute of Astronomy - Ruhr University of Bochum, Universitätsstr. 150, 44801, Bochum, Germany*
[15] *Argelander Institute of Astronomy - University of Bonn, Auf dem Hügel 71, 53121 Bonn, Germany*
[16] *Waterloo Centre for Astrophysics - University of Waterloo, 200 University Ave W, Waterloo, ON N2L 3G1, Canada*
[17] *Department of Physics and Astronomy - University of Waterloo, 200 University Ave W, Waterloo, ON N2L 3G1, Canada*
[18] *Institute of Cosmology and Gravitation - University of Portsmouth, Dennis Sciama Building, Portsmouth, PO1 3FX, UK*

Accepted for publication in MNRAS on Jan. 2022

ABSTRACT

Galaxy clusters are biased tracers of the underlying matter density field. At very large radii beyond about 10 Mpc/h, the shear profile shows evidence of a second-halo term. This is related to the correlated matter distribution around galaxy clusters and proportional to the so-called halo bias. We present an observational analysis of the halo bias-mass relation based on the AMICO galaxy cluster catalog, comprising around 7000 candidates detected in the third release of the KiDS survey. We split the cluster sample into 14 redshift-richness bins and derive the halo bias and the virial mass in each bin by means of a stacked weak lensing analysis. The observed halo bias-mass relation and the theoretical predictions based on the ΛCDM standard cosmological model show an agreement within 2σ. The mean measurements of bias and mass over the full catalog give $\mathrm{M_{200c}} = (4.9 \pm 0.3) \times 10^{13} \mathrm{M_\odot}/h$ and $\mathrm{b_h}\sigma_8^2 = 1.2 \pm 0.1$. With the additional prior of a bias-mass relation from numerical simulations, we constrain the normalization of the power spectrum with a fixed matter density $\Omega_\mathrm{m} = 0.3$, finding $\sigma_8 = 0.63 \pm 0.10$.

Key words: astronomical data bases: catalogues – galaxies: clusters: general – Physical Data and Processes: gravitational lensing: weak – Cosmology: cosmological parameters

⋆ E-mail: lorenzo.ingoglia@unina.it

1 INTRODUCTION

Clusters of galaxies occupy a special place in the hierarchy of cosmic structures as they are the most massive gravitationally bound systems in the Universe. According to the hierarchical scenario of the evolution of cosmic structure (Peebles 1980; Voit 2005), they arise from the collapse of initial density perturbations having a typical comoving scale of about 10 Mpc/h (Peebles 1993; Borgani 2008). Above these scales, gravitational clustering is essentially in a linear regime and the dynamics are mostly driven by the Hubble flow, while the non-linear regime is prominent on smaller scales. Moreover, in the inner cluster regions, astrophysical processes such as gas cooling, star formation, feedback from supernovae and active galactic nuclei modify the evolution of the halo properties like, the density profile, the subhalo mass function, etc. (Rasia et al. 2004, 2006; Giocoli et al. 2010a; Despali et al. 2014, 2016; Angelinelli et al. 2020). Galaxy clusters thus provide an ideal tool to study the physical mechanisms driving the formation and evolution of cosmic structures in the mildly non-linear regime (Tormen 1998; Springel et al. 2001).

Massive galaxy clusters, composed of a large amount of dark matter (about 85%, see e.g. White & Rees 1978), are expected to grow at the highest peaks of the underlying matter distribution. This establishes a clear correlation between the galaxy cluster mass and the underling matter clustering amplitude. As already shown by Kaiser (1984), the enhanced clustering of Abell galaxy clusters is explained by assuming that they form in the high-density regions. As a consequence, galaxy clusters are biased tracers of the background matter field. Several groups have further developed this idea within the framework of the Press & Schechter (1974) formalism (e.g., Mo & White 1996; Sheth & Tormen 1999; Sheth et al. 2001; Giocoli et al. 2010b), deriving quantitative predictions for the correlation between the halo density field and the underlying matter distribution within the hierarchical scenario for the formation of cosmic structures. The relation between the cluster dark matter halo density contrast, $\delta_{\rm h}$, and the dark matter density contrast in the linear regime, $\delta_{\rm m}$, is described by the so-called halo bias parameter, $\rm b_h$, defined as (Tinker et al. 2010)

$$\rm b_h = \delta_h/\delta_m \ . \qquad (1)$$

Measurements of the halo bias as a function of the halo mass therefore represent an important test for cosmological models.

The total matter distribution of a galaxy cluster can be broken down in a "one-halo" term, which determines its halo matter component on scales smaller than the halo virial radius, and a "two-halo" term for the correlated matter of the surrounding structures, which is prominent on scales much larger than the virial radius. The first component is usually identified with the galaxy cluster halo and can be described by a Navarro-Frenk-White dark matter profile (Navarro et al. 1997). The second component, directly proportional to the halo bias, stems from mass elements in distinct pairs of halos. The two terms of the halo profile correlate in such a way that the bias follows an increasing function of mass (Kaiser 1984; Cole & Kaiser 1989; Mo et al. 1996). This relation has been shown and modeled in several studies based on N-body numerical simulations (e.g. Seljak & Warren 2004; Tinker et al. 2005, 2010).

Weak gravitational lensing (WL) is a suitable approach to investigate the halo model and to measure its major parameters: the mass and the bias. Gravitational lensing relates the deflection of light to the mass distribution along the line-of-sight. As gravitational lensing is based on the very well-tested theory of general relativity and does not rely on the hypothesis of dynamical equilibrium, it allows robust measurements of the mass of cosmic structures and cosmological parameters. WL by galaxy clusters is detected via statistical measurement of source galaxy shears, and provides an efficient way to derive mass density profiles without requiring any assumption about their composition or dynamical state. For example, WL analysis allows us to reach scales up to ~ 30 Mpc/h from the center and therefore to directly measure the halo bias (Covone et al. 2014).

Stacking the shear measurements of cluster background galaxies is a common practice to increase the lensing signals and compensate for the typical low signal-to-noise ratio (SNR hereafter) in the shear profiles of individual galaxy clusters (see for instance Sereno & Covone 2013). This method also makes it possible to arrange the stacked density profiles as a function of the cluster properties, such as their redshift or their richness.

Several authors have probed the dependence of the halo bias on mass (Seljak et al. 2005; Johnston et al. 2007a; Covone et al. 2014; Sereno et al. 2015b; van Uitert et al. 2016). These studies have obtained results consistent with the theoretical predictions, but the large uncertainty in the measurements did not allow them to discriminate between different theoretical models. Moreover, recently Sereno et al. (2018) found a peculiar galaxy cluster at z ~ 0.62 in the PZS2LenS sample (Sereno et al. 2017) showing an extreme value of the halo bias, well in excess of the theoretical predictions. This result motivates further observational work in order to probe with higher accuracy the halo bias-mass relation. Large sky surveys providing deep and high-quality photometric data and reliable catalogs of galaxy clusters are essential.

In this work we perform a novel measurement of the bias-mass relation by using the photometric data from the third data release of KiDS (de Jong et al. 2013, 2017) and the galaxy cluster catalog identified using the Adaptive Matched Identifier of Clustered Objects detection algorithm (AMICO, Bellagamba et al. 2018). This catalog is optimal for a stacked WL analysis because of its large size (an effective area of 360.3 square degrees) and its dense field (an effective galaxy number density of $\rm n_{eff} = 8.53\ arcmin^{-2}$), which allows us to split the stacked WL signal into different bins of cluster redshift and richness while keeping a sufficiently high SNR in each of them. KiDS images are deep enough (limiting magnitudes are 24.3, 25.1, 24.9, 23.8 in *ugri*, respectively) to include numerous sources (almost 15 million) and large enough to compute the profile up to the scales where the bias dominates. This study is part of a series of papers based on AMICO galaxy clusters in the third data release of KiDS. Previous and ongoing publications have presented the detection algorithm (Bellagamba et al. 2018), the cluster catalog (Maturi et al. 2019), the calibration of WL masses (Bellagamba et al. 2019), and constraints on cosmological parameters otained from cluster counts (Lesci et al. 2020), WL (Giocoli et al. 2021) and cluster clustering (Nanni et al. prep).

Following the method explained in Bellagamba et al. (2019), we derive mass density profiles from almost 7000 clusters, which is among the largest cluster samples for this kind of analysis. We stack the lensing signal in richness and redshift cluster bins, calibrate the halo parameters and investigate the mass-bias relation. Throughout this paper we assume a spatially flat ΛCDM model with the following matter, dark energy and baryonic density parameters at the present time $\Omega_{\rm m} = 1 - \Omega_\Lambda = 0.3$, $\Omega_{\rm b} = \Omega_{\rm m} - \Omega_{\rm c} = 0.05$ and Hubble parameter $H_0 = 100h$ km s^{-1} Mpc^{-1} with $h = 0.7$.

2 DATA

For an accurate lensing signal, we have to look for deep and dense source samples in such way that the statistical number of background sources increases while the contamination of foreground and cluster member galaxies is small.

Our work is based on the optical wide-field imaging Kilo-Degree Survey (KiDS, de Jong et al. 2013), split into an equatorial stripe (KiDS-N), and a second one centered around the South Galactic Pole (KiDS-S). The survey encompasses four broad-band filters (*ugri*) managed by the OmegaCAM wide-field imager (Kuijken 2011), presently located on the VLT Survey Telescope (VST, Capaccioli & Schipani 2011). The data set we use for this work is the Data Release 3[1] (DR3, de Jong et al. 2017) and covers a total area of approximately 450 deg^2 in five patches following the GAMA survey convention (Driver et al. 2011, G9/G12/G15 within KiDS-N and G23/GS within KiDS-S). This intermediate release includes one third of the final KiDS area, which will ultimately reach 1350 deg^2.

2.1 Cluster catalog

We use the galaxy cluster catalog obtained from the application of the Adaptive Matched Identifier of Clustered Objects algorithm (AMICO, Bellagamba et al. 2018) on KiDS DR3 data (AK3, hereafter). AMICO was selected to form part of the *Euclid* analysis pipeline (Euclid Collaboration et al. 2019). The algorithm exploits the Optimal Filtering technique (Maturi et al. 2005; Bellagamba et al. 2011) and aims at maximising the SNR for the detection of objects following a physical model for clusters. Specifically, it identifies overdensities of galaxies associated with galaxy clusters taking into account their spatial, magnitude, and photometric redshift distributions (Radovich et al. 2017).

The AK3 catalog is fully described in Maturi et al. (2019). It contains 7988 candidate galaxy clusters covering an effective area of 377 deg^2. Clusters are detected above a fixed threshold of SNR = 3.5. AK3 encompasses an intrinsic richness (defined as the sum of membership probabilities below a consistent radial and magnitude threshold across redshift) range of $2 < \lambda_* < 140$ and a redshift range $0.1 \leq z < 0.8$. The richness and redshift distributions are presented in Figure 1. From the figure we can see that the richness slightly increases with redshift. Conversely,

[1] http://kids.strw.leidenuniv.nl/DR3

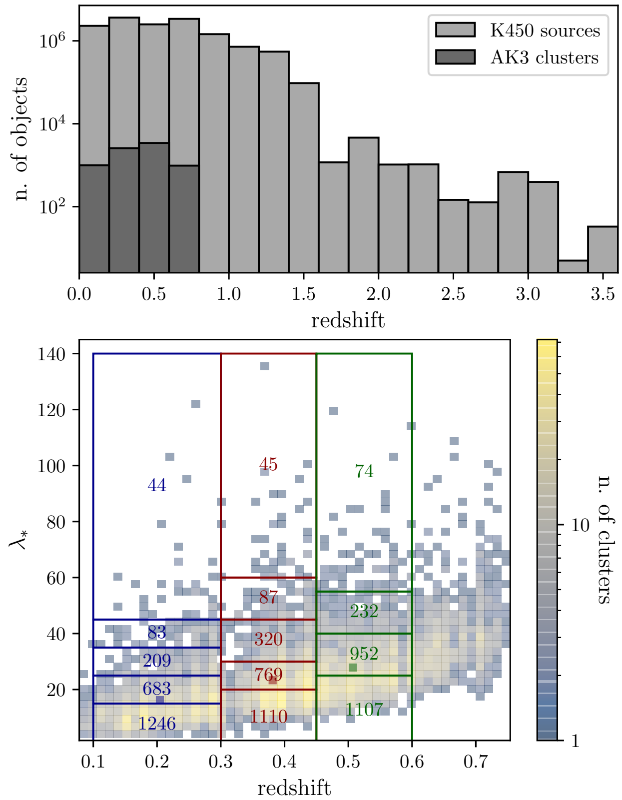

Figure 1. *Top panel*: Redshift distributions of AK3 clusters (dark gray) and K450 galaxies (light gray). *Bottom panel*: AK3 clusters in the redshift-richness plane with SNR ≥ 3.5. Colored rectangles correspond to the redshift-richness bins used in the following analysis (see Section 3.4); the number of clusters enclosed in each bin is displayed. Single colored squares show the mean values in each redshift bin computed as in Equation (17).

poor and distant clusters are not detected due to their low SNR. These blank regions are usually associated to low levels of completeness (i.e. the fraction between detected and mock galaxy clusters), as shown in Figure 13 of Maturi et al. (2019).

2.2 Shear catalog

The halo lensing signal relies on the selection of background galaxies relative to galaxy clusters. Hildebrandt et al. (2017) presented a complete tomographic cosmic shear analysis of the KiDS-450 catalog (K450), updated from earlier works on KiDS-DR1 and -DR2 (de Jong et al. 2015; Kuijken et al. 2015). The shear is estimated using the *lens*fit likelihood based model-fitting method (Miller et al. 2007, 2013; Kitching et al. 2008; Fenech Conti et al. 2017) on galaxy *r*-band images for which the best-seeing dark time is reserved. Photometric redshifts are derived from K450 galaxy photometry in the *ugri*-bands. They are estimated with a Bayesian code (BPZ, Benítez 2000) following the methods used for CFHTLenS data in Hildebrandt et al. (2012). The redshift distribution of the galaxies is shown on the top panel of Figure 1 in light-gray.

The survey covers 454 tiles, which after masking overlapping tiles, provides an effective area of 360.3 $\deg^2$. It comprises 14,650,348 sources and has an effective number density (as defined in Heymans et al. 2012) of $n_{\rm eff} = 8.53\ \rm arcmin^{-2}$.

3 METHOD

In this section we provide a short introduction to the WL formalism. We then describe the numerical method to derive the WL signal of galaxy clusters from the shapes of background sources. We discuss the selections of lens-source pairs that improve the stacked measurement and remove those for which the shear distorts the final signal. Finally, we stack the individual lens shear profiles in bins of cluster redshift and richness for an accurate measurement of the halo parameters.

3.1 Weak-lensing formalism

In gravitational lensing, the matter distribution curves space-time and modifies the the path of light rays from background sources, manifesting in a distortion of their intrinsic shape. Shape distortion yields isotropic or anisotropic deformation, called convergence, κ, and shear, γ, respectively. The tangential component of the shear γ_+ encodes the density of the intervening matter distributed between the source and us. Massive objects such as galaxy clusters are therefore dominant in the information that γ_+ encapsulates, as we will present later. For a review, see e.g. Bartelmann & Schneider (2001); Schneider (2006); Kilbinger (2015).

The source shape distortion can be expressed in terms of the deflection potential ψ. It is described by the Jacobian matrix through the second derivatives of the potential, $\psi_{ij} \equiv \partial_i \partial_j \psi$

$$\mathcal{A} \equiv (\delta_{ij} - \psi_{ij}) = \begin{pmatrix} 1-\kappa-\gamma_1 & -\gamma_2 \\ -\gamma_2 & 1-\kappa+\gamma_1 \end{pmatrix} , \tag{2}$$

in which the convergence κ is defined by the Poisson equation $\nabla^2\psi \equiv 2\kappa$ and the complex shear $\gamma \equiv \gamma_1 + i\gamma_2$ is given by $\gamma_1 = \frac{1}{2}(\psi_{11} - \psi_{22})$ and $\gamma_2 = \psi_{12}$.

Sources initially have an intrinsic unlensed ellipticity ϵ_s, which is converted by cosmic shear into the observed ellipticity ϵ. One describes this deformed ellipse by its minor and major axes (a, b), and from the position angle ϕ of the source relatively to the lens, $\epsilon = |\epsilon| e^{2i\phi}$, where $|\epsilon| = (a - b)/(a + b)$.

It is convenient to factor out the multiplicative term $(1-\kappa)$ from Equation (2) and thereby introduce the reduced shear observable $g \equiv \gamma/(1-\kappa)$ and its conjugate version g^*. Considering $|g| \le 1$, Seitz & Schneider (1997) relate shear and ellipticity by

$$\epsilon = \frac{\epsilon_s + g}{1 + g^* \epsilon_s} . \tag{3}$$

In the WL limit $\gamma \ll 1$ and $\kappa \ll 1$, yielding $\epsilon \approx \epsilon_s + g$. Assuming that sources are randomly oriented, their complex intrinsic ellipticities average to zero, so $\langle\epsilon\rangle = \langle\gamma\rangle$. Therefore, the average ellipticity of background galaxies is a direct observable of the shear induced by foreground matter.

The two components of the complex shear are defined relative to a local Cartesian space and are conveniently decomposed into a tangential and a cross component,

$$\begin{aligned} \gamma_+ &= -\Re\left(\gamma e^{-2i\phi}\right) = -(\gamma_1 \cos 2\phi + \gamma_2 \sin 2\phi) , \\ \gamma_\times &= -\Im\left(\gamma e^{-2i\phi}\right) = -(\gamma_2 \cos 2\phi - \gamma_1 \sin 2\phi) , \end{aligned} \tag{4}$$

respectively. Noticing the minus sign in the exponential, it is agreed that for an axially symmetric mass distribution the tangential component returns a positive value around an overdensity, while a negative value characterizes underdensities. On the other hand, the cross component of the shear does not hold any mass information, and thus averages to zero, in the absence of systematic uncertainties. It is possible to relate the shear to a physical quantity, the excess surface mass density $\Delta\Sigma$, as (Sheldon et al. 2004)

$$\Delta\Sigma(R) \equiv \bar{\Sigma}(<R) - \Sigma(R) = \Sigma_{\rm cr}\gamma_+(R) , \tag{5}$$

where $\Sigma(R)$ is the surface mass density and $\bar{\Sigma}(<R)$ its mean value within the projected radius R, and $\Sigma_{\rm cr}$ is the critical surface mass density, given by

$$\Sigma_{\rm cr} \equiv \frac{c^2}{4\pi G} \frac{D_s}{D_l D_{ls}} , \tag{6}$$

where c is the speed of light, G is the gravitational constant and D_s, D_l and D_{ls} are the angular diameter distances from the observer to the source, from the observer to the lens and from the lens to the source, respectively.

The reduced shear is a more direct observable than the shear, which remains an approximation of the source ellipticities. However, the reduced shear is not directly included in the definition of the differential excess surface density, so we link these two quantities using $\kappa \equiv \Sigma/\Sigma_{\rm cr}$ in Equation (5) and derive

$$g_+ = \frac{\Delta\Sigma}{\Sigma_{\rm cr} - \Sigma} . \tag{7}$$

3.2 Measurement of the lensing signal

Since the ellipticity is an indirect observable of the shear, we denote the corresponding excess surface mass density for $\Sigma_{\rm cr}\epsilon_{+/\times}$ as $\widetilde{\Delta\Sigma}_{+/\times}$. We compute the lensing signal at a given distance from the cluster center by stacking the radial position and the ellipticity of the i-th galaxy source over the j-th radial annulus. Thereby, we assess the two observables using their weighted mean

$$R_j = \left(\frac{\sum_{i\in j} w_{ls,i} R_i^{-\alpha}}{\sum_{i\in j} w_{ls,i}}\right)^{-1/\alpha} ; \ \widetilde{\Delta\Sigma}_j = \left(\frac{\sum_{i\in j} w_{ls,i}\Sigma_{{\rm cr},i}\epsilon_i}{\sum_{i\in j} w_{ls,i}}\right) \frac{1}{1+K_j} , \tag{8}$$

where the lens-source weight of the i-th source is $w_{ls,i} = w_{s,i}\Sigma_{{\rm cr},i}^{-2}$ and $w_{s,i}$ is the inverse-variance source weight as defined in Miller et al. (2013). Here, K_j is the weighted mean of the *lens*fit multiplicative bias m_i introduced to calibrate the shear (see Fenech Conti et al. 2017),

$$K_j = \frac{\sum_{i\in j} w_{ls,i} m_i}{\sum_{i\in j} w_{ls,i}} . \tag{9}$$

The effective radius is estimated with a shear-weighted mean and computed by approximating the shear profile as a power-law, with $\alpha = 1$. Sereno et al. (2017), which explored different methods to assess the mean radius, found that this configuration is less dependent on the binning scheme. We compute the average inverse surface critical density to derive the effective redshift of the background sources z_{back} in each radial bin (Sereno et al. 2017)

$$\Sigma_{cr}^{-1}(z_{back}) = \frac{\sum_{i\in j} w_{s,i}\Sigma_{cr,i}^{-1}}{\sum_{i\in j} w_{s,i}} \ . \quad (10)$$

This estimate permits us to compute the modelled reduced shear in Equation (7) as further described in Section 4.

A preliminary measurement of the statistical errors of the two observables in Equation (8) is given by the weighted standard deviation of the radial distances and by the standard error of the weighted mean, i.e.

$$\sigma_{R,j}^2 = \frac{\sum_{i\in j} w_{ls,i}\left(R_i - R_j\right)^2}{\sum_{i\in j} w_{ls,i}}; \quad \sigma_{\widetilde{\Delta\Sigma},j}^2 = \frac{1}{\sum_{i\in j} w_{ls,i}} \ , \quad (11)$$

respectively. A more complete way to assess the uncertainty given by the averaged signal is to compute the covariance matrix as in Appendix A. This statistical measurement of the noise includes the errors which propagate among the bins.

In the following, we provide lensing profiles sampled in 30 annuli corresponding to 31 logarithmically equi-spaced radii in the range $[0.1, 30]$ Mpc/h. This choice is justified since our analysis both requires small and large scales to identify the two terms of the halo model. We discard the four inner annuli of the the measured shear profile to avoid contamination from cluster member galaxies and the contribution of the BCG in the resulting density profiles (Bellagamba et al. 2019). Effects of miscentering are minimized as the lensing signal is considered only for $R \gtrsim 0.2$ Mpc/h. This measurement is also repeated around random lens points to compensate for the systematic signal, as discussed in Appendix B.

We illustrate the process of stacking the shear signal in Figure 2, where a 2D distribution of selected sources around the AK3 cluster J225151.12-332409 is shown (more details in Section 3.3). For visual convenience in the illustration, we highlighted only 12 of the 31 radii in the radial range $[0.35, 3]$ Mpc/h. The tangential and the cross components of $\widetilde{\Delta\Sigma}$ associated to the 10 annuli are additionally displayed in the bottom panel.

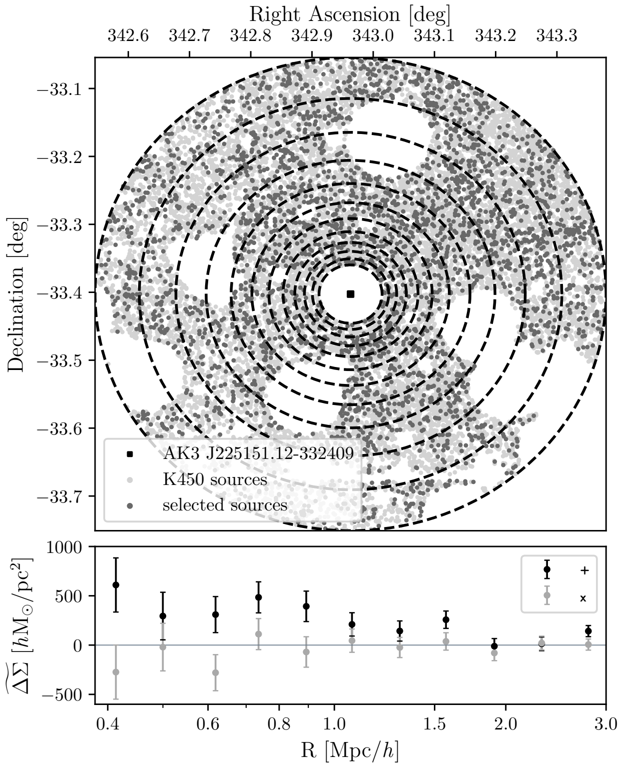

Figure 2. *Top panel*: Illustration of eleven of the thirty annuli in the radial range $[0.35, 3]$ Mpc/h,for the cluster AK3 J225151.12-332409. The sources shown are selected following the cut discussed in Section 3.3.1. Blank regions indicate masks (Hildebrandt et al. 2017). *Bottom panel*: Tangential and cross components of the excess surface mass density (Equation 8) of J225151.12-332409. Vertical error bars are derived from Equation (11).

3.3 Selection of lens-source pairs

An effective discrimination between background lensed sources, and foreground and cluster member galaxies is necessary to accurately derive the halo density profile. We subsequently select background galaxies using photometric redshifts or their position in the (r-i) vs (g-r)-color-color (hereafter dubbed gri-CC) plane.

3.3.1 Background galaxies

A thorough selection of sources allows us to minimize contamination from misplaced galaxies and their incorrect shear. This step is essential as contaminated galaxies usually dilute the resulting lensing signal (Broadhurst et al. 2005; Medezinski et al. 2007). We first select members in the source catalog with

$$z_s > z_l + \Delta z \ , \quad (12)$$

where z_s is the best-fitting BPZ photometric redshift of the source, z_l is the lens redshift and $\Delta z = 0.05$ is a secure interval to balance uncertainties coming from photometric redshifts.

Then, we applied a more accurate redshift filter following the work of Bellagamba et al. (2019) and Sereno et al. (2017),

$$(0.2 \le z_s \le 1) \wedge (\texttt{ODDS} \ge 0.8) \wedge \left(z_{s,min} > z_l + \Delta z\right) \ . \quad (13)$$

The ODDS parameter from the KiDS shear catalog accounts for the probability distribution function (PDF) of the redshift: a high value indicates a high reliability of the best photo-z estimate. The parameter $z_{s,min}$ measures the lower bound of the 2σ confidence interval of the PDF.

A complementary approach for selecting galaxies is based on the source distribution in the gri-CC plane. Medezinski et al. (2010) highlight a strong correlation between the location in the (r-i) vs (g-r) diagram and the galaxy redshift. Following an original proposal by Oguri et al. (2012), Bellagamba et al. (2019) exploit a relevant selection which filters KiDS galaxies beyond $z_s \simeq 0.7$, obtaining

$$(g - r < 0.3) \vee (r - i > 1.3) \vee (g - r < r - i) \ . \quad (14)$$

This selection was tested in Covone et al. (2014), Sereno

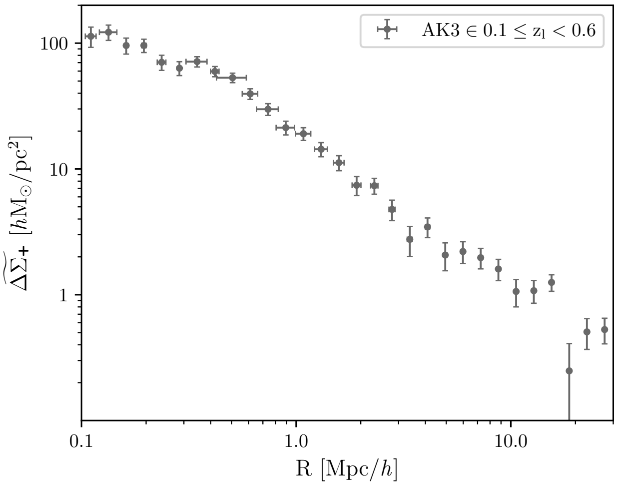

Figure 3. The stacked matter density profile of AK3 clusters with $0.1 \leq z_l < 0.6$. The signal is computed assuming the combined selections given in Equation (15). Horizontal and vertical bars are derived from Equation (11).

et al. (2017, 2018) and Bellagamba et al. (2019), and conserves 97 percent of galaxies with CFHTLenS spectroscopic redshifts above $z_s \gtrsim 0.63$ (Sereno et al. 2017). In Appendix C, we discuss the alternative color-color selection presented in Medezinski et al. (2010) and the contamination fraction that leads the two colour-colour cuts in the COSMOS field.

Finally, we formulate the selection of the background sources by combining the following Equations as follows

$$(12) \wedge [(13) \vee (14)] \ . \tag{15}$$

As a further restriction for the selection presented in this study, we restricted the source redshifts to the range $z_s > 0.2$. This complementary selection is assumed since a large fraction of sources are below this limit, which might increase the contamination of nearby clusters (Sereno et al. 2017).

3.3.2 *Foreground clusters*

We consider galaxy clusters selected in the redshift range $z_l \in [0.1, 0.6[$, as done in Bellagamba et al. (2019). We select clusters at $z_l < 0.6$ because the *gri*-CC cut is very effective for sources at $z_s > 0.6$. Furthermore remote clusters convey a lower density of background sources. Objects at $z_l < 0.1$ are discarded because of the reduced lensing power of low mass clusters (see Figure 1) and the inferior photometric redshift accuracy of the sources. The final sample consists of 6961 clusters (87.1% of the whole catalog). In Figure 3 we plot the mass density profile obtained for the complete cluster sample assuming the combined selection of sources given in Equation (15).

3.4 Shear data stacked in bins

Stacking the signal permits us to constrain the two parameters of the halo model (see Section 4) and derive a generic halo bias-mass relation (see Section 6.3). We consider 14 cluster bins combined in redshift and richness. Table 1 shows the binning pattern, also displayed in cells in the z_l vs λ_* diagram in Figure 1. The binning scheme mostly follows Bellagamba et al. (2019) to provide nearly uniform WL SNR per bin. The only difference is for the last redshift bin, in which a larger number of clusters are considered for intermediate richness ranges. In this way, we compensate for the numerous galaxy clusters in the higher richness bin and homogenize the distribution of clusters in this redshift bin with the two other redshift bins.

Table 1. Redshift-richness bins for the WL analysis.

z_l	λ_*				
$[0.1, 0.3[$	$[0, 15[$	$[15, 25[$	$[25, 35[$	$[35, 45[$	$[45, 140[$
$[0.3, 0.45[$	$[0, 20[$	$[20, 30[$	$[30, 45[$	$[45, 60[$	$[60, 140[$
$[0.45, 0.6[$	$[0, 25[$	$[25, 40[$	$[40, 55[$	$[55, 140[$	

Considering the j-th radial bin of the k-th galaxy cluster, the corresponding stacked observable in the K-th cluster bin is

$$O_{j,K} = \frac{\sum_{k \in K} W_{j,k} O_{j,k}}{\sum_{k \in K} W_{j,k}} \ , \tag{16}$$

with $W_{j,k} = \sum_{i \in j} w_{ls,i}$. The shear estimate is not accurate since the correction of the multiplicative bias has already been applied via Equation (8) to the signal of each individual galaxy cluster, while it should be corrected over the averaged measure of the bin. We compute the effective value of the cluster observable O_k, e.g. richness or redshift of cluster k, among the cluster bins K through a lensing-weighted mean (e.g. Umetsu et al. 2014)

$$O_K = \frac{\sum_{k \in K} W_k O_k}{\sum_{k \in K} W_k} \ , \tag{17}$$

where $W_k = \sum_j W_{j,k}$ is the total weight of the cluster k for the whole area of the cluster profile.

The analysis of covariance is performed by computing all the observable quantities using a bootstrap method with replacement and resampling the source catalog 1000 times. In addition, we combined the shear signal with a covariance matrix computed over the realizations of the bootstrap sampling. We also paid attention to the cross-covariances between the redshift-richness bins. As a final step, we subtract the signal around random points from the stacked profiles, and the corresponding error is added in quadrature. The final covariance signal can alternatively be assessed with a jackknife method, where the lensing signal is measured over regions of the sky. This way, there is no longer any need to combine cluster and random covariance matrices, since the statistical covariance is directly computed from the subtracted lensing signal (Singh et al. 2017). Covariances and random signals aim to compensate for the statistical noise and the systematic effects. We discuss these two contributions in detail in Appendices A and B.

4 HALO MODEL

In this section we explore the theoretical mass density distribution of the halo, also called the halo model. A composite density profile is then fitted to the measured tangential reduced shear given in Equation (7). All the terms in this relation depend on the surface density Σ. It is computed by the projection over the line of sight of the excess matter density $\Delta\rho$ in a sphere centered on the halo as

$$\Sigma(R) = \int_{-\infty}^{\infty} \Delta\rho\left(\sqrt{R^2+\chi^2}\right) d\chi \; . \quad (18)$$

$\Delta\rho$ includes the two terms of the halo model from the halo-matter correlation function ξ_{hm}

$$\Delta\rho = \bar{\rho}_m \xi_{hm} \; , \quad (19)$$

and the mean matter density $\bar{\rho}_m \equiv \Omega_m \rho_c$ must be computed in physical units at the redshift of the sample. The critical density ρ_c is related to the first of the Friedmann equations, and is defined as

$$\rho_c = \frac{3H(z)^2}{8\pi G} \; . \quad (20)$$

In WL, we average this quantity over the disk to derive the mean surface density enclosed within the radius R

$$\overline{\Sigma}(<R) = \frac{2}{R^2}\int_0^R R'\Sigma(R')\,dR' \; . \quad (21)$$

In the following and for the terms contributing to the halo model, we are interested in the main lens structure (Section 4.1), which comprises the total mass of the halo and its concentration. In addition, we include the contribution of possibly miscentered density profiles in Section 4.2. Finally, Section 4.3 completes the halo model with the correlated matter component and allows the cosmological study from the analysis of the halo bias. In Figure 4 we display, as an example, the complete model for a given mass, concentration, bias and redshift of the halo.

4.1 Main halo component

The correlation between the halo and its own matter content is given by the halo matter density profile ρ_h

$$\xi_{1h} = \frac{\rho_h}{\bar{\rho}_m} - 1 \; . \quad (22)$$

Analytic calculations and numerical simulations suggest that dark matter halos have a symmetric density profile in a spherical aperture (Navarro et al. 1996). More recent studies look at the impact of the triaxiality of the halos as a new source of uncertainty in the WL signal (Oguri et al. 2005; Meneghetti et al. 2010; Sereno & Umetsu 2011). This systematic involves a larger scatter of the mass and over-estimates the concentration when triaxial clusters are aligned with the line of sight. Several works, such as Navarro et al. (1997); Bullock et al. (2001) provided a specific analytical form for the halo distribution, also called the Navarro-Frenk-White (NFW) density profile, in which the density varies with the distance from the center r as

$$\rho_{\rm NFW} = \frac{\rho_s}{(r/r_s)(1+r/r_s)^2} \; , \quad (23)$$

where $\rho_s = \rho_c\delta_c$ is the scale density and r_s the scale radius. The overdensity contrast δ_c can be expressed as a function of the concentration c and the overdensity factor Δ as

$$\delta_c = \frac{\Delta c^3}{3m\,(c)} \; . \quad (24)$$

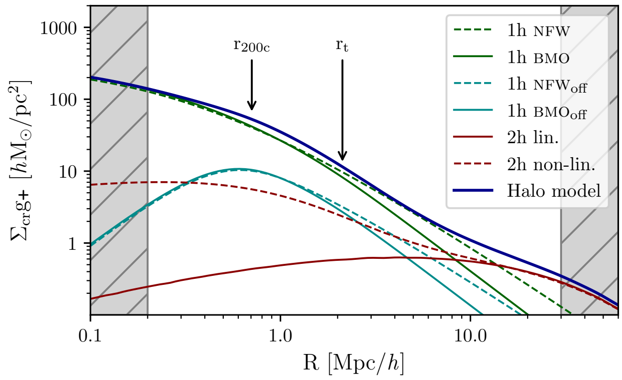

Figure 4. The halo model (blue) is composed of the BMO halo mass profile (thick green, Baltz et al. 2009), its off-centered contribution (thick cyan, Johnston et al. 2007b) and the second term derived from the linear matter power spectrum (thick red, Eisenstein & Hu 1999). For comparison, we show the centered / off-centered NFW mass profile (dashed green / cyan, Navarro et al. 1997) and the surrounding matter term with a non-linear power spectrum (dashed red, Takahashi et al. 2012). The density profile is computed in this example for a halo at $z_l = 0.2$ with a total mass $M_{200c} = 10^{14}$ $M_\odot/h$, a concentration $c_{200c} = 4$ and a bias set at $b_h = 1$ (with $\sigma_8 = 0.83$). The variance and the fraction of an off-centered population contribute to the profile with $\sigma_{\rm off} = 0.25$ Mpc/h and $f_{\rm off} = 0.25$. Finally, the reduced shear is given for an effective source redshift $z_s = 1$, while the non-shaded area reveals the range allowed by the stacked WL analysis.

The function m(c) depends the choice of density profile and on the concentration parameter as in Equation(26). Therefore, we adopt the common virial value $\Delta = 200c$, relating to a spherical volume with a density 200 times higher than the critical density of the Universe. Hence, we parametrize the scale radius as $r_s = r_{200c}/c_{200c}$. We leave the concentration within that sphere free in order to study the relation between the mass and the concentration in Section 6.2. A second approach would be to consider an existing mass-concentration scaling relation, e.g. from Merten et al. (2015b) based on X-ray selected galaxy clusters of the Cluster Lensing And Supernova Survey with Hubble (CLASH, Postman et al. 2012), or from simulations (e.g. Child et al. 2018). The 3D NFW profile can be analytically converted into a 2D version and thereby extended to an excess surface mass density version following Golse & Kneib (2002).

The NFW profile has a non-physical divergence of its total mass (Takada & Jain 2003). The Baltz-Marshall-Oguri (BMO, Baltz et al. 2009) profile is a smoothly truncated version of the NFW profile which allows to circumvent this problem with infinite mass. This profile presents the following shape

$$\rho_{\rm BMO} = \frac{\rho_s}{(r/r_s)(1+r/r_s)^2}\left(\frac{r_t^2}{r^2+r_t^2}\right)^2 \; . \quad (25)$$

We set the truncation radius to $r_t = 3r_{200c}$ in the following analysis (Covone et al. 2014; Sereno et al. 2017; Bellagamba et al. 2019). The BMO profile also provides less biased estimates of mass and concentration with respect to the NFW profile, and better describes the density profile at the transition scales between the one-halo and two-halo terms (Oguri

& Hamana 2011). Baltz et al. (2009) provide an analytical expression for the surface mass density. The function m in Equation (24) differs according to the profile as (Oguri & Hamana 2011)

$$\begin{aligned} m_{\rm NFW} &= \ln(1+c) - \frac{c}{1+c} \\ m_{\rm BMO} &= \frac{\tau^2}{2(\tau^2+1)^3(1+c)(\tau^2+c^2)} \\ &\times \Big[c(\tau^2+1)\{c(c+1) - \tau^2(c-1)(2+3x) - 2\tau^4\} \\ &+ \tau(c+1)(\tau^2+c^2)\{2(3\tau^2-1)\arctan(c/\tau) \\ &+ \tau(\tau^2-3)\ln(\tau^2(1+c)^2/(\tau^2+c^2))\}\Big] \,, \end{aligned} \tag{26}$$

where $\tau \equiv r_t/r_s$. We display the NFW and BMO surface mass density profiles in Figure 4. We indicate r_{200c} and r_t locations with vertical arrows.

4.2 Miscentering correction

The detection of clusters is based on the identification of galaxy overdensities, hence the adopted cluster center corresponds to the peak in the projected space of the galaxy distribution. This peak may not coincide with the barycenter of the DM distribution. In reality, we expect the detected pixel position of the cluster center to possibly be shifted with respect to the center of the halo. Skibba & Macciò (2011) and George et al. (2012) discussed the importance of locating the centers of dark matter halos in order to properly estimate their mass profiles. Miscentering is expected to be a small with respect to the cluster radius, under the assumption that light traces dark matter (Zitrin et al. 2011a,b; Coe et al. 2012; Merten et al. 2015a; Donahue et al. 2016). However, radial miscentering is larger for optical clusters selected in a survey with a complex mask footprint.

Hence, we introduce the radial displacement of the cluster center $R_{\rm off}$, while the off-centered density profile is the average of the centered profile over a circle drawn around the incorrect center (Yang et al. 2006; Johnston et al. 2007b)

$$\Sigma_{\rm off}(R|R_{\rm off}) = \frac{1}{2\pi}\int_0^{2\pi} \Sigma_{\rm cen}\left(\sqrt{R^2 + R_{\rm off}^2 + 2RR_{\rm off}\cos\theta}\right) d\theta \,. \tag{27}$$

This term holds for an isolated galaxy cluster. We extend the profile to a global population of galaxy clusters so that the off-centered contribution is given by

$$\overline{\Sigma}_{\rm off}(R|\sigma_{\rm off}) = \int_0^{\infty} P(R_{\rm off},\sigma_{\rm off})\Sigma_{\rm off}(R|R_{\rm off})dR_{\rm off} \,, \tag{28}$$

where the displaced distances $R_{\rm off}$ follows a Rayleigh distribution with parameter $\sigma_{\rm off}^2$ (Simet et al. 2017; Melchior et al. 2017)

$$P(R_{\rm off},\sigma_{\rm off}) = \frac{R_{\rm off}}{\sigma_{\rm off}^2}\exp\left[-\frac{1}{2}\left(\frac{R_{\rm off}}{\sigma_{\rm off}}\right)^2\right] . \tag{29}$$

Considering $f_{\rm off}$ as the fraction of the off-centered population, the total miscentered density profile can be modelled as

$$\Sigma_{\rm mis}(R|\sigma_{\rm off},f_{\rm off}) = (1-f_{\rm off})\Sigma_{\rm cen}(R) + f_{\rm off}\overline{\Sigma}_{\rm off}(R|\sigma_{\rm off}) \,. \tag{30}$$

Since this mainly impacts the central region of the halo profile, we reduce the correction to the one-halo component of the model. The miscentering effect is illustrated in Figure 4 with the two elements of the above sum. From the figure, we can also see that the miscentering parameters are degenerate with the halo concentration.

4.3 Correlated matter component

On large scales, the lensing signal of the halo is dominated by correlated matter, e.g. neighbouring halos or filaments, rather than its own matter content. The two-halo term usually contributes to the whole profile at $R \gtrsim 10$ Mpc/*h*. Following the standard approach, this signal is proportional to the matter-matter correlation function ξ_m through the halo bias b_h

$$\xi_{2h} = b_h \xi_m \,. \tag{31}$$

We derive the matter correlation function at radius r from the Fourier transform of the dimensionless matter power spectrum $\Delta^2(k) \equiv P(k)k^3/(2\pi^2)$, and the first-order spherical Bessel function $j_0(x) = \sin x/x$

$$\xi_m = \int_0^{\infty} \frac{\Delta^2(k)}{k} j_0(kr)dk \,. \tag{32}$$

We illustrate the second term of the surface mass density profile in Figure 4 assuming bias $b_h = 1$. We also display results given by the linear matter power spectrum (Eisenstein & Hu 1998, 1999) and by the non-linear matter power spectrum computed assuming the so-called halofit model (Takahashi et al. 2012). A halo mass of $M_{200c} = 10^{14}$ $M_\odot/h$ and concentration of $c_{200c} = 4$ contribute 15% and 25%, resptively, to the whole profile at the intermediate scale $R = 3.16$ Mpc/*h*, considering the BMO miscentered profile as the one-halo term. We focus on the linear version, since we provide a comparative analysis with theoretical mass-bias relations (e.g. Tinker et al. 2010) derived from simulations, where results are given in terms of "peak height" in the linear density field. However, it is important to keep in mind that the non-linear version of the power spectrum shows a non-negligible contribution of mass fluctuations at small and intermediate scales. The second term of the halo model is parameterized in terms of a degenerate value of the halo bias with σ_8^2. This parameter defines the rms fluctuations $\sigma(M)$ for a mass enclosed in a comoving sphere of radius 8 Mpc/*h*. This actually corresponds to the typical scale for the formation of galaxy clusters. The parameter σ_8^2 also derives from the matter power spectrum as a normalization factor and permits cosmological inference of the product $b_h\sigma_8^2$.

4.4 Total halo model

The total surface mass density profile is modelled with the following terms and their associated marginalized parameters

$$\Sigma_{\rm tot} = \Sigma_{\substack{1h\\ \rm BMO\\ \rm mis}}(M_{200c}, c_{200c}, \sigma_{\rm off}, f_{\rm off}) + \Sigma_{\substack{2h\\ \rm lin}}(b_h\sigma_8^2) \,. \tag{33}$$

Mass and bias are the two most critical variables among the five free parameters since they both act on the amplitudes of the one-halo and two-halo terms, respectively. For example, Figure 4 shows Equation (33) in blue with $z_l = 0.2$, $z_s = 1$, $M_{200c} = 10^{14}$ $M_\odot/h$, $c_{200c} = 4$, $\sigma_{\rm off} = 0.25$ Mpc/*h*, $f_{\rm off} = 0.25$ and $b_h\sigma_8^2 = 0.83^2$.

In Section 5, we describe the numerical method used to assess the posteriors and best estimates given by the data derived in Sections 2 and 3 with the model described in this Section. Bayesian inference allows us to correlate the different halo parameters together and completes the cosmological study.

5 MCMC METHOD

In Bayesian statistics, the Monte Carlo Markov Chain (MCMC) method is commonly used to sample posterior distributions. The best parameters are found with the maximum likelihood distribution, giving the highest probability of the sample (also given by minimizing the χ^2-distribution). In this specific study, the likelihood function is the joint probability of getting the measurement $\widetilde{\Delta\Sigma}$ with the parameters $\theta = [\log_{10} M_{200c}, c_{200c}, \sigma_{off}, f_{off}, b_h\sigma_8^2]$ given the model $\Delta\Sigma$. This probability distribution is assumed to be normal and multiplied over the radial bins i, j of the profile to provide a global approximation of the variable

$$\mathcal{L}(\theta) \equiv p\left(\widetilde{\Delta\Sigma}|\theta\right) \propto \exp\left(-\frac{\chi^2}{2}\right) , \tag{34}$$

where

$$\chi^2 = \sum_{i,j}\left(\widetilde{\Delta\Sigma}_i - \Delta\Sigma_i\right) C_{ij}^{-1}\left(\widetilde{\Delta\Sigma}_j - \Delta\Sigma_j\right) , \tag{35}$$

and C_{ij} is the covariance matrix described in Appendix A.

The χ^2 parameter is a good indicator of the goodness of fit of a statistical model. Its probability distribution depends on the degree of freedom which is the difference between the number of observations considered in the analysis and the number of variables in the halo model, here df $= 26 - 5 = 21$. In a goodness-of-fit test, the null hypothesis assumes that there is no significant difference between the observed and the expected values. Considering a significance level of $\alpha = 0.01$ defining the critical χ^2 values on the left and right tails of the distribution, the null hypothesis is verified if $8.9 < \chi^2 < 38.9$.

The likelihood is defined in the prior uniform distribution of the halo parameters having the following conservative bounds (Bellagamba et al. 2019):

- $\log_{10}(M_{200c}/(M_\odot/h)) \in [12.5, 15.5]$
- $c_{200c} \in [1, 20]$
- $\sigma_{off} \in [0, 0.5]$ Mpc/h
- $f_{off} \in [0, 0.5]$
- $b_h\sigma_8^2 \in [0, 20]$

We based the Bayesian inference on the `emcee`[2] algorithm (Foreman-Mackey et al. 2013), which uses an affine-invariant sampling method initially introduced in Goodman & Weare (2010). The cosmological parameters are defined for the fit as in Section 1.

We adopted an ensemble sampler with 32 walkers over a chain of 10,000 steps, giving a total size of 320,000 walkers to sample the posterior distribution. This scheme was already adopted in McClintock et al. (2019). We define the burn-in phase as being twice the integrated autocorrelation time τ_f of our chain f. In addition, we tested the convergence of the MCMC by running the potential scale reduction factor $\hat{R}$ (see Gelman & Rubin 1992). Convergence is reached if the criterion $\hat{R} < 1.1$ is satisfied.

In Figure 5, we show the joint posterior distributions given by the sampler for the total profile shown in Figure 3. In the case of a normal PDF (as for the halo mass and bias), the 16*th*-84*th* and 2*th*-98*th* percentiles highlight 1σ and 2σ confidence regions forming ellipsoids in the 2D parameter space. In the opposite case, the percentiles show distorted ellipsoidal regions which define the errors on the parameter. For example the f_{off} posterior distribution gives errors larger than the prior boundaries, while we expect the posterior of the parameter to follow a Gaussian-like distribution within the limits defined by the prior function. This effect suggests that the parameter is imprecisely constrained. Nevertheless, the sampler distributions of the parameters of interest (i.e. mass, concentration and bias) converge significantly, which makes it possible to consistently exploit their relation. For the following, we define the error on the parameters as the 1σ confidence interval, specifically approximated here with the region where 68% of walkers lie around the mean.

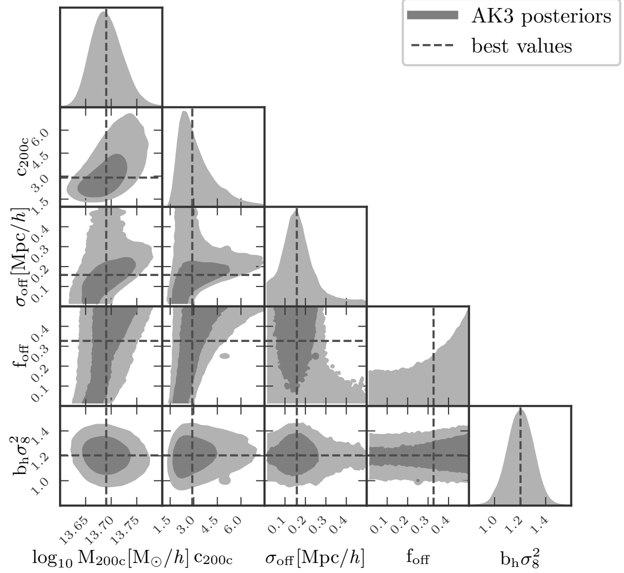

Figure 5. Posterior distributions arising from the halo model and the density profile derived in this study. The median of the marginalized distribution of the mass, concentration, off-centering parameters and bias are displayed as dashed lines. The 2D posterior distributions also show the 68% and 95% confidence regions in shaded grey regions.

6 RESULTS

We obtain the stacked radial shear profiles for the AMICO KiDS-DR3 galaxy clusters split into 14 redshift-richness bins, from 0.2 to 30 Mpc/h. We use the MCMC method presented in Section 5 to fit the profiles with the halo model discussed in Section 4. Data and fitted models are shown

[2] `https://emcee.readthedocs.io/`

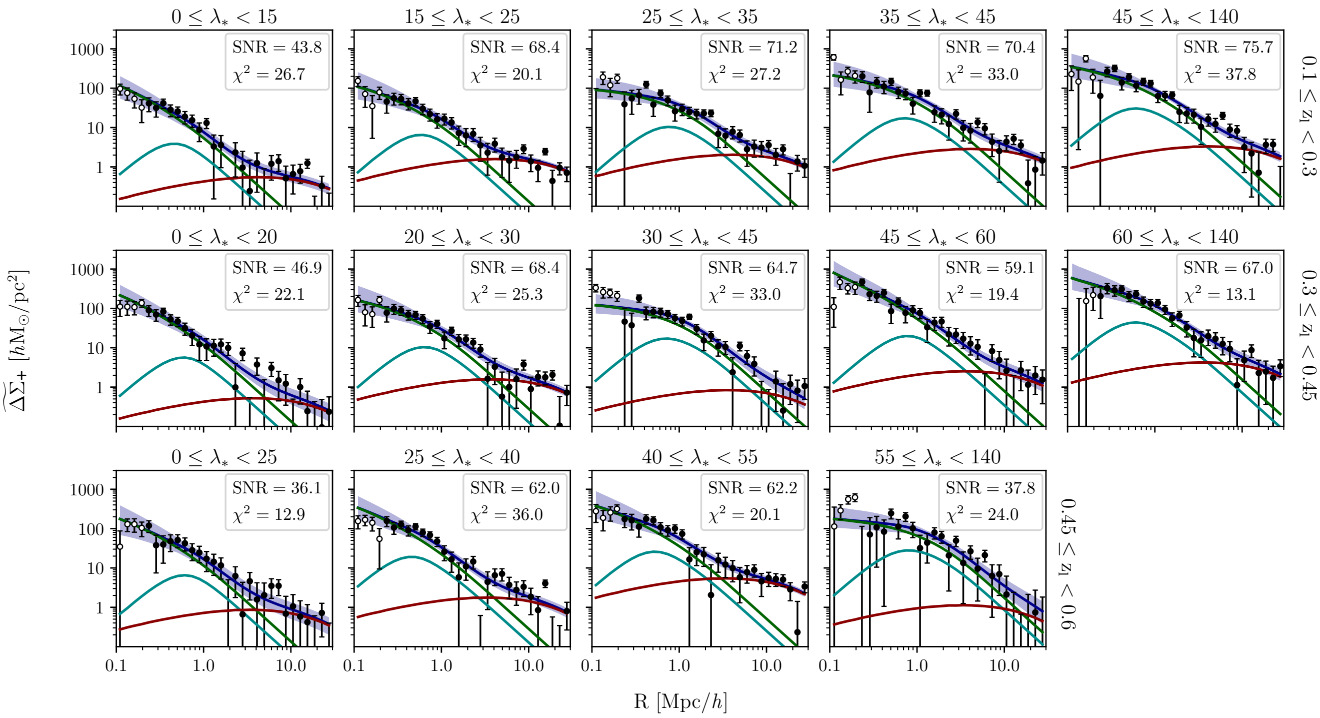

Figure 6. The stacked shear profiles and the halo model (blue) corresponding to the fitted parameters, with the 1σ confidence interval (blue region). Each row corresponds to a redshift bin, while each panel corresponds to an associated richness bin. The top right legends show the SNR, computed from each radial bin and summed over the [0.2, 30] Mpc/h radial range, and the χ^2 computed as in Equation (35) given by the 50*th* percentile parameters. The model components: the main halo term (green), the off-centered contribution (cyan), and the correlated matter term (red). Empty points show the first four radial bins not considered in the fit.

Table 2. Mass, concentration and bias resulting from the fit with their errors given in separate rows as different redshift and richness bins. These values correspond to the 16*th*, 50*th* and 84*th* percentiles of the posterior distributions. We also show the mass measurement in the radial range [0.2, 3.16] Mpc/h in brackets. Mean richness ($\bar{\lambda}_*$), lens redshift ($\bar{z}_l$) and source redshift ($\bar{z}_s$) are computed from Equations (17) and (10) and their errors are assumed to be the rms weighted sample deviation. We report both the number of clusters N_l and the fraction of clusters relative to the full selected cluster sample in each redshift-richness bin (column 6).

z_l	λ_*	$\bar{z}_l$	$\bar{\lambda}_*$	$\bar{z}_s$	N_l	$\log_{10}(M_{200c}/(M_\odot/h))$	c_{200c}	$b_h\sigma_8^2$
[0.1, 0.6[	[0, 140[	0.372 ± 0.005	19.92 ± 0.50	0.763 ± 0.004	6961 (100.0%)	$13.69^{+0.03}_{-0.03}$ $(13.68^{+0.03}_{-0.03})$	$2.90^{+1.43}_{-0.70}$	$1.20^{+0.10}_{-0.10}$
[0.1, 0.3[	[0, 15[	0.192 ± 0.004	10.25 ± 0.21	0.700 ± 0.004	1246 (17.9%)	$13.24^{+0.08}_{-0.08}$ $(13.23^{+0.08}_{-0.08})$	$9.27^{+6.85}_{-5.05}$	$0.60^{+0.18}_{-0.18}$
[0.1, 0.3[	[15, 25[	0.216 ± 0.005	18.94 ± 0.28	0.726 ± 0.006	683 (9.8%)	$13.56^{+0.08}_{-0.08}$ $(13.58^{+0.08}_{-0.07})$	$4.25^{+5.18}_{-2.05}$	$1.71^{+0.24}_{-0.25}$
[0.1, 0.3[	[25, 35[	0.226 ± 0.009	29.09 ± 0.51	0.742 ± 0.011	209 (3.0%)	$14.01^{+0.07}_{-0.07}$ $(14.04^{+0.07}_{-0.07})$	$1.64^{+1.00}_{-0.46}$	$2.19^{+0.46}_{-0.46}$
[0.1, 0.3[	[35, 45[	0.232 ± 0.017	39.61 ± 0.83	0.740 ± 0.020	83 (1.2%)	$14.29^{+0.06}_{-0.07}$ $(14.30^{+0.06}_{-0.07})$	$3.17^{+2.23}_{-1.10}$	$3.07^{+0.76}_{-0.77}$
[0.1, 0.3[	[45, 140[	0.228 ± 0.019	56.05 ± 5.86	0.747 ± 0.022	44 (0.6%)	$14.53^{+0.05}_{-0.06}$ $(14.52^{+0.06}_{-0.06})$	$3.95^{+2.25}_{-1.21}$	$3.56^{+1.01}_{-1.04}$
[0.3, 0.45[	[0, 20[	0.374 ± 0.005	15.13 ± 0.38	0.860 ± 0.002	1110 (15.9%)	$13.60^{+0.08}_{-0.08}$ $(13.60^{+0.08}_{-0.08})$	$9.31^{+6.57}_{-4.58}$	$0.52^{+0.28}_{-0.26}$
[0.3, 0.45[	[20, 30[	0.388 ± 0.005	24.16 ± 0.39	0.863 ± 0.003	769 (11.0%)	$13.87^{+0.07}_{-0.07}$ $(13.93^{+0.07}_{-0.07})$	$3.65^{+3.71}_{-1.54}$	$1.57^{+0.36}_{-0.35}$
[0.3, 0.45[	[30, 45[	0.390 ± 0.008	35.94 ± 0.94	0.863 ± 0.004	320 (4.6%)	$14.20^{+0.06}_{-0.06}$ $(14.19^{+0.06}_{-0.06})$	$1.63^{+0.82}_{-0.43}$	$0.83^{+0.52}_{-0.47}$
[0.3, 0.45[	[45, 60[	0.393 ± 0.015	50.94 ± 1.86	0.866 ± 0.008	87 (1.2%)	$14.40^{+0.08}_{-0.08}$ $(14.39^{+0.07}_{-0.08})$	$10.65^{+5.73}_{-4.52}$	$2.51^{+1.02}_{-1.02}$
[0.3, 0.45[	[60, 140[	0.381 ± 0.022	75.81 ± 9.29	0.860 ± 0.012	45 (0.6%)	$14.64^{+0.06}_{-0.06}$ $(14.66^{+0.06}_{-0.06})$	$5.11^{+3.15}_{-1.62}$	$4.20^{+1.42}_{-1.43}$
[0.45, 0.6[	[0, 25[	0.498 ± 0.006	19.76 ± 0.53	0.887 ± 0.003	1107 (15.9%)	$13.60^{+0.10}_{-0.11}$ $(13.58^{+0.10}_{-0.11})$	$6.53^{+7.74}_{-3.97}$	$0.82^{+0.40}_{-0.39}$
[0.45, 0.6[	[25, 40[	0.518 ± 0.008	30.75 ± 0.74	0.888 ± 0.003	952 (13.7%)	$13.94^{+0.06}_{-0.06}$ $(13.93^{+0.06}_{-0.06})$	$8.43^{+6.54}_{-3.76}$	$1.68^{+0.47}_{-0.46}$
[0.45, 0.6[	[40, 55[	0.513 ± 0.018	46.14 ± 1.54	0.888 ± 0.006	232 (3.3%)	$14.19^{+0.07}_{-0.08}$ $(14.23^{+0.07}_{-0.08})$	$6.18^{+5.77}_{-2.65}$	$5.16^{+0.89}_{-0.91}$
[0.45, 0.6[	[55, 140[	0.516 ± 0.028	66.69 ± 8.22	0.888 ± 0.012	74 (1.1%)	$14.56^{+0.08}_{-0.10}$ $(14.54^{+0.10}_{-0.11})$	$1.50^{+0.77}_{-0.36}$	$1.07^{+1.21}_{-0.75}$

in Figure 6. The SNR is computed as $\widetilde{\Delta\Sigma}_j/\sigma_{\widetilde{\Delta\Sigma}_j}$ from Equations (8) and (11) and summed over the radial bins j.

Table 2 shows the best fit values for the halo mass, the concentration and the halo bias in each cluster bin with the 68% confidence bounds. The parameters computed over the stacked profile of the full catalog are also displayed in the first row, and correspond to the dashed values shown in Figure 5 with $\chi^2 = 29.8$, which suggests that the goodness-of-fit test has been passed, as for the other bins. The mean redshift and the mean richness of the lenses are computed as in Equation (17), while the mean redshift of the sources is the effective redshift z_{back} in Equation (10). We additionally measure the mass from a fitting in the radial range [0.2, 3.16] Mpc/h assuming the same priors for the full profile, unlike the bias derived from Tinker et al. (2010). These measurements are in good agreements with Bellagamba et al. (2019) and show for the two lower redshift bins a relative percentage difference within ∼ 5% (see Figure 7). This variation could be explained by the different choice for the radial bins within 3.16 Mpc/h: 14 logarithmically equispaced annuli were used in the previous study, while in this work we selected the radial bins within 3.16 Mpc/h over the full radial range of the shear profile. These two definitions make the profiles and the derived measurements of the mass slightly different.

In the following, we investigate the correlations of the mass with the cluster richness (see Section 6.1), with the concentration (see Section 6.2) and with the bias (see Section 6.3).

6.1 Halo mass-richness relation

The average redshift and richness of the lenses in each redshift bin are shown in Figure 1, and follow the global trend given by the removal of low mass clusters at high redshift for AK3 clusters with SNR < 3.5. Figure 6 shows that the differential density at a given radius increases with richness, suggesting a clear correlation between cluster mass and richness. Figure 7 shows the relation between the mass and the effective richness of the cluster bins. We fit this relation assuming the following power law in logarithmic scale

$$\log_{10}\frac{M_{200c}}{M_{piv}} = \alpha + \beta\log_{10}\frac{\lambda_*}{\lambda_{piv}} + \gamma\log_{10}\frac{E(z)}{E(z_{piv})}\ , \qquad (36)$$

where $E(z) \equiv H(z)/H_0$ and $M_{piv} = 10^{14} M_\odot/h$, $\lambda_{piv} = 30$, and $z_{piv} = 0.35$ corresponding to the median values for AK3 (Bellagamba et al. 2019). We estimate the parameters of this multi-linear function applying an orthogonal distance regression method (`ODR`[3]), involving mass, richness and redshift uncertainties. The fit gives

- $\alpha = 0.007 \pm 0.019$
- $\beta = 1.72 \pm 0.09$
- $\gamma = -1.35 \pm 0.70$.

As Figure 7 shows, these results are in remarkable agreement with Bellagamba et al. (2019) despite the different definition of richness bins at high redshifts and the different fitting method. In addition, they are also perfectly consistent with Lesci et al. (2020) and Sereno et al. (2020), regardless of the different approaches employed to fit the scaling relation.

[3] `https://docs.scipy.org/doc/scipy/reference/odr.html`

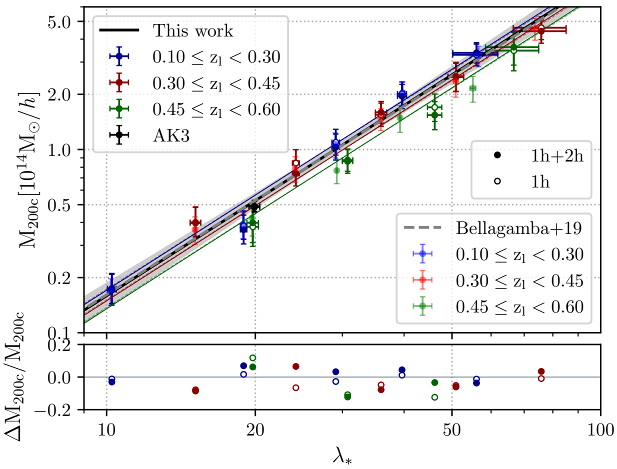

Figure 7. Mass-richness scaling relation for the full catalog (black) and for the low (blue), intermediate (red) and high (green) redshift bins. The thick line corresponds to the model formulated in Equation (36). Full and empty data points represent the measurements over the whole radial profile and over the central region of the halo, respectively. We compared our results with those presented in Bellagamba et al. (2019). The fainter colored points represent the data and the dashed lines represent the model. The relative change with respect to the results of this work is displayed in the bottom panel.

The positive correlation between shear signal and richness is shown in Figure 6 at large radii and implies a strong correlation between the bias and the mass. The SNR of individual radial bins at large scales is relatively low due to the poor quality of the shear produced by low mass clusters, and increases with the richness. The highest redshift-richness bin shows a particularly low SNR with a low amplitude for the shear profile, where usually we expect the signal amplitudes at small and large scales to be high in large richness bins. The poor quality of the lensing signal in this specific bin also impacts the halo mass and bias with a downward trend.

6.2 Halo mass-concentration relation

Halo concentration is determined by the mean density of the Universe at the epoch of halo formation (Neto et al. 2007; Giocoli et al. 2012). Thus, clusters that assemble later are expected to have a lower concentration than older clusters, formed when the mean density was higher. This determines a clear correlation with the halo mass in such a way that the halo concentration is expected to be a decreasing function of the halo mass. This is supported by our results shown in Figure 8. We compare the results with the concentration and mass measured with stacked WL data from 130,000 SDSS galaxy groups and clusters (Johnston et al. 2007a) and 1176 CFHTLenS galaxy clusters (Covone et al. 2014). These analyses are consistent within 1σ. The large and asymmetric error bars for the concentration reflect the high sensitivity of this parameter to the inner region, which is poorly covered by our WL analysis. Sereno & Covone (2013), Umetsu et al. (2014) and Sereno et al. (2015a) discussed the effects stemming from the different choices and forms of the priors, and found a log-uniform prior might underestimate the concentration. As done for the redshift-mass-richness relation, we fitted the redshift-concentration-mass relation with a power-law function (Duffy et al. 2008), given as

$$\log_{10} c_{200c} = \alpha + \beta \log_{10} \frac{M_{200c}}{M_{piv}} + \gamma \log_{10} \frac{1+z}{1+z_{piv}} . \quad (37)$$

We assume the pivot mass and redshift have the same values as in Equation (36), while the multi-linear regression is processed with the `ODR` routine over the full sample. We find

- $\alpha = 0.62 \pm 0.10$
- $\beta = -0.32 \pm 0.24$
- $\gamma = 0.71 \pm 2.51$.

The large error on γ suggests a weak constraint of the redshift evolution due to the sparse number of data points (Sereno et al. 2017). The black line in Figure 8 shows the fitted power law with the 1σ uncertainty interval, assumed as the range defined by the standard deviations of the estimated parameters and derived from the diagonal terms of the asymptotic form of the covariance matrix (see Fuller 1987). Because of the small set of data points, the fit in each redshift bin does not provide consistent results for the coefficients. In Figure 8, we also show the theoretical relations between mass and concentration given by six different analyses of numerical simulations (Duffy et al. 2008; Dutton & Macciò 2014; Meneghetti et al. 2014; Diemer & Kravtsov 2015; Child et al. 2018; Diemer & Joyce 2019; Ishiyama et al. 2020). In the corresponding mass range, our results are in good agreement with the theoretical predictions, but have a steeper and lower relation with respect to the results obtained by Sereno et al. (2017) on the PSZ2LenS sample. The average concentration for the full AK3 catalog seems to show a lower value than Equation (37) and the theoretical expectations, but still remains in the 1σ confidence interval.

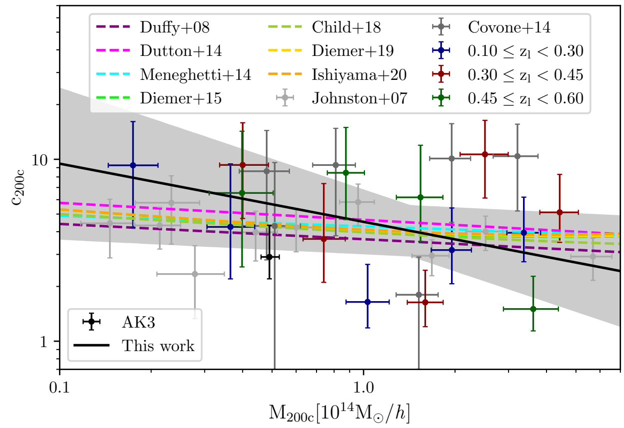

Figure 8. The relation between the mass and the halo concentration for the full catalog (black) and for the low (blue), intermediate (red) and high (green) redshift bins. The results on the concentration are compared with calibrated data from a stacked WL analysis on SDSS and CFHTLenS galaxy clusters (Johnston et al. 2007a; Covone et al. 2014). The thick black line reports the best estimate of the linear regression for Equation (37) with its 1σ confidence region. The relation is contrasted with results given by different theoretical analyses (Duffy et al. 2008; Dutton & Macciò 2014; Meneghetti et al. 2014; Diemer & Kravtsov 2015; Child et al. 2018; Diemer & Joyce 2019; Ishiyama et al. 2020).

6.3 Halo mass-bias relation

In Figure 9 we show the correlation between the cluster mass and the halo bias for the different redshift bins. The corresponding values are also reported in Table 2. These results are also in good agreement with previous results based on stacked WL studies on SDSS (Johnston et al. 2007a) and CFHTLens (Covone et al. 2014; Sereno et al. 2015b) galaxy clusters. As expected with the fourth richness bin at the highest redshift, the Bayesian inference of the halo bias shows a low SNR consistent with the poor quality of the lensing signal at large scales.

Tinker et al. (2010) calibrated the dependence of the large-scale bias on the mass by analysing the clustering of dark matter halos based on dark-matter only cosmological simulations, and obtained a 6% scatter from simulation to simulation. Alternatively, Seljak & Warren (2004) and Bhattacharya et al. (2011) also derived the average halo bias relation as a function of the cluster mass from *N*-body simulations. These bias-mass theoretical relations are reported in Figure 9 using the corresponding values of σ_8 in Table 3. Due to the limited number of points, the data in each redshift bin do not exhibit a strong correlation with the theoretical bias given at the effective redshift of the bin. The black lines present an agreement within 2σ with all our measurements except the third richness point for the high redshift bin, which agrees within 3σ due to its high amplitude. We

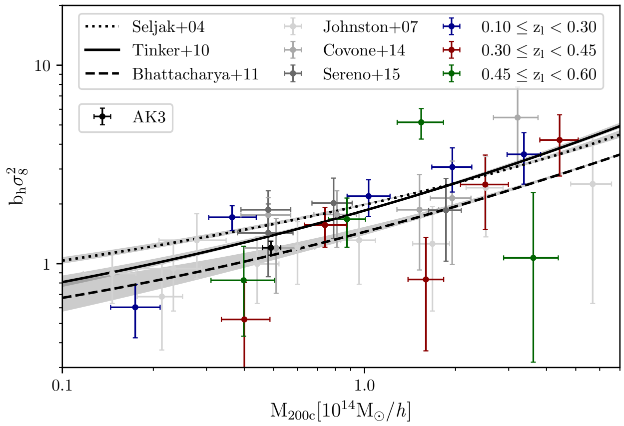

Figure 9. Halo bias-mass relation for the full catalog (black) and for the low (blue), intermediate (red) and high (green) redshift bins. The results on the halo bias are compared with calibrated data from a stacked WL analysis on SDSS and CFHTLenS galaxy clusters (Johnston et al. 2007a; Covone et al. 2014; Sereno et al. 2015b). Theoretical relations are derived from Seljak & Warren (2004); Tinker et al. (2010); Bhattacharya et al. (2011) and respectively displayed as dotted, thick and dashed lines. These functions are computed within their confidence interval using the values of σ_8 reported in Table 3.

attribute this statistical fluctuation to the low number of clusters in this region of richness-redshift space, since the few and uneven number of objects results in a poorer statistical measurement of the stacked lensing signal.

Table 3. Median, 16*th* and 84*th* percentiles of the posterior distribution for σ_8. We also show the difference, $\Delta\sigma_8$, between σ_8 measured on the median mass values, and σ_8 measured on the mass 16*th* and 84*th* percentile values.

The cosmological parameter is given for three relations derived from numerical simulations.

simulation	σ_8	$\Delta\sigma_8$
Seljak & Warren (2004)	$1.01^{+0.05}_{-0.05}$	0.02
Tinker et al. (2010)	$0.63^{+0.11}_{-0.10}$	0.01
Bhattacharya et al. (2011)	$0.66^{+0.19}_{-0.27}$	0.12

6.4 Constraint on σ_8

Since the halo bias is degenerate with σ_8^2, it is important to obtain independent constraints on this cosmological parameter within a ΛCDM framework. Here we let σ_8 be a free parameter in the theoretical mass-bias relation and fit the $b_h\sigma_8^2$ results with the method described in Section 5, assuming a uniform prior $\sigma_8 \in [0.2, 2.0]$. We use a diagonal covariance matrix, where the variance terms are the square of the errors on the bias defined by the 68% confidence regions. We do not account for the errors on the mass, hence accurate mass measurements are essential to constrain σ_8.

The resulting best fit values are shown in Table 3. Bhattacharya et al. (2011) used the “peak-background split” approach of Sheth & Tormen (1999) to fit the parameters of the mass function. The authors note that the bias function does not match the numerical results as well as direct calibrations, which could explain the discrepancy with respect to the results obtained with the two other relations. In order to estimate the effect of the mass uncertainty on cosmological inference, we measured σ_8 at masses corresponding to the 16*th* and 84*th* percentiles and noticed a difference with the median masses smaller than the statistical uncertainty of the parameter (see Table 3).

Figure 10 shows the three posterior distributions for σ_8 obtained in this work compared with the results from the cosmic microwave backround measurements by Planck (Planck Collaboration et al. 2020, Table 2, TT,TE,EE+lowE+lensing) and WMAP (Hinshaw et al. 2013, Table 3, WMAP-only Nine-year). Our constraint on σ_8 with the Seljak & Warren (2004) model, which has a sharp posterior that peaks around $\sigma_8 \sim 1$, highlights a discrepancy larger than 3σ with CMB values. The posteriors given by the Tinker et al. (2010) and Bhattacharya et al. (2011) models overlap within 2σ and 1σ with the CMB data, respectively, but the Bhattacharya et al. (2011) posterior is clearly different from a normal distribution. Because of the small size of the sample and the poor quality of the bias-mass measurements in some bins, our results yield quite broad posteriors that are necessarily in agreement with WMAP and Planck median values.

Finally in Figure 11 we present our reference result from Tinker et al. (2010) in the broader context of recent measurements of σ_8. This model was calibrated for a range of overdensities with respect to the mean density of the universe and can easily be converted to overdensities with respect to the critical density, which makes the bias more reliable for the mass definition M_{200c}. In addition, our $b_h\sigma_8^2$ results given by the Tinker et al. (2010) relation are more reliable

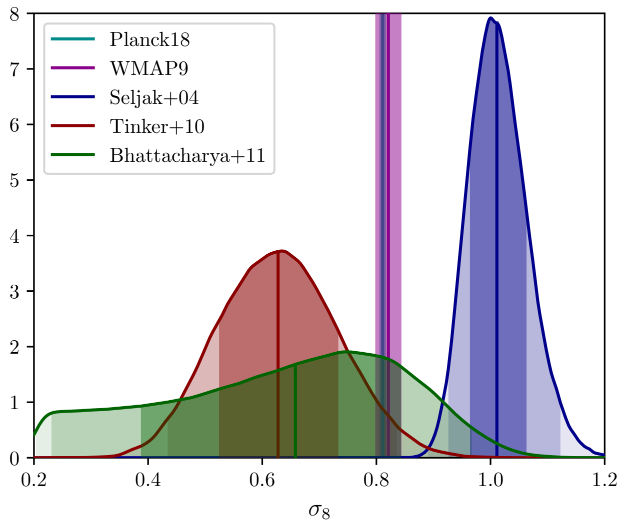

Figure 10. Posterior distribution for σ_8. The probability function is shown for three halo bias-mass relations, i.e. Seljak & Warren (2004), Tinker et al. (2010) and Bhattacharya et al. (2011), shown in blue, red and green, respectively. The dark to light shaded regions correspond to the $1-2-3\sigma$ intervals. We compare these distributions with the median values of Planck (cyan, Planck Collaboration et al. 2020, Table 2, TT,TE,EE+lowE+lensing) and WMAP (magenta, Hinshaw et al. 2013, Table 3, WMAP-only Nine-year).

in comparative terms, since studies referenced in this paper base their analyses on this relation. In particular, we display the results from clustering and cluster counts studies based on the AK3 galaxy clusters sample (Nanni et al. prep; Lesci et al. 2020), from cluster counts analyses done on SDSS-DR8 and 2500 deg^2 SPT-SZ Survey data (Costanzi et al. 2019; Bocquet et al. 2019), from galaxy clustering and weak lensing in DES-Y3 (DES Collaboration et al. 2021), and from cosmic shear analysis based on the HSC-Y1 and KiDS-DR4 catalogs (Hikage et al. 2019; Asgari et al. 2021, respectively). We also show the results from Planck (Planck Collaboration et al. 2020, Table 2) and WMAP (Hinshaw et al. 2013, Table 3) measurements.

Since the amplitude of the matter power spectrum correlates with the mean matter density, all these studies derived the combined parameter $S_8 \equiv \sigma_8\sqrt{\Omega_m/0.3}$. In this work we computed a direct measurement of σ_8, dependent on the specific cosmological model assumed in our analysis. In the figure, we indicate with different symbols the measurements of σ_8 obtained without assuming specific values of the cosmological parameters (empty dots) and those assuming $\Omega_m = 0.3$ (filled dots). Our results are closer to those obtained fixing $\Omega_m = 0.3$, as a low inference of Ω_m induces a higher estimate of σ_8, and vice versa. For example, Planck Collaboration et al. (2020) results show a posterior mean slightly higher than $\Omega_m = 0.3$, while for cosmic shear studies it is slightly lower, hence when fixing Ω_m to 0.3 there is a shift in σ_8 to larger values for Planck Collaboration et al. (2020) and lower values for cosmic shear surveys. However, the $2-3\sigma$ regions for the posteriors of the three theoretical relations agree with the results of these external references, regardless of the cosmological dependencies considered, but

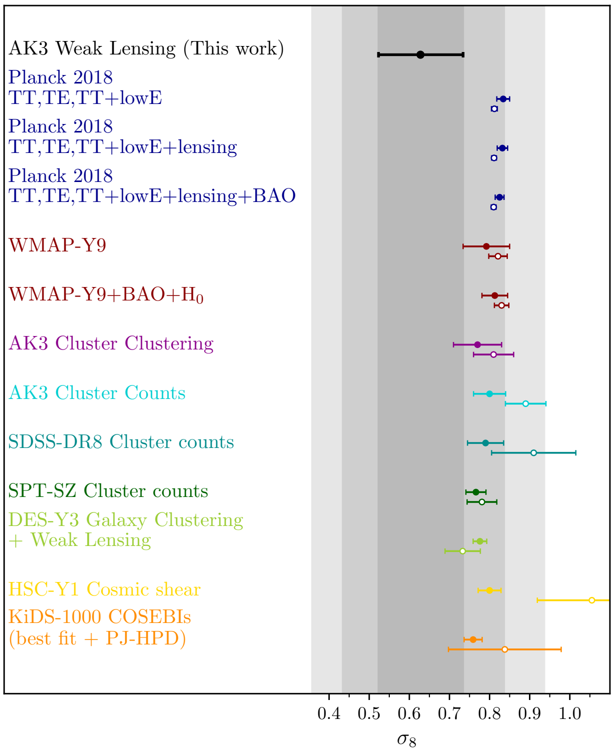

Figure 11. Comparison with literature results. Our reference σ_8 value is obtained assuming the Tinker et al. (2010) model. We show the median, 16*th* and 84*th* percentiles. We present from top to bottom results obtained in this work (black), Planck Collaboration et al. (2020) (blue), Hinshaw et al. (2013) (red), Nanni et al. (prep) (magenta), Lesci et al. (2020) (cyan), Costanzi et al. (2019) (turquoise), Bocquet et al. (2019) (green), DES Collaboration et al. (2021) (light green), Hikage et al. (2019) (yellow) and Asgari et al. (2021) (orange). We show the relative constraints on σ_8 in a free cosmology (empty dots) and assuming $\Omega_m = 0.3$ (filled dots). The shaded regions correspond to the 99.7%, 95% and 68% confidence intervals.

still have to be taken carefully into consideration because of the poor constraint. The gap of σ_8 results from Seljak & Warren (2004) to Tinker et al. (2010) or Bhattacharya et al. (2011) also stresses the importance of the theoretical model when constraining cosmological parameters in a stacked WL analysis.

7 SUMMARY AND DISCUSSION

We investigated the halo bias from a revised stacked WL analysis presented in Bellagamba et al. (2019) on 6961 AMICO galaxy clusters identified in the recent KiDS-DR3 field. We divided the catalog into 14 bins in redshift and richness and for each of them we derived the excess surface mass density profiles. We selected sources from their photometric redshifts or *gri*-colors. We compared the two color-color selections presented in Medezinski et al. (2010) and Oguri et al. (2012) with COSMOS accurate photometric redshifts in order to carry the most effective cut out for KiDS sources. The final WL profiles are obtained by subtracting the signals given by a large number of random lenses. We computed the covariances by applying the bootstrap technique to the cluster and random shears, and added together the matrices to assess the uncertainties of the final profiles. We performed the Bayesian inference of the halo parameters with a MCMC method run over a radial range from 0.2 to 30 Mpc/h.

We modelled the WL signal from galaxy clusters by including the contribution of a truncated version of the NFW profile, which includes a correction for the off-centered galaxy clusters and a correlated matter term originating from the linear matter power spectrum.

Our measurements of the halo mass within 3.16 Mpc/h agree with the results obtained by Bellagamba et al. (2019) with a relative difference estimated on the order of 5%. From the full radial range, we obtained halo masses and derived the mass-richness relation given by Equation (36) with $\alpha = 0.007 \pm 0.019$, $\beta = 1.72 \pm 0.09$ and $\gamma = -1.35 \pm 0.70$, in remarkable agreement with Bellagamba et al. (2019). We also studied the halo mass-concentration relation modelled as in Equation (37). We obtained $\alpha = 0.62 \pm 0.10$, $\beta = -0.32 \pm 0.24$ and $\gamma = 0.71 \pm 2.51$. The constraints show a steeper but consistent relation with respect to theoretical results derived from the analysis of numerical simulations.

Our results on the halo bias are consistent with previous measurements and with simulations in a ΛCDM framework. Some data points are affected by a relatively low SNR, as the number of galaxy clusters in the given redshift-richness bins is limited. These effects and the small number of richness bins prohibited the detection of any trend for the halo bias with the effective redshift of the clusters in each redshift bin. The measurements over the stacked profile of the full AK3 catalog give $b_h\sigma_8^2 = 1.2 \pm 0.1$ located at $M_{200c} = 4.9 \pm 0.3 \times 10^{13} M_\odot/h$, in good agreement with ΛCDM predictions.

In the fitting procedure, the halo bias parameter is degenerate with the amplitude of the power spectrum σ_8. This last cosmological parameter is fitted with the theoretical mass-bias relations given in Seljak & Warren (2004), Tinker et al. (2010) and Bhattacharya et al. (2011). Assuming a flat ΛCDM cosmological model with $\Omega_m = 1 - \Omega_\Lambda = 0.3$, we found $\sigma_8 = 1.01^{+0.05}_{-0.05}$; $0.63^{+0.11}_{-0.10}$; $0.66^{+0.19}_{-0.27}$ for the three above mentioned relations. These results present slight deviations with respect to the latest WMAP or Planck σ_8 estimates, but agree within 2σ, with the exception of the results based on the Seljak & Warren (2004) posterior, which shows a sharper distribution centered on a larger value of σ_8. Other works, based on cluster clustering, cluster counts and cosmic shear analyses, report values of σ_8 in agreement with our estimates within 2σ, either assuming Ω_m fixed or free. The importance of the choice of the theoretical model for the halo bias also highlights the difficulty in constraining this cosmological parameter in a WL analysis.

For future work, we are interested in combining the inference on σ_8 with Ω_m to constrain the parameter $S_8 \equiv \sigma_8\sqrt{\Omega_m/0.3}$, which would compliment the study on σ_8 in this paper and Ω_m in Giocoli et al. (2021). Specifically, Giocoli et al. (2021) provided a similar analysis on the AK3 galaxy clusters with a stacked shear profile up to 35 Mpc/h and recovered consistent mass measurements with respect to Bellagamba et al. (2019) and this paper. The binning scheme differs from this work since the cluster amplitude as a binning property was favored, while we opted for richness. This mainly affects the scaling relation between the mass and the cluster richness or amplitude. The impact of the truncation radius has been deeply investigated in Giocoli et al. (2021), here we performed a robust analysis of the covariances and cross-covariances and studied the effects of the lensing signal systematics in each patch of the field through the random signal. Both studies were carried out with independent numerical pipelines and followed a process of cross-validation among the KiDS collaboration.

The methodology used in this work will constitute a baseline for future KiDS Data Releases (Kuijken et al. 2019) and similar but larger data sets that combine cluster and shear catalogs. Upcoming surveys, such as *Euclid* (Euclid Collaboration et al. 2019) and LSST (LSST Dark Energy Science Collaboration 2012), will provide promising data sets allowing for further statistical analyses in deeper and wider fields. These data sets will be fundamental for the study of the halo properties such as mass and bias with stacked WL analyses, and will allow robust estimates of the main cosmological parameters.

ACKNOWLEDGEMENTS

The authors acknowledge Shahab Joudaki for the thorough review of the manuscript. LI is grateful to Nicolas Martinet for a relevant discussion on the multiplicative bias and BPZ PDFs, and Peter Melchior for his fruitful comments on the cross-covariance.

Based on data products from observations made with ESO Telescopes at the La Silla Paranal Observatory under programme IDs 177.A-3016, 177.A-3017 and 177.A-3018, and on data products produced by Target/OmegaCEN, INAF-OACN, INAF-OAPD and the KiDS production team, on behalf of the KiDS consortium. OmegaCEN and the KiDS production team acknowledge support by NOVA and NWO-M grants. Members of INAF-OAPD and INAF-OACN also acknowledge the support from the Department of Physics & Astronomy of the University of Padova, and of the Department of Physics of Univ. Federico II (Naples). We acknowledge the KiDS collaboration for the public data realises and the various scientists working within it for the fruitful and helpful discussions. MS acknowledges financial contribution from contract ASI-INAF n.2017-14-H.0 and contract INAF mainstream project 1.05.01.86.10. CG, FM and LM acknowledge the grants ASI n.I/023/12/0, ASI-INAF n. 2018-23-HH.0 and PRIN MIUR 2015 Cosmology and Fundamental Physics: illuminating the Dark Universe with Euclid". CG and LM are also supported by PRIN-MIUR 2017 WSCC32 "Zooming into dark matter and proto-galaxies with massive lensing clusters". CG acknowledges support from the Italian Ministry of Foreign Affairs and International Cooperation, Directorate General for Country Promotion.

This paper makes use of the astronomical data analysis software `TOPCAT` (Taylor 2005), and packages available in the Python's open scientific ecosystem, including `numpy` (Harris et al. 2020), `scipy` (Virtanen et al. 2020), `matplotlib` (Hunter 2007), `astropy` (Astropy Collaboration et al. 2018), `emcee` (Foreman-Mackey et al. 2013), `ray` (Liang et al. 2017; Moritz et al. 2017), `colossus` (Diemer 2018) and `cluster toolkit`[4]. Data analysis has been carried out with Fornax Physics Department computing cluster of the University Federico II of Naples.

APPENDIX A: COVARIANCES

Stacked WL signals are a comprehensive assessment of the profile given by a galaxy cluster population, but possible deviations arise due to statistical uncertainties and systematic biases. While the systematic noise can be efficiently corrected for using the random fields (see Appendix B), the statistical uncertainty of the stacked shear is essentially described by its covariance matrix. It can be decomposed into the contributions of large intrinsic variations of the shapes of galaxies (shape noise, e.g. Mandelbaum et al. 2013; Sereno & Ettori 2015; Viola et al. 2015), correlated and uncorrelated structures (e.g. Hoekstra 2001, 2003; Hoekstra et al. 2011; Umetsu et al. 2011; Gruen et al. 2015), and intrinsic scatter of the mass measurement (e.g. Metzler et al. 2001; Gruen et al. 2011; Becker & Kravtsov 2011; Gruen et al. 2015). The statistical uncertainty is dominated by the shape noise of the sources (McClintock et al. 2019), which has already been accounted for in Equation (11). However, since galaxies contribute to the signal in different radial and redshift-richness bins, we may expect covariance terms to be significant between radii in identical and distinct stacked profiles. We therefore construct the covariance matrix from each pair of radial bins ij over $\mathrm{N} = 1000$ bootstrap realizations of the source catalog,

$$\mathrm{C_{ij}} = \frac{\sum_{\mathrm{n}\in\mathrm{N}} \left(\widetilde{\Delta\Sigma}_{\mathrm{i,n}} - \overline{\widetilde{\Delta\Sigma}}_{\mathrm{i}}\right)\left(\widetilde{\Delta\Sigma}_{\mathrm{j,n}} - \overline{\widetilde{\Delta\Sigma}}_{\mathrm{j}}\right)}{\mathrm{N}-1}\,, \tag{A1}$$

with $\overline{\widetilde{\Delta\Sigma}} = \sum_{\mathrm{n}\in\mathrm{N}} \widetilde{\Delta\Sigma}_{\mathrm{n}}/\mathrm{N}$.

Figure A1 displays the correlation matrices $\mathrm{R_{ij}} = \mathrm{C_{ij}}/\sqrt{\mathrm{C_{ii}C_{jj}}}$ derived from the covariance profile for the cluster bin $\mathrm{z_l}\otimes\lambda_* = [0.3, 0.45[\otimes[30, 45[$ and the cross-covariances with the low and high redshift-richness bins $[0.1, 0.3[\otimes[0, 15[$ and $[0.45, 0.6[\otimes[55, 140[$. The correlation matrix does not show any strong contribution from off-diagonal terms, while the diagonal components encompass the majority of the statistical noise. We still consider the full covariance of each individual cluster bin to quantify the statistical uncertainty of the stacked WL signal, in order to account for the dependency between the radii of the bin when fitting the data. Furthermore, we combine uncertainties of the galaxy cluster signal and the random signal detailed in Appendix B by summing their covariances. These matrices are used when measuring the halo parameters in Section 5.

APPENDIX B: RANDOM FIELDS

We performed stacked shear analysis around random lens points following the same process used in Section 3. This spurious signal characterizes the residual systematic effects, usually coming either from the edges of the detector (Miyatake et al. 2015), the imperfect correction of optical distortion (Mandelbaum et al. 2005) or the incorrect estimation of

[4] https://github.com/tmcclintock/cluster_toolkit/

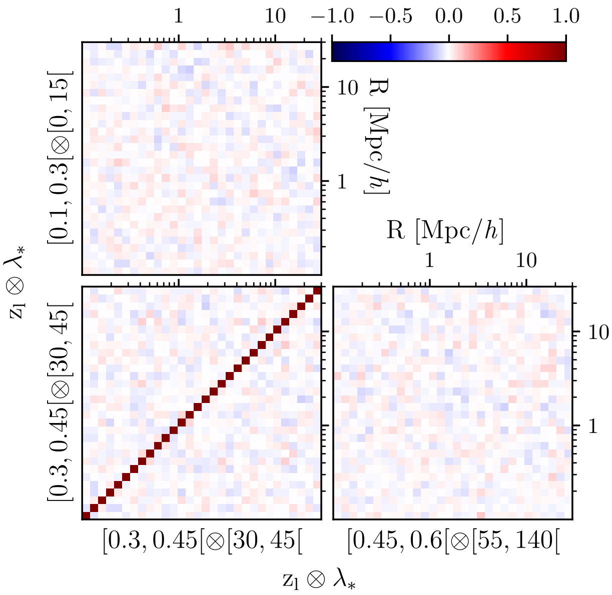

Figure A1. Bootstrap correlation matrix of $\widetilde{\Delta\Sigma}$, computed from $z_l \otimes \lambda_*$ selected bins. Here, we investigate the bin $[0.3, 0.45[\otimes[30, 45[$ correlated with itself (bottom left panel), with the bin $[0.1, 0.3[\otimes[0, 15[$ (top panel) and with the bin $[0.45, 0.6[\otimes[55, 140[$ (bottom right panel). The statistical uncertainty is mainly provided by the diagonal terms, while the off-diagonal terms are nearly consistent with zero, suggesting that radial and redshift-richness bins do not correlate.

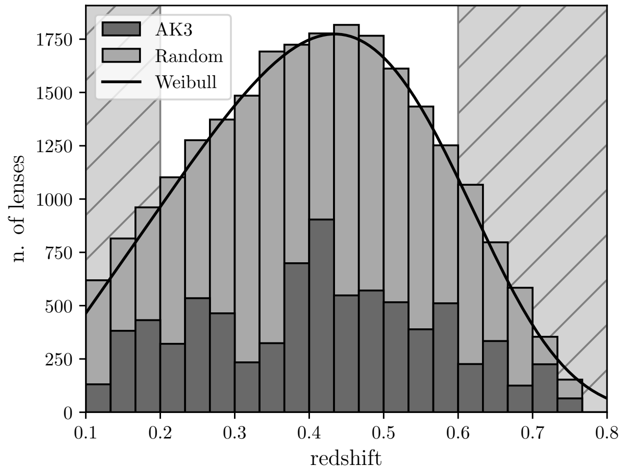

Figure B1. The redshift distribution of AK3 and random lenses. The random redshifts are sampled with an inverse transform method from the PDF described in Equation (B1). The black curve describes this function and aims at simulating the distribution of the AK3 redshifts. The shaded regions delineate the redshift range of selected clusters discussed in Section 3.3.2.

the redshift (McClintock et al. 2019). If none of these effects impact the profile, the random stacked shear should vanish, while it deviates from zero as soon as the systematic bias is apparent (Miyatake et al. 2015). The random signal is finally subtracted from the shear profiles of the stacked bins to correct for these uncertainties.

We built a random catalog over the full [RA,Dec] sources range considering the K450 footprint of masked areas. Each equatorial random position is uniformly sampled over a `Nside=2048` pixel HEALPIX map and associated to a redshift random position. We sample random redshift from an inverse transform method, assuming AK3 redshifts to follow a Weibull distribution (e.g. Pen et al. 2003),

$$n \equiv \frac{\beta}{\Gamma\left(\frac{1+\alpha}{\beta}\right)} \frac{1}{z_0} \left(\frac{z_l}{z_0}\right)^{\alpha} \exp\left[-\left(\frac{z_l}{z_0}\right)^{\beta}\right] . \tag{B1}$$

The parameters α, β and z_0 are marginalized and constrained to track the real distribution of AK3 redshifts. We find

- $\alpha = 1.06$
- $\beta = 4.81$
- $z_0 = 0.59$

Figure B1 shows the distribution of random and AK3 lenses. Random redshifts follow the Weibull distribution and tend to recover the same distribution as clusters of galaxies for a more realistic representation of the random signal.

Rykoff et al. (2016) suggest an efficient way to generate a random richness component from a depth map of the source catalog. However, their study is based on the redMaPPer algorithm for cluster detection which considerably differs from AMICO. Moreover, due to the absence of a depth map in K450 we cannot assign richness parameters to our random catalog. Still, the presence of random redshifts is a robust feature for the random catalog as we can associate the stacked random signal to each redshift bin. Finally, the number of random points exceed the number of real galaxy clusters by 15976 lenses in order to fully cover the 3D field of AK3 lenses.

A simple test to check the correct processing of the subtraction of the systematics is to look at the tangential and cross stacked shear profile of the random lenses. The top panels of Figure B2 presents three different profiles derived from AK3 cross, random cross and random tangential signals. While the tangential component of random points remain consistent with zero, the cross signal of the lower redshift bin reveals that systematics largely impact the shear in the last radial bins, and consequently might distort the estimation of the halo bias if no correction is applied. Looking deeply in the cross signal of the five KiDS DR3 patches, we observe that only three of them are significantly affected. We relate this systematic to the geometry of the field, which at some point is irregular in those specific patches. Indeed, since the lower redshift bin needs a larger field of view (FoV) to compute stacked shear over a fixed large radial profile, the resulting signal is much more sensitive to the discontinuities of the field (e.g. isolated tiles). Hamana et al. (2013) suggest that the point spread function (PSF) in the shape measurement of galaxies located at the edge of the FoV is imperfectly corrected. This biased PSF anisotropy sensitively impacts the shear of galaxies, which consequently breaks the symmetry of the intrinsic ellipticity and leads to a non-zero cross component. However, since the subtraction of the two signals gives a signal consistent with zero, the correction suppresses this systematic effect and the final version of the data is ready for the analysis (see Section 5).

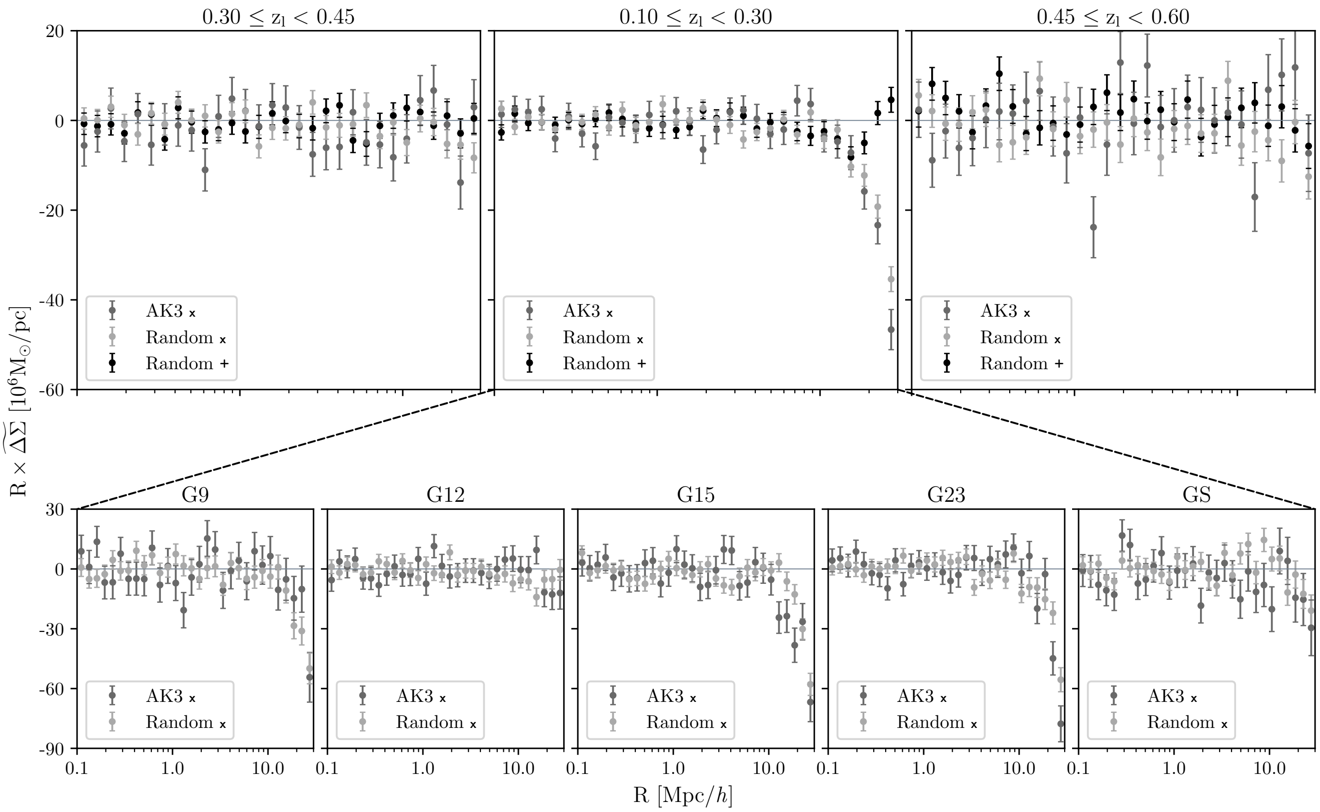

Figure B2. Differential density profiles of the cross component of AK3 lenses and the cross and tangential components of random lenses in the three redshift bins. The cross signals in the five KiDS DR3 patches of the lower redshift bin are also displayed. A significant deviation from the zero horizontal line indicates the presence of a systematic effect. It reveals an incomplete correction of the PSF of galaxies located close to the FoV edge.

APPENDIX C: COLOR-COLOR SELECTIONS

In this section we compare the color-color selection discussed in Section 3.3.1 with an additional *gri*-CC cut. More specifically, Figure 3 in Medezinski et al. (2010) lays out in colored areas various populations of sources for three different Subaru clusters (e.g. cluster members in green). The paper shows in particular *gri*-CC selected sources in the galaxy cluster A1703, for which Broadhurst et al. (2008) and Oguri et al. (2009) initially performed a WL analysis. Two singular areas in the color-color plane are clearly identified as background sources of A1703, efficiently selected at $z_s \gtrsim 0.6$ and displayed in blue/red in the figure of the study. They present the following segmentation

$$[(g-r < 2.17(r-i) - 0.37) \wedge (g-r < 1.85 - 0.6(r-i))] \\ \vee (g-r < 0.47 - 0.4(r-i)) \vee (r-i < -0.06)\ . \tag{C1}$$

In order to evaluate the efficiency of the *gri*-CC cuts explored in this study (Equations 14 and C1), we are interested in testing them over the COSMOS 30-Bands photometric catalog[5] (Ilbert et al. 2009). The full sample consists of 385,065 galaxies with very accurate photometric redshifts reliable up to magnitude $i < 25$. In Figure C1, we present the COSMOS sources selected with the two *gri*-CC criteria. As a comparison, we generate evolving tracks using the GALEV[6] code (Kotulla et al. 2009) for the Hubble - de Vaucouleurs galaxy morphological types (Non-barred spiral Sa-type, Barred-spiral Sb-type, Lenticular S0-type and Elliptical E-type). We are interested in the contamination of objects belonging to the redshift range of $0.2 < z_s < 0.6$, in agreement with the selection of clusters done in Section 3.3.2. The cut shown in Oguri et al. (2012) encompasses 125,754 galaxies with 96.2% background sources for the corresponding redshift threshold $z_s \geq 0.6$. On the other hand, the selection done by Medezinski et al. (2010) counts 170,429 (35.5% more), and 94.6% of them lie over $z_s \geq 0.6$. Both cuts efficiently remove contaminating members, we see a higher number of background COSMOS galaxies for Equation (C1), while the contamination fraction given by Equation (14) is fully consistent with Sereno et al. (2017).

Besides this observation, a more reliable analysis would be to consider the cross-matched catalog COSMOS⊗K450 as the 47,619 COSMOS sources within K450. The lower panel of the figure provides this distribution and shows 14,857 of them to be filtered by Oguri et al. (2012) and 20,540 by Medezinski et al. (2010). Respectively, 94.3% and 85.2% of selected sources appear to be uncontaminated. These statis-

[5] https://irsa.ipac.caltech.edu/data/COSMOS/

[6] http://www.galev.org/

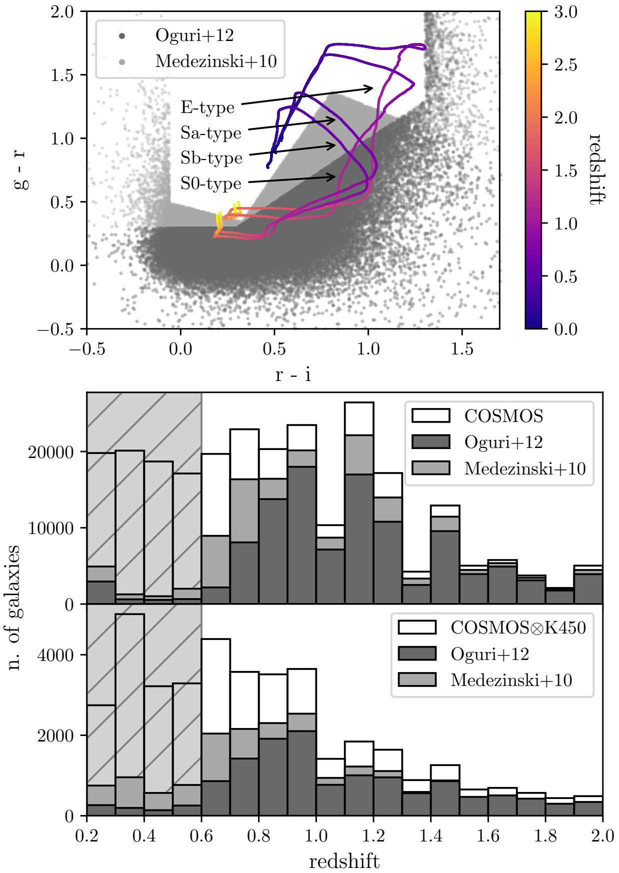

Figure C1. *Top panel*: (r-i) vs (g-r) diagram. We show the selections discussed in this article, following previous complementary works (Equations 14 and C1, Oguri et al. 2012; Medezinski et al. 2010, respectively). We additionally show the evolving tracks of spiral, lenticular and elliptical galaxies in the *gri*-CC plane obtained using the GALEV code (Kotulla et al. 2009). *Bottom panels*: COSMOS (Ilbert et al. 2009) and COSMOS⊗K450 photometric redshift distributions for the full samples and for their dedicated *gri*-CC selections. The shaded region highlights the contamination area, which corresponds to the cluster redshift range $[0.1, 0.6[$ covered in Section 3.3.2.

tics highlights a higher contamination from Equation (C1) and a more efficient removal of contaminated K450 sources for Equation (14), but still has some drawbacks due to the limited number of objects. Another explanation for the main difference between the two cuts is the unequal reduction of galaxies from COSMOS to the cross match data set. K450 sources in COSMOS are few at $z_s > 1$, where Medezinski et al. (2010) is consequently selecting more sources than Oguri et al. (2012) in COSMOS only, while the proportion of galaxies at $z_s < 1$ remains high in both catalogs. In that sense, we prefer to retain Equation (14) as the principal *gri*-CC selection for this work.

REFERENCES

Angelinelli M., Vazza F., Giocoli C., Ettori S., Jones T. W., Brunetti G., Brüggen M., Eckert D., 2020, MNRAS, 495, 864
Asgari M., et al., 2021, A&A, 645, A104
Astropy Collaboration et al., 2018, AJ, 156, 123
Baltz E. A., Marshall P., Oguri M., 2009, J. Cosmology Astropart. Phys., 2009, 015
Bartelmann M., Schneider P., 2001, physrep, 340, 291
Becker M. R., Kravtsov A. V., 2011, ApJ, 740, 25
Bellagamba F., Maturi M., Hamana T., Meneghetti M., Miyazaki S., Moscardini L., 2011, mnras, 413, 1145
Bellagamba F., Roncarelli M., Maturi M., Moscardini L., 2018, MNRAS, 473, 5221
Bellagamba F., et al., 2019, MNRAS, 484, 1598
Benítez N., 2000, ApJ, 536, 571
Bhattacharya S., Heitmann K., White M., Lukić Z., Wagner C., Habib S., 2011, ApJ, 732, 122
Bocquet S., et al., 2019, ApJ, 878, 55
Borgani S., 2008, Cosmology with Clusters of Galaxies. Springer Netherlands, p. 24, doi:10.1007/978-1-4020-6941-3_9
Broadhurst T., Takada M., Umetsu K., Kong X., Arimoto N., Chiba M., Futamase T., 2005, The Astrophysical Journal Letters, 619, L143
Broadhurst T., Umetsu K., Medezinski E., Oguri M., Rephaeli Y., 2008, ApJ, 685, L9
Bullock J. S., Kolatt T. S., Sigad Y., Somerville R. S., Kravtsov A. V., Klypin A. A., Primack J. R., Dekel A., 2001, MNRAS, 321, 559
Capaccioli M., Schipani P., 2011, The Messenger, 146, 2
Child H. L., Habib S., Heitmann K., Frontiere N., Finkel H., Pope A., Morozov V., 2018, ApJ, 859, 55
Coe D., et al., 2012, ApJ, 757, 22
Cole S., Kaiser N., 1989, MNRAS, 237, 1127
Costanzi M., et al., 2019, MNRAS, 488, 4779
Covone G., Sereno M., Kilbinger M., Cardone V. F., 2014, apjl, 784, L25
DES Collaboration et al., 2021, arXiv e-prints, p. arXiv:2105.13549
Despali G., Giocoli C., Tormen G., 2014, MNRAS, 443, 3208
Despali G., Giocoli C., Angulo R. E., Tormen G., Sheth R. K., Baso G., Moscardini L., 2016, MNRAS, 456, 2486
Diemer B., 2018, ApJS, 239, 35
Diemer B., Joyce M., 2019, ApJ, 871, 168
Diemer B., Kravtsov A. V., 2015, ApJ, 799, 108
Donahue M., et al., 2016, ApJ, 819, 36
Driver S. P., et al., 2011, MNRAS, 413, 971
Duffy A. R., Schaye J., Kay S. T., Dalla Vecchia C., 2008, MNRAS, 390, L64
Dutton A. A., Macciò A. V., 2014, MNRAS, 441, 3359
Eisenstein D. J., Hu W., 1998, ApJ, 496, 605
Eisenstein D. J., Hu W., 1999, ApJ, 511, 5
Euclid Collaboration et al., 2019, A&A, 627, A23
Fenech Conti I., Herbonnet R., Hoekstra H., Merten J., Miller L., Viola M., 2017, mnras, 467, 1627
Foreman-Mackey D., Hogg D. W., Lang D., Goodman J., 2013, PASP, 125, 306
Fuller W. A., 1987, Measurement error models. Wiley-Interscience
Gelman A., Rubin D. B., 1992, Statistical Science, 7, 457
George M. R., et al., 2012, apj, 757, 2
Giocoli C., Tormen G., Sheth R. K., van den Bosch F. C., 2010a, MNRAS, 404, 502
Giocoli C., Bartelmann M., Sheth R. K., Cacciato M., 2010b, MNRAS, 408, 300
Giocoli C., Tormen G., Sheth R. K., 2012, MNRAS, 422, 185
Giocoli C., et al., 2021, arXiv e-prints, p. arXiv:2103.05653
Golse G., Kneib J. P., 2002, A&A, 390, 821
Goodman J., Weare J., 2010, Communications in Applied Mathematics and Computational Science, 5, 65
Gruen D., Bernstein G. M., Lam T. Y., Seitz S., 2011, MNRAS, 416, 1392
Gruen D., Seitz S., Becker M. R., Friedrich O., Mana A., 2015, MNRAS, 449, 4264

Hamana T., Miyazaki S., Okura Y., Okamura T., Futamase T., 2013, PASJ, 65, 104
Harris C. R., et al., 2020, Nature, 585, 357âĂŞ362
Heymans C., et al., 2012, mnras, 427, 146
Hikage C., et al., 2019, PASJ, 71, 43
Hildebrandt H., et al., 2012, mnras, 421, 2355
Hildebrandt H., et al., 2017, mnras, 465, 1454
Hinshaw G., et al., 2013, ApJS, 208, 19
Hoekstra H., 2001, A&A, 370, 743
Hoekstra H., 2003, MNRAS, 339, 1155
Hoekstra H., Donahue M., Conselice C. J., McNamara B. R., Voit G. M., 2011, apj, 726, 48
Hunter J. D., 2007, Computing in Science & Engineering, 9, 90
Ilbert O., et al., 2009, apj, 690, 1236
Ishiyama T., et al., 2020, arXiv e-prints, p. arXiv:2007.14720
Johnston D. E., et al., 2007a, arXiv e-prints, p. arXiv:0709.1159
Johnston D. E., Sheldon E. S., Tasitsiomi A., Frieman J. A., Wechsler R. H., McKay T. A., 2007b, apj, 656, 27
Kaiser N., 1984, ApJ, 284, L9
Kilbinger M., 2015, Reports on Progress in Physics, 78, 086901
Kitching T. D., Miller L., Heymans C. E., van Waerbeke L., Heavens A. F., 2008, MNRAS, 390, 149
Kotulla R., Fritze U., Weilbacher P., Anders P., 2009, MNRAS, 396, 462
Kuijken K., 2011, The Messenger, 146, 8
Kuijken K., et al., 2015, mnras, 454, 3500
Kuijken K., et al., 2019, A&A, 625, A2
LSST Dark Energy Science Collaboration 2012, arXiv e-prints, p. arXiv:1211.0310
Lesci G. F., et al., 2020, arXiv e-prints, p. arXiv:2012.12273
Liang E., Liaw R., Nishihara R., Moritz P., Fox R., Gonzalez J., Goldberg K., Stoica I., 2017, CoRR, abs/1712.09381
Mandelbaum R., et al., 2005, MNRAS, 361, 1287
Mandelbaum R., Slosar A., Baldauf T., Seljak U., Hirata C. M., Nakajima R., Reyes R., Smith R. E., 2013, mnras, 432, 1544
Maturi M., Meneghetti M., Bartelmann M., Dolag K., Moscardini L., 2005, aap, 442, 851
Maturi M., Bellagamba F., Radovich M., Roncarelli M., Sereno M., Moscardini L., Bardelli S., Puddu E., 2019, MNRAS, 485, 498
McClintock T., et al., 2019, MNRAS, 482, 1352
Medezinski E., et al., 2007, apj, 663, 717
Medezinski E., Broadhurst T., Umetsu K., Oguri M., Rephaeli Y., Ben'itez N., 2010, mnras, 405, 257
Melchior P., et al., 2017, mnras, 469, 4899
Meneghetti M., Rasia E., Merten J., Bellagamba F., Ettori S., Mazzotta P., Dolag K., Marri S., 2010, A&A, 514, A93
Meneghetti M., et al., 2014, ApJ, 797, 34
Merten J., et al., 2015a, ApJ, 806, 4
Merten J., et al., 2015b, ApJ, 806, 4
Metzler C. A., White M., Loken C., 2001, ApJ, 547, 560
Miller L., Kitching T. D., Heymans C., Heavens A. F., van Waerbeke L., 2007, MNRAS, 382, 315
Miller L., et al., 2013, MNRAS, 429, 2858
Miyatake H., et al., 2015, ApJ, 806, 1
Mo H. J., White S. D. M., 1996, MNRAS, 282, 347
Mo H. J., Jing Y. P., White S. D. M., 1996, MNRAS, 282, 1096
Moritz P., et al., 2017, CoRR, abs/1712.05889
Nanni F., Marulli L. Moscardini F., Veropalumbo e., in prep., AMICO galaxy clusters in KiDS-DR3: constraints on cosmological parameters and on the mass-richness relation from the clustering of galaxy clusters, in preparation
Navarro J. F., Frenk C. S., White S. D. M., 1996, ApJ, 462, 563
Navarro J. F., Frenk C. S., White S. D. M., 1997, ApJ, 490, 493
Neto A. F., et al., 2007, MNRAS, 381, 1450
Oguri M., Hamana T., 2011, MNRAS, 414, 1851
Oguri M., Takada M., Umetsu K., Broadhurst T., 2005, The Astrophysical Journal, 632, 841
Oguri M., et al., 2009, ApJ, 699, 1038
Oguri M., Bayliss M. B., Dahle H., Sharon K., Gladders M. D., Natarajan P., Hennawi J. F., Koester B. P., 2012, MNRAS, 420, 3213
Peebles P. J. E., 1980, The large-scale structure of the universe. Princeton University Press
Peebles P. J. E., 1993, Principles of Physical Cosmology. Princeton University Press
Pen U.-L., Lu T., van Waerbeke L., Mellier Y., 2003, MNRAS, 346, 994
Planck Collaboration et al., 2020, A&A, 641, A6
Postman M., et al., 2012, ApJS, 199, 25
Press W. H., Schechter P., 1974, ApJ, 187, 425
Radovich M., et al., 2017, aap, 598, A107
Rasia E., Tormen G., Moscardini L., 2004, MNRAS, 351, 237
Rasia E., et al., 2006, MNRAS, 369, 2013
Rykoff E. S., et al., 2016, ApJS, 224, 1
Schneider P., 2006, in Proceedings, 33rd Advanced Saas Fee Course on Gravitational Lensing: Strong, Weak, and Micro: Les Diablerets, Switzerland, April 7-12, 2003. pp 269–451 (arXiv:astro-ph/0509252), doi:10.1007/978-3-540-30310-7_3
Seitz C., Schneider P., 1997, A&A, 318, 687
Seljak U., Warren M. S., 2004, MNRAS, 355, 129
Seljak U., et al., 2005, Phys. Rev. D, 71, 043511
Sereno M., Covone G., 2013, MNRAS, 434, 878
Sereno M., Ettori S., 2015, mnras, 450, 3675
Sereno M., Umetsu K., 2011, MNRAS, 416, 3187
Sereno M., Giocoli C., Ettori S., Moscardini L., 2015a, MNRAS, 449, 2024
Sereno M., Veropalumbo A., Marulli F., Covone G., Moscardini L., Cimatti A., 2015b, MNRAS, 449, 4147
Sereno M., Covone G., Izzo L., Ettori S., Coupon J., Lieu M., 2017, MNRAS, 472, 1946
Sereno M., et al., 2018, Nature Astronomy, 2, 744
Sereno M., et al., 2020, MNRAS, 497, 894
Sheldon E. S., et al., 2004, aj, 127, 2544
Sheth R. K., Tormen G., 1999, MNRAS, 308, 119
Sheth R. K., Mo H. J., Tormen G., 2001, MNRAS, 323, 1
Simet M., McClintock T., Mandelbaum R., Rozo E., Rykoff E., Sheldon E., Wechsler R. H., 2017, mnras, 466, 3103
Singh S., Mandelbaum R., Seljak U., Slosar A., Vazquez Gonzalez J., 2017, MNRAS, 471, 3827
Skibba R. A., Macciò A. V., 2011, MNRAS, 416, 2388
Springel V., White S. D. M., Tormen G., Kauffmann G., 2001, MNRAS, 328, 726
Takada M., Jain B., 2003, MNRAS, 340, 580
Takahashi R., Sato M., Nishimichi T., Taruya A., Oguri M., 2012, ApJ, 761, 152
Taylor M. B., 2005, in Shopbell P., Britton M., Ebert R., eds, Astronomical Society of the Pacific Conference Series Vol. 347, Astronomical Data Analysis Software and Systems XIV. p. 29
Tinker J. L., Weinberg D. H., Zheng Z., Zehavi I., 2005, ApJ, 631, 41
Tinker J. L., Robertson B. E., Kravtsov A. V., Klypin A., Warren M. S., Yepes G., Gottlöber S., 2010, ApJ, 724, 878
Tormen G., 1998, MNRAS, 297, 648
Umetsu K., Broadhurst T., Zitrin A., Medezinski E., Coe D., Postman M., 2011, ApJ, 738, 41
Umetsu K., et al., 2014, ApJ, 795, 163
Viola M., et al., 2015, MNRAS, 452, 3529
Virtanen P., et al., 2020, Nature Methods, 17, 261
Voit G. M., 2005, Reviews of Modern Physics, 77, 207
White S. D. M., Rees M. J., 1978, MNRAS, 183, 341
Yang X., Mo H. J., Van Den Bosch F. C., Jing Y. P., Weinmann S. M., Meneghetti M., 2006, Monthly Notices of the Royal Astronomical Society, 373, 1159
Zitrin A., Broadhurst T., Barkana R., Rephaeli Y., Benítez N., 2011a, MNRAS, 410, 1939

Zitrin A., Broadhurst T., Coe D., Umetsu K., Postman M., Benítez N., Meneghetti M., et al. M., 2011b, ApJ, 742, 117
de Jong J. T. A., Verdoes Kleijn G. A., Kuijken K. H., Valentijn E. A., 2013, Experimental Astronomy, 35, 25
de Jong J. T. A., et al., 2015, aap, 582, A62
de Jong J. T. A., et al., 2017, aap, 604, A134
van Uitert E., Gilbank D. G., Hoekstra H., Semboloni E., Gladders M. D., Yee H. K. C., 2016, A&A, 586, A43

The data underlying this article will be shared on reasonable request to the corresponding author.